



Mixed experimental/theoretical study of quantum dot sensitized solar cells

Alexandra Szemjonov

► To cite this version:

Alexandra Szemjonov. Mixed experimental/theoretical study of quantum dot sensitized solar cells. Chemical Physics [physics.chem-ph]. Université Pierre et Marie Curie - Paris VI, 2016. English. NNT : 2016PA066301 . tel-01467109

HAL Id: tel-01467109

<https://theses.hal.science/tel-01467109>

Submitted on 14 Feb 2017

HAL is a multi-disciplinary open access archive for the deposit and dissemination of scientific research documents, whether they are published or not. The documents may come from teaching and research institutions in France or abroad, or from public or private research centers.

L'archive ouverte pluridisciplinaire **HAL**, est destinée au dépôt et à la diffusion de documents scientifiques de niveau recherche, publiés ou non, émanant des établissements d'enseignement et de recherche français ou étrangers, des laboratoires publics ou privés.

THESE DE DOCTORAT DE
L'UNIVERSITE PIERRE ET MARIE CURIE

**MIXED EXPERIMENTAL/THEORETICAL STUDY OF QUANTUM DOT
SENSITIZED SOLAR CELLS**

Présentée le 22 Septembre 2016 par

ALEXANDRA SZEMJONOV

Pour obtenir le grade de

Docteur de l'Université Pierre et Marie Curie

Ecole doctorale de Chimie Physique et Chimie Analytique de Paris Centre
(ED388)

Devant un jury composé de :

Pr. Alexis Markovits	Professeur – Université Pierre et Marie Curie	Président du jury
Pr. Régis Gautier	Professeur – Ecole Nationale Supérieure de Chimie de Rennes	Rapporteur
Pr. Thierry Toupance	Professeur – Université Bordeaux 1	Rapporteur
Dr. Pascal Boulet	Maître de Conférences-HDR - Aix-Marseille Université	Examineur
Dr. Peter Reiss	Chercheur – CEA Grenoble	Examineur
Dr. Sandrine Ithurria	Maître de Conférences – Ecole Supérieure de Physique et de Chimie Industrielles	Examinatrice
Dr. Thierry Pauporté	Directeur de Recherche – Institut de Recherche de Chimie Paris	Directeur de thèse
Dr. Frédéric Labat	Maître de Conférences - Institut de Recherche de Chimie Paris	Co-encadrant

ACKNOWLEDGEMENTS

I owe my sincere thanks to many people without whom the realization of this work would not have been possible.

First of all, I am much obliged to my thesis supervisors Thierry Pauporté and Frédéric Labat who attentively coordinated my work and who were always available when I needed help or advice. I would like to thank Ilaria Ciofini for her invaluable support, insights and feedback on my work.

I am indebted to my fellow Master, PhD students and postdocs in Chimie ParisTech who I met in the last three years: Jasmina, Diane, Chloé, Liam, Ashwani, Stefania, Luca, Indira, Chiara, Stefania, Vinca, Davide, Marianna, Li, Alistar, Marta, Malvina, Federica, Cecilia, Alessandra, Enzo, Daria, Vincenzo, Antonio, Valentino in the CTM lab, and Sana, Jie, Yuly, Mongia, Ricardo, Maria, Pengjiu, Zhipeng, Suchinda, Karmel, Mariem, Dorra, Akiko, Deborah, Jadwiga, Fanny, Natalie, Sacha, Atul, Jenny, John, Jinlei, Federico, Simon in the MPOE and other labs of the school, and the list is probably not even exhaustive. I received a lot of scientific and friendly help from you, and we spent many great moments inside and outside of the school. I owe many thanks to Patrick for his help with informatical problems, Jean-François for his technical support, Odile for her help and advice in Raman spectroscopy, and the secretaries of the school who helped me out of many administrative problems: Catherine, Ikrame, Elisabeth and Matinou.

I acknowledge Benoit Dubertret for welcoming me in the LPEM lab at ESPCI for the synthesis of nanoplatelets and quantum dots. Special thanks go to Sandrine Ithurria for teaching me the synthesis methods and for useful discussions. I would like to thank Armel Descamps-Mandine for his help and endless patience with the long SEM experiments. I am grateful to the the lab's PhD students, postdocs and other researchers: Nicolas Lequeux, Silvia, Chloé, Djamila, Emmanuel, Brice, Mariana, Anusuya, Aude, Michel, Fatima, Gary, Sophie and Thomas for their help with the experiments and solving technical problems, as well as for creating a cheerful ambiance in the lab with lots of music.

I owe a lot to my Parisian friends, some of whom already moved abroad, but we still keep in touch: Liping, Sijie, Javier, Mariana and Andreea. Your optimism, open-mindedness and creativity are an endless source of inspiration for me. I am grateful to have my Hungarian friends who can always cheer me up even from a large distance, and who enlighten all my visits back to my home country: Zsófi, Évi, Kati and Panni.

It is needless to say that I have no words to express my gratitude towards my family all over Europe, especially my sister Krisztina and my mother for their solid support, encouragement and love.

ABSTRACT

The general aim of this thesis was to contribute to a better understanding of the procedures governing the performance of quantum dot sensitized solar cells. A mixed theoretical/experimental approach was used to analyze the semiconductor components of these devices and the interfaces formed between them. Regarding the theoretical part of this thesis, we first identified a computational protocol that accurately and efficiently describes the bulk and surface geometrical and electronic properties of the chosen sensitizer material, CdSe. Then, we simulated CdSe nanoplatelets of various thicknesses, passivated by different ligands with the chosen computational protocol. Next, a model of the sensitizer - wide band gap semiconductor heterostructure was built and its structural, vibrational and electronic properties were calculated. In the meantime, computational results were compared to experimental data, with nice agreements found between the results obtained by the two approaches. Experimentally, wide band gap semiconductors both in the form of ZnO and TiO₂ nanorod arrays and sensitizer nanocrystals (CdSe nanoplatelets and quantum dots) were synthesized. The WBSC substrates were sensitized both by *ex situ* and *in situ* grown CdSe QDs. The as-prepared semiconductor systems were characterized by UV-VIS absorption and Raman spectroscopy. Finally, solar cells based on these heterostructures were fabricated and tested. The applied combined theoretical/experimental approach made it possible to cross-validate the capacity of computational and experimental methods for the characterization of the semiconductor systems studied in this thesis. Moreover, general guidelines for the screening of QDSC components could be drawn from the obtained results. The here proposed mixed theoretical/experimental approach can be extended to other semiconductor heterostructures in a wide variety of optoelectronic applications, and it could contribute to a better understanding of the working principle of these devices and improve their performance.

RESUME

Le but général de cette thèse était de mieux comprendre les procédures qui gouvernent la performance des cellules solaires à boîtes quantiques. Une approche mixte théorique/expérimentale a été utilisée pour analyser les composants semi-conducteurs de ces dispositifs, ainsi que les interfaces qui se forment entre eux. En ce qui concerne la partie théorique de cette thèse, tout d'abord on a identifié un protocole computationnel qui décrit d'une façon précise et efficace les propriétés géométriques et électroniques du bulk et les surfaces de CdSe, ce qui est le matériau qu'on a choisi comme composé sensibilisant de nos cellules solaires. Après, les nanoplaquettes CdSe de plusieurs épaisseurs et passivé par plusieurs ligands distincts ont été simulés avec le protocole computationnel choisi. Ensuite, une hétéro-structure sensibilisant – semi-conducteurs à large bande interdite a été modélisée, et ses propriétés structurelles, vibrationnelles et électroniques ont été calculées. En même temps, les résultats théoriques étaient comparés avec les données expérimentales, et des accords satisfaisants ont été trouvés entre les deux approches. Expérimentalement, des semi-conducteurs à large bande interdite sous la forme des nanobâtons de ZnO et de TiO₂, ainsi que des nanocristaux sous forme des nanoplaquettes et des boîtes quantiques CdSe ont été synthétisées. Les nanobâtons ont été sensibilisés à la fois avec des nanocristaux CdSe préparés *ex situ* et *in situ*. Les systèmes semi-conducteurs ainsi préparés ont été caractérisés par spectroscopie d'absorption UV-VIS et Raman. Enfin, des cellules solaires incorporant ces hétérostructures semi-conducteurs ont été fabriquées et testées. L'approche combinée expérimentale/théorique qu'on a utilisée dans cette thèse a rendu possible de contre-valider la capacité des méthodes expérimentales et théoriques pour caractériser les systèmes semi-conducteurs étudiés lors de cette thèse. De plus, on a pu établir des indications générales pour la sélection des composants pour les cellules solaires à boîtes quantiques. L'approche mixte expérimentale/théorique présentée dans ce manuscrit peut être étendue pour étudier des hétérostructures semi-conducteurs dans une vaste gamme des applications optoélectroniques, et peut contribuer à mieux comprendre leur fonctionnement et à améliorer leur performance.

TABLE OF CONTENTS

Chapter I	CONTEXT.....	1
I.1.	Global energy trends.....	1
I.2.	Photovoltaic technology.....	2
I.3.	Quantum dot sensitized solar cells.....	5
I.3.1.	Working principle.....	8
I.3.2.	Components.....	8
I.3.2.1.	Quantum dots.....	8
I.3.2.2.	Wide band gap semiconductors.....	10
I.3.2.3.	Transparent conductive oxide glass.....	11
I.3.2.4.	Electrolytes.....	12
I.3.2.5.	Counter electrodes.....	14
I.4.	Solar spectra.....	14
I.5.	Solar cell efficiency factors.....	15
I.6.	State of art.....	17
I.6.1.	Experimental challenges.....	17
I.6.2.	Modeling challenges.....	19
I.7.	Goals and outline of the thesis.....	23
	References.....	25
Chapter II	THEORETICAL AND EXPERIMENTAL METHODS.....	33
II.1.	Theoretical methods.....	33
II.1.1.	The Schrödinger equation	33
II.1.2.	Hartree-Fock method.....	35
II.1.3.	Density functional theory.....	39
II.1.4.	The Kohn-Sham method.....	40
II.1.5.	Exchange-correlation functionals.....	42
II.1.6.	Modeling periodic systems.....	44
a)	Bulk crystals.....	44
b)	Crystal surfaces.....	47
II.1.6.	Basis sets for periodic DFT calculations.....	48
a)	Localized basis sets.....	48
b)	Plane wave basis sets.....	50
II.2.	Experimental methods.....	52
II.2.1.	Synthesis of CdSe nanoplatelets and quantum dots.....	52
II.2.2.	Synthesis of 1D wide band gap semiconductor nanostructures.....	55
a)	ZnO nanorods.....	56
b)	TiO ₂ nanorods.....	60
II.2.3.	Attachment of quantum dots to wide band gap semiconductors.....	63
a)	Sensitization by linker-assisted attachment.....	63
b)	Sensitization by the SILAR method.....	66
II.2.4.	Assembly of solar cells.....	68
a)	All-solid-state QDSCs.....	68
b)	QDSCs with liquid electrolyte.....	69
II.2.7.	Characterization methods.....	71

	References.....	72
Chapter III	BULK AND SURFACE PROPERTIES OF CdSe.....	78
III.1.	Context.....	78
III.2.	Computational details.....	79
III.3.	Bulk properties of CdSe.....	81
III.3.1.	Structural features.....	81
III.3.2.	Energetics and electronic properties.....	84
III.4.	Surface properties of CdSe.....	90
III.4.1.	Geometrical properties.....	90
III.4.2.	Electronic properties.....	92
III.5.	Conclusion.....	94
	References.....	96
Chapter IV	CADMIUM SELENIDE NANOPATELETS.....	99
IV.1.	Context.....	99
IV.2.	Experimental details.....	99
IV.3.	Computational details.....	100
IV.4.	Theoretical model of the CdSe zinc blende (100) surface.....	102
IV.5.	Geometrical investigation.....	104
IV.6.	Adsorption energies.....	107
IV.7.	Electronic properties.....	108
IV.8.	Conclusions.....	114
	References.....	116
Chapter V	HYBRID SEMICONDUCTOR HETEROSTRUCTURES.....	118
V.1.	Context.....	118
V.2.	ZnO and TiO ₂ nanorod arrays.....	119
V.3.	Attachment of CdSe nanoplatelets to WBSC via SH ⁻ ligands.....	122
V.4.	Attachment of CdSe nanoplatelets to WBSC via OH ⁻ ligands.....	128
V.5.	Attachment of CdSe nanoplatelets to WBSC via MPA ligands.....	130
V.6.	Attachment of CdSe quantum dots to WBSC.....	133
V.7.	Conclusion.....	134
	References.....	136
Chapter VI	TOWARDS THE MODELING OF QDSCs: SENSITIZER – OXIDE HETEROSTRUCTURES.....	138
VI.1.	Context.....	138
VI.2.	Experimental details.....	139
VI.3.	Computational details.....	140
VI.4.	Structural features of the CdSe.SH – ZnO system.....	142
VI.5.	Vibrational features.....	146
VI.6.	Electronic properties.....	155
VI.7.	Conclusions.....	158
	References.....	161
Chapter VII	QUANTUM DOT SENSITIZED SOLAR CELLS.....	163
VII.1.	QDSCs based on <i>ex-situ</i> prepared CdSe nanocrystalss.....	163
VII.1.1.	All-solid-state QDSCs.....	163
VII.1.2.	QDSCs with liquid electrolytes.....	165
a)	ZnO-based QDSCs.....	165
b)	TiO ₂ -based QDSCs.....	166

VII.2.	QDSCs based on <i>in-situ</i> prepared CdSe QDs.....	166
VII.2.1.	QDSCs with a ZnO substrate.....	167
VII.2.2.	QDSCs with a TiO ₂ substrate.....	175
VII.3.	Conclusion.....	178
	References.....	181
CONCLUSIONS AND PERSPECTIVES.....		182
PUBLICATIONS RELATED TO THE THESIS.....		187
PRESENTATIONS AT SCIENTIFIC EVENTS.....		187
LIST OF FIGURES.....		189
LIST OF TABLES.....		195
ANNEXES		197
	Annexe I. Geometrical and electronic properties of the CdSe.SH (9L) – ZnO system.....	197
	Annexe II. J-V curves of the solar cells tested in Chapter VII.....	201

I.1. Global energy trends

At present, nearly 80% of the yearly energy consumption of $5.67 \cdot 10^{20}$ J/year which is equivalent to a total of ≈ 18 terawatts (TW)¹ is provided by fossil fuels such as coal, petroleum and natural gas.² Although the U.S. Energy Information Administration (EIA) predicts a 56% growth in global energy consumption by 2040,³ the fossil energy sources can still account for the increased global energy demands at least until 2050.⁴ However, as fossil fuels are converted to energy, they produce greenhouse gases (such as carbon dioxide, methane and nitrous oxide) and other harmful pollutants (ash, sulphur oxide etc.). The use of fossil fuels thus contributes to global warming, as it has been pointed out in the Fourth Assessment Report of the Intergovernmental Panel on Climate Change (IPCC),⁵ and the deterioration of the quality of air. If the global energy demand continues to be satisfied by fossil energy sources at the present rate, the atmospheric CO₂ concentration could rise above 685 ppm, which would lead to a 3-6 °C rise in global average temperature,⁶ and have catastrophic consequences on the climate and the environment.

Consequently, more and more effort has been invested in the last decades into the research of alternative, environmentally friendly and renewable energy sources. In 2014, for the first time in 40 years and despite the increasing energy use, global carbon emissions associated with energy consumption remained stable while the economy grew, which is attributed to the increasing use of renewable energy sources.⁷ Solar energy is by far the most exploitable choice among them: $3.85 \cdot 10^{24}$ J/year, equivalent to a power of 120000 TW/year energy reaches the Earth from the Sun,⁸ which is four orders of magnitude larger than the current global energy use. In comparison, the yearly maximum energy supply of other renewable energy sources is only a small fraction of that of solar energy: 1.5 TW/year is exploitable from hydroelectric power, 2 TW/year energy from tides and ocean currents, 2-4 TW/year from wind power and 12 TW/year from geothermal energy.^{9,10} However, in order to make solar energy a widespread energy source, scalability, cost and conversion efficiency issues need to be solved.^{11,12}

Chapter I. Context

I.2. Photovoltaic technology

Photovoltaic (PV) technologies aim at the direct conversion of solar energy into electricity. The classical way is based on the photovoltaic effect: the creation of voltage and electric current upon exposure to light in an assembly of a *p*- and a *n*-type material in close contact, forming a *p-n junction*. *p*- and *n*-type materials are derived from the bulk material by doping it with electron acceptors or donors, respectively. For instance, silicon can be made *p*-type (*n*-type) by doping with atoms that contain less (more) valence electrons than silicon, for example with aluminium (phosphor).

Two important semiconductor characteristics are defined in *Figure I.1 c*). The band gap (E_{gap}) is the minimal energy required to excite an electron from its bound state in the valence band (VB) into a free state in the conduction band (CB). The Fermi level (E_F) represents the chemical potential of the electrons. While the E_F is in the middle of the band gap in an ideal intrinsic (non-doped) semiconductor, it is closer to the top of VB (bottom of CB) in a *p*-type (*n*-type) semiconductor.

In the *p-n junction*, the *n*-type region has a high electron concentration, and the *p*-type region has a high hole concentration. Therefore, when the two semiconductors are put in contact, electrons from the *n*-type side diffuse freely to the *p*-type side. Similarly, holes diffuse from the *p*- to the *n*-type region (*Figure I.1 a*). This diffusion of the charge carriers through the junction causes a *diffusion current*. The free charge carriers are quickly swept out from the area around the junction, which is thus called *depletion region* (*Figure I.1 b*). These displaced electrons and holes leave behind charged dopant atom sites fixed to the crystal lattice: positive ion cores are left behind in the *n*-type, and negative ion cores in the *p*-type material, forming an electric (*built-in*) field, which works against the above described charge *diffusion*, and sweeps back the electrons and holes that are trying to cross the depletion region, causing a *drift current*.

In equilibrium, the electron *drift* and *diffusion current*, as well as the hole *drift* and *diffusion current* are balanced out, and the net current in the device is zero. If a positive voltage is

Chapter I. Context

applied to the *p-type*, and a negative voltage to the *n-type* region, an electric field opposing the *built-in field* of the *depletion region* is applied across the device, and the *diffusion current* is increased. This is called *forward bias*. In case of *reverse bias*, a voltage is applied across the device such that the *built-in field* increases, and the *diffusion current* decreases.

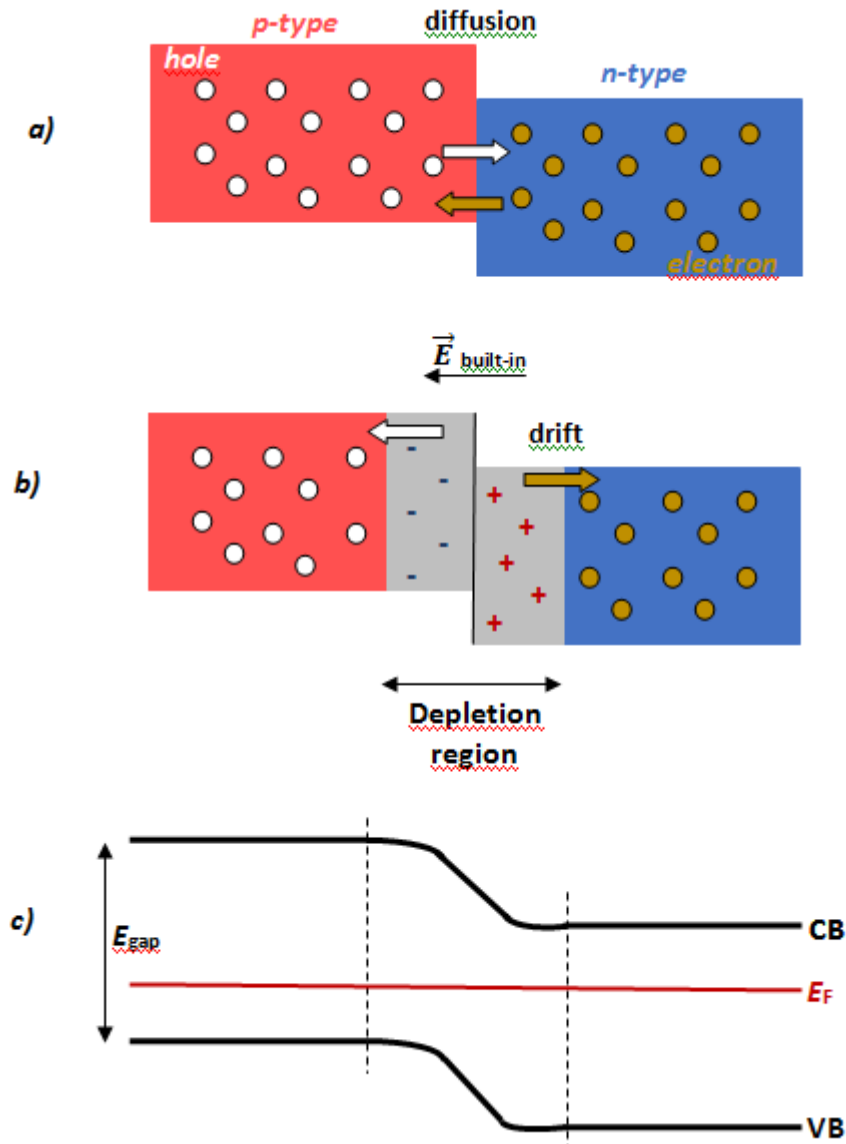


Figure 1.1. a) Diffusion of free charge carriers between a p- and an n-type material. b) Formation of a depletion region with a built-in electric field in a p-n junction. c) Band energy levels in the p-n junction.

There are two major processes leading to a current generation in *p-n semiconductor junctions*. The first one is the absorption of light by the semiconductor material. If the energy

Chapter I. Context

of the incident light is equal or superior to the band gap, electrons are promoted from the VB to the CB, leaving holes behind in the VB, and electron-hole pairs are thus created. The second process is the collection of charge carriers. The *built-in field* in the *depletion region* spatially separates the electrons and the holes and thus prevents recombination. Electrons and holes are driven towards different collectors, and if the terminals of the *p*- and *n*-type material are connected, the charge carriers can leave the device, and flow through the external circuit: a photogenerated current has been created.

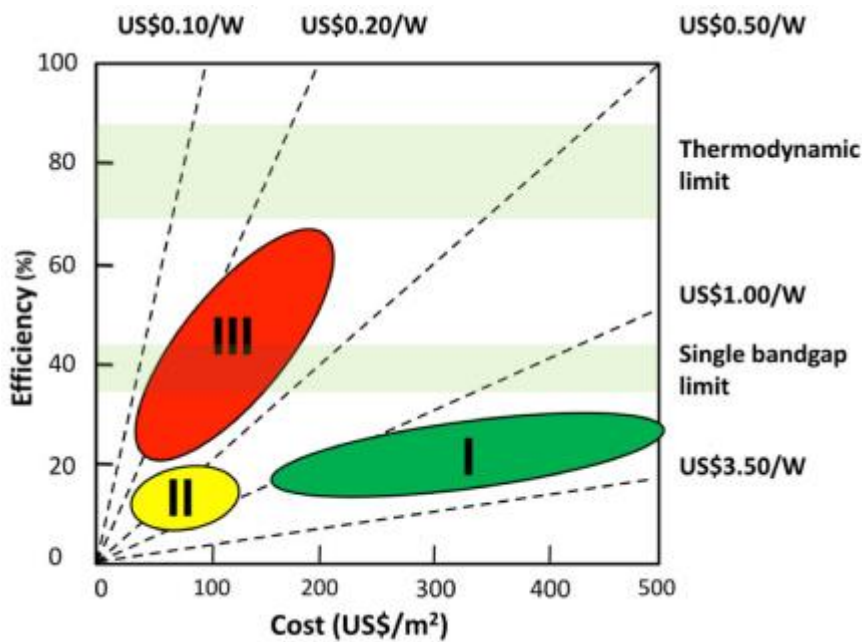


Figure I.2. First, second and third generation photovoltaic cells. Adapted from Ref. 13

One of the most commonly used classifications of single junction photovoltaic solar cells is based on the cost-efficiency relationship, as illustrated in *Figure I.2*. Currently *first generation* solar cells made of crystalline silicon dominate the commercial market, although the high purity of the initial material makes them expensive.¹⁴ Also, silicon has an indirect band gap with a low absorption coefficient, which implies the use of thick absorber layers in the devices. *Second generation* thin film PV technologies exploit simpler/cheaper industrial processes and offer larger scaling module integration (potentially of flexible substrates), much lower materials consumption/cost plus reduced payback time compared to crystalline silicon (c-Si) based technologies.¹⁵ Currently amorphous/microcrystalline (a/m-Si) silicon,

Chapter I. Context

CdTe and $\text{Cu}(\text{In}_{1-x}\text{Ga}_x)\text{S}_{2-y}\text{Se}_y$ (CIGSSe) based technologies dominate the thin film PV market. Whilst a-Si cells suffer from relatively low conversion efficiency (the best laboratory power conversion efficiency [PCE] is 13.4% measured at Sharp), thin film CdTe offers a record PCE of 22.1% (First Solar), and CIGSSe offers a record PCE of 22.3% (Solar Frontier).¹⁶ Despite the improvement with respect to first generation solar cells, second generation solar cells in general still require relatively costly high purity materials and some of them are based on rare resource elements, prepared with tedious and complicated processing conditions, *Third generation* solar cells gather new solar cell concepts which are very low cost and/or have a very high efficiency. They include multijunction solar cells, organic photovoltaic cells and also organic/inorganic or inorganic/inorganic hybrid devices, such as dye-, quantum dot (QD)- and perovskite-sensitized solar cells. The main advantages of the new concept *third generation* devices include low-cost materials and fabrication techniques,¹⁷ and the possibility to overcome the theoretical efficiency limit of single junction devices¹⁸ established by Shockley and Queisser. They obtained a maximum power conversion efficiency of 31% for a semiconductor single junction with a band gap of 1.4 eV.¹⁹ Their calculation was based on the following assumptions. 1) Every incident photon with an energy greater than or equal to the band gap of the semiconductor produces one electron-hole pair. 2) The photon energy above the band gap is converted to heat (thermalization loss). In reality, the efficiency of solar cells is lower than the ideal calculated value, mainly due to light reflection, non-radiative charge recombinations and ohmic losses.

I.3. Quantum dot sensitized solar cells

I.3.1. Working principle

The novelty of hybrid solar cells compared to first and second generation solar cells is that the different steps of the photovoltaic procedure (light absorption, charge separation and charge transport) are realized in different materials, and can thus be optimized separately. The components of QDSCs will be described in more detail in section I.6. In brief, QDSCs are composed of an *n-type* wide band gap semiconductor (WBSC, typically ZnO or TiO_2) of large surface area, sensitized by semiconductor nanocrystals (quantum dots). This semiconductor

Chapter I. Context

heterostructure is grown on a transparent conductive oxide (TCO) coated glass. The TCO layer is usually made of fluorine doped tin oxide ($\text{SnO}_2\text{:F}$), denoted as FTO. The cell is completed by an electrolyte which contains a redox couple (typically $\text{S}^{2-}/\text{S}_n^{2-}$) and a counter electrode (CE). The working principle of these devices is also illustrated in *Figure I.3*, and the schematic illustration of the charge generation, transfer and recombination processes is reported in *Figure I.4*.

The absorption of light excites an electron from the VB to the CB of a QD (procedure **A** on *Figure I.4*). Then, it is injected to the CB of the WBSC (**B**), which increases the Fermi level of the WBSC. This upshifted, out-of-equilibrium energy level is called *quasi-Fermi level*, and is denoted as E_{qf} on *Figure I.4*. In the next step, the WBSC transfers the excited electrons towards the FTO layer of a glass substrate (**C**). The FTO-coated glass leads the photogenerated electrons towards the external circuit. The oxidized QD is regenerated by hole injection from a redox species present in the electrolytic solution (**D**), characterized by its redox potential (μ). As illustrated in *Figure I.4*, an important solar cell parameter, the open circuit voltage (V_{oc}) is defined as the difference between the quasi-Fermi level of the WBSC and the redox potential of the electrolyte:

$$V_{\text{oc}} = E_{\text{qf}} - \mu \quad (\text{I.1})$$

The electrolytic solution is then regenerated by reduction at the counter electrode (**E**). The main parasitic recombination pathways that decrease the device performance occur between electrons already injected to the WBSC and holes left in the QD (**F**), electrons in the TCO and holes in the electrolyte (**G**), electrons already injected to the WBSC and holes in the electrolyte (**H**), and electrons in the QD and holes in the electrolyte (**I**). Another possible recombination phenomenon can occur if the QD gets back to its initial state before injecting the electron to the CB of the metal oxide (**J**).

Chapter I. Context

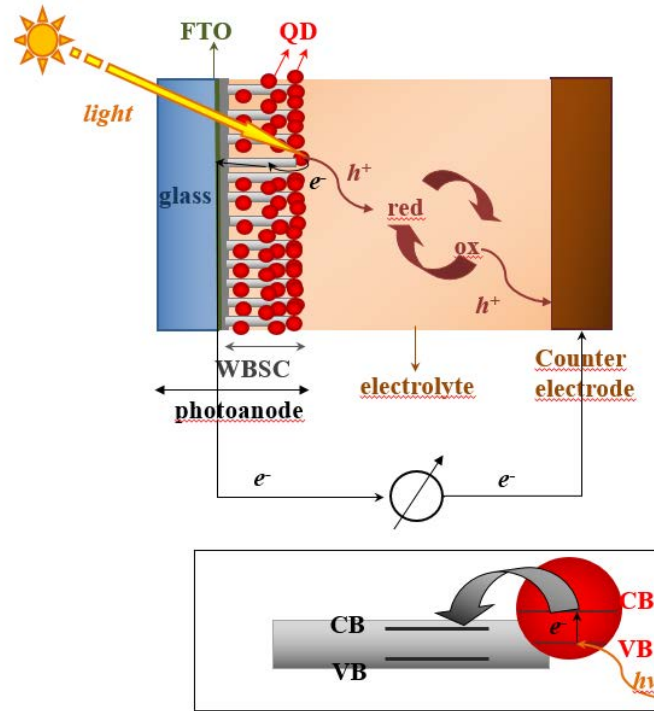


Figure I.3. Working principle of quantum dot sensitized solar cells. The scheme at the bottom shows the electron injection from the quantum dot to the semiconductor oxide.

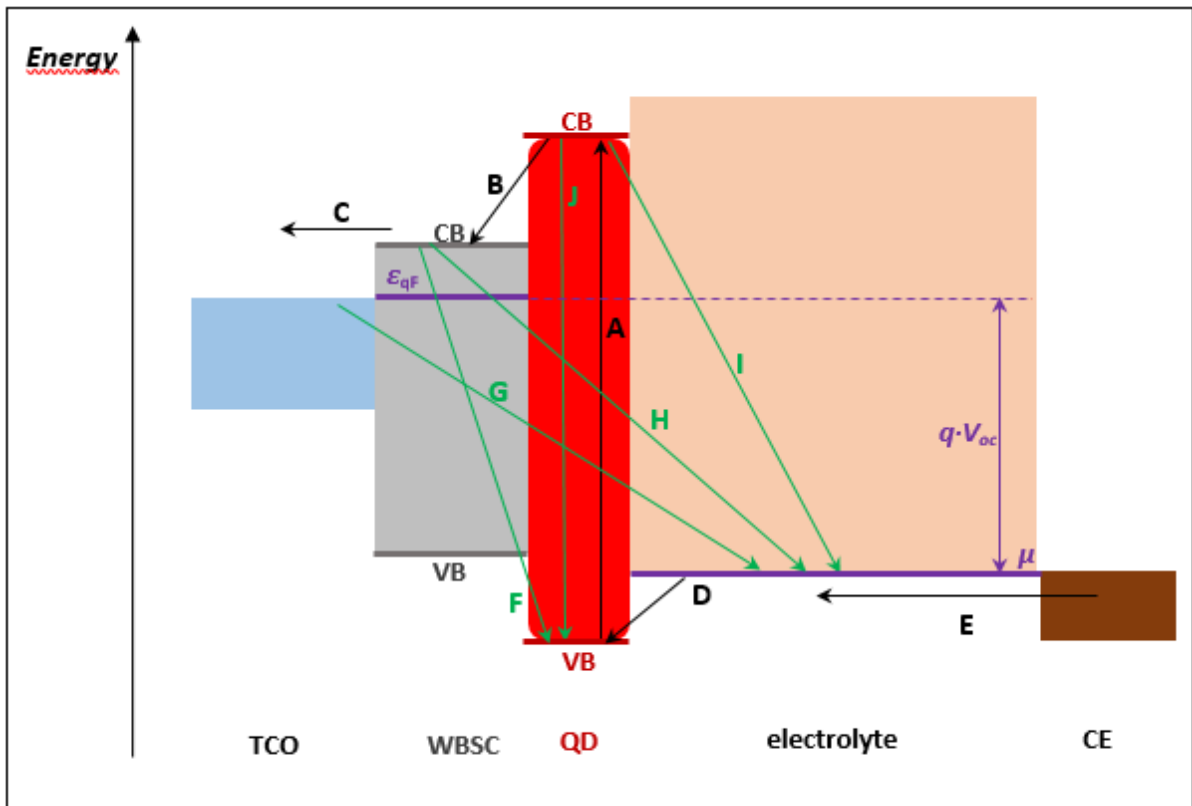


Figure I.4. Main charge generation, transfer and recombination processes in a QDSC. Favorable electron transfer procedures are marked with a black. Undesired electron-hole recombinations are marked with a green arrow.

I.3.2. Components

I.3.2.1 Quantum dots

Quantum dots (QDs) are typically II-VI, III-V or IV-VI semiconductor nanocrystals whose size is in the order of a few nanometers in all dimensions. Most common materials investigated as QDs include CdS²⁰, CdSe²¹, CdTe²², PbS²³, PbSe²⁴, Bi₂S₃²⁵, Sb₂S₃²⁶, InAs²⁷ and CuInS₂²⁸ quantum dots. Their nanometric size is comparable to their *Bohr exciton radius* (a_b), which is calculated according to the following equation:

$$a_b = \frac{\hbar^2}{e^2} \left(\frac{1}{m_e^*} + \frac{1}{m_h^*} \right) \quad (I.2)$$

where \hbar is the reduced Planck constant, ϵ is the dielectric constant of the material, e is the electronic charge, m_e^* and m_h^* are the effective masses of electrons and holes, respectively. Physically, the *Bohr radius* represents the average electron-hole distance in an *exciton*, which is an electron-hole pair bound by *Coulombic forces*. Excitons are created in the semiconductor material upon the absorption of a photon with an energy greater than or equal to the semiconductor band gap. Once the diameter of a material is smaller than its Bohr radius, the excitons become so strongly bound that they can be considered as an entity moving in the crystal lattice. However, their movement is strongly limited by the size of QDs, or, in other words, they are spatially confined in 3 dimensions. In case of 1 dimensional (1D) nanoobjects like nanowires/nanorods, these *quantum confinement effects* arise in 2 dimensions, and in case of quasi-2 dimensional (2D) objects such as nanoplatelets, they occur only in 1 dimension. The *quantum confinement effect* has a strong impact on the energy level distribution: the band gap of nanoobjects increases with decreasing size, and their energy levels become more discretized. These are both very advantageous properties for photovoltaic applications, as explained in the following.

Chapter I. Context

Tuning the band gap energy of the light absorbing component of quantum dots is an important step in optimizing the solar cell performance. Too low a band gap results in efficiency losses due to the thermalization of the photon energy excess with respect to the sensitizer's band gap energy. In the case of high band gap, a large proportion of the photons of the incident light is not absorbed, since their energy is inferior to that of the quantum dot's band gap. Based on Shockley and Queisser's calculations, for a single junction, these losses are minimal at a band gap of around 1.3-1.4 eV.¹⁹ However, to optimize photovoltaic conversion, it would be desirable to absorb light in the whole solar spectra. This could actually be possible by combining QDs with several band gap energies.²⁹ The development of synthesis methods has made it possible to fine tune the nanoparticle size and thus the band gap of various quantum dot materials, making the engineering of solar light absorption possible.³⁰⁻³²

The discretization of energy levels could also make it possible to exceed the Shockley-Queisser efficiency limit. If a photon with an energy greater than the band gap of the semiconductor materials is absorbed, an electron-hole pair with excess kinetic energy is generated first. These carriers are called *hot electrons* and *hot holes*. In a bulk material with a continuum of electronic states, they are relaxed to the top of VB or the bottom of CB by collective vibration of the interacting atoms in the system (phonon emission). However, the discretization of energy levels slows down the relaxation process, especially if the distance between the energy levels is higher than the phonon energies. This phenomenon called *phonon bottleneck* facilitates generating a current of hot carriers before they are relaxed. Two approaches have been proposed to exploit the high energy of hot carriers. In the first one, hot carriers are extracted before their thermalization, and a higher photocurrent can be generated by the device. This phenomenon called *hot electron transfer* has been observed for instance between PbS QDs and a TiO₂ single crystal.³³ Moreover, Lee et al. demonstrated making use of hot carriers in a complete photovoltaic device.³⁴ In the second approach, if the incident photon energy is at least two times higher than the band gap, the energy released during the relaxation of hot carriers can theoretically create new excitons, which results in an increased current. This is called *multiple exciton generation* (MEG). Multiple electron transfer has been reported between MPA-capped CdSe QDs and ZnO nanowires.³⁵ Beard and coworkers have demonstrated a photocurrent exceeding 100% due to MEG in a depleted

Chapter I. Context

heterojunction solar cell based on PbSe QDs and ZnO.¹⁸ However, taken all together, these promising concepts have brought little improvement in device efficiency, since their application to actual solar cells requires a very high control level of the interfaces.³⁶

Among the above listed QD materials, cadmium chalcogenides have attracted considerable attention because of their easy, low fabrication cost,^{37–39} controllable size,^{40,41} photostability⁴² and also the possibility to break the Shockley-Queisser limit via multiple exciton generation.^{43,44} In this thesis, we have concentrated on CdSe nanocrystals, which had previously been synthesized in various shapes: spherical nanoparticles,⁴⁵ nanorods (NRs)⁴⁶, nanoribbons,⁴⁷ tetrapods⁴⁸, nanosheets⁴⁹ and nanoplatelets⁵⁰. Regarding the latter, CdSe zinc blende nanoplatelets (NPLs) are versatile structures which can be fabricated with a well-defined thickness controlled at an atomic scale in the (100) direction.⁴⁰ These quasi two-dimensional nanocrystals have been proven to be useful for a broad range of applications ranging from single-photon sources⁵¹ to biophotonics⁵². Compared to QDs and NRs, they show much narrower excitonic absorption and photoemission bands^{50,53} and higher photoluminescence quantum yields.⁵⁴ Taken all together, quasi two-dimensional nanoplatelets exhibit promising properties for photovoltaics, and are interesting alternatives of QDs as sensitizers. Although classical spherical QDs as sensitizers have also been considered in this thesis, we mainly focused on quasi two-dimensional semiconductor nanoplatelets (NPLs).

I.3.2.2 Wide band gap semiconductors

In QDSCs, QDs are associated to a selective contact which is classically made of a wide band gap semiconductor (WBSC). The role of this component is to receive the electrons from the QD conduction band after electron injection, and to transport charges to the front FTO contact. As the QDs are the only light absorbing components of the cells, a selection criteria for WBSCs is that their band gap is wide enough so that its absorption range does not overlap with the solar spectrum. In order to ensure the efficient electron injection from the sensitizer towards the WBSC, the CB edge of the WBSC material needs to be at lower energy compared to the sensitizer CB edge energy. ZnO and TiO₂ meet these requirements if paired with classically used QD materials, and are classically used as WBSC materials in QDSCs.

Chapter I. Context

These materials have band gaps (3.20^{55} for TiO_2 and 3.37 eV^{56} for ZnO) and also CB band positions.⁵⁷ Although TiO_2 is more used in QDSCs than ZnO , the latter has some more advantageous properties. It has a higher electron mobility ($200\text{-}300 \text{ cm}^2 \text{ V s}^{-1}$) than TiO_2 ($0.1\text{-}4 \text{ cm}^2 \text{ V s}^{-1}$)⁵⁷, and it is easier to synthesize in highly oriented nanostructures.^{58–60} As high QDSC efficiencies have been reached both with ZnO -^{61,62} and TiO_2 -based photoanodes,^{63,64} both semiconductors were considered in this thesis.

It has been shown for dye sensitized solar cells that increasing the WBSC surface area, and thus increasing the amount of sensitizers adsorbed on the WBSC leads to higher IPCE values.^{65,66} Numerous different kinds of nanostructured ZnO and TiO_2 nanostructures morphologies with high surface area have thus been synthesized, including nanoparticle films and more exotic ones such as DNA-like,⁶⁷ flower-like^{68,69} or hierarchical spherical nanoarchitectures.⁷⁰ One dimensional nanostructures like nanorods, nanowires and nanotubes are precisely oriented, therefore they provide excellent charge streaming pathways^{71–73} and an improved electron diffusion length with respect to nanoparticle films.^{74,75} It is also to note that the transported electrons in the commonly used nanoparticle films suffer charge trapping and recombination losses at the grain boundaries,^{76,77} whereas this phenomenon is reduced in the case of one-dimensional nanostructures.^{78–80} As a result, charge transport and photon-to-charge carrier generation efficiency are significantly increased with respect to devices incorporating nanoparticle-based photoanodes.^{30,81} In this thesis, we thus chose to synthesize ZnO and TiO_2 in the form of 1D nanorods and nanowires.

I.3.2.3. Transparent conductive oxide glass

The wide band gap semiconductor is grown on a conductive layer deposited on the side of a glass substrate (*Figure I.3.*). The conductivity of this layer is necessary to ensure a good electron transport towards the external circuit, while high transparency is required to let the incident light reach the sensitizer of the cell. In most cases, the conductive layer is made of fluorine doped tin oxide ($\text{SnO}_2\text{:F}$, FTO), although tin-doped indium oxide ($\text{In}_2\text{O}_3\text{:Sn}$, ITO) has also been used in several studies.^{82,83} The thicker this layer is, the more conductive it is, although less transparent as well. Thus, a compromise has to be found between the two

Chapter I. Context

parameters. In the present thesis, 2.2 mm thick glass substrates coated with a FTO layer of 15 ohms per square resistance were used for the preparation of the photoanodes.

I.3.2.4. Electrolytes

As the I^-/I_3^- redox couple applied in dye-sensitized solar cells causes the photocorrosion of typically used QD materials such as cadmium chalcogenides,^{84,85} alternative electrolytes have been developed to replace it. The most commonly used redox electrolyte for QDSC application is the sulfide/polysulfide (S^{2-}/S_n^{2-}) electrolyte, which have been shown to increase the photoanode stability because of the formation of a cadmium sulfoselenide layer on the QD's surface.⁸⁶ Other redox electrolytes, including Co^{2+}/Co^{3+} ⁸⁷ and ferricyanide/ferrocyanide⁸⁸ have also been investigated.

The hole transporting role of the redox electrolyte is shown through the example of the sulfide/polysulfide (S^{2-}/S_n^{2-}) electrolyte which was used in this thesis. As the photoexcited electron is injected from the QD to the WBSC, the holes accumulated in the QD are scavenged by the reduced species (S^{2-}) of the redox electrolyte, which is thus oxidized. (*Equation I.3*). The resulting compound (S) is complexed by sulfide anions (*Equation I.4*), and the complex species get reduced to the initial sulfide ion in contact with the electrons of the counter-electrode (*Equation I.5*).⁸⁴



However, the exact mechanism of the process is still controversial. For example, Kamat et al. observed sulfide radicals as intermediate products of the oxidation-reduction processes.⁸⁶ The drawback of sulfide/polysulfide redox electrolytes is their relatively high redox potential which limits the open-circuit voltage at around 0.65 V, a value is significantly lower than that achieved in dye-sensitized solar cells (1.0 V) using cobalt redox species.^{89–92} Decreasing the charge recombination rate between the photoanode components and the electrolyte is another challenging issue. Du et al. demonstrated that the introduction of well-chosen

Chapter I. Context

additives in the electrolyte solution can reduce recombination phenomena and contribute to a better photovoltaic performance.⁹³

Nevertheless, liquid electrolytes do not provide long-term stability for QDSCs. Solvent evaporation, leakage and corrosion are the major drawbacks related to the use of liquid electrolytes.^{94,95} Due to these disadvantages, *solid-state electrolytes* have also been applied in QDSCs. In these fully solid-state devices, organic molecules or a polymer electrolyte replaces the liquid redox electrolyte. Typical examples of solid-state electrolyte materials applied in QDSCs include poly(3-hexylthiophene-2,5-diyl)⁹⁶ (P3HT), quatertiphenes⁹⁷ and 2,2',7,7'-tetrakis[N,N-di(4-methoxyphenyl)amino]-9,9'-spirobifluorene (denoted as spiro-OMeTAD)⁹⁸. Despite the promising concept, solar cells assembled with *solid state electrolytes* show much lower performance than those with liquid electrolytes. For instance, a power conversion efficiency of 1% has been reported for a QDSC based on PbS and CdS QD-sensitized TiO₂ and a spiro-OMeTAD electrolyte,⁹⁹ and 0.3% for a cell based on CdSe QD-sensitized TiO₂ and quatertiphenes as hole transporting material (HTM).⁹⁷ The main reason for this low performance is probably the incomplete pore filling of the photoanode by HTM.⁹⁹

Finally, *quasi-solid state electrolytes* (including gel electrolytes and highly viscous ionic liquid electrolytes) have also been proposed, resulting in higher solar cell efficiencies. For instance, Wang et al. reported a power conversion efficiency of 4.0% for a CdS/CdSe QD-sensitized solar cell with a TiO₂ photoanode and a natural polysaccharide (Konjac glucomannan) –based quasi-solid state electrolyte¹⁰⁰ or Karageorgopoulos et al. measured an overall efficiency of 4.5% for solar cells using a CdS/CdSe-sensitized ZnO photoanode and a polysulfide-based ionic liquid.¹⁰¹

Although the expression 'hole transport material' is most often applied for *solid state electrolytes*, all the above described electrolytes play the same hole transporting role in hybrid solar cells. Therefore, in the following, *solid*, *quasi-solid state* and *liquid electrolytes* will all be referred to as *hole transport materials (HTMs)*.

Chapter I. Context

I.3.2.5. Counter electrodes

Counter electrodes (CEs) are expected to have a high electrocatalytic activity for the regeneration of the redox couple of the electrolyte, high conductivity and no willingness to react with the rest of the solar cell components. A typical CE in dye-sensitized solar cell (DSSCs) consists of a platinized conducting glass substrate, and is usually referred to as a Pt counter electrode. However, while Pt electrodes are highly catalytic for the reduction of I_3^- in the iodine/iodide electrolyte, this is not the case for the sulfide/polysulfide electrolyte. Sulphur compounds tend to chemisorb on Pt surfaces, poison the electrode, and hinder the electrocatalytic effect.¹⁰² The high overpotential for the electrolyte regeneration results in low power conversion efficiencies.^{103–105} Consequently, a wide variety of other materials (such as CoS¹⁰⁶, Cu₂S¹⁰⁴, Au¹⁰⁵, PbS¹⁰⁷ and Cu₂ZnSnSe₄¹⁰⁸) have been investigated, among which Cu₂S gave the best results.^{103,104} However, Cu₂S counter electrodes have some drawbacks. With an extended use, they might contaminate the electrolyte and the photoanode.^{104,106} In case of *solid-state* QDSCs, a thin layer of Au^{109,110} evaporated on the HTM layer is typically applied as a counter electrode. Pt¹⁰¹ and Cu₂S¹¹¹ CEs have been combined with *quasi-solid state* electrolytes.

I.4. Solar spectra

As the actual solar irradiation received by the device is influenced by numerous conditions, such as weather, time of the day, geographic location, latitude, orientation etc., the evaluation of solar cell characteristics and the comparison of different solar cells around the world would be extremely difficult. It was thus necessary to standardize measuring conditions. The currently accepted standards have been established by the American Society for Testing and Materials (ASTM). *Figure I.5* shows two important standard spectra, AM0 and AM1.5G. The number in the abbreviation shows the quantity of air mass that the light passes through. Therefore, AM0 stands for Air Mass 0, and corresponds to the spectra after having crossed 0 atmosphere. AM0, is thus used for extraterrestrial applications. The total incident power obtained by the integration of the curve is $1366.1 \text{ W m}^{-2} \text{ nm}^{-1}$. Due to scattering and absorption by the Earth atmosphere, the solar irradiance is decreased once it reaches the

Chapter I. Context

Earth. AM1 corresponds to the solar irradiance measured at the sea level at the Equator, at a solar zenith angle of $z=0^\circ$, after having crossed one atmosphere. AM1.5 corresponds to 1.5 atmosphere thickness, at a solar zenith angle of $z=48.2^\circ$. Therefore, it is a closer approximation to the solar irradiance spectra measured at the world's densely populated areas at temperate altitudes (North America, Europe, China, Japan, Australia, South Africa). The commonly used AM1.5G spectrum is based on the G173 standard, and is used for terrestrial applications including both diffuse and direct light. By convention, it corresponds to an integrated solar power of 1000 W m^{-2} . The AM1.5D spectrum, also based on ASTM G173, only includes direct light, and corresponds to an integrated power of 888 W m^{-2} .

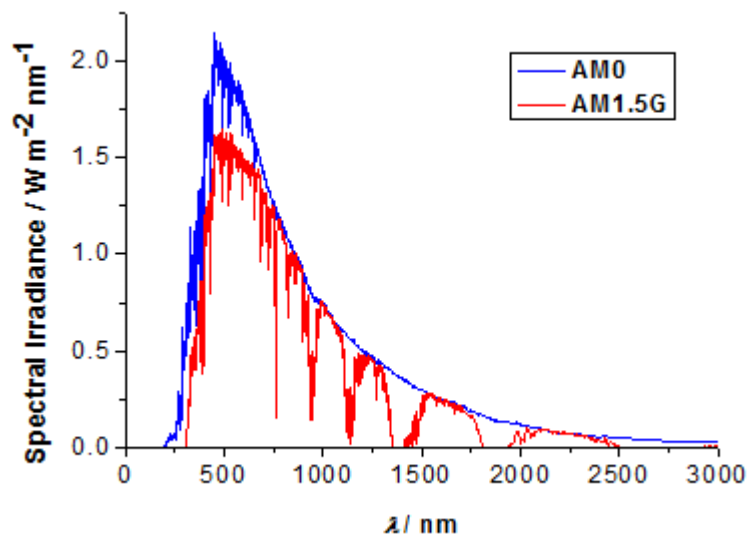


Figure I.5. Solar irradiance spectra references according to the ASTM standards.

I.5. Solar cell efficiency factors

In order to evaluate the performance of a solar cell, an external bias is applied to the device, and its current-voltage (I - V) characteristics are measured under illumination and in the dark. The current-voltage (I - V) curve of a typical photovoltaic cell is illustrated in *Figure I.6*. The most important points of this I - V curve are the short-circuit current (I_{sc}), the open-circuit voltage (V_{oc}), the maximum power output (P_m), and the current (I_m) and voltage (V_m) corresponding to P_m . In more detail, I_{sc} is the maximum generated photocurrent, which corresponds to zero applied voltage. V_{oc} , previously defined in *Equation I.1* and *Figure I.4.*, is the maximum voltage available from the solar cell, which occurs at zero current.

Chapter I. Context

It is straightforward to obtain an important solar cell efficiency parameter, the fill factor (FF) from the measured I - V curve. The fill factor evaluates the solar cell performance with respect to its maximum power output (P_m), and it is defined as:

$$FF = \frac{I_m \cdot V_m}{I_{sc} \cdot V_{oc}} \quad (I.6)$$

The graphical interpretation is displayed in *Figure I.6*. FF is thus the ratio of the area defined by the maximum power output (violet dashed lines) and the rectangle defined by I_{sc} and V_{oc} (green dashed lines). A FF value of 1 corresponds to an ideal cell where all photogenerated carriers are collected, and there are no resistance losses.

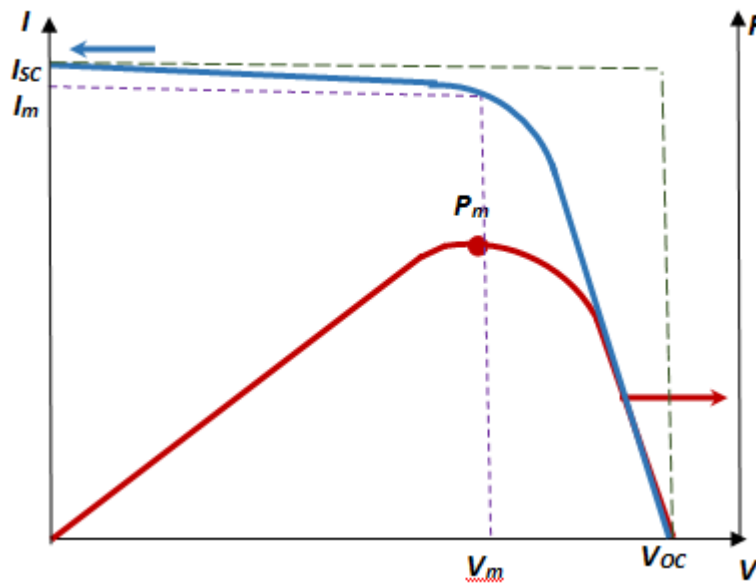


Figure I.6. Current-voltage characteristics of a photovoltaic cell under illumination.

The most important device evaluation parameter is the maximum photovoltaic power conversion efficiency. It is defined as the fraction of incident power (P_{in}) which is converted to electricity:

$$\eta = \frac{I_m \cdot V_m}{P_{in}} \quad (1.7)$$

The IPCE (incident photon to current efficiency) is the ratio of the charge carriers collected at the electrodes and the number of incident photons. Determining the short-circuit currents at different wavelengths of incident light, we can obtain the IPCE from the following expression:

$$IPCE = \frac{1240 \cdot I_{sc}}{\lambda \cdot P_{inc}} \quad (1.8)$$

where P_{inc} is the incident light power (W cm^{-2}), λ is the wavelength of incident light (in nm), and I_{sc} is the short circuit current density expressed in A cm^{-2} .

I.6. State of art

I.6.1. Experimental challenges

The first reported complete quantum dot sensitized solar cell dates back to 1998, and was demonstrated by Zaban et al.¹¹². Their QDSC contained nanoporous TiO_2 electrodes sensitized with InP QDs, and the device was completed with a Pt counter electrode and a I^-/I_3^- electrolyte solution. As detailed in the previous sections, great progress has been made since then by finding more suitable materials, such as sulfide/polysulfide based redox electrolytes and Cu_2S counter electrodes. It is particularly notable that QDSC efficiencies doubled in the last 4 years from 5.4%¹¹³ to 11.6%,¹¹⁴ and many efficiency improvements have been achieved by surface treatments of the nanocrystals and of the wide band gap metal oxides. Two important challenges can be addressed with well-chosen surface treatments: 1) alignment of energy levels through surface dipoles on the nanocrystals¹¹⁵ and 2) passivation of trap states at the semiconductor surfaces and interfaces that reduce conductivity and serve as recombination centres.^{116–118} Trap states at semiconductor surfaces and interfaces are also responsible for the Fermi level pinning: they pin the Fermi level of the WBSC at a certain energy value within the band gap, which is thus unable to shift

Chapter I. Context

up when the WBSC receives electron injection from the sensitizer. In consequence, the available open circuit voltage (defined on *Figure I.4* and in *Equation I.1.*) will be well below the predicted energy level.¹¹⁹

In the following, a few important milestones achieved since 2014, during the course of this PhD are highlighted. Most of them are oriented towards the surface engineering of the WBSC and QD surface in order to dramatically reduce recombination reactions, as described above, and they also pave the way for future research directions. Wang et al. deposited a Mn-modified CdSe layer on the $\text{TiO}_2/\text{CdSe}_x\text{Te}_{1-x}$ photoanode surface, which acted as a passivation layer, and also increased the photoanode's light absorption. Their solar cell reached an efficiency of 8.1%.¹²⁰ Ren et al. modified the surface of both CdSeTe QDs and of the mesoporous crystalline TiO_2 layer. They deposited a ZnS/SiO_2 layer onto CdSeTe QDs, added an amorphous TiO_2 coating on the surface of TiO_2 nanoparticles, and reached a power conversion efficiency of 9.0%.¹²¹ They demonstrated in their study that recombination at the QD- TiO_2 interface was reduced due to amorphous TiO_2 interlayer. Another approach to efficiently suppress surface trap states on QDs is to construct core/shell nanocrystals. Yang et al. optimized the CdS shell on CdSeTe cores, and attached them to TiO_2 film electrodes.¹²² They demonstrated that the solar cells based on these photoanodes are significantly more efficient than using plain CdSeTe QDs, and reported a solar cell efficiency of 9.48%. Jiao et al. measured accelerated electron injection rate from ZnTe/CdSe core/shell QDs towards the TiO_2 substrate, and the efficiency of their solar cells reached 7.17%.¹²³ Chuang et al. increased the power conversion efficiency of their devices from 6.0 to 8.55% by choosing the right ligands treatment on their PbS QD layered film on a ZnO nanoparticle substrate.^{124,125} The different surface ligands altered the energy band levels of the QDs to increase light absorption and to separate charges more efficiently. Kim et al. applied surface ligand treatments on PbS QDs in a similar spirit to modulate the band alignment between the self-assembled PbS QD film and the ZnO substrate.¹²⁶ They achieved a V_{oc} of as high as 0.66 V and a J_{sc} of 23.95 mA cm^{-2} , and reported a solar cell efficiency of 10.7%.

Despite a large amount of research investment, the highest reported power conversion efficiency for quantum dot sensitized solar cells is 11.6%.¹¹⁴ This performance is still well below the highest efficiency of other solar cell types,¹⁶ such as the 25% for silicon based

Chapter I. Context

devices,¹²⁷ 21% for thin-film chalcogenide solar cells,¹²⁸ and 22.1% for perovskite sensitized solar cells.¹²⁹ However, there is still a lot of potential to exploit in QDSCs. It is to note that QDSC efficiencies demonstrate constant growth over time, in contrast to DSSC efficiencies that have been nearly stagnant over the last few years,¹⁶ and the current record efficiency of a certified 11.6%¹¹⁴ is already close to that of 11.9% for dye-sensitized solar cells.¹³⁰ Also, while perovskite solar cells are by far the best performing devices among the family of sensitized solar cells, QDSCs are significantly more stable over time.

In a recent study, Bozyigit et al. established the first consistent model accounting for the processes that limit QDSC performance, and how trap states are involved.¹³¹ They quantified charge carrier transport, trapping and recombination in nanocrystal solar cells, and provided guidelines for the design of future QDSCs based on their charge transfer model. The study can be summarized in two points. *Firstly*, in order to make the most of the quantum confinement effect, it should be considered that charge carrier mobility is increased in small QDs, and in consequence, charge extraction is improved, and the short-circuit current is higher. On the other hand, however, smaller QDs have more surface trap states that are rapidly found by carriers with high mobility. Therefore the *best electron injection efficiency is expected for intermediate nanocrystal sizes*. *Secondly*, ligand treatments on semiconductor QDs can introduce surface dipoles,¹²⁵ which should increase the tunnel barriers for one carrier, and decrease barriers for the other, as Bozyigit et al. argued. Consequently, *well-chosen ligands can balance out the electron and hole mobilities* to limit recombination.

I.6.2. Modeling challenges

Atomistic *ab initio* descriptions of quantum dots have provided invaluable insights into the geometrical and electronic properties of these semiconductor nanocrystals, and provided explanations or additional details of physical chemical phenomena relevant to their photovoltaic application. In the following, a few notable theoretical studies are cited, which all applied density functional theory (DFT)-based computational methods. Voznyy et al modeled CdSe clusters, and computed the density of states of QDs with and without surface passivation ligands (oleic acid modeled as acetic acid for simplicity).¹³² They demonstrated how the amount of ligands and their adsorption geometry can introduce trap states at

Chapter I. Context

different energies in the band gap. Based on their model, they provided an explanation of the QD blinking and the variations in their emission lifetimes and wavelengths by the diffusion of mobile ligands on the crystal surfaces. However, as what concerns methodology, plane wave basis sets and a functional within the generalized gradient approximation (GGA) were considered. Time-dependent (TD) and real-time (RT) dependent DFT has been used with Gaussian-type orbital (GTO) basis sets to simulate the structure and the optical absorption spectra of CdSe QDs.¹³³ These model clusters were so-called “magic-size” clusters that contain 6, 13 or 34 CdSe units, and are of exceptional stability with respect to other cluster sizes in the same order of magnitude. In this study, GGA was found to be a good compromise to calculate both geometry and optical spectra. Considering the latter, hybrid functionals associated with higher computational cost would have been even more accurate. In another study, the electronic and optical properties of CdSe clusters with complementary passivation by carboxylic and amine ligands were calculated with a GGA functional and a plane wave basis set.¹³⁴ Most notably, the computed optical absorption spectrum was in very good agreement with the experimental one. Moreover, additional molecular dynamics simulations made it possible to explain the origin of the widening of the spectral lines by vibrations and the structural variations of the ligand configurations. Solution effects were also taken into account in the computational study of cysteine-capped CdSe clusters by Cui et al,¹³⁵ who used a hybrid DFT functional and Gaussian-type orbital basis sets in their study. The authors examined how the solution and ligand affect the size-dependent properties of CdSe QDs, and also described the different adsorption patterns of ligands on the CdSe QD surfaces in different solvents. Based on their results, they predicted that structural distortions introduced by the ligands, added to the solvent effects can reverse the redshift tendency of excitonic peaks as the QD size increases. To cite a few examples of mixed experimental/theoretical studies, DFT calculations have been very useful for confirming and completing the experimentally postulated nature of tiostannate ligand – CdSe QD interactions,¹³⁶ establishing a probable mechanism for the removal of carboxylic acid ligands from CdSe QDs during ligand exchange reactions¹³⁷ or to shed light on the details of the passivation of PbS QDs with CdCl₂.¹³⁸ As what concerns the modeling of two-dimensional nanoplatelets, they were much less extensively studied. The very few notable theoretical works on these nanocrystals include the simulation of their electronic properties, such as band structures and exciton binding energies by a semi-empirical tight-binding method^{139,140}

Chapter I. Context

and DFT calculations with GGA functionals and plane wave basis sets to explore their electronic surface states and dielectric self-energy profiles.¹⁴¹

Regarding WBSCs, several examples of the DFT modeling of ZnO^{142,143}, as well as of TiO₂ nanostructures for hybrid solar cells^{144–146} are known. In these DFT studies, the geometrical and electronic ground-state properties are simulated using hybrid functionals and GTO basis sets or^{142,144,145} GGA functionals with plane wave basis sets.¹⁴³ The lowest optical transition energies of 1D, 2D and 3D ZnO nanostructures have also been computed with time-dependent DFT, including solvent effects, using hybrid functional and GTO basis sets, in good agreement with experimental data.¹⁴³

To take a step further after presenting previous works on the bare components of a QDSC, several studies have analyzed sensitizer – semiconductor oxide heterostructures, or in other words, have gone as far as modeling the photoanodes of these devices. Patrick et al established an atomistic model of the Sb₂S₃/TiO₂ interface using GGA functionals and plane wave basis sets.¹⁴⁷ The model consisted of a Sb₂S₃ nanoribbon running in parallel with a TiO₂ anatase (101) surface, the two forming a lattice-matched interface free of defects and recombination centers, with a prospective ideal open circuit voltage as high as 1.6 V. The rest of the studies concentrated on TiO₂ surfaces sensitized by model ZnSe/CdS core-shell,^{148,149} CdSe,^{150–153} CdS,¹⁵⁴ PbSe,¹⁵⁰ and PbS¹⁵⁵ clusters referring to spherical QDs. Prezhdo's group performed several studies using a combination of TD- DFT and non-adiabatic molecular dynamics (NAMD) to describe charge separation, charge and energy transfer, relaxation and charge recombination at interfaces formed between QDs and TiO₂ surfaces.^{156–158} In the DFT study of Dong et al, using the B3LYP hybrid functional, the authors described the electronic coupling between CdS QDs and TiO₂ nanotubes (NTs) and demonstrated the possibility of an electron transfer from the sulphur atoms of the CdS QDs towards the TiO₂ NT surface and how the nanotube structure makes it possible to provide a one-dimensional electron pathway through the titanium d orbitals.¹⁵⁴ Nadler et al constructed a model system that contains a methylamine-capped (CdSe)₁₃ cluster linked to a (TiO₂)₃₈ nanoparticle *via* a mercaptopropionate bridge.¹⁵³ They demonstrated the possibility of electron injection from the QD towards the WBSC by calculating the frontier molecular orbitals of the system, which was also confirmed by the simulation of the optical spectrum of

Chapter I. Context

the system by real-time TD-DFT (RT-TDDFT) calculations with localized basis sets and the hybrid B3LYP functional. Azpiroz et al reported a DFT study on the comparison of electron injection efficiency from core-only (ZnSe) and core/shell (ZnSe/CdS) QDs towards TiO_2 ¹⁴⁸ and explained the better efficiency found with core/shell sensitizers by the weaker coupling between the newly injected electrons on the WBSC and the holes trapped in the sensitizer core. They also demonstrated the emergence of a dipole at this interface, which shifts up the conduction band level of TiO_2 and increases the open-circuit voltage.¹⁴⁹ The latter had also been observed experimentally for similar systems by Zaban et al.¹⁵⁹

As described above, most of the QDSC photoanode models published so far are limited to a WBSC surface sensitized by small model QDs with a diameter in the order of 1.5-2 nm, although the experimentally prepared ones are often larger.^{30,160} No extended semiconductor interfaces were involved in these publications, with the exception of Patrick et al's study,¹⁴⁷ which still discussed a lattice-matched heterostructure system without significant surface reconstructions. Only very few examples of computational studies on semiconductor interfaces formed between compounds with a large lattice-mismatch can be found in the literature.^{161–165} Heavy computational costs limited these calculations to an interface made between a single^{161–163} or a double adsorbate layer¹⁶⁴ and a substrate surface. Moreover, DFT was applied using local density and generalized gradient approximations that are known to severely underestimate band gaps,¹⁶⁶ while hybrids can approximate them with an error of a few percent with respect to experimental data.¹⁶⁷

Another limitation of current 3rd generation photovoltaic research is that studies rely heavily on a few materials the synthesis of which is already well-established. New QDSC materials are often discovered by trial and error, and most theoretical investigations invest effort in describing and understanding physical chemical phenomena in already discovered systems. Much less contributions to the discovery of new potential systems is known,^{168–171} where it is particularly challenging to define the selection metrics to find materials that satisfy several contradictory conditions. Also, these high throughput screening studies concentrated on the properties of separate QDSC components, while (within available computational and experimental resources) it would also be interesting to define selection criteria based on how these compounds actually behave in the cell during the photovoltaic procedure.

I.7. Goals and outline of the thesis

As we can conclude from the current state of art, and as also stressed in recent reviews,^{172–174} *future breakthroughs in QDSCs research are expected from band gap engineering and passivating surface/interface treatments of the semiconductors*. In this thesis, we targeted these challenges with a combined theoretical/experimental approach. As an interesting alternative to spherical quantum dots, quasi-2D CdSe nanoplatelets were studied as sensitizers. The advantages of studying nanoplatelets are twofold. First, due to the quantum confinement effects arising from their thickness of typically a few nanometers, their excitonic and charge carrier properties can be easily tuned: either by changing their thickness⁵⁰ or by varying the passivating ligands on their surface.¹⁷⁵ Second, from a modeling point of view, their precisely controlled thickness provides a good basis for building stacked models, allowing an easier comparison between experimental and theoretical data.

The interest of combining computational and experimental methods to study these systems lies in the difficulties and high costs of experimentally obtaining an accurate description of the electronic properties of semiconductor surfaces and interfaces at an atomic scale^{176–179}. In particular, density functional theory (DFT)-based computational approaches have been proven to be useful tools to describe and to predict the structural and electronic properties of individual components of third generation solar cells such as organic dyes^{180,181}, QDs,^{182,133} TiO₂^{144,183} and ZnO^{142,184} surfaces, as well as the interfaces formed between them.^{155,185,186,165} Furthermore, they have been efficiently applied for computing macroscopic characteristics (such as short circuit current and IPCE curves) of dye sensitized solar cells (DSSCs).^{187,188} In consequence, they are expected to be highly relevant and useful for studying QDSCs as well. While calculations give access to information that is experimentally hardly (or currently not at all) measurable, computational protocols need to be validated by experimental data. The two methods thus mutually complete each other to give new insights into the working principle of QDSCs and contribute to their rational design.

Chapter I. Context

Regarding the structure of this manuscript, **Chapter II** describes the computational, instrumental and synthesis methods used in this thesis. In **Chapter III**, a computational benchmark study was carried out to find a low-cost, yet highly accurate method to describe the bulk and surface properties of CdSe, the chosen sensitizer material. In **Chapter IV**, a theoretical model of the aforementioned quasi-2D CdSe nanoplatelets of different thicknesses, passivated by various ligands is established. The theoretical study, using the previously identified computational protocol was validated by experimental results. In **Chapter V**, ZnO and TiO₂ nanorods are sensitized by CdSe nanoplatelets of different thicknesses, linked together using various ligands. The as-prepared heterostructures are characterized by physical chemical methods to identify the system which will be studied in more detail in the next chapter. **Chapter VI** is a combined theoretical/experimental investigation about ZnO nanorods sensitized by sulfide-passivated CdSe nanoplatelets, with a special focus on the semiconductor interface properties. Finally, the assembly and the characterization of solar cells based on the previously studied nanocrystal/oxide heterostructures are described in **Chapter VII**. The thesis is closed with the general conclusions and perspectives.

References

- (1) International Energy Agency. *Key World Energy Statistics 2015*; 2015.
- (2) *Energy Information Administration Monthly Energy Report*; Washington, 2016.
- (3) <https://www.eia.gov/>.
- (4) Liu, Z. *Global Energy Interconnection*; Elsevier, 2015.
- (5) International Panel on Climate Change. In *Climate Change 2007: The Physical Science Basis*; Solomon, S., Qin, D., Manning, M., Chen, Z., Marquis, M., Averyt, K. B., M. Tignor, Miller, H. L., Eds.; Cambridge University Press: Cambridge, UK and New York, NY, USA, 2007.
- (6) The OECD environmental outlook to 2050. Key findings on climate change.
- (7) Renewable Energy Policy Network for the 21st century. *Renewables 2015. Global Status Report. Key Findings*; 2015.
- (8) Goldemberg, J.; Johansson, T. B. *World Energy Assessment Overview, 2004 Update. United Nations Development Programme*; New York, 2004.
- (9) Lewis, N. S. *Chemical Challenges in Renewable Energy*.
- (10) Kamat, P. V. Meeting the Clean Energy Demand: Nanostructure Architectures for Solar Energy Conversion. *Phys. Chem.* **2007**, 392, 2834–2860.
- (11) Xiao, X.; Lee, K.; Forrest, S. R. Scalability of Multi-Junction Organic Solar Cells for Large Area Organic Solar Modules. *Appl. Phys. Lett.* **2015**, 106 (21), 213301.
- (12) Nozik, A. J. Exciton Multiplication and Relaxation Dynamics in Quantum Dots: Applications to Ultra-High Efficiency Solar Photon Conversion. *Inorg. Chem.* **2005**, 44 (20), 6893.
- (13) Kuang, Y.; Vece, M. Di; Rath, J. K.; Dijk, L. Van; Schropp, R. E. I. Elongated Nanostructures for Radial Junction Solar Cells. *Rep. Prog. Phys.* **2013**, 76 (10), 106502.
- (14) Saga, T. Advances in Crystalline Silicon Solar Cell Technology for Industrial Mass Production. *NPG Asia Mater.* **2010**, 2 (3), 96–102.
- (15) Boreland, M.; Bagnall, D. *Current and Future Photovoltaics (Commissioned Report for Office of Science and Innovation – Foresight and Horizon Scanning Centre – Energy Project)*; 2001.
- (16) <http://www.nrel.gov/ncpv/>.
- (17) Jun, H. K.; Careem, M. a.; Arof, a. K. Quantum Dot-Sensitized Solar Cells—perspective and Recent Developments: A Review of Cd Chalcogenide Quantum Dots as Sensitizers. *Renew. Sustain. Energy Rev.* **2013**, 22, 148–167.
- (18) Beard, M. C.; Luther, J. M.; Semonin, O. E.; Nozik, A. J. Third Generation Photovoltaics Based on Multiple Exciton Generation in Quantum Confined Semiconductors. *Acc. Chem. Res.* **2013**, 46 (6), 1252–1260.
- (19) Shockley, W.; Queisser, H. J. Detailed Balance Limit of Efficiency of P-N Junction Solar Cells. *J. Appl. Phys.* **1961**, 32 (3), 510.
- (20) Concina, I.; Memarian, N.; Selopal, G. S.; Natile, M. M.; Sberveglieri, G.; Vomiero, a. Spray-Assisted Silar Deposition of Cadmium Sulphide Quantum Dots on Metal Oxide Films for Excitonic Solar Cells. *J. Power Sources* **2013**, 240, 736–744.
- (21) Yu, Y.; Kamat, P. V.; Kuno, M. A CdSe Nanowire/Quantum Dot Hybrid Architecture for Improving Solar Cell Performance. *Adv. Funct. Mater.* **2010**, 20, 1464–1472.
- (22) Lekha, P.; Balakrishnan, A.; Subramanian, K. R. V.; Nair, S. V. Size Dependent Electron Transfer from CdTe Quantum Dots Linked to TiO₂ Thin Films in Quantum Dot Sensitized Solar Cells. *Mater. Chem. Phys.* **2013**, 141, 216–222.
- (23) Dai, Q.; Chen, J.; Lu, L.; Tang, J.; Wang, W. PbS Quantum Dots Prepared by Pulsed Laser Deposition for Photovoltaic Applications and Ligand Effects on Device Performance. *Appl. Phys. Lett.* **2013**, 102 (20), 203904.
- (24) Guijarro, N.; Lana-villarreal, T.; Lutz, T.; Haque, S. A.; Gomez, R. Sensitization of TiO₂ with PbSe Quantum Dots by SILAR: How Mercaptophenol Improves Charge Separation. *J. Phys. Chem. Lett.* **2012**, 3, 3367–3372.
- (25) Peter, L. M.; Wijayantha, K. G. U.; Riley, D. J.; Waggett, J. P. Band-Edge Tuning in Self-Assembled Layers of Bi₂S₃ Nanoparticles Used to Photosensitize Nanocrystalline TiO₂. *J. Phys. Chem. B* **2003**, 107 (33),

Chapter I. Context

- 8378–8381.
- (26) Boix, P. P.; Larramona, G.; Jacob, A.; Delatouche, B.; Bisquert, J. Hole Transport and Recombination in All-Solid Sb₂S₃-Sensitized TiO₂ Solar Cells Using CuSCN As Hole Transporter. *J. Phys. Chem. C* **2012**, *116*, 1579–1587.
- (27) Yu, P.; Zhu, K.; Norman, A. G.; Ferrere, S.; Frank, A. J.; Nozik, A. J. Nanocrystalline TiO₂ Solar Cells Sensitized with InAs Quantum Dots. *J. Phys. Chem. B* **2006**, *110* (50), 25451–25454.
- (28) Santra, P. K.; Nair, P. V.; Thomas, K. G.; Kamat, P. V. CuInS₂-Sensitized Quantum Dot Solar Cell. Electrophoretic Deposition, Excited-State Dynamics, and Photovoltaic Performance. *J. Phys. Chem. Lett.* **2013**, *4*, 722–729.
- (29) Sargent, E. H. Infrared Photovoltaics Made by Solution Processing. *Nat. Photonics* **2009**, *3* (6), 325–331.
- (30) Kongkanand, A.; Tvrdy, K.; Takechi, K.; Kuno, M.; Kamat, P. V. Quantum Dot Solar Cells. Tuning Photoresponse through Size and Shape Control of CdSe-TiO₂ Architecture. *J. Am. Chem. Soc.* **2008**, *130*, 4007–4015.
- (31) Owen, J. S.; Chan, E. M.; Liu, H.; Alivisatos, A. P. Precursor Conversion Kinetics and the Nucleation of Cadmium Selenide Nanocrystals. *J. Am. Chem. Soc.* **2010**, *132* (51), 18206–18213.
- (32) Yu, W. W.; Qu, L.; Guo, W.; Peng, X. Experimental Determination of the Extinction Coefficient of CdTe, CdSe, and CdS Nanocrystals. *Chem. Mater.* **2003**, *15* (17), 2854–2860.
- (33) Tisdale, W. A.; Williams, K. J.; Timp, B. A.; Norris, D. J.; Aydil, E. S.; Zhu, X.-Y. Hot-Electron Transfer from Semiconductor Nanocrystals. *Science* (80-.). **2010**, *328*, 1543.
- (34) Lee, Y. K.; Lee, H.; Park, J. Y. Tandem-Structured, Hot Electron Based Photovoltaic Cell with Double Schottky Barriers. *Sci. Rep.* **2014**, *4*, 4580.
- (35) Zidek, K.; Zheng, K.; Abdellah, M.; Lenngren, N.; Chabera, P.; Pullerits, T. Ultrafast Dynamics of Multiple Exciton Harvesting in the CdSe-ZnO System: Electron Injection versus Auger Recombination. *Nano Lett.* **2012**, *12* (12), 6393–6399.
- (36) Xie, Y.; Teunis, M. B.; Pandit, B.; Sardar, R.; Liu, J. Molecule-like CdSe Nanoclusters Passivated with Strongly Interacting Ligands: Energy Level Alignment and Photoinduced Ultrafast Charge Transfer Processes. *J. Phys. Chem. C* **2015**, *119* (5), 2813–2821.
- (37) Flamee, S.; Cirillo, M.; Abe, S.; De Nolf, K.; Gomes, R.; Aubert, T.; Hens, Z. Fast, High Yield, and High Solid Loading Synthesis of Metal Selenide Nanocrystals. *Chem. Mater.* **2013**, *25* (12), 2476–2483.
- (38) Jasieniak, J.; Bullen, C.; Van Embden, J.; Mulvaney, P. Phosphine-Free Synthesis of CdSe Nanocrystals. *J. Phys. Chem. B* **2005**, *109* (44), 20665–20668.
- (39) Yang, Y. A.; Wu, H.; Williams, K. R.; Cao, Y. C. Synthesis of CdSe and CdTe Nanocrystals without Precursor Injection. *Angew. Chemie* **2005**, *44* (41), 6712–6715.
- (40) Ithurria, S.; Dubertret, B. Quasi 2D Colloidal CdSe Platelets with Thicknesses Controlled at the Atomic Level. *J. Am. Chem. Soc.* **2008**, *130* (49), 16504–16505.
- (41) Li, Z.; Peng, X. Size/shape-Controlled Synthesis of Colloidal CdSe Quantum Disks: Ligand and Temperature Effects. *J. Am. Chem. Soc.* **2011**, *133* (17), 6578–6586.
- (42) Bang, J. H.; Kamat, P. V. Quantum Dot Sensitized Solar Cells. A Tale of Two Semiconductor Nanocrystals: CdSe and CdTe. *ACS Nano* **2009**, *3* (6), 1467–1476.
- (43) Schaller, R. D.; Sykora, M.; Jeong, S.; Klimov, V. I.; Studied, N.; Photoluminescence, T. High-Efficiency Carrier Multiplication and Ultrafast Charge Separation in Semiconductor Nanocrystals Studied via Time-Resolved Photoluminescence High-Efficiency Carrier Multiplication and Ultrafast Charge Separation in Semiconductor. *J. Phys. Chem. B* **2006**, 25332–25338.
- (44) Franceschetti, A.; Zhang, Y. Multiexciton Absorption and Multiple Exciton Generation in CdSe Quantum Dots. *Phys. Rev. Lett.* **2008**, *100* (136805), 1–4.
- (45) Nag, A.; Kovalenko, M. V.; Lee, J.; Liu, W.; Spokoyny, B.; Talapin, D. V. Metal-Free Inorganic Ligands for Colloidal Nanocrystals: S²⁻, HS⁻, Se²⁻, HSe⁻, Te²⁻, HTe⁻, TeS₃²⁻, OH⁻, and NH₂⁻ as Surface Ligands. *J. Am. Chem. Soc.* **2011**, *133*, 10612–10620.
- (46) Baker, J. L.; Widmer-Cooper, A.; Toney, M. F.; Geissler, P. L.; Alivisatos, A. P. Device-Scale Perpendicular Alignment of Colloidal Nanorods. *Nano Lett.* **2010**, *10*, 195–201.
- (47) Jie, J. S.; Zhang, W. J.; Jiang, Y.; Lee, S. T. Single-Crystal CdSe Nanoribbon Field-Effect Transistors and Photoelectric Applications. *Appl. Phys. Lett.* **2006**, *89* (133118), 1–3.
- (48) Manna, L.; Milliron, D. J.; Meisel, A.; Scher, E. C.; Alivisatos, A. P. Controlled Growth of Tetrapod-Branched Inorganic Nanocrystals. *Nat. Mater.* **2003**, *2*, 382–385.
- (49) Son, J. S.; Wen, X.-D.; Joo, J.; Chae, J.; Baek, S.-I.; Park, K.; Kim, J. H.; An, K.; Yu, J. H.; Kwon, S. G.; et al. Large-Scale Soft Colloidal Template Synthesis of 1.4 Nm Thick CdSe Nanosheets. *Angew. Chemie* **2009**, *48*, 6861–6864.

Chapter I. Context

- (50) Ithurria, S.; Tessier, M. D.; Mahler, B.; Lobo, R. P. S. M.; Dubertret, B.; Efros, A. L. Colloidal Nanoplatelets with Two-Dimensional Electronic Structure. *Nat. Mater.* **2011**, *10* (12), 936–941.
- (51) Guzelturk, B.; Martinez, P. L. H.; Zhang, Q.; Xiong, Q.; Sun, H.; Sun, X. W.; Govorov, A. O.; Demir, H. V. Excitonics of Semiconductor Quantum Dots and Wires for Lighting and Displays. *Laser Photon. Rev.* **2014**, *8* (1), 73–93.
- (52) Li, M.; Zhi, M.; Zhu, H.; Wu, W.-Y.; Xu, Q.-H.; Jhon, M. H.; Chan, Y. Ultralow-Threshold Multiphoton-Pumped Lasing from Colloidal Nanoplatelets in Solution. *Nat. Commun.* **2015**, *6*, 8513.
- (53) Achtstein, A. W.; Schliwa, A.; Prudnikau, A.; Hardzei, M.; Artemyev, M. V.; Thomsen, C.; Woggon, U. Electronic Structure and Exciton-Phonon Interaction in Two-Dimensional Colloidal CdSe Nanosheets. *Nano Lett.* **2012**, *12* (6), 3151–3157.
- (54) Tessier, M. D.; Javaux, C.; Maksimovic, I.; Lorient, V.; Dubertret, B. Spectroscopy of Single CdSe Nanoplatelets. *ACS Nano* **2012**, *6* (8), 6751–6758.
- (55) Madelung, O. *Semiconductors: Data Handbook*, 3rd editio.; Springer-Verlag Berlin Heidelberg, 2004.
- (56) Tang, H.; Lévy, F.; Berger, H.; Schmid, P. E. Urbach Tail of Anatase TiO₂. *Phys. Rev. B* **1995**, *52* (11), 7771–7774.
- (57) Zhang, Q. F.; Dandeneau, C. S.; Zhou, X. Y.; Cao, G. Z. ZnO Nanostructures for Dye-Sensitized Solar Cells. *Adv. Mater.* **2009**, *21* (41), 4087–4108.
- (58) Weintraub, B.; Zhou, Z.; Li, Y.; Deng, Y. Solution Synthesis of One-Dimensional ZnO Nanomaterials and Their Applications. *Nanoscale* **2010**, *2* (9), 1573–1587.
- (59) Gonzalez-Valls, I.; Lira-Cantu, M. Vertically-Aligned Nanostructures of ZnO for Excitonic Solar Cells: A Review. *Energy Environ. Sci.* **2008**, *2* (1), 19–34.
- (60) Pauporte, T.; Bataille, G.; Joulaud, L.; Vermersch, F. J. Well-Aligned ZnO Nanowire Arrays Prepared by Seed-Layer-Free Electrodeposition and Their Cassie - Wenzel Transition after Hydrophobization. *J. Phys. Chem. C* **2010**, *114*, 194–202.
- (61) Zhu, Z.; Qiu, J.; Yan, K.; Yang, S. Building High-Efficiency CdS/CdSe-Sensitized Solar Cells with a Hierarchically Branched Double-Layer Architecture. *ACS Appl. Mater. Interfaces* **2013**, *5* (10), 4000–4005.
- (62) Chuang, C.-H. M.; Brown, P. R.; Bulović, V.; Bawendi, M. G. Improved Performance and Stability in Quantum Dot Solar Cells through Band Alignment Engineering. *Nat. Mater.* **2014**, *13* (May), 1–6.
- (63) Carey, G. H.; Levina, L.; Comin, R.; Voznyy, O.; Sargent, E. H. Record Charge Carrier Diffusion Length in Colloidal Quantum Dot Solids via Mutual Dot-To-Dot Surface Passivation. *Adv. Mater.* **2015**, 1–6.
- (64) Zhang, J.; Gao, J.; Church, C. P.; Miller, E. M.; Luther, J. M.; Klimov, V. I.; Beard, M. C. PbSe Quantum Dot Solar Cells with More than 6% Efficiency Fabricated in Ambient Atmosphere. *Nano Lett.* **2014**, *14*, 6010–6015.
- (65) O'Regan, B.; Gratzel, M. A Low-Cost, High-Efficiency Solar Cell Based on Dye-Sensitized Colloidal TiO₂ Films. *Nature* **1991**, *353*, 737–740.
- (66) Gratzel, M. Photoelectrochemical Cells. *Nature* **2001**, *414*, 338–344.
- (67) Wang, Y.; Yang, H.; Xu, H. DNA-like Dye-Sensitized Solar Cells Based on TiO₂ Nanowire-Covered Nanotube Bilayer Film Electrodes. *Mater. Lett.* **2010**, *64* (2), 164–166.
- (68) Senthil, T. S.; Muthukumarasamy, N.; Thambidurai, M.; Balasundaraprabhu, R.; Agilan, S. Light Conversion Efficiency of Flower like Structure TiO₂ Thin Film Solar Cells. *J. Sol-Gel Sci. Technol.* **2010**, *58* (1), 296–301.
- (69) Sudhagar, P.; Chandramohan, S.; Kumar, R. S.; Sathyamoorthy, R.; Hong, C.-H.; Kang, Y. S. Fabrication and Charge-Transfer Characteristics of CdS QDs Sensitized Vertically Grown Flower-like ZnO Solar Cells with CdSe Cosensitizers. *Phys. Status Solidi* **2011**, *208* (2), 474–479.
- (70) Liao, J.-Y.; Lei, B.-X.; Kuang, D.-B.; Su, C.-Y. Tri-Functional Hierarchical TiO₂ Spheres Consisting of Anatase Nanorods and Nanoparticles for High Efficiency Dye-Sensitized Solar Cells. *Energy Environ. Sci.* **2011**, *4* (10), 4079.
- (71) Wang, C.; Jiang, Z.; Wei, L.; Chen, Y.; Jiao, J.; Eastman, M.; Liu, H. Photosensitization of TiO₂ Nanorods with CdS Quantum Dots for Photovoltaic Applications: A Wet-Chemical Approach. *Nano Energy* **2012**, *1* (3), 440–447.
- (72) Yu, K.; Chen, J. Enhancing Solar Cell Efficiencies through 1-D Nanostructures. *Nanoscale Res. Lett.* **2008**, *4* (1), 1–10.
- (73) Law, M.; Greene, L. E.; Johnson, J. C.; Saykally, R.; Yang, P. Nanowire Dye-Sensitized Solar Cells. *Nat. Mater.* **2005**, *4* (6), 455–459.
- (74) Ohsaki, Y.; Masaki, N.; Kitamura, T.; Wada, Y.; Okamoto, T.; Sekino, T.; Niihara, K.; Yanagida, S. Dye-Sensitized TiO₂ Nanotube Solar Cells: Fabrication and Electronic Characterization. *Phys Chem Chem*

Chapter I. Context

- Phys* **2005**, 7 (24), 4157–4163.
- (75) Archana, P. S.; Jose, R.; Vijila, C.; Ramakrishna, S. Improved Electron Diffusion Coefficient in Electrospun TiO₂ Nanowires. *J. Phys. Chem. C* **2009**, 113, 21538–21542.
- (76) Fisher, A. C.; Peter, L. M.; Ponomarev, E. A.; Walker, A. B.; Wijayantha, K. G. U. Intensity Dependence of the Back Reaction and Transport of Electrons in Dye-Sensitized Nanocrystalline TiO₂ Solar Cells. *J. Phys. Chem. B* **2000**, 104 (5), 949–958.
- (77) Oekermann, T.; Zhang, D.; Yoshida, T.; Minoura, H. Electron Transport and Back Reaction in Nanocrystalline TiO₂ Films Prepared by Hydrothermal Crystallization. *J. Phys. Chem. B* **2004**, 108, 2227–2235.
- (78) Zhang, W.; Xie, Y.; Xiong, D.; Zeng, X.; Li, Z.; Wang, M.; Cheng, Y.-B.; Chen, W.; Yan, K.; Yang, S. TiO₂ Nanorods: A Facile Size- and Shape-Tunable Synthesis and Effective Improvement of Charge Collection Kinetics for Dye-Sensitized Solar Cells. *ACS Appl. Mater. Interfaces* **2014**, 6 (12), 9698–9704.
- (79) Sander, M. S.; Côté, M. J.; Gu, W.; Kile, B. M.; Tripp, C. P. Template-Assisted Fabrication of Dense, Aligned Arrays of Titania Nanotubes with Well-Controlled Dimensions on Substrates. *Adv. Mater.* **2004**, 16 (22), 2052–2057.
- (80) Jiu, J.; Isoda, S.; Wang, F.; Adachi, M. Dye-Sensitized Solar Cells Based on a Single-Crystalline TiO₂ Nanorod Film. *J. Phys. Chem. B* **2006**, 110 (5), 2087–2092.
- (81) Baker, D. R.; Kamat, P. V. Photosensitization of TiO₂ Nanostructures with CdS Quantum Dots: Particulate versus Tubular Support Architectures. *Adv. Funct. Mater.* **2009**, 19 (5), 805–811.
- (82) Pradhan, D.; Leung, K. T. Vertical Growth of Two-Dimensional Zinc Oxide Nanostructures on ITO-Coated Glass: Effects of Deposition Temperature and Deposition Time. *J. Phys. Chem. C* **2008**, 112 (5), 1357–1364.
- (83) Lupan, O.; Guérin, V. M.; Tiginyanu, I. M.; Ursaki, V. V.; Chow, L.; Heinrich, H.; Pauporté, T. Well-Aligned Arrays of Vertically Oriented ZnO Nanowires Electrodeposited on ITO-Coated Glass and Their Integration in Dye Sensitized Solar Cells. *J. Photochem. Photobiol. A Chem.* **2010**, 211 (1), 65–73.
- (84) Lee, Y.-L.; Chang, C.-H. Efficient Polysulfide Electrolyte for CdS Quantum Dot-Sensitized Solar Cells. *J. Power Sources* **2008**, 185 (1), 584–588.
- (85) Tachibana, Y.; Akiyama, H. Y.; Ohtsuka, Y.; Torimoto, T.; Kuwabata, S. CdS Quantum Dots Sensitized TiO₂ Sandwich Type Photoelectrochemical Solar Cells. *Chem. Lett.* **2007**, 36 (1), 88–89.
- (86) Chakrapani, V.; Baker, D.; Kamat, P. V. Understanding the Role of the Sulfide Redox Couple (S²⁻/S(n)²⁻) in Quantum Dot-Sensitized Solar Cells. *J. Am. Chem. Soc.* **2011**, 133 (24), 9607–9615.
- (87) Lee, H. J.; Chang, D. W.; Park, S.-M.; Zakeeruddin, S. M.; Grätzel, M.; Nazeeruddin, M. K. CdSe Quantum Dot (QD) and Molecular Dye Hybrid Sensitizers for TiO₂ Mesoporous Solar Cells: Working Together with a Common Hole Carrier of Cobalt Complexes. *Chem. Commun.* **2010**, 46, 8788–8790.
- (88) Tachibana, Y.; Umekita, K.; Otsuka, Y.; Kuwabata, S. Performance Improvement of CdS Quantum Dots Sensitized TiO₂ Solar Cells by Introducing a Dense TiO₂ Blocking Layer. *J. Phys. D. Appl. Phys.* **2008**, 41 (10), 102002.
- (89) Akimov, A. V.; Neukirch, A. J.; Prezhdov, O. V. Theoretical Insights into Photoinduced Charge Transfer and Catalysis at Oxide Interfaces. **2013**.
- (90) Ning, Z.; Fu, Y.; Tian, H. Improvement of Dye-Sensitized Solar Cells: What We Know and What We Need to Know. *Energy Environ. Sci.* **2010**, 3 (9), 1170.
- (91) Hodes, G. Comparison of Dye- and Semiconductor-Sensitized Porous Nanocrystalline Liquid Junction Solar Cells. *J. Phys. Chem. C* **2008**, 112 (46), 17778–17787.
- (92) Mora-Sero, I.; Bisquert, J. Fermi Level of Surface States in TiO₂ Nanoparticles. *Nano Lett.* **2003**, 3, 945–949.
- (93) Du, J.; Meng, X.; Zhao, K.; Li, Y.; Zhong, X. Performance Enhancement of Quantum Dot Sensitized Solar Cells by Adding Electrolyte Additives. *J. Mater. Chem. A* **2015**, 3, 17091–17097.
- (94) Sinke, W. C.; Wienk, M. M. Solid-State Organic Solar Cells. *Nature* **1998**, 395, 544–555.
- (95) Li, B.; Wang, L.; Kang, B.; Wang, P.; Qiu, Y. Review of Recent Progress in Solid-State Dye-Sensitized Solar Cells. *Sol. Energy Mater. Sol. Cells* **2006**, 90 (5), 549–573.
- (96) Qian, J.; Liu, Q.-S.; Li, G.; Jiang, K.-J.; Yang, L.-M.; Song, Y. P3HT as Hole Transport Material and Assistant Light Absorber in CdS Quantum Dots-Sensitized Solid-State Solar Cells. *Chem. Commun. (Camb)*. **2011**, 47 (22), 6461–6463.
- (97) Barceló, I.; Campiña, J. M.; Lana-Villarreal, T.; Gómez, R. A Solid-State CdSe Quantum Dot Sensitized Solar Cell Based on a Quaterthiophene as a Hole Transporting Material. *Phys. Chem. Chem. Phys.* **2012**, 14 (16), 5801–5807.
- (98) Lee, H.; Wang, M.; Chen, P.; Gamelin, D. R.; Zakeeruddin, S. M.; Grätzel, M.; Nazeeruddin, M. K.

Chapter I. Context

- Efficient CdSe Quantum Dot-Sensitized Solar Cells Prepared by an Improved Successive Ionic Layer Adsorption and Reaction Process. *Nano Lett.* **2009**, 9 (12), 4221–4227.
- (99) Lee, H.; Leventis, H. C.; Moon, S.-J.; Chen, P.; Ito, S.; Haque, S. a.; Torres, T.; Nüesch, F.; Geiger, T.; Zakeeruddin, S. M.; et al. PbS and CdS Quantum Dot-Sensitized Solid-State Solar Cells: “Old Concepts, New Results.” *Adv. Funct. Mater.* **2009**, 19, 2735–2742.
- (100) Wang, S.; Zhang, Q.-X.; Xu, Y.-Z.; Li, D.-M.; Luo, Y.-H.; Meng, Q.-B. Single-Step in-Situ Preparation of Thin Film Electrolyte for Quasi-Solid State Quantum Dot-Sensitized Solar Cells. *J. Power Sources* **2013**, 224, 152–157.
- (101) Karageorgopoulos, D.; Stathatos, E.; Vitoratos, E. Thin ZnO Nanocrystalline Films for Efficient Quasi-Solid State Electrolyte Quantum Dot Sensitized Solar Cells. *J. Power Sources* **2012**, 219, 9–15.
- (102) Loucka, T. Adsorption and Oxidation of Organic Compounds on a Platinum Electrode Partly Covered by Adsorbed Sulphur. *Electroanal. Chem. Interfacial Electrochem.* **1972**, 36, 355–367.
- (103) Mora-Sero, I.; Gimenez, S.; Fabregat-Santiago, F.; Gomez, R.; Shen, Q.; Toyoda, T.; Bisquert, J. Recombination in Quantum Dot Sensitized Solar Cells. *Acc. Chem. Res.* **2009**, 42 (11), 1848–1857.
- (104) Radich, J. G.; Dwyer, R.; Kamat, P. V. Cu₂S Reduced Graphene Oxide Composite for High-Efficiency Quantum Dot Solar Cells. Overcoming the Redox Limitations of S²⁻/Sn²⁻ at the Counter Electrode. *J. Phys. Chem. Lett.* **2011**, 2, 2453–2460.
- (105) Giménez, S.; Mora-Seró, I.; Macor, L.; Guijarro, N.; Lana-Villarreal, T.; Gómez, R.; Diguna, L. J.; Shen, Q.; Toyoda, T.; Bisquert, J. Improving the Performance of Colloidal Quantum-Dot-Sensitized Solar Cells. *Nanotechnology* **2009**, 20 (29), 295204.
- (106) Yang, Z.; Chen, C.-Y.; Liu, C.-W.; Chang, H.-T. Electrocatalytic Sulfur Electrodes for CdS/CdSe Quantum Dot-Sensitized Solar Cells. *Chem. Commun. (Camb).* **2010**, 46 (30), 5485–5487.
- (107) Tachan, Z.; Shalom, M.; Hod, I.; Rühle, S.; Tirosh, S.; Zaban, A. PbS as a Highly Catalytic Counter Electrode for Polysulfide-Based Quantum Dot Solar Cells. *J. Phys. Chem. C* **2011**, 115 (13), 6162–6166.
- (108) Zeng, X.; Zhang, W.; Xie, Y.; Xiong, D.; Chen, W.; Xu, X.; Wang, M.; Cheng, Y.-B. Low-Cost Porous Cu₂ZnSnSe₄ Film Remarkably Superior to Noble Pt as Counter Electrode in Quantum Dot-Sensitized Solar Cell System. *J. Power Sources* **2013**, 226, 359–362.
- (109) Boix, P. P.; Lee, Y. H.; Fabregat-Santiago, F.; Im, S. H.; Mora-Sero, I.; Bisquert, J.; Seok, S. Il. From Flat to Nanostructured Photovoltaics: Balance between Thickness of the Absorber and Charge Screening in Sensitized Solar Cells. *ACS Nano* **2012**, 6 (1), 873–880.
- (110) Chang, J. A.; Rhee, J. H.; Im, S. H.; Lee, Y. H.; Kim, H.; Seok, S. Il; Nazeeruddin, M. K.; Gratzel, M. High-Performance Nanostructured Inorganic-Organic Heterojunction Solar Cells. *Nano Lett.* **2010**, 10 (7), 2609–2612.
- (111) Yu, Z.; Zhang, Q.; Qin, D.; Luo, Y.; Li, D.; Shen, Q.; Toyoda, T.; Meng, Q. Highly Efficient Quasi-Solid-State Quantum-Dot-Sensitized Solar Cell Based on Hydrogel Electrolytes. *Electrochem. commun.* **2010**, 12 (12), 1776–1779.
- (112) Zaban, A.; Micic, O.; Gregg, B. A.; Nozik, A. J. Photosensitization of Nanoporous TiO₂ Electrodes with InP Quantum Dots. *Langmuir* **1998**, 14 (11), 3153–3156.
- (113) Santra, P. K.; Kamat, P. V. Mn-Doped Quantum Dot Sensitized Solar Cells: A Strategy to Boost Efficiency over 5%. *J. Am. Chem. Soc.* **2012**, 134 (5), 2508–2511.
- (114) Du, J.; Du, Z.; Hu, J.-S.; Pan, Z.; Shen, Q.; Sun, J.; Long, D.; Dong, H.; Sun, L.; Zhong, X.; et al. Zn-Cu-In-Se Quantum Dot Solar Cells with a Certified Power Conversion Efficiency of 11.6%. *J. Am. Chem. Soc.* **2016**, 138, 4201–4209.
- (115) Santra, P. K.; Palmstrom, A. F.; Tanskanen, J. T.; Yang, N.; Bent, S. F. Improving Performance in Colloidal Quantum Dot Solar Cells by Tuning Band Alignment through Surface Dipole Moments. *J. Phys. Chem. C* **2015**, 119 (6), 150115141647007.
- (116) Tang, J.; Kemp, K. W.; Hoogland, S.; Jeong, K. S.; Liu, H.; Levina, L.; Furukawa, M.; Wang, X.; Debnath, R.; Cha, D.; et al. Colloidal-Quantum-Dot Photovoltaics Using Atomic-Ligand Passivation. *Nat. Mater.* **2011**, 10 (10), 765–771.
- (117) Ip, A. H.; Thon, S. M.; Hoogland, S.; Voznyy, O.; Zhitomirsky, D.; Debnath, R.; Levina, L.; Rollny, L. R.; Carey, G. H.; Fischer, A.; et al. Hybrid Passivated Colloidal Quantum Dot Solids. *Nat. Nanotechnol.* **2012**, 7 (9), 577–582.
- (118) Bae, W. K.; Joo, J.; Padilha, L. A.; Won, J.; Lee, D. C.; Lin, Q.; Koh, W. K.; Luo, H.; Klimov, V. I.; Pietryga, J. M. Highly Effective Surface Passivation of Pbse Quantum Dots through Reaction with Molecular Chlorine. *J. Am. Chem. Soc.* **2012**, 134 (49), 20160–20168.
- (119) Henry, C. H. Limiting Efficiencies of Ideal Single and Multiple Energy Gap Terrestrial Solar Cells. *J. Appl. Phys.* **1980**, 51 (8), 4494–4500.

Chapter I. Context

- (120) Wang, G.; Wei, H.; Luo, Y.; Wu, H.; Li, D.; Zhong, X.; Meng, Q. A Strategy to Boost the Cell Performance of CdSexTe1-X Quantum Dot Sensitized Solar Cells over 8% by Introducing Mn Modified CdSe Coating Layer. *J. Power Sources* **2016**, *302*, 266–273.
- (121) Ren, Z.; Wang, J.; Pan, Z.; Zhao, K.; Zhang, H.; Li, Y.; Zhao, Y.; Mora-Sero, I.; Bisquert, J.; Zhong, X. Amorphous TiO₂ Buffer Layer Boosts Efficiency of Quantum Dot Sensitized Solar Cells to over 9%. *Chem. Mater.* **2015**, *27* (24), 8398–8405.
- (122) Yang, J.; Wang, J.; Zhao, K.; Izuishi, T.; Li, Y.; Shen, Q.; Zhong, X. CdSeTe/CdS Type-I Core/Shell Quantum Dot Sensitized Solar Cells with Efficiency over 9%. *J. Phys. Chem. C* **2015**, *119* (52), 28800–28808.
- (123) Jiao, S.; Shen, Q.; Mora-Sero, I.; Wang, J.; Pan, Z.; Zhao, K.; Kuga, Y.; Zhong, X.; Bisquert, J. Band Engineering in Core / Shell ZnTe / CdSe for Photovoltage and Efficiency Enhancement in Exciplex Quantum Dot Sensitized Solar Cells. *ACS Nano* **2015**, *9* (1), 908–915.
- (124) Chuang, C.-H. M.; Brown, P. R.; Bulovic, V.; Bawendi, M. G. Improved Performance and Stability in Quantum Dot Solar Cells through Band Alignment Engineering. *Nat. Mater.* **2014**, *13* (May), 1–6.
- (125) Brown, P. R.; Kim, D.; Lunt, R. R.; Zhao, N.; Bawendi, M. G.; Grossman, J. C.; Bulovic, V. Energy Level Modification in Lead Sulfide Quantum Dot Thin Films through Ligand Exchange. *ACS Nano* **2014**, *8* (6), 5863–5872.
- (126) Kim, G. H.; García De Arquer, F. P.; Yoon, Y. J.; Lan, X.; Liu, M.; Voznyy, O.; Yang, Z.; Fan, F.; Ip, A. H.; Kanjanaboos, P.; et al. High-Efficiency Colloidal Quantum Dot Photovoltaics via Robust Self-Assembled Monolayers. *Nano Lett.* **2015**, *15* (11), 7691–7696.
- (127) Zhao, J.; Wang, A.; Green, M. A.; Ferrazza, F. 19.8% Efficient “Honeycomb” Textured Multicrystalline and 24.4% Monocrystalline Silicon Solar Cells. *Appl. Phys. Lett.* **1998**, *73* (14), 1991–1993.
- (128) M, P.; P, J.; D, H.; S, P.; W, W.; R, W.; E, L.; R, M.; W., W. CIGS Thin-Film Solar Cells with an Improved Efficiency of 20.8%. In *29th European Photovoltaic Solar Energy Conference*; Amsterdam, 2014.
- (129) Bi, D.; Tress, W.; Dar, M. I.; Gao, P.; Luo, J.; Renevier, C.; Schenk, K.; Abate, A.; Giordano, F.; Correa Baena, J.-P.; et al. Efficient Luminescent Solar Cells Based on Tailored Mixed-Cation Perovskites. *Sci. Adv.* **2016**, *2* (1), e1501170–e1501170.
- (130) Komiya R, Fukui A, Murofushi N, Koide N, Yamanaka R, K. H. I. Improvement of the Conversion Efficiency of a Monolithic Type Dye-Sensitized Solar Cell Module. In *Technical Digest, 21st International Photovoltaic Science and Engineering Conference*; Fukuoka, 2011.
- (131) Bozyigit, D.; Lin, W. M. M.; Yazdani, N.; Yarema, O.; Wood, V. A Quantitative Model for Charge Carrier Transport, Trapping and Recombination in Nanocrystal-Based Solar Cells. *Nat. Commun.* **2015**, *6*, 6180.
- (132) Voznyy, O. Mobile Surface Traps in CdSe Nanocrystals with Carboxylic Acid Ligands. *J. Phys. Chem. C* **2011**, *115* (32), 15927–15932.
- (133) Nadler, R.; Sanz, J. F. Simulating the Optical Properties of CdSe Clusters Using the RT-TDDFT Approach. *Theor. Chem. Acc.* **2013**, *132* (4), 1342.
- (134) Voznyy, O.; Morkath, J. H.; Jain, A.; Sargent, E. H.; Schwingenschlögl, U. Computational Study of Magic-Size CdSe Clusters with Complementary Passivation by Carboxylic and Amine Ligands. *J. Phys. Chem. C* **2016**, *120*, 10015–10019.
- (135) Cui, Y.; Lou, Z.; Wang, X.; Yu, S.; Yang, M. A Study of Optical Absorption of Cysteine-Capped CdSe Nanoclusters Using First-Principles Calculations †. *Phys. Chem. Chem. Phys.* **2015**, *17*, 9222–9230.
- (136) Protesescu, L.; Nachttegaal, M.; Voznyy, O.; Borovinskaya, O.; Rossini, A. J.; Emsley, L.; Copret, C.; Gonthier, D.; Sargent, E. H.; Kovalenko, M. V. Atomistic Description of Thiostannate-Capped CdSe Nanocrystals: Retention of Four-Coordinate SnS₄ Motif and Preservation of Cd-Rich Stoichiometry. *J. Am. Chem. Soc.* **2015**, *137* (5), 1862–1874.
- (137) Margraf, J. T.; Ruland, A.; Sgobba, V.; Guldi, D. M.; Clark, T. Theoretical and Experimental Insights into the Surface Chemistry of Semiconductor Quantum Dots. *Langmuir* **2013**, *29* (49), 15450–15456.
- (138) Thon, S. M.; Ip, A. H.; Voznyy, O.; Levina, L.; Kemp, K. W.; Carey, G. H.; Masala, S.; Sargent, E. H. Role of Bond Adaptability in the Passivation of Colloidal Quantum Dot Solids. *ACS Nano* **2013**, *7* (9), 7680–7688.
- (139) Benchamekh, R.; Gippius, N. a.; Even, J.; Nestoklon, M. O.; Jancu, J.-M.; Ithurria, S.; Dubertret, B.; Efron, A. L.; Voisin, P. Tight-Binding Calculations of Image-Charge Effects in Colloidal Nanoscale Platelets of CdSe. *Phys. Rev. B* **2014**, *89* (3), 035307.
- (140) Benchamekh, R.; Even, J.; Jancu, J.; Nestoklon, M.; Ithurria, S.; Dubertret, B.; Voisin, P. Electronic and Optical Properties of Colloidal CdSe Nanoplatelets. *Nanosctructures Phys. Technol.* **2012**, *56*.
- (141) Even, J.; Pedesseau, L.; Kepenekian, M. Electronic Surface States and Dielectric Self-Energy Profiles in Colloidal Nanoscale Platelets of CdSe. *Phys Chem Chem Phys* **2014**, *16* (45), 25182–25190.
- (142) Labat, F.; Ciofini, I.; Adamo, C. Modeling ZnO Phases Using a Periodic Approach: From Bulk to Surface and Beyond. *J. Chem. Phys.* **2009**, *131* (4), 044708.

Chapter I. Context

- (143) De Angelis, F.; Armelao, L. Optical Properties of ZnO Nanostructures: A Hybrid DFT/TDDFT Investigation. *Phys. Chem. Chem. Phys.* **2011**, *13* (2), 467–475.
- (144) Labat, F.; Baranek, P.; Domain, C.; Minot, C.; Adamo, C. Density Functional Theory Analysis of the Structural and Electronic Properties of TiO₂ Rutile and Anatase Polytypes: Performances of Different Exchange-Correlation Functionals. *J. Chem. Phys.* **2007**, *126*, 154703.
- (145) Labat, F.; Baranek, P.; Adamo, C. Structural and Electronic Properties of Selected Rutile and Anatase TiO₂ Surfaces : An Ab Initio Investigation. *J. Chem. Theory Comput.* **2008**, *4*, 341–352.
- (146) Bai, Y.; Mora-Sero, I.; De Angelis, F.; Bisquert, J.; Wang, P. Titanium Dioxide Nanomaterials for Photovoltaic Applications. *Chem. Rev.* **2014**, *114* (19), 10095–10130.
- (147) Patrick, C. E.; Giustino, F. Structural and Electronic Properties of Semiconductor-Sensitized Solar-Cell Interfaces. *Adv. Funct. Mater.* **2011**, *21*, 4663–4667.
- (148) Azpiroz, J. M.; Infante, I.; De Angelis, F. First-Principles Modeling of Core/Shell Quantum Dot Sensitized Solar Cells. *J. Phys. Chem. C* **2015**, *119* (22), 12739–12748.
- (149) Azpiroz, J. M.; Ronca, E.; De Angelis, F. Photoinduced Energy Shift in Quantum-Dot-Sensitized TiO₂: A First-Principles Analysis. *J. Phys. Chem. Lett.* **2015**, *6* (8), 1423–1429.
- (150) Wang, L.; Long, R.; Prezhdo, O. V. Time-Domain Ab Initio Modeling of Photoinduced Dynamics at Nanoscale Interfaces. *Annu. Rev. Phys. Chem.* **2015**, *66*, 549–579.
- (151) Tafen, D. N.; Long, R.; Prezhdo, O. V. Dimensionality of Nanoscale TiO₂ Determines the Mechanism of Photoinduced Electron Injection from a CdSe Nanoparticle. *Nano Lett.* **2014**, *14* (4), 1790–1796.
- (152) Tafen, D. N.; Prezhdo, O. V. Size and Temperature Dependence of Electron Transfer between CdSe Quantum Dots and a TiO₂ Nanobelt. *J. Phys. Chem. C* **2015**, *119* (10), 5639–5647.
- (153) Nadler, R.; Sanz, J. F. Effect of Capping Ligands and TiO₂ Supporting on the Optical Properties of a (CdSe)₁₃ Cluster. *J. Phys. Chem. A* **2015**, *119* (7), 1218–1227.
- (154) Dong, C.; Li, X.; Qi, J. First-Principles Investigation on Electronic Properties of Quantum Dot-Sensitized Solar Cells Based on Anatase TiO₂ Nanotubes. *J. Phys. Chem. C* **2011**, *115*, 20307–20315.
- (155) Azpiroz, J. M.; Ugalde, J. M.; Etgar, L.; Infante, I.; De Angelis, F. The Effect of TiO₂ Surface on the Electron Injection Efficiency in PbS Quantum Dot Solar Cells: A First-Principles Study. *Phys. Chem. Chem. Phys.* **2015**, *17* (8), 6076–6086.
- (156) Long, R.; Prezhdo, O. V. Dopants Control Electron to Hole Recombination at Perovskite to TiO₂. *ACS Nano* **2015**, *9* (11), 11143–11155.
- (157) Guo, Z.; Prezhdo, O. V.; Hou, T.; Chen, X.; Lee, S.; Li, Y. Fast Energy Relaxation by Trap States Decreases Electron Mobility in TiO₂ Nanotubes: Time-Domain Ab Initio Analysis. *J. Phys. Chem. Lett.* **2014**, *5*, 1642–1647.
- (158) Tafen, D. N.; Prezhdo, O. V. Size and Temperature Dependence of Electron Transfer between CdSe Quantum Dots and a TiO₂ Nanobelt. *J. Phys. Chem. C* **2015**, *119* (10), 5639–5647.
- (159) Buhbut, S.; Itzhakov, S.; Hod, I.; Oron, D.; Zaban, A. Photo-Induced Dipoles: A New Method to Convert Photons into Photovoltage in Quantum Dot Sensitized Solar Cells. *Nano Lett.* **2013**, *13* (9), 4456–4461.
- (160) Santra, P. K.; Kamat, P. V. Tandem-Layered Quantum Dot Solar Cells: Tuning the Photovoltaic Response with Luminescent Ternary Cadmium Chalcogenides. *J. Am. Chem. Soc.* **2013**, *135* (2), 877–885.
- (161) Gómez Díaz, J.; Ding, Y.; Koitz, R.; Seitsonen, A. P.; Iannuzzi, M.; Hutter, J. Hexagonal Boron Nitride on Transition Metal Surfaces. *Theor. Chem. Acc.* **2013**, *132* (4), 1350.
- (162) Mohn, C. E.; Stein, M. J.; Allan, N. L. Oxide and Halide Nanoclusters on Ionic Substrates: Heterofilm Formation and Lattice Mismatch. *J. Mater. Chem.* **2010**, *20* (46), 10403.
- (163) Muck, T.; Wagner, J. W.; Hansen, L.; Wagner, V.; Geurts, J.; Ivanov, S. V. Vibration Dynamics and Interfacial Chemistry of the CdSe / BeTe Interface. *Phys. Rev. B* **2004**, *69* (24), 245314.
- (164) Rache Salles, B.; Kunc, K.; Eddrief, M.; Etgens, V. H.; Finocchi, F.; Vidal, F. Hexagon-on-Cube versus Cube-on-Cube Epitaxy: The Case of ZnSe(111) on SrTiO₃ (001). *Phys. Rev. B* **2009**, *79* (15), 155312.
- (165) Trejo, O.; Roelofs, K. E.; Xu, S.; Logar, M.; Sarangi, R.; Nordlund, D.; Dadlani, A. L.; Kravec, R.; Dasgupta, N. P.; Bent, S. F.; et al. Quantifying Geometric Strain at the PbS QD-TiO₂ Anode Interface and Its Effect on Electronic Structures. *Nano Lett.* **2015**, *15* (12), 7829–7836.
- (166) Corà, F.; Alfredsson, M.; Mallia, G.; Middlemiss, D. S.; Mackrodt, W. C.; Dovesi, R.; Orlando, R. The Performance of Hybrid Density Functionals in Solid State Chemistry. In *Structure and Bonding*; Springer-Verlag Berlin Heidelberg, 2004; Vol. 113, p 171.
- (167) Xiao, H.; Tahir-Kheli, J.; Goddard, W. a. Accurate Band Gaps for Semiconductors from Density Functional Theory. *J. Phys. Chem. Lett.* **2011**, *2* (3), 212–217.
- (168) Yu, L.; Kokenyesi, R. S.; Keszler, D. A.; Zunger, A. Inverse Design of High Absorption Thin-Film Photovoltaic Materials. *Adv. Energy Mater.* **2013**, *3* (1), 43–48.

Chapter I. Context

- (169) Yu, L.; Zunger, A. Identification of Potential Photovoltaic Absorbers Based on First-Principles Spectroscopic Screening of Materials. *Phys. Rev. Lett.* **2012**, *108* (6), 1–5.
- (170) Volonakis, G.; Filip, M. R.; Haghighirad, A. A.; Sakai, N.; Wenger, B.; Snaith, H. J.; Giustino, F. Lead-Free Halide Double Perovskites via Heterovalent Substitution of Noble Metals. *J. Phys. Chem. Lett.* **2016**, *7* (7), 1254–1259.
- (171) Filip, M. R.; Giustino, F. Computational Screening of Homovalent Lead Substitution in Organic-Inorganic Halide Perovskites. *J. Phys. Chem. C* **2016**, *120* (1), 166–173.
- (172) Kouhnavard, M.; Ikeda, S.; Ludin, N. A.; Ahmad Khairudin, N. B.; Ghaffari, B. V.; Mat-Teridi, M. A.; Ibrahim, M. A.; Sepeai, S.; Sopian, K. A Review of Semiconductor Materials as Sensitizers for Quantum Dot-Sensitized Solar Cells. *Renew. Sustain. Energy Rev.* **2014**, *37*, 397–407.
- (173) Duan, J.; Zhang, H.; Tang, Q.; He, B.; Yu, L. Recent Advances in Critical Materials for Quantum Dot-Sensitized Solar Cells: A Review. *J. Mater. Chem. A* **2015**, *3* (34), 17497–17510.
- (174) Carey, G. H.; Abdelhady, A. L.; Ning, Z.; Thon, S. M.; Bakr, O. M.; Sargent, E. H. Colloidal Quantum Dot Solar Cells. *Chem. Rev.* **2015**, *115*, 12732–12763.
- (175) Szemjonov, A.; Pauporté, T.; Ithurria, S.; Lequeux, N.; Dubertret, B.; Ciofini, I.; Labat, F. Ligand-Stabilized CdSe Nanoplatelet Hybrid Structures with Tailored Geometric and Electronic Properties. New Insights from Theory. *RSC Adv.* **2014**, *4* (99), 55980–55989.
- (176) Xu, F.; Zhou, W.; Navrotsky, A. Cadmium Selenide: Surface and Nanoparticle Energetics. *J. Mater. Res.* **2011**, *26* (05), 720–725.
- (177) Sigle, D. O.; Hugall, J. T.; Ithurria, S.; Dubertret, B.; Baumberg, J. J. Probing Confined Phonon Modes in Individual CdSe Nanoplatelets Using Surface-Enhanced Raman Scattering. *Phys. Rev. Lett.* **2014**, *113* (8), 087402.
- (178) Zardo, I.; Conesa-Boj, S.; Peiro, F.; Morante, J. R.; Arbiol, J.; Uccelli, E.; Abstreiter, G.; Fontcuberta i Morral, a. Raman Spectroscopy of Wurtzite and Zinc-Blende GaAs Nanowires: Polarization Dependence, Selection Rules, and Strain Effects. *Phys. Rev. B* **2009**, *80* (24), 245324.
- (179) Rumyantseva, A.; Kostcheev, S.; Adam, P.-M.; Gaponenko, S. V.; Vaschenko, S. V.; Kulakovich, O. S.; Ramanenka, A. A.; Guzatov, D. V.; Korbutyak, D.; Dzhagan, V.; et al. Nonresonant Surface-Enhanced Raman Scattering of ZnO Quantum Dots with Au and Ag Nanoparticles. *ACS Nano* **2013**, *7* (4), 3420–3426.
- (180) Le Bahers, T.; Pauporté, T.; Scalmani, G.; Adamo, C.; Ciofini, I. A TD-DFT Investigation of Ground and Excited State Properties in Indoline Dyes Used for Dye-Sensitized Solar Cells. *Phys. Chem. Chem. Phys.* **2009**, *11* (47), 11276–11284.
- (181) Venkatraman, V.; Abburu, S.; Alsberg, B. K. Artificial Evolution of Coumarin Dyes for Dye Sensitized Solar Cells. *Phys. Chem. Chem. Phys.* **2015**, *17* (41), 27672–27682.
- (182) Jose, R.; Zhanpeisov, N. U.; Fukumura, H.; Baba, Y.; Ishikawa, M. Structure-Property Correlation of CdSe Clusters Using Experimental Results and First-Principles DFT Calculations. *J. Am. Chem. Soc.* **2006**, *128* (2), 629–636.
- (183) Moellmann, J.; Ehrlich, S.; Tonner, R.; Grimme, S. A DFT-D Study of Structural and Energetic Properties of TiO₂ Modifications. *J. Phys. Condens. Matter* **2012**, *24* (42), 424206.
- (184) Cooke, D. J.; Marmier, A.; Parker, S. C. Surface Structure of (10(-)10) and (11(-)20) Surfaces of ZnO with Density Functional Theory and Atomistic Simulation. *J. Phys. Chem. B* **2006**, *110* (15), 7985–7991.
- (185) Mosconi, E.; Ronca, E.; Angelis, F. De. First-Principles Investigation of the TiO₂/Organohalide Perovskites Interface: The Role of Interfacial Chlorine. *J. Phys. Chem. Lett.* **2014**, *5*, 2619–2625.
- (186) Odobel, F.; Bahers, T. L. E.; Pauporte, T. Promising Anchoring Groups for ZnO-Based Hybrid Materials: A Periodic Density Functional Theory Investigation. *Int. J. Quantum Chem.* **2012**, *112* (9), 2062–2071.
- (187) Le Bahers, T.; Labat, F.; Pauporté, T.; Lainé, P. P.; Ciofini, I. Theoretical Procedure for Optimizing Dye-Sensitized Solar Cells: From Electronic Structure to Photovoltaic Efficiency. *J. Am. Chem. Soc.* **2011**, *133* (20), 8005–8013.
- (188) Le Bahers, T.; Pauporté, T.; Lainé, P. P.; Labat, F.; Adamo, C.; Ciofini, I. Modeling Dye-Sensitized Solar Cells : From Theory to Experiment. *J. Phys. Chem. Lett.* **2013**, *4*, 1044–1050.

Chapter II. Theoretical and experimental methods

II.1. Theoretical methods

II.1.1 The Schrödinger equation

The theoretical methods used in this thesis are based on solving the time-independent Schrödinger equation:

$$H\Psi = E\Psi \quad (\text{II.1.})$$

where the H operator is the Hamiltonian of the system, E is an eigenvalue and Ψ is an eigenvector of H , corresponding to the system's energy and wavefunction, respectively. In more detail, the Hamiltonian is expressed in the following form:

$$H = -\frac{1}{2} \sum_A^{\text{nuclei}} \frac{\nabla_A^2}{M_A} - \frac{1}{2} \sum_i^{\text{electrons}} \nabla_i^2 + \sum_A^{\text{nuclei}} \sum_{B>A}^{\text{nuclei}} \frac{Z_A Z_B}{R_{AB}} - \sum_A^{\text{nuclei}} \sum_i^{\text{electrons}} \frac{Z_A}{R_{iA}} + \sum_i^{\text{electrons}} \sum_{j>i}^{\text{electrons}} \frac{1}{r_{ij}} = T_N + T_e + V_{NN} + V_{Ne} + V_{ee} \quad (\text{II.2.})$$

where $\nabla = (\frac{\partial}{\partial x}, \frac{\partial}{\partial y}, \frac{\partial}{\partial z})$ is the nabla operator in a 3 dimensional Cartesian coordinate system, M stands for the mass of nuclei, Z for the nuclear charges, R and r for the inter-particle distances. In Equation II.2, the first and second terms correspond to the kinetic energy of the nuclei and of the electrons of the system, respectively. The third term describes the repulsive Coulombic interaction between nuclei, the fourth term corresponds to the attractive Coulombic interaction between electrons and nuclei, and the fifth term to the repulsive Coulombic interaction between electrons.

The solution of this equation can be simplified by considering that the mass of electrons is negligible with respect to those of the nuclei. By applying the Born-Oppenheimer approximation, which is based on the assumption that electrons move around stationary

Chapter II. Theoretical and experimental methods

nuclei ($T_N = 0$), the Hamiltonian can be decoupled, and written as the sum of an electronic (H_e) and a nuclear Hamiltonian (H_N):

$$H = H_e + H_N \quad (II.3)$$

where

$$H_e = T_e + V_{Ne} + V_{ee} \quad (II.4)$$

and

$$H_N = V_{NN} \quad (II.5)$$

The wavefunction is a product of an electronic (Ψ_e) and a nuclear wavefunction (Ψ_N):

$$\Psi = \Psi_e \times \Psi_N \quad (II.6)$$

In the crude Born-Oppenheimer approximation, the position of the nuclei is considered fix, their coordinates are thus treated as parameters (\mathbf{R}_N) in the Schrödinger equation. In consequence, one can solve a simplified Schrödinger equation depending only on the position of the electrons (\mathbf{r}_n).

$$H_e \Psi_e^{\mathbf{R}_N}(\mathbf{r}_n) = E_e^{\mathbf{R}_N} \Psi_e^{\mathbf{R}_N}(\mathbf{r}_n) \quad (II.7)$$

The total energy of the system can thus be written in the following form:

$$E_{tot} = E_e^{\mathbf{R}_N} + T_N \quad (II.8)$$

In an n-electron system, Ψ is a function of $3n$ variables corresponding to the x , y and z coordinates of \mathbf{r}_1 , \mathbf{r}_2 , ... \mathbf{r}_n , which makes calculations very demanding in terms of time and computational cost. Moreover, because of the bielectronic term in (V_{ee}) in Equation (II.4.),

Chapter II. Theoretical and experimental methods

the Schrödinger equation can be solved analytically only for a few simple cases like the H atom, the hydrogen molecular ion or hydrogenoid systems. Therefore, several approximative methods have been developed, which are based either on the Hartree-Fock (HF) method or the density functional theory (DFT). The former is described shortly in the next subsection, followed by an introduction into DFT-based computational methods that we used in this thesis to calculate the properties of the materials that we studied.

II.1.2. Hartree-Fock method

If we assume that there is no interaction between the electrons of the system, the multielectronic Hamiltonian is decomposed into monoelectronic operators $[h_1(i)]$, resulting in the following equations:

$$h_1(i)\varphi_i(\mathbf{r}_i) = \epsilon_i \varphi_i(\mathbf{r}_i) \quad (II.9)$$

where the ϵ_i eigenvalues correspond to the orbital energies, the sum of which makes up the electronic energy of the system:

$$E_s = \sum_i^n \epsilon_i \quad (II.10)$$

\mathbf{r}_i corresponds to the vectorial position of an electron i and the φ_i one-electron functions are called *orbitals*, the product of which would make up the multielectronic wavefunction. However, if the inter-electronic interactions are taken into account, ϕ_i spin-orbital functions are used instead of φ_i to express the multielectronic wavefunction of the system. With a non-relativistic Hamiltonian, the latter can be written as the product of a spin (σ_i) and a space function (ψ_i), within the *orbital approximation*:

$$\phi_i(\mathbf{r}_i, s_i) = \psi_i(\mathbf{r}_i) \sigma_i(s_i) \quad (II.11)$$

Chapter II. Theoretical and experimental methods

where the spin function is $\sigma_i = \pm \frac{1}{2}$. The multielectronic wavefunction formed from the spin-orbital functions (ϕ_i) must satisfy the Pauli principle by changing sign if two electrons are exchanged, which is possible if it is written in the form of the Slater determinant:

$$\Phi_{Slater} = \frac{1}{\sqrt{n!}} \begin{vmatrix} \phi_1(\mathbf{r}_1) & \cdots & \phi_n(\mathbf{r}_1) \\ \vdots & \ddots & \vdots \\ \phi_1(\mathbf{r}_n) & \cdots & \phi_n(\mathbf{r}_n) \end{vmatrix} \quad (\text{II.12})$$

with $\frac{1}{\sqrt{n!}}$ as the normalization constant, and with the condition that the space functions are orthonormal to each other:

$$\langle \psi_i | \psi_j \rangle = \delta_{ij} \quad (\text{II.13})$$

with δ_{ij} corresponding to the Dirac delta.

The Hartree-Fock energy (E_0^{HF}) can be determined using the variational principle. For a given electronic configuration, the space functions ψ_i are varied until the Slater determinant (Φ_0) associated with the minimal energy E_0 that corresponds to the fundamental state of the system is obtained.

$$E_0^{HF} = \frac{\langle \Phi_0 | H_e | \Phi_0 \rangle}{\langle \Phi_0 | \Phi_0 \rangle} \geq E_0 \quad (\text{II.14})$$

In a closed-shell system, where electrons are organized in pairs on $n/2$ doubly occupied molecular orbitals, the HF energy is the sum of mono- (h_{ii}) and bielectronic terms (J_{ij} and K_{ij}):

$$E_0^{HF} = 2 \sum_i^{n/2} h_{ii} + \sum_i^{n/2} \sum_j^{n/2} (2J_{ij} - K_{ij}) \quad (\text{II.15})$$

Chapter II. Theoretical and experimental methods

where J_{ij} (K_{ij}) is known as the Coulomb (exchange) integral.

The interaction of a given electron i with the other electrons and the nuclei can be included in an approximative way: an effective field is defined, in which each electron i is affected by the potential generated by the nuclei and the average field of the other electrons. In this field, the molecular orbitals ϕ_i are eigenvectors of an effective operator known as the Fock operator F , and the energy levels of the system can be determined by solving the following monoelectronic *Hartree-Fock equations*:

$$F\phi_i = \epsilon_i \phi_i \quad (\text{II.16})$$

where ϵ_i are the eigenvalues of the Fock operator and correspond to the system's Koopmans ionization energies.¹ The Fock operator is expressed as:

$$F(1) = h_1(1) + v_1^{HF} = h_1(1) + \sum_j^{n/2} [2J_j(1) - K_j(1)] \quad (\text{II.17})$$

where v_1^{HF} is the above mentioned effective potential felt by electron (1) .

Upon Roothaan's proposition,² the molecular orbitals ϕ_i are developed on the basis of atom-centered functions χ_μ called *atomic orbitals*. This approach is known as the *linear combination of atomic orbitals (LCAO)* approximation:

$$\phi_i = \sum_{\mu}^m c_{\mu i} \chi_{\mu} \quad (\text{II.18})$$

with $c_{\mu i}$ coefficients. The size of the basis set χ_μ is chosen as a compromise between precision and computational cost. A complete (infinite) basis set would correspond to the so-called HF limit. The matrix representation of the Fock operator on the basis of the χ_μ atomic orbitals is expressed as:

Chapter II. Theoretical and experimental methods

$$\langle \chi_\mu | F | \chi_\nu \rangle = F_{\mu\nu} \quad (II.19)$$

And the S overlap matrix is written as

$$\langle \chi_\mu | \chi_\nu \rangle = S_{\mu\nu} \quad (II.20)$$

Now the (II.14) variational problem takes up the following form:

$$E_0^{HF} = \frac{\sum_\mu \sum_\nu c_\mu^* c_\nu F_{\mu\nu}}{\sum_\mu \sum_\nu c_\mu^* c_\nu S_{\mu\nu}} \geq E_0 \quad (II.21)$$

Instead of varying ψ_i space functions, we are now seeking the c_μ , c_ν coefficients that minimize the energy of the system. In other words, the new, simplified problem is:

$$\frac{\partial E_0^{HF}}{\partial c_\mu} = 0 \quad (II.22)$$

After executing the derivation in Equation (II.22), (II.21) is transformed into the following secular matrix equation:

$$\sum_\mu F_{\mu\nu} c_{\nu i} = \epsilon_i \sum_\mu S_{\mu\nu} c_{\nu i} \quad (II.23)$$

$$FC = SC\epsilon$$

Equation (II.23) is solved in an iterative way, using the self-consistent field (SCF) procedure. In the first SCF cycle, the equation is solved using an initial guess of the coefficients c_μ , c_ν , and a new series of coefficients is thus obtained. The SCF procedure is continued until a predefined convergence threshold on energy between two SCF cycles is reached.

We note that the HF method computes exchange exactly, while correlation is completely neglected.

Chapter II. Theoretical and experimental methods

II.1.3. Density functional theory

Density functional theory (DFT) is a quantum mechanical method to investigate the electronic structure of many-body systems, such as molecules and condensed phases. DFT has gained popularity among chemists, physicists and material scientists due to the accurate results obtained at low computational cost. DFT has its conceptual roots in the Thomas-Fermi model from 1927^{3,4}, which is based on the approximation that electrons are distributed uniformly in small ΔV volumes of a system, but the electron density (ρ) varies from one ΔV volume element to the other. The overall electron density depends only on the 3 spatial coordinates (x, y, z) expressed by the \mathbf{r} vector, as shown in *Equation II.24*.

$$\rho(\mathbf{r}) = \int_{\mathbf{r}_2} \dots \int_{\mathbf{r}_n} \Psi(\mathbf{r}_1, \dots, \mathbf{r}_n) \Psi^*(\mathbf{r}_1, \dots, \mathbf{r}_n) d\mathbf{r}_2 \dots d\mathbf{r}_n \quad (\text{II.24})$$

According to the Thomas-Fermi model, the kinetic energy of electrons, as well as the potentials describing classical electron-electron and electron-nucleus interactions can be expressed only in terms of electron density. ρ is a function of only 3 variables, while the many-body wavefunction of the Schrödinger equation depends on $3n$ variables in the Born-Oppenheimer approximation. In this way, the Thomas-Fermi model is an important step towards simplifying calculations. However, the model provides poor results for realistic systems, partly due to its basic assumption that electrons are uncorrelated. This drawback was improved by Dirac⁵ who proposed to include an electron exchange energy term that also depended solely on $\rho(\mathbf{r})$.

Later, Hohenberg and Kohn established two theorems that made it possible for the electron density to become the basis of quantum mechanical calculations and paved the way for modern DFT calculations in 1964.⁶ The *first Hohenberg-Kohn theorem* states that every observable property of a system is a *functional* (a function from vector space into its underlying scalar field) of the electronic density. Most importantly, the total energy of the system can be written as

Chapter II. Theoretical and experimental methods

$$E[\rho(\mathbf{r})] = T_e[\rho(\mathbf{r})] + V_{ee}[\rho(\mathbf{r})] + V_{Ne}[\rho(\mathbf{r})] \quad (\text{II.25})$$

As all electrons feel the same $v(\mathbf{r})$ *external potential*, the $V_{Ne}[\rho(\mathbf{r})]$ term can be expressed as

$$V_{Ne}[\rho(\mathbf{r})] = \int_{\mathbf{r}_1} \dots \int_{\mathbf{r}_n} \Psi(\mathbf{r}_1, \dots, \mathbf{r}_n) \Psi^*(\mathbf{r}_1, \dots, \mathbf{r}_n) \sum_i v(\mathbf{r}_i) d\mathbf{r}_1 \dots d\mathbf{r}_n = \int \rho(\mathbf{r}) v(\mathbf{r}) \quad (\text{II.26})$$

The total energy functional is thus written as

$$E[\rho(\mathbf{r})] = F[\rho(\mathbf{r})] + \int \rho(\mathbf{r}) v(\mathbf{r}) d\mathbf{r} \quad (\text{II.27})$$

where the $F[\rho(\mathbf{r})]$ term is the *Hohenberg-Kohn functional* defined as:

$$F[\rho(\mathbf{r})] = T_e[\rho(\mathbf{r})] + V_{ee}[\rho(\mathbf{r})] \quad (\text{II.28})$$

The *second Hohenberg-Kohn theorem* states that in case $\rho_0(\mathbf{r})$ corresponds to the system's ground state electron density and E_0 to its ground state energy, then $E[\rho] > E_0$ for any $\rho \neq \rho_0$. Therefore, finding the ground state energy of a system in function of its electron density is a variational problem: one is seeking the electron density closest to ρ_0 in order to minimize the total energy. However, it is not possible to analytically solve this problem as we do not know the exact formula of $V_{ee}[\rho]$.

II.1.4. The Kohn-Sham method

Kohn and Sham developed a method in 1965 to overcome the problem of expressing $V_{ee}[\rho]$.⁷ It is introduced by considering a reference system with no electron-electron interactions which has the same ground-state electron density as the interacting system we want to study. Without electron-electron interactions, the properties of the reference system can be calculated by solving one-electron Schrödinger equations. Therefore, its wave function can be exactly represented by a Slater determinant defined in *Equation II.12*. In the following,

Chapter II. Theoretical and experimental methods

the single-electron wavefunctions known as *Kohn-Sham (KS) orbitals* $[\varphi_i(\mathbf{r}_i)]$, with $i = 1, \dots, n]$ are used to express the electron density. The kinetic energy of the non-interacting reference system is written as:

$$T_s[\rho] = \sum_{i=1}^N \left\langle \varphi_i \left| -\frac{\hbar^2}{2m} \nabla^2 \varphi_i \right. \right\rangle \quad (\text{II.29})$$

In the next step, we suppose that the reference system is affected by an effective potential v_{eff} , which is expressed as the sum of terms describing nuclear-electron and electron-electron interactions:

$$v_{\text{eff}}(\mathbf{r}) = v(\mathbf{r}) + \frac{\delta J[\rho(\mathbf{r})]}{\delta \rho(\mathbf{r})} + \frac{\delta E_{\text{xc}}[\rho(\mathbf{r})]}{\delta \rho(\mathbf{r})} \quad (\text{II.30})$$

where $v(\mathbf{r})$ corresponds to the nuclear-electron potential, $J[\rho]$ is the classical Coulombic term of the electron-electron interaction:

$$J[\rho] = \frac{1}{2} \int \frac{\rho(\mathbf{r})\rho(\mathbf{r}')}{|\mathbf{r} - \mathbf{r}'|} d\mathbf{r} d\mathbf{r}' \quad (\text{II.31})$$

and $E_{\text{xc}}[\rho]$ is the *exchange-correlation functional* which accounts for the differences between the real interacting and the non-interacting reference system with $T[\rho]$ as the kinetic energy of the real interacting system:

$$E_{\text{xc}}[\rho] = T[\rho] - T_s[\rho] + V_{\text{ee}}[\rho] - J[\rho] \quad (\text{II.32})$$

We now have all the elements to construct the *Kohn-Sham Hamiltonian* (H_{KS}):

$$H_{\text{KS}} = -\frac{\hbar^2}{2m} \nabla^2 + v_{\text{eff}}(\mathbf{r}) \quad (\text{II.33})$$

The resulting Schrödinger equation is written in the following form:

$$\left[-\frac{\hbar^2}{2m} \nabla^2 + v_{\text{eff}}(\mathbf{r}) \right] \varphi_i = \sum_{j=1}^N \varepsilon_{ij} \varphi_j \quad (\text{II.34})$$

Equation II.34 is solved in a *self-consistent* iterative way, very similarly to HF calculations. First, an initial guess of $\rho(\mathbf{r})$ is used to calculate the corresponding $v_{\text{eff}}(\mathbf{r})$ and solve the KS equations to obtain φ_i . A new electron density is then constructed from these KS orbitals, and the procedure is continued until convergence on orbital energies is reached. In this way, Kohn and Sham established an appealing method for the calculation of the ground-state properties of multi-electronic systems. However, as the exact form of the *exchange-correlation functional* is not known, it has to be approximated. Selected methods for describing $E_{\text{xc}}(\rho)$ are presented in the next section.

II.1.5. Exchange-correlation functionals

In the first step of this work presented in **Chapter III**, our goal was to find an accurate and reasonably low-cost computational protocol to describe the geometric and electronic properties of CdSe. In more particular, as we focused on materials for photovoltaic applications, the accuracy in computing band gaps was considered a priority. We planned to test two types of exchange-correlation functionals: functionals in the Generalized Gradient Approximation (GGA) and hybrid functionals. Both are known to provide accurate lattice parameters for a wide range of semiconductors,^{8,9} but while GGAs are computationally less expensive than hybrids,⁹ they are also known to severely underestimate band gaps.¹⁰ On the other hand, well-chosen hybrids can reproduce experimental band gaps of these systems with very low error.^{8,10,11} As several contradictory criteria needs to be considered when choosing an exchange-correlation functional, benchmark studies are necessary to identify the best compromise.

GGA functionals depend on the local electron density and on its first derivative ($\nabla\rho$) in order to account for rapid changes in $\rho(\mathbf{r})$ over small regions of space. More precisely, they are generally described in the following form:

Chapter II. Theoretical and experimental methods

$$E_{xc}^{GGA}[\rho(\mathbf{r})] = \int \rho(\mathbf{r}) \epsilon_{xc}^{hom}[\rho(\mathbf{r})] F_{xc}[\rho(\mathbf{r}), \nabla \rho(\mathbf{r})] d\mathbf{r} \quad (II.35)$$

In Equation II.35, ϵ_{xc}^{hom} is the exchange-correlation energy in a homogeneous electron gas that has the same electron density in the \mathbf{r} point as the studied system. F_{xc} , known as the *enhancement factor*, depends both on the electron density and its gradient. Several parametrization schemes have been proposed for GGAs among which we can find *semi-empirical* functionals that are fitted to experimental or *ab initio* data, and also purely *non-empirical* ones. In **Chapter III** of this work, we tested the semi-empirical BLYP^{12,13} and BPW91^{12,14}, and the non-empirical PBE¹⁵ functionals.

The origin of the severe underestimation of band gaps computed by GGA functionals is the spurious *self-interaction error* (SIE):^{8,10} Coulombic and approximated exchange self-interaction energies are not cancelled out. In purely Hartree-Fock calculations, this does not lead to a problem, since Coulomb self-interaction terms are perfectly cancelled out by the exact exchange self-interaction terms. It is thus a plausible idea to include a portion of HF exchange in the exchange term in order to decrease the SIE and reach a partial cancellation. The as-constructed *hybrid functionals* are written in the general form of Equation II.36:

$$E_{xc}^{hyb} = \alpha E_x^{HF} + (1 - \alpha) E_x^{GGA} + E_c^{GGA} \quad (II.36)$$

In the above equation, the exchange-correlation functional is separated into an exchange (E_x) and a correlation term (E_c). The α coefficient is either *a priori* set to be a specific value based on theoretical arguments (like the PBE0 functional¹⁶), or fitted to experimentally measured or calculated properties from a database (for example B3LYP^{17,18}, B3PW91^{17,19}, O3LYP²⁰, X3LYP²¹ etc. functionals). Hybrids with a fixed α coefficient are called *global hybrids*, and all hybrids considered in this thesis (PBE0, B3LYP and B3PW91) belong to this group of functionals. Another notable group of hybrids is formed by the range-separated hybrid (RSH) functionals, which include different amount of exact HF exchange depending on the electron electron distance. Some examples of RSH functionals include HSE06,^{15,22} HISS^{23,24} and LC-wPBE.²⁵

Chapter II. Theoretical and experimental methods

It is noteworthy that although hybrid functionals can both be used with plane-wave (PW) and Gaussian-type orbitals (GTO) basis sets (both presented in subsection II.1.7), calculations remain so far computationally much more expensive with PW.²⁶ On the other hand, when combined with Gaussian-type basis sets, hybrids can efficiently be applied to periodic systems,^{27,28} even to very large ones.²⁹ For systems like semiconductor heterostructures we intended to study in this thesis, the use of Gaussian-type basis sets was therefore more suitable with hybrid functionals.

II. 1.6. Modeling periodic systems

II.1.6. a) Bulk crystals

The semiconductor crystals studied in this thesis are highly ordered systems that can be represented by a *unit cell*. A crystal's *unit cell* is the smallest unit of volume that contains all structural and symmetry information to build up the macroscopic structure of the crystal lattice in *direct space* by translation with the primitive *lattice vectors* (\mathbf{a}_1 , \mathbf{a}_2 , \mathbf{a}_3) or their linear combination: $n_1\mathbf{a}_1 + n_2\mathbf{a}_2 + n_3\mathbf{a}_3$.

For the formalism of modeling these periodic systems, another definition is particularly interesting: in *reciprocal space*, the crystal structure is built up by translation with the (\mathbf{b}_1 , \mathbf{b}_2 , \mathbf{b}_3) basis vectors or their linear combination: $N_1\mathbf{b}_1 + N_2\mathbf{b}_2 + N_3\mathbf{b}_3$. These (\mathbf{b}_1 , \mathbf{b}_2 , \mathbf{b}_3) vectors are determined from:

$$\mathbf{a}_i \cdot \mathbf{b}_j = 2\pi\delta_{ij} \quad (\text{II.37})$$

where δ_{ij} stands for the Dirac delta. In consequence, the \mathbf{b} vectors in *reciprocal space* are perpendicular to a plane defined by two \mathbf{a} basis vectors with a different index in *direct space*. A unit cell in *reciprocal space* is defined by connecting a chosen origin point of the reciprocal space with its nearest neighbors. A plane perpendicular to these lines is drawn at their midpoint. The smallest volume enclosed by these planes is called the *first Brillouin zone*. By

Chapter II. Theoretical and experimental methods

considering second, third etc. nearest neighbors, second, third etc. *Brillouin zones* can also be defined. By applying the symmetry operations of the point group of the lattice, the *irreducible Brillouin zone* (IBZ) is obtained.

As crystals can ideally be built up by the periodic repetition of the *unit cell*, the electronic structure of crystals also shows a periodic pattern, which can be described by imposing *periodic boundary conditions* (PBCs) to the wavefunction of the system. According to *Bloch's theorem*, electron wave functions in these systems can be expressed solely on a basis of *Bloch functions* (BFs). BFs are periodic wavefunctions written in the following general form:

$$\phi_{\mathbf{k}}(\mathbf{r}) = e^{i\mathbf{k}\cdot\mathbf{r}} u_{\mathbf{k}}(\mathbf{r}) \quad (\text{II.38})$$

In the above equation, \mathbf{r} denotes the vector position in real space, \mathbf{k} is the crystal wave vector in reciprocal space and $u_{\mathbf{k}}(\mathbf{r})$ is a periodic function that follows the periodicity of the crystal defined by its \mathbf{a}_i lattice vectors ($i=1, 2, 3$):

$$u_{\mathbf{k}}(\mathbf{r}) = u_{\mathbf{k}}(\mathbf{r} + \mathbf{a}_i) \quad (\text{II.39})$$

It is thus assured that

$$\phi_{\mathbf{k}}(\mathbf{r} + \mathbf{a}_i) = e^{i\mathbf{k}\cdot\mathbf{r}} \phi_{\mathbf{k}}(\mathbf{r}) \quad (\text{II.40})$$

In consequence, the probability density is the same if the wave function is displaced by a lattice vector, since the imaginary terms in *Equation II.40* cancel out. Therefore, as illustrated by *Equation II.41*, the electronic structure mirrors the structural periodicity of the crystal:

$$|\phi_{\mathbf{k}}(\mathbf{r})|^2 = |\phi_{\mathbf{k}}(\mathbf{r} + \mathbf{a}_i)|^2 \quad (\text{II.41})$$

In the LCAO approach for molecules, a finite number of molecular orbitals (MOs) are developed on a basis of atomic orbitals (AOs), as we have seen in *Equation II.18*. In a crystal, an infinite number of unit cells (described individually by MOs) are repeated periodically in

Chapter II. Theoretical and experimental methods

three dimensions, therefore the system should be described using an infinite number of MOs (and consequently AOs). However, two arbitrarily chosen unit cells contain a group of atoms in the exact same geometrical arrangement. As the interaction between the atom-centered AOs depends on the inter-atomic distances, there is zero difference in the energy in the different unit cells. The MOs are thus delocalized in a periodic pattern over the crystalline lattice, and are called crystalline orbitals (COs). The COs ($\Psi_{i,\mathbf{k}}$) are developed on a basis of Bloch functions ($\phi_{\mu,\mathbf{k}}$):

$$\Psi_{i,\mathbf{k}}(\mathbf{r}) = \sum_{\mu} c_{\mu,i}(\mathbf{k}) \phi_{\mu,\mathbf{k}}(\mathbf{r}) \quad (\text{II.42})$$

with $c_{\mu,i}$ coefficients that are determined using the variational principle, by solving the matrix equations introduced in *Equation II.23*, on the basis of Bloch functions:

$$\mathbf{H}^{\mathbf{k}} \mathbf{C}^{\mathbf{k}} = \mathbf{S}^{\mathbf{k}} \mathbf{C}^{\mathbf{k}} \mathbf{E}^{\mathbf{k}} \quad (\text{II.43})$$

where $\mathbf{H}^{\mathbf{k}}$ is the matrix representation of the Hamiltonian on the basis of Bloch functions, $\mathbf{C}^{\mathbf{k}}$ is the matrix containing the $c_{\mu,i}$ coefficients of *Equation II.42*, $\mathbf{S}^{\mathbf{k}}$ is the overlap matrix, $\mathbf{E}^{\mathbf{k}}$ is the diagonal matrix containing the eigenvalues $\epsilon^{\mathbf{k}}$. Because of the PBCs, these calculations are limited to the first BZ of the system. However, with an infinite N number of unit cells in the lattice, the number of \mathbf{k} points is also infinite. In consequence, the II.43. matrix equations need to be solved for an infinite number of \mathbf{k} points in the first BZ, which would be impossible. However, in practice, the calculated properties actually converge with the number of the used \mathbf{k} points. In consequence, a small number of \mathbf{k} points are already sufficient for the sampling of the first BZ.

Two types of basis functions are commonly used to represent Bloch functions in DFT calculations of periodic systems: *localized* and *plane wave* basis sets that are introduced in more detail in the subsection **II.1.7**.

Chapter II. Theoretical and experimental methods

II.1.6. b) Crystal surfaces

In order to simulate the surface properties of crystals, we used a slab model to which two-dimensional PBCs were imposed instead of three-dimensional ones. A slab is a slice of material with a predefined thickness, cut out of the bulk along a given crystal plane, and is terminated by two free surfaces, as illustrated in *Figure II.1*. After optimizing the structure of slabs of different thicknesses, the adequacy of the model is checked by considering the convergence of chosen properties, such as band gaps and surface formation energies with respect to slab thickness. For further investigations, we use slabs with converged properties.

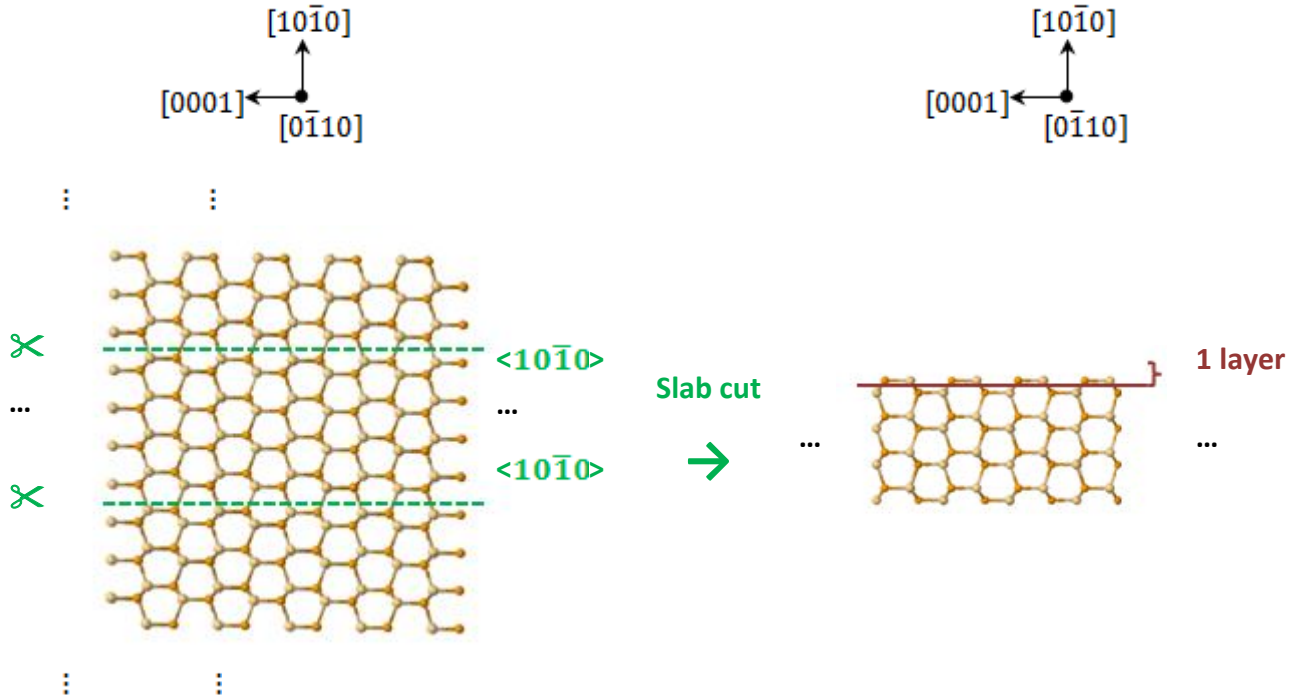


Figure II.1. Schematic illustration of the creation of an 8 layers thick $\langle 10\bar{1}0 \rangle$ slab from the bulk form of wurtzite CdSe

Defining a slab might change stoichiometry, and in consequence, result in charged systems. Moreover, as the coordination around surface atoms is altered, residual dipole moments perpendicular to the crystal surface might arise. In some cases, crystal symmetry can allow charges and dipole moments to partially or entirely cancel out in the system. This is the basis of Tasker's classification of ionic crystal surfaces, which is schematically illustrated in *Figure II.2*.³⁰

Chapter II. Theoretical and experimental methods

- *Type 1* surfaces consist of neutral planes with an equal number of cations and anions. The system is globally neutral with no residual dipole moment normal to the surface. *Type 1* surfaces are non-polar.
- *Type 2* consists of symmetrically arranged charged planes. Similarly to *Type 1*, these systems are globally neutral with no residual dipole moment perpendicular to the surface. *Type 2* surfaces are also non-polar.
- *Type 3* surfaces are also built up from charged planes but are globally charged with a nonzero dipole moment normal to their surface. *Type 3* surfaces are polar.

Type 1 and *2* surfaces are stabilized by small relaxations of the surface atoms, and have low surface energies. However, in case of *Type 3* surfaces, the adsorption of charged compounds³⁰ or a substantial surface reconstruction with the addition of adatoms and vacancies is required to neutralize and stabilize the system.³¹

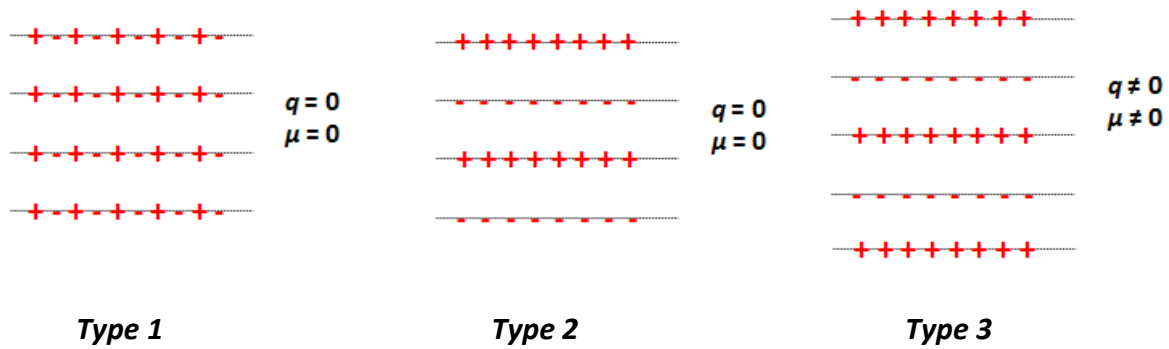


Figure II.2. Schematic illustration of Tasker's classification of ionic crystal surfaces.³⁰ q corresponds to the overall charge of the system, while μ to the dipole moment perpendicular to the crystal surface.

II.1.7. Basis sets for periodic DFT calculations

II.1.7.a) Localized basis sets

All calculations in this thesis were performed with the CRYSTAL09^{32,33} and CRYSTAL14^{33,34} codes, which use a linear combination of atomic orbitals (LCAO) approach to self-consistently solve both Hartree-Fock and Kohn-Sham equations. CRYSTAL calculations are based on crystalline orbitals (COs, Ψ_{ik}) that are defined as linear combinations of Bloch

Chapter II. Theoretical and experimental methods

functions (BFs, $\phi_{\mu,\mathbf{k}}$), as described by the Equation (II.42). BFs are described in terms of localized (atom-centered) atomic orbitals (AOs, $\varphi_{\mu}(\mathbf{r})$) on a set of lattice vectors \mathbf{a} :

$$\phi_{\mu,\mathbf{k}}(\mathbf{r}) = \sum_{\mathbf{a}} \varphi_{\mu}(\mathbf{r} - \mathbf{A}_{\mu} - \mathbf{a}) e^{i\mathbf{k} \cdot \mathbf{a}} \quad (\text{II.44})$$

In Equation II.44, \mathbf{A}_{μ} is the coordinate of the nucleus in the reference cell on which φ_{μ} is centered. As shown in Equation II.45, the AOs are expressed as linear combinations of a finite n_G number of Gaussian-type functions (GTFs, denoted as G in Equation II.45) with fixed d_j coefficients and α_j exponents:

$$\sum_{\mathbf{g}} \varphi_{\mathbf{k}}(\mathbf{r} - \mathbf{A} - \mathbf{a}) = \sum_j^{n_G} d_j G(\alpha_j, \mathbf{r} - \mathbf{A} - \mathbf{a}) \quad (\text{II.45})$$

GTFs are described as the product of a radial ($R_l(\mathbf{r})$) and an angular ($Y_l^m(\theta, \varphi)$) term:

$$G(\mathbf{r}) = A Y_l^m(\theta, \varphi) R_l(\mathbf{r}) = A Y_l^m(\theta, \varphi) r^l e^{-\alpha r^2} \quad (\text{II.46})$$

where A is the normalization term, α is the above mentioned exponential coefficient and Y_l^m is a spherical harmonic associated with the angular (l) and the magnetic (m) quantum numbers and depends on the angular variables θ and φ . The mathematical formula of GTF-based basis sets makes the calculation of HF exchange faster and simpler with respect to other types of basis sets based on Slater functions with a radial dependence $\sim r^{n-1} e^{-r}$ (where n is the principle quantum number). However, GTFs describe poorly the electrons in the proximity of the nuclei, which is overcome by taking into account the linear combination of *primitive* Gaussians to get *contracted* Gaussian functions, and the latter are used as basis functions.

In the simplest case of a *minimal basis set*, one Gaussian basis function is used for each atomic orbital. Auxiliary functions with an additional node called *polarization functions* can be added to this minimal basis set to increase its flexibility in describing chemical bonds. In

Chapter II. Theoretical and experimental methods

practice, it is realized adding p-functions to a basis set containing s orbitals, d-functions to a basis set with p orbitals etc. Another common modification is to “*augment*” basis sets, or in other words, to add *diffuse functions* to provide a better description of the distant tails of Gaussian functions. In periodic systems, however, care must be taken to avoid numerical problems with diffuse functions, and they are omitted in most cases.

Because of the important role that valence electrons play in the formation of chemical bonding, valence orbitals are often represented by more than one basis function, and are correspondingly called *valence double zeta*, *triple zeta* etc. basis sets. In order to reduce computational costs and/or to include relativistic effects, one can replace the core electrons of an atom with *effective core potentials (ECPs)*, and treat only the valence electrons explicitly. However, separation into core and valence electrons is by no means trivial, especially in case of heavy elements. As a consequence, *small-* and *large-core ECPs* are available for a large number of elements. Comparison with experimental results or calculations using accurate all electron (AE) basis sets can help choose the right ECP for calculations. In this work, in order to find the best compromise in computational cost and accuracy, we tested both AE basis sets and different kinds of ECPs, as detailed in **Chapter III**.

II.1.7. b) Plane wave basis sets

Although not used in this thesis, plane-wave basis sets are very widely applied with DFT calculations on crystals, and are shortly introduced here. The plane waves of a periodic system can be described by the following equation:

$$\Phi_{\mathbf{K}_n}^{\mathbf{k}}(\mathbf{r}) = \frac{1}{\sqrt{N\Omega_0}} e^{i\mathbf{r}(\mathbf{k}+\mathbf{K}_n)} \quad (\text{II.47})$$

where $N = N_1 \cdot N_2 \cdot N_3$, Ω_0 corresponds to the volume of the unit cell, \mathbf{K}_n to a vector in reciprocal space. The crystalline orbitals are then constructed by taking the linear combination of plane waves:

Chapter II. Theoretical and experimental methods

$$\Psi_i^{\mathbf{k}}(\mathbf{r}) = \sum_{n \leq m} c_{in}^{\mathbf{k}}(\mathbf{K}_n) \Phi_{\mathbf{K}_n}^{\mathbf{k}}(\mathbf{r}) \quad (II.48)$$

where m is an integer determined from the following relation:

$$(\mathbf{k} + \mathbf{K}_n)^2 \leq E_{cutoff} \quad (II.49)$$

where E_{cutoff} is a kinetic energy limit. The precision (but also the cost) of the calculation increases with an increasing E_{cutoff} . As the wavefunction strongly oscillates near the nuclei, the *frozen core* approximation is generally applied: core electrons are represented by a potential called *pseudopotential*, and only the valence electrons are treated explicitly. Pseudopotentials with several formalisms have been utilized with plane wave basis sets. A few notable examples include norm-conserving^{35,36} and ultra-soft pseudopotentials.³⁷

Another method to treat plane waves is based on *augmented plane waves* (APW). In this approach, the space is divided into spherical atom-centered “atomic regions” and “inter-atomic” regions containing the bonds. The basis functions are constructed from partial atomic waves in the former and from a combination of envelop functions in the latter regions. A generalization of the APW and pseudopotential methods is the *projector augmented wave* (PAW) method, which allows to calculate all-electron observables using the pseudo wavefunction from a pseudopotential calculation.³⁸ This is done with the help of a T transformation operator that transforms the fictitious pseudo wavefunction into the ‘real’ all-electron wavefunction, and T is defined such that the two wavefunctions differ only in the “atomic regions”. PAW calculations have only been considered in some selected cases in this thesis.

II.2. Experimental methods

II.2.1. Synthesis of CdSe quantum dots and nanoplatelets

One of the preliminary goals of the thesis was to examine the effect of quantum confinement of the sensitizer nanocrystals on solar cell efficiency. For this purpose, it is desirable to well-know and control the size of the nanocrystals. For this reason, we decided to use CdSe nanoplatelets (NPLs), the synthesis of which was previously well-established by Ithurria et al.^{39,40} These nano-objects have typically a thickness of a few nanometers and lateral dimensions of 40-100 nm, therefore they can be considered as *quasi-two dimensional* nanocrystals. The authors demonstrated that the CdSe NPLs are formed by the continuous lateral extension of CdSe nanocrystal seeds.³⁹ After nucleation of the seed crystals, the NPL thickness remained fixed and did not grow further during NPL formation. By controlling the synthesis conditions, they could control the NPL thickness at the monolayer scale. It was also manifested by a precise control over the band gap of the nanocrystals.⁴¹ Moreover, the optoelectronic properties of the as-synthesized CdSe nanoplatelets turned-out to be very appealing.^{41,42} It is particularly noteworthy that these systems show much narrower excitonic absorption and photoemission bands⁴³ and higher photoluminescence quantum yields than spherical QDs or quasi one-dimensional nanorods (NRs).⁴²

As quasi two-dimensional semiconductor, NPLs have been demonstrated useful for a broad range of applications from single-photon sources⁴⁴ to biophotonics.⁴⁵ These singular properties led us to test the possibility of applying them in QDSCs in replacement of classical spherical QDs. Advantages of such systems are twofold. First, due to the quantum confinement effects arising from their thickness of typically a few nanometers, their excitonic and charge carrier properties can be readily tuned, either by changing their thickness⁴¹ or by varying the passivating ligands on their surface.⁴⁶ Second, from a modeling point of view, these structures provide a good basis for building stacked models, allowing an easier comparison between experimental and theoretical data. In this thesis, we mainly

Chapter II. Theoretical and experimental methods

focused on NPLs as sensitizer materials, but also tested spherical QDs in a few experiments to compare the properties of NPL-WBSC and QD-WBSC heterostructures.

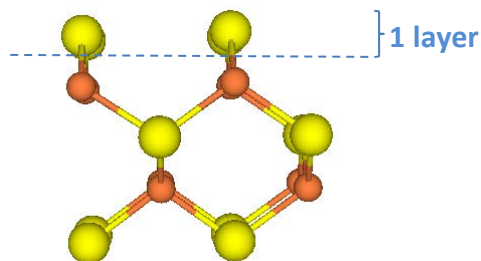


Figure II.3. Structural model of a 5 layers thick CdSe zinc blende(100) nanoplatelet with the definition of one atomic monolayer (ML)

We have synthesized quasi-2D CdSe NPLs or several thicknesses (7, 9, 11 and 13 MLs). One atomic monolayer (ML) of a NPL stands for an atomic layer composed exclusively of cadmium or selenium atoms in the same $\langle 100 \rangle$ plane, as illustrated in *Figure II.3*. The synthesis of NPLs of different thicknesses was based on previous works by Ithurria et al.^{39–42,47} In a typical CdSe NPL synthesis protocol, a cadmium and a selenium precursor were decomposed in the presence of a non-coordinating solvent (octadecene, ODE) and an acetate salt (cadmium acetate was used $[\text{Cd}(\text{OAc})_2]$ in this thesis). The roles of acetate salt was to hinder the nanocrystal growth in the $[100]$ direction, and to promote the lateral growth of the CdSe seed crystals. If acetate is present in the initial reaction solution, the lateral growth of the nano-objects is promoted, and the resulting NPLs are thin. If it is injected into the solution when it already contains relatively large CdSe seed crystals, thicker CdSe NPLs are synthesized.

The initial mixture for the synthesis of the thinner (5 and 7 MLs thick) NPLs contained cadmium acetate bihydrate ($\text{Cd}(\text{OAc})_2 \cdot 2\text{H}_2\text{O}$), oleic acid (OA), and octadecene (ODE). While the mixture was degassed at low temperature ($\sim 90^\circ\text{C}$) for ~ 1 hour, NPL seeds were nucleated in the solution. Then, it was heated up to a given temperature and the anionic precursor in the form of trioctyl phosphine-selenide (TOP-Se) was injected. At low temperature ($\sim 100^\circ\text{C}$), 5 ML thick NPL were prepared, while at higher temperature ($\sim 190^\circ\text{C}$), 7 ML thick NPLs were obtained. We can note that we never prepared 5MLs thick NPLs

Chapter II. Theoretical and experimental methods

for this thesis, but previously obtained experimental data⁴¹ on these NPLs are used in **Chapters IV and V**. The synthesis of 7 MLs thick CdSe NPLs was based on Ref. 39. Briefly, 240 mg $\text{Cd}(\text{OAc})_2 \cdot 2\text{H}_2\text{O}$, 150 μl of OA and 12 ml of octadecene (ODE) were degassed in a three-neck flask under vacuum flow at 90 °C for 1 hour. The mixture was then heated to 190 °C under argon flow. When this temperature was reached, 150 μl of 1M TOP-Se, was injected, and the synthesis was pursued at this temperature for 40 minutes. Finally, the mixture was quenched, and 2ml of OA and 30 ml of hexane were added. The NPLs were separated by centrifugation and re-suspended in 30 ml of hexane.

9 and 11 MLs thick NPLs, were synthesized by introducing an acetate salt into the reaction mixture at a temperature superior to the nucleation temperature of quantum dots that serve as seeds for growing the NPLs (180 °C). In order to obtain 9MLs thick NPLs, we followed the protocole described in ref. 41. An initial reaction mixture of 0.3 ml of cadmium myristate $[\text{Cd}(\text{myr})_2]$, 0.15 mmol Se powder and 10 ml of ODE were degassed at room temperature for ~20 minutes in a three neck flask. Then, under argon flow, the temperature was set to 240 °C. When the mixture color turned orange (at around 200 °C), 0.2 mmol of $\text{Cd}(\text{Ac})_2 \cdot 2\text{H}_2\text{O}$ was introduced through a neck. After 5 minutes at 240 °C, the mixture was quenched, and 2 ml of OA and 35 ml of hexane were added. The NPLs were separated by centrifugation and re-suspended in 10 ml of hexane. The synthesis of 11 MLs thick NPLs was based on ref. 42. In a three neck flask, 0.3 mmol of $\text{Cd}(\text{myr})_2$ and 10 ml of ODE were degassed for 20 minutes. Then, under argon flow, the mixture was heated up to 240 °C and a suspension of 0.15 mmol of selenium mesh sonicated in 1 ml ODE was injected. After 1 minute, 0.4 mmol of $\text{Cd}(\text{Ac})_2 \cdot 2\text{H}_2\text{O}$ was introduced through a neck. After 10 minutes at 240 °C, the mixture was quenched and 2 ml of OA and 35 ml of hexane were added. The NPLs were separated by centrifugation and were re-suspended in 10 ml of hexane.

The synthesis of 13 atomic layers thick NPLs was inspired by ref. 48. The selenium precursor was produced in a glove box. 0.15 mmol of selenium mesh were introduced in 1 ml of N-methylformamide (NMF), then 0.3 mmol of NaBH_4 dissolved in 0.5 ml of NMF were added dropwise in order to reduce Se to Se^{2-} . The flask was stirred open (in order to release H_2) during 10 minutes. 0.1 mmol of $\text{Cd}(\text{Ac})_2 \cdot 2\text{H}_2\text{O}$ dissolved in 1 ml of NMF served as a cadmium precursor. For obtaining the CdSe NPLs, 200 ml of the 9 MLs thick CdSe nanoplatelets, 800

Chapter II. Theoretical and experimental methods

ml of hexane, 0.5 ml of NMF and 25 ml of the selenium precursors were stirred for 5 minutes in a flask. The as-obtained NPLs were capped with selenium and presented a total of 11 atomic layers. In order to remove the excess of selenium precursor, the NPLs in NMF were precipitated with ethanol, centrifuged and re-suspended in NMF. Then 200 ml of the cadmium precursors was added to the NPLs and let to react for 2 minutes. The resulting 13 layers thick NPLs were purified by centrifugation with ethanol and resuspended in NMF. They were transferred back to hexane by adding hexane and OA to the NPLs in NMF.

The synthesis of QDs is based on ref. 49. Briefly, 0.4 mmol CdO powder, 1.2 mmol myristic acid (MA) and 10 ml ODE were introduced in a three neck flask, and degassed under Ar for 10 minutes. The mixture was heated up to 270 °C during rigorous stirring. In the meantime, heterogeneous Se-ODE precursor was prepared by dissolving 0.4 mmol Se powder in 2 ml ODE. The mixture was sonicated for 15 minutes to disperse Se. When the temperature of 270 °C was reached, 1 ml of Se precursor solution was injected into the reaction mixture. Immediately after Se injection, the temperature was set to 260 °C. 8 minutes later, the reaction was stopped by cooling down the reaction mixture. The QDs were redispersed in 10 ml of toluene. Next, 10 ml isopropanol and 10 ml methanol were added, and the mixture was centrifuged at 5000 rpm for 7 minutes. After this cleaning step, QD precipitated as pellets at the bottom of the vial. The solution was discarded and the QDs redispersed in 10 ml of toluene. Next, 12 mmol oleic acid was added to the QD pellets to replace the original oleic acid bounded to their surface. The purification step was repeated using methanol as a nonsolvent, and the OA-passivated QD pellets were re-suspended in toluene.

II.2.2. Synthesis of 1D wide band gap semiconductor nanostructures

Several methods have been reported in the literature for the synthesis of 1D nanostructures such as nanorods (NRs) and nanowires (NWs) of ZnO and TiO₂. They include vapor-phase^{50,51} methods (such as chemical vapor deposition⁵² and physical vapor deposition⁵³), hydrothermal⁵⁴ and solvothermal growth⁵⁵, template-assisted syntheses (including template-based hydrolysis, template filling,⁵⁶ electrochemical,⁵⁷ electrophoretic⁵⁸ and atomic layer deposition⁵⁹), sol-gel methods^{60,61} and electrospinning^{62,63}. Among these, solution-phase methods, especially hydrothermal growth, are outstanding due to easy and

Chapter II. Theoretical and experimental methods

low-cost handling, environmental friendliness, high control of morphology^{64,65} and relatively low synthesis temperatures (25-200 °C).⁶⁶ According to these advantages, these methods were selected for the synthesis of ZnO and TiO₂ 1D nanostructures in this work.

In this thesis, ZnO and TiO₂ nanorods/nanowires were synthesized for two purposes, referred to as *purpose 1*) and 2) in the following:

- 1) CdSe nanoplatelets of different thicknesses were linked to ZnO/TiO₂ substrates using different bifunctional linkers. **The first goal of these experiments was to characterize the interfaces formed between the two semiconductors.** Subsequently, solar cells were tested based on selected ZnO/TiO₂ NR – CdSe NPL heterostructure photoanodes. **The final objective of this study was to test the applicability of pre-synthesized CdSe NPLs in QDSCs.** To our knowledge, no solar cells have been reported in the literature using this type of sensitizers. In more particular, no application of quasi-two dimensional CdSe NPLs in solar cells is known.
- 2) We grew CdSe QDs directly on ZnO/TiO₂ NR arrays with the successive ionic layer adsorption and reaction (SILAR) method, which will be detailed in section II.2.3. b), and **tested solar cells based on these sensitized photoanodes.**

II.2.2. a) ZnO nanorods/nanowires

The hydrothermal synthesis of ZnO wurtzite 1D nanostructures contains a OH⁻ and a Zn²⁺ precursor (most often Zn(NO₃)₂). A widely used OH⁻ source in the hydrothermal synthesis of ZnO 1D nanostructures is hexamethylene tetramine (HMTA) (*Figure II.4.*),^{64,67,68} which is a highly water soluble, non-ionic tetradentate cyclic ternary amine. It acts as a weak base, which slowly hydrolyzes in water when the temperature is increased, gradually releasing OH⁻ through NH₄OH base production, as described by *Equations II.50-52.*⁶⁹

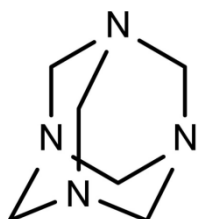
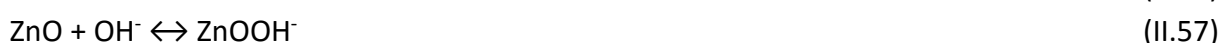


Figure II.4. Molecular structure of hexamethylene tetramine (HMTA).

Chapter II. Theoretical and experimental methods



The degree of the supersaturation of Zn^{2+} species is controlled by changing the pH and/or the Zn^{2+} concentration. For example, it increases by increasing the pH, or decreased by adding a Zn^{2+} complexing agents in the form of ammonium compounds, such as NH_4OH or NH_4NO_3 , as illustrated by *Equation II.58*. Therefore, the obtained ZnO structures will be the result of several delicate equilibria between the Zn^{2+} , hydroxide and chelating species. The main reactions involved in the ZnO crystal growth are illustrated by *Equations II.53-58*.



In order to obtain vertically aligned ZnO nanorods, crystal growth must be gradual under a low degree of supersaturation. However, in this case, the resulting particles size distribution is rather large due to the variations in nucleation time. In order to achieve a more homogeneous size distribution of the nanostructures, the nucleation step and the growth step must be separated by using seeded substrates. They can be prepared using several techniques, such as spin coating, dip coating, spray pyrolysis or radio frequency magnetron sputtering.^{65,70} Spin coating with well-chosen parameters can provide a homogeneous and highly structured ZnO seed layer on the substrate that gives rise to high density of nanorods/nanowires with their *c* axis perpendicular to the substrate surface.⁷¹⁻⁷³ Typically, a 5 mM $\text{Zn}(\text{CH}_3\text{COO})_2$ solution in ethanol is spin-coated at a rate of 2000 rpm for 30s on a rigorously cleaned FTO glass substrate. This step can be repeated several times to produce a thick blocking layer that prevents recombination between the FTO glass and the hole transporting material.^{71,74} The deposited layer is then heated to decompose the Zn precursor and produce ZnO seeds. Typical annealing temperatures at this step range between 250 and 350 °C for 20-30 min.⁷¹⁻⁷³

Chapter II. Theoretical and experimental methods

Due to the anisotropic nature of the ZnO wurtzite unit cell with polar (0001) and apolar (1000) faces, the ZnO grains have a tendency to grow as elongated rods in the c-direction. Some additives, such as polyethylenimine (PEI)^{73,75} and ethylenediamine (EDA)⁷⁶ adsorb selectively on the apolar ZnO surfaces, which further favors the growth along the c-axis. In particular, we tested PEI in this thesis, which is a non-polar polymer with a large amount of amine groups that can be protonated in a wide range of pH values. The positively charged PEI is strongly adsorbed on the negatively charged lateral planes of ZnO, which promotes vertical growth of nanorods/nanowires.^{75,77} Moreover, PEI has a similar buffering effect to NH_3 , since it chelates Zn^{2+} ions. Therefore, besides controlling the growth direction of ZnO crystals, it prevents the precipitation of ZnO crystals in the bulk solution, while ZnO nanorods/nanowires can still grow on the seeded substrate at a satisfactory rate.

The synthesis of ZnO nanorod arrays for *purpose 1*) is based on a hydrothermal method described by Xu *et al.*⁷³ The FTO-coated TEC 15 glasses were thoroughly cleaned first by detergent and deionized (DI) water. They were then sonicated for 15 min in ethanol and for 15 min in acetone. A ZnO seed layer was grown on the clean FTO glasses by spin-coating a 5 mM solution of $\text{Zn}(\text{Ac})_2$ in ethanol at 3000 rpm for 30s 15 times. The spin-coated substrate was annealed for 20 min at 300 °C in a furnace with the following ramping program:

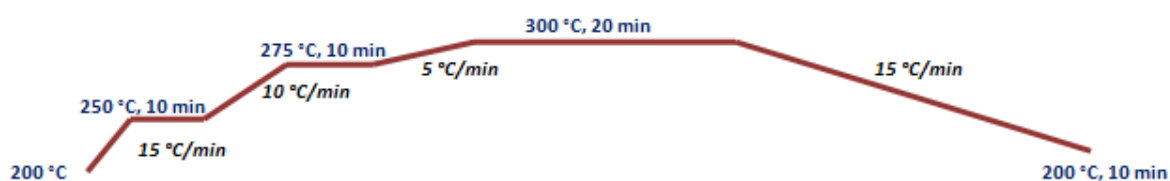


Figure II.5. Ramping program for the thermal treatment of seeded FTO glasses prepared with the spin-coating of $\text{Zn}(\text{Ac})_2$ solution with method 1).

Xu *et al* reported that the growth rate of ZnO nanowires is as high as 4.5 $\mu\text{m}/\text{h}$ in the first two hours.⁷³ As the CdSe NPLs that we intended to link to the nanostructured ZnO substrate are extended nanocrystals with lateral dimensions of 40-100 nm, we supposed it is difficult to reach a high and homogeneous CdSe NPL coverage on the side facets of these long nanorods. Therefore, we decided to apply a synthesis time of only 1h. The seeded substrates

Chapter II. Theoretical and experimental methods

were immersed in 100 ml growth solution in a closed container, which was put in an oven preheated at 96 °C for 1h. The growth solution was composed of 25 mM $\text{Zn}(\text{NO}_3)_2$, 12.5 mM HMTA and 0.45 M NH_3 . In order to further decrease the nanorod length, no PEI was added to the growth solution. The samples were placed at an angle of 45° against the wall of the container, with their seeded side facing down, as shown in *Figure II.6*. Their opposing side was coated with a scotch tape to protect it of precipitates formed in the bulk solution. After the containers were taken out of the oven, and the solution cooled down, the sample was removed from the container and the tape was removed.

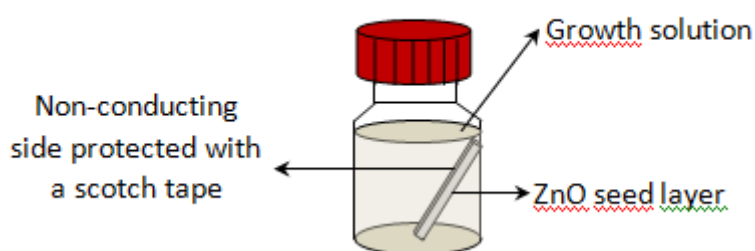


Figure II.6. Experimental setup for the ZnO NR growth.

In order to eliminate organic residues from the samples the samples were rinsed with deionized water and let to dry naturally. Finally, they were annealed at 450°C for 30 min with the ramping program shown in *Figure II.7*:

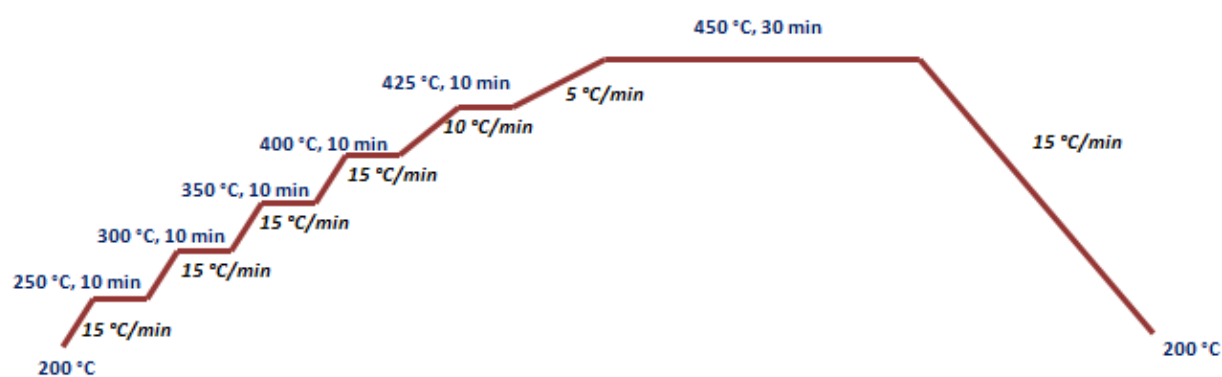


Figure II.7. Ramping program for the thermal treatment of hydrothermally grown ZnO NR arrays.

For *purpose 2*), the hydrothermal synthesis of ZnO nanorods was based on a previous work.⁷¹ The FTO-coated TEC 15 glasses were cleaned as described above. Then, they were spin-coated 5 times with a 5 mM solution of $\text{Zn}(\text{Ac})_2$ in ethanol at 3000 rpm for 30s, and the

Chapter II. Theoretical and experimental methods

films were annealed at 250°C for 20 min. This procedure was repeated two times, and the as-prepared seeded samples were annealed at 350°C for 1h with a ramping program illustrated in *Figure II.8*. A solution containing 0.04 M $\text{Zn}(\text{NO}_3)_2$ and 0.8 M NaOH was preheated for 6 min at 88°C in an oven. As a pre-treatment prior to the hydrothermal growth, the samples were immersed in this solution for 16 min at the same temperature. Then, the same growth solution was prepared in a 100 ml container as detailed above.⁷³ The seeded and pretreated samples were immersed in this solution as in *Figure II.6*, and placed in a furnace for 10h at 93°C. They were then rinsed with deionized water and let to dry naturally. Finally, they were annealed at 450°C for 30 min using the ramping program illustrated in *Figure II.7*.

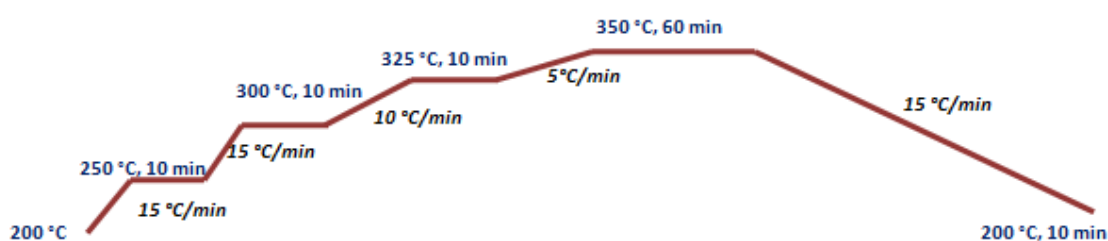


Figure II.8. Ramping program for the thermal treatment of seeded FTO glasses prepared by the spin-coating of $\text{Zn}(\text{Ac})_2$ solution with method 2).

II.2.2. b) TiO_2 nanorods

The 2% lattice mismatch between the cubic SnO_2 and TiO_2 allows the epitaxial growth of rutile TiO_2 nanorods on bare FTO coated glasses.^{78–80} However, a thick homogeneous seed layer is necessary in QDSC to prevent the charge recombination occurring at the FTO and the hole transporting material interface.^{71,74} Therefore, prior to nanorod growth, a TiO_2 seed layer was prepared by spin coating on the FTO/glass substrate. Then, in a typical hydrothermal synthesis, DI water and concentrated HCl were mixed. After stirring for a few minutes, the Ti(IV) precursor (for example titanium butoxide^{79,81} or titanium isopropoxide^{80,82}) was added dropwise, and the mixture was stirred for a few more minutes. In the literature, the hydrothermal synthesis was typically conducted on TEC-15 FTO glasses immersed in the growth solution in a stainless steel autoclave in an oven at 150–220 °C for 1–24h.^{79–82} After synthesis, the autoclave was taken out of the oven and cooled down to room temperature. The substrates were rinsed with DI water and dried in ambient air. Similarly to

Chapter II. Theoretical and experimental methods

the hydrothermal synthesis of ZnO nanorods, a final annealing step was performed at around 450-500°C for 1h.

Huang et al proposed the following mechanism for the hydrothermal growth of TiO₂ nanorods:⁸⁰



Where Ti(IV)_p and Ti(IV)_c stand for the titanium precursor and complex, respectively. HCl has a double role in the synthesis:

- It participates in the hydrolysis of the precursor and in the complexation of Ti(IV), as shown in *Equation II.60*.
- Chloride ions are also known to hinder the growth of rutile in the [110] direction, and promote growth along the [001] direction.^{83,84} This further contributes to the growth of TiO₂ nanorods elongated along the c axis, which is already the favored crystal shape based on the symmetry of rutile crystals⁸⁵ and on the relative surface energy of TiO₂ rutile crystal planes.⁸⁶

During this hydrothermal synthesis, two processes compete with each other: crystal growth and dissolution. Aydil reported that the growth of nanorods is favored at short reaction times (inferior to 20h) due to the high supersaturation of the Ti precursor in the growth solution.⁷⁹ However, at long synthesis times, the crystal growth rate decreases, and dissolution at high-energy surfaces, such as the FTO-TiO₂ interface becomes important. The TiO₂ film thus peels off. At higher synthesis temperature, such as 200°C, equilibrium between crystal growth and dissolution is reached after 6h. The acidity of the growth solution is another sensitive issue. It was found that an approximate 50-50% ratio of DI water and HCl is ideal for TiO₂ nanorod growth.⁷⁹ If the ratio of acid is lower, the titanium precursor precipitates as TiO₂ at the bottom of the autoclave, and none remains available for hydrothermal growth. On the other hand a higher acid concentration hinders the hydrolysis of the titanium precursor.

Chapter II. Theoretical and experimental methods

The synthesis of TiO₂ rutile nanorods for *purposes 1)* and *2)* was based on a previous work by Kim *et al*⁸⁷. First, the FTO-coated glasses were cleaned as described above. Then, they were spin coated with a 0.15 M titanium (IV) diisopropoxide bis(acetylacetonate) (denoted as TIPA) solution in butanol, and heated at 125 °C for 5 min. After the spin-coated film has cooled down to room temperature, this procedure was repeated twice with a 0.30 M solution, and the FTO glasses were annealed at 500 °C for 15 min in a furnace with the ramping program illustrated in *Figure II.9*.

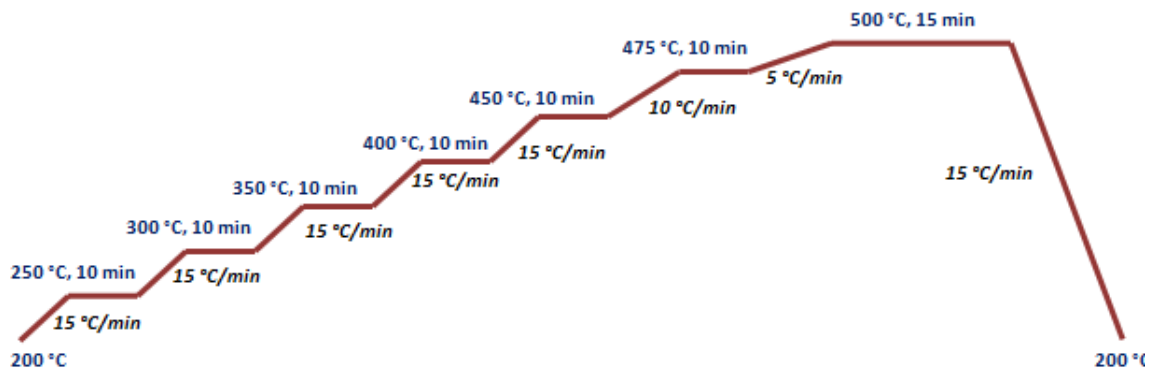


Figure II.9. Ramping program for the thermal treatment of seeded FTO glasses prepared with the spin-coating of TIPA solution.

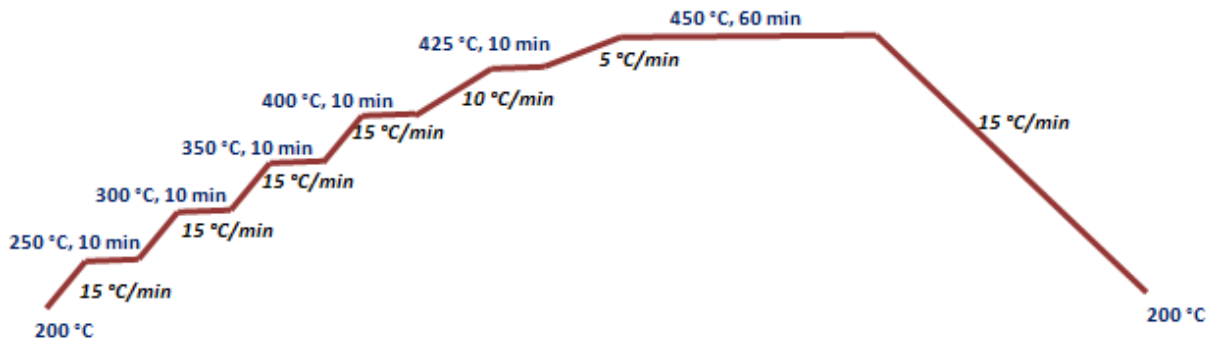


Figure II.10. Ramping program for the thermal treatment of hydrothermally grown TiO₂ NR arrays.

Based on the work by Kim *et al*,⁸⁸ TiO₂ nanorods were grown on the as-prepared seed layer in a stainless steel autoclave with a Teflon liner. The growth solution was made by mixing 20 ml deionized water with 20 ml 37% hydrochloric acid, and then adding 0.7 ml titanium (IV) n-butoxide dropwise. The substrates were positioned at an angle of 45° with the seeded layer facing against the wall of the Teflon liner, similarly to the ZnO nanorod synthesis. The

Chapter II. Theoretical and experimental methods

autoclave was placed in an oven preheated at 170 °C for 3 hours. After the autoclave was taken out and cooled down naturally, the samples were rinsed with deionized water, dried and annealed at 450°C for 1h with the program shown in *Figure II.10*.

II.2.3. Attachment of quantum dots to wide band gap semiconductors

The sensitization of WBSCs by quantum dots can be grouped into two major categories: *in situ* (synthesis of quantum dots directly on the WBSC surface) and *ex situ* (attachment of previously prepared quantum dots) techniques.⁸⁹ *In situ* methods include chemical bath deposition (CBD)⁹⁰ and successive ionic layer absorption and reaction (SILAR),⁹¹ spray pyrolysis deposition (SPD)⁹² and electrospray technique⁹³. These techniques are known to provide high surface coverage and direct connection between the QD and the WBSC, but the surface size, shape and passivation are poorly controlled, contrary to *ex situ* methods, which, on the other hand, result in low and less reproducible surface coverage.⁹⁴ A disadvantage of *ex situ* sensitization methods, such as direct adsorption (DA)⁹⁵ and linker-assisted adsorption (LAA)⁹⁶ is the longer processing time compared to *in situ* sensitization approaches like CBD or SILAR.⁹⁷ In this thesis, we tested both *ex situ* and *in situ* methods for sensitizing ZnO NRs and TiO₂ NRs by CdSe nanocrystals by using linker-assisted attachment and the SILAR methods, respectively.

II.2.3. a) Sensitization by linker-assisted attachment

In case of linker-assisted attachment, bifunctional linker molecules are used to connect the sensitizers to the WBSC surface. One of the functional groups of these linkers is connected to the WBSC, while the other one is connected to the QD. In the most minimalistic case of an atomic linker, the bifunctional linker can be an atom that uses two of its valence electrons to form covalent bonds both with the QD and the WBSC. *A priori*, applying these linkers could have several advantages in quantum dot sensitized solar cells.

- 1) It had been pointed out in previous studies that the electron transfer rate constant exponentially decreases with the length of the linker molecule,^{98–101} as described by *Equation II.61*:¹⁰²

Chapter II. Theoretical and experimental methods

$$H(E) = H^0(E) \cdot \exp \left[\left(-\frac{1}{2} \right) \cdot \beta \cdot d_{DA} \right] \quad (\text{II.61})$$

where d_{DA} is the separation distance between the donor and the acceptor, β is the attenuation rate, and $H^0(E)$ is the electronic coupling at $d_{DA} = 0$. Therefore, an atomic linker must largely improve the charge transfer rate between the QD and the WBSC compared to longer linkers. Indeed, in a previous study by Yun¹⁰³, TiO₂ nanoparticle films were sensitized with CdSe QDs using either atomic (S^{2-} ions) or molecular (3-mercaptopropionic acid, MPA in *Figure II.11*) linkers. They obtained higher photovoltaic efficiency parameters for QDSCs based on sulfide-capped QDs than those applying MPA-linked QDs.

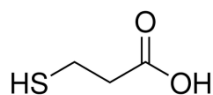


Figure II.11. Molecular structure of 3-Mercapto-propionic acid.

- 2) Moreover, if the QDs are deposited on the WBSC surface in films that are thicker than a monolayer, it is also desirable to achieve high electron mobility between QDs, within the sensitizer film. Several studies demonstrated that atomic linkers outperform molecular ones in this aspect.^{104,105}
- 3) Proper treatment with atomic ligands can improve the air stability of QD films.¹⁰⁶
- 4) Atomic ligands can serve as efficient passivation layers and contribute to reduce recombination between QDs and WBSCs^{103,107}

Two main approaches have been developed for LAA. In *method 1*, the WBSC coated electrode is first immersed in a solution containing the linker molecule that is adsorbed on the semiconductor oxide surface. Then, the chemically modified WBSC substrate is immersed into a solution containing the pre-synthesized QDs. Alternatively, in *method 2*, QDs can first be coated by linker molecules, and subsequently be attached to the WBSC surface.¹⁰⁸

With our chosen synthesis protocol, CdSe NPLs and QDs are passivated by oleic acid ligands with long carbohydrate chains. For photovoltaic application, it is necessary to exchange

Chapter II. Theoretical and experimental methods

these large organic molecules to well-chosen shorter ligands, which can also serve as bifunctional linkers. Among the two approaches described above, *method 2* was thus the more suitable sensitization method to apply in this thesis. As a first step of the ligand assisted attachment, the initial OA ligands were exchanged to short bifunctional ones. We considered both atomic (OH^- and SH^-), and molecular ligands (MPA). Next, a dispersion of the NPLs/QDs was dropcasted on the ZnO or TiO_2 substrates, and the solvent was evaporated.

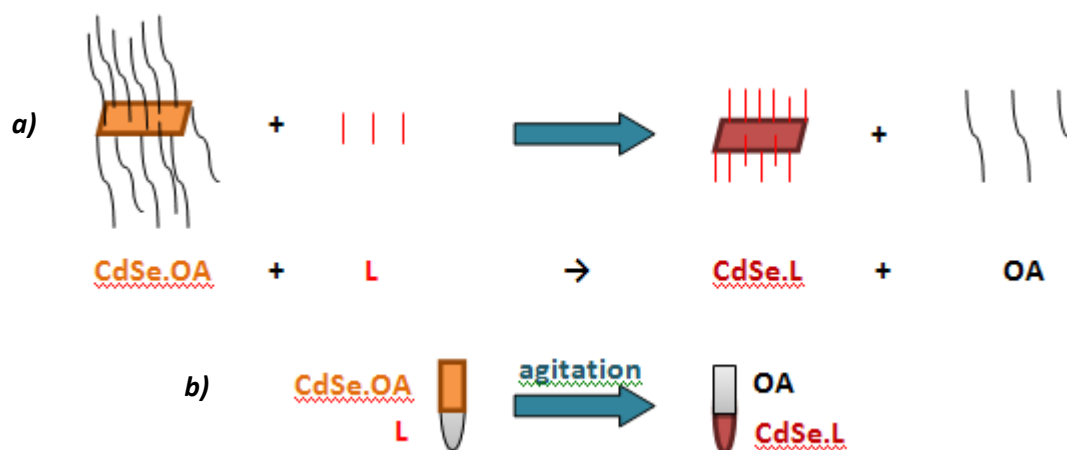


Figure II.12. a) Schematic illustration of biphasic ligands exchange reactions on CdSe NPLs. The short polar bifunctional linker is denoted as L. CdSe.OA and CdSe.L stand for CdSe NPLs passivated by oleic acid and the L linker, respectively. b) Biphasic exchange transfer.

In the case of the OH^- and SH^- ligands, ligand exchange reactions were based on ref. 109. The precursor of SH^- was prepared as follows. 0.1 mmol of NaHS was dissolved in 1 ml NMF in a vial. For obtaining a OH^- precursor, 0.1 mmol of KOH was dissolved in 1 ml of NMF in a vial. Then, in a flask, 200 μl of the CdSe NPLs or QDs, 800 μl of hexane, 0.5 ml of NMF and 40 μl of the SH^- (respectively OH^-) precursors were stirred for 5 minutes. The NPLs were completely transferred from the non-polar to the polar phase due to the ligand exchange. These biphasic reactions are schematically illustrated in *Figure II.12*. In the following, the as-prepared CdSe nanocrystals passivated by SH^- and OH^- ligands are denoted as **CdSe.SH** and **CdSe.OH**, respectively. In order to sensitize the ZnO or TiO_2 nanorod arrays, 50 μl of the CdSe.SH or CdSe.OH dispersions was dropcasted on the substrates. Then, they were heated at 150°C for 5 min to evaporate the NMF solvent. This temperature was low enough not to damage the structure of the CdSe nanocrystals. The sensitized samples are denoted as **CdSe.SH – ZnO**, **CdSe.OH – ZnO**, **CdSe.SH – TiO_2** and **CdSe.OH – TiO_2** in the rest of the manuscript.

Chapter II. Theoretical and experimental methods

The ligand exchange with MPA was done as follow. 200 μl of MPA was added to 100 μl of CdSe NPLs dispersion in hexane in a vial, which was kept at 60°C for at least 6 hours. The resulting MPA-passivated NPLs were separated by centrifugation and re-suspended in NMF. They were rendered water-soluble by adding 2 mg of potassium tert-butoxide to deprotonate the carboxylate group of MPA. The NPLs were then precipitated in NMF. They were subsequently separated by centrifugation and redispersed in an aqueous solution with a basic pH to keep the carboxylate groups deprotonated. The pH of this aqueous solution was adjusted to 13 by addition of mashed NaOH pellets. The as-prepared CdSe nanocrystals are denoted as **CdSe.MPA** in the following. The ZnO and TiO₂ nanorod arrays were sensitized by CdSe.MPA nanocrystals by dropcasting a basic aqueous dispersion of CdSe.MPA onto the substrates, similarly to the work published by Pan et al.¹¹⁰ Water was fully evaporated by leaving the samples in ambient air for 3h. The obtained sensitized samples are denoted as **CdSe.MPA – ZnO** and **CdSe.MPA – TiO₂**.

II.2.3. b) Sensitization by the SILAR method

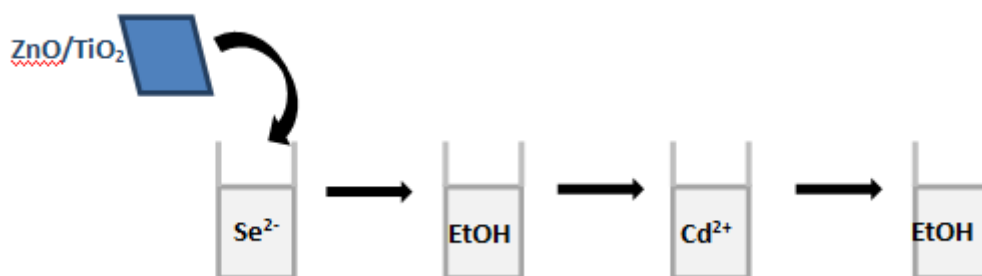


Figure II.13. Schematic illustration of one SILAR cycle.

SILAR is a popular and widely used method in the literature for photoanode sensitization.^{111–114} Its main advantages include simplicity, short processing time (a few minutes to hours) and nearly stoichiometric QD composition.¹¹⁵ The SILAR process we applied is schematically illustrated in *Figure II.13*. The glass substrates with a ZnO or TiO₂ nanorod arrayed layer were first immersed into the Se²⁻ precursor solution for 1 min. Then, the excess of Se²⁻ was rinsed by immersing the substrates into ethanol for a few seconds. Then the samples were dipped into the Cd²⁺ precursor solution for 1 min, and the excess of Cd²⁺ was eliminated by immersing them into ethanol for a few seconds. One Se²⁻ and one Cd²⁺ ion deposition define

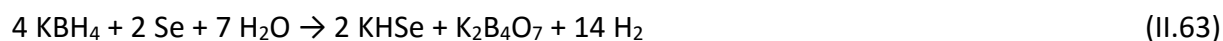
Chapter II. Theoretical and experimental methods

altogether one SILAR cycle. The size of CdSe nanocrystals can be controlled by the number of SILAR cycles.¹¹⁶

Hydrothermally grown ZnO nanorod⁷¹ and TiO₂ nanorod arrays^{87,88} were sensitized by CdSe QDs using the SILAR method based on the work of Deng and coworkers.⁷¹ The Cd²⁺ precursor solution was prepared by dissolving 0.32 g Cd(OAc)₂ in 40 ml ethanol. In order to prepare the Se precursor solution, 0.1330 g SeO₂ was dissolved in 40 ml DI water in an Erlenmeyer flask and stirred for 3 minutes under argon. Then, 0.13 g KBH₄ was added and the solution color turned from colorless transparent to a turbid coral red one. After the addition of all the KBH₄ powder, the solution started to effervesce with small bubbles, and a color- and an odorless gas left the beaker. The fizzing and the gas formation lasted for approximately 3-4 minutes. It is supposed that the KBH₄ reduces SeO₂ into colloidal Se with H₂ gas formation at this stage, as described by *Equation II.62*.



After the stopping of bubbling, the flask was put again under Ar atmosphere and stirred for 1.5 hours. The gas(es) (presumably only H₂) formed during the reduction were by-passed by an extractor hood. During this time, the coral red colored solution became darker and darker until it reached a black color. As its color deepened, it also became more and more transparent. After around 1 hour of stirring under Ar, the black solution gradually started to become colorless. A full transparency was reached after around 1.5 hours. We can suppose that Se was further reduced to Se²⁻ as it slowly reacted with the remaining KBH₄ under Ar environment:¹¹⁷



As the Se nanoparticles were gradually dissolved, the solution became clearer and clearer. The deepening of the color is explained by the decrease in size of the suspended Se nanoparticles, which induces the enlargement of the band gap. The introduction of Ar gas into the flask is important to keep the oxygen level low in the system, as Se²⁻ can quickly oxidized to Se in air. We also tried to prepare this Se²⁻ precursor in ethanol in a dry N₂ filled

Chapter II. Theoretical and experimental methods

glovebox, in a manner similar to the protocol reported by Huang and coworkers.⁸⁰ In our experiments, the ethanolic solution darkened slower than the aqueous one under Ar. After the black color persisted for more than 3 hours, we stopped the reaction and used the black precursor solution for SILAR experiment. This precursor solution was found unfit for the sensitization, confirming the unsuccessful reduction of Se to Se^{2-} under these experimental conditions.

We also tested the effect of adding a sulfide interlayer between the ZnO NRs and the CdSe QDs. This was realized by dipping the substrate into a S^{2-} and then into a Cd^{2+} precursor solution in a “0th SILAR cycle”, followed by the above described 12-cycle SILAR process. The S^{2-} solution was prepared by dissolving NaSH in 40 ml DI water in the same concentration as in the case of the Se^{2-} precursor solution. In order to follow the sensitization processes, CdSe QD – ZnO or TiO_2 heterostructures were characterized by UV-VIS absorption, Raman spectroscopy and XRD after every two SILAR cycle, up to 12 cycles, which was reported to be the ideal number of SILAR cycles by Deng et al.⁷¹ Solar cells were tested with photoanodes prepared with 6 and 12 SILAR cycles.

II.2.4. Assembly of solar cells

II.2.4. a) All-solid state QDSCs

We used a solid hole-transport layer based on 2,2',7,7'-Tetrakis-(N,N-di-4-methoxyphenylamino)-9,9'-spirobifluorene (abbreviated as spiro-OMeTAD), which is an amorphous organic p-type semiconductor with a large band gap and a hole mobility in the range of $10^{-5} - 10^{-4} \text{ cm}^2 \text{ V}^{-1} \text{ s}^{-1}$.¹¹⁸ The molecular structure of spiro-OMeTAD is illustrated in *Figure II.14*. Spiro-OMeTAD is reported to have a particularly efficient pore filling when dissolved in toluene and chlorobenzene.¹¹⁹ Its transport properties can further be improved by adding additives,¹¹⁸ such as 4-tert-butylpyridine (TBP) and lithium-bis(trifluoromethylsulfonyl)imide (LiTFSI). While TBP retards the electron-hole recombination rate,¹²⁰ LiTFSI accelerates the electron injection, and thus increases J_{sc} .^{121,122} In this thesis, for the preparation of the solid HTM, 40 mg spiro-OMeTAD, 14.25 ml tert-butylpyridine, and 17.5 μl

Chapter II. Theoretical and experimental methods

of LiTFSI solution (prepared by dissolving 520 mg LiTFSI in 1 ml acetonitrile), were dissolved in 1 ml chlorobenzene. 40 μ L of this spiro-OMeTAD solution was spin coated on the sensitized substrates at 2000 rpm for 15 s. Finally, the counter electrode was made by a silver contact evaporated on the top of the HTM.

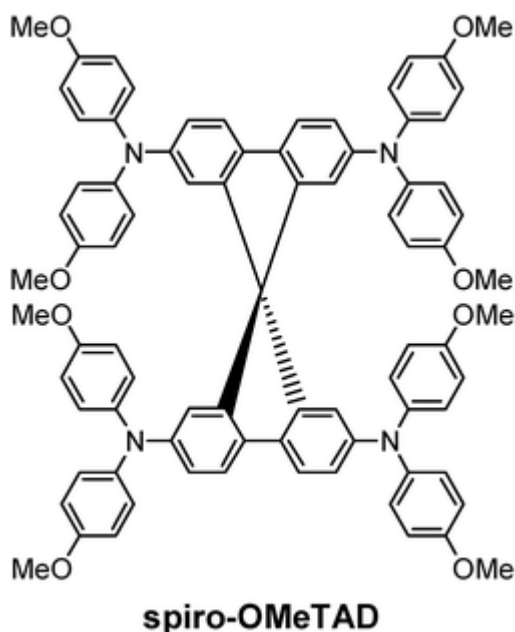


Figure II.14. Molecular structure of spiro-OMeTAD.

II.2.4.b) QDSCs with liquid electrolyte

The preparation of the liquid electrolyte was based on the work by Jiao et al.¹²³ A solution of 2.0 M Na₂S, 2.0 M S and 0.2 M KCl was prepared in DI water. After stirring the mixture for at least 2h, the solution became homogeneous and brown colored. The Cu₂O counter-electrode was prepared as described by Jiao et al.¹²³ A brass foil was polished and first sonicated in trichloroethylene for 20 minutes, then cleaned by ethanol and deionized water. Then, it was immersed in a 1.0 M HCl solution at 70 °C for 10 min. Then, it was washed by DI water, and immersed in the above described liquid electrolyte at room temperature for 10 min in order to produce a Cu₂S layer. It was then rinsed with DI water and dried with air flow. The prepared liquid electrolyte-based QDSC is schematically illustrated in *Figure II.15*.
c).

Chapter II. Theoretical and experimental methods

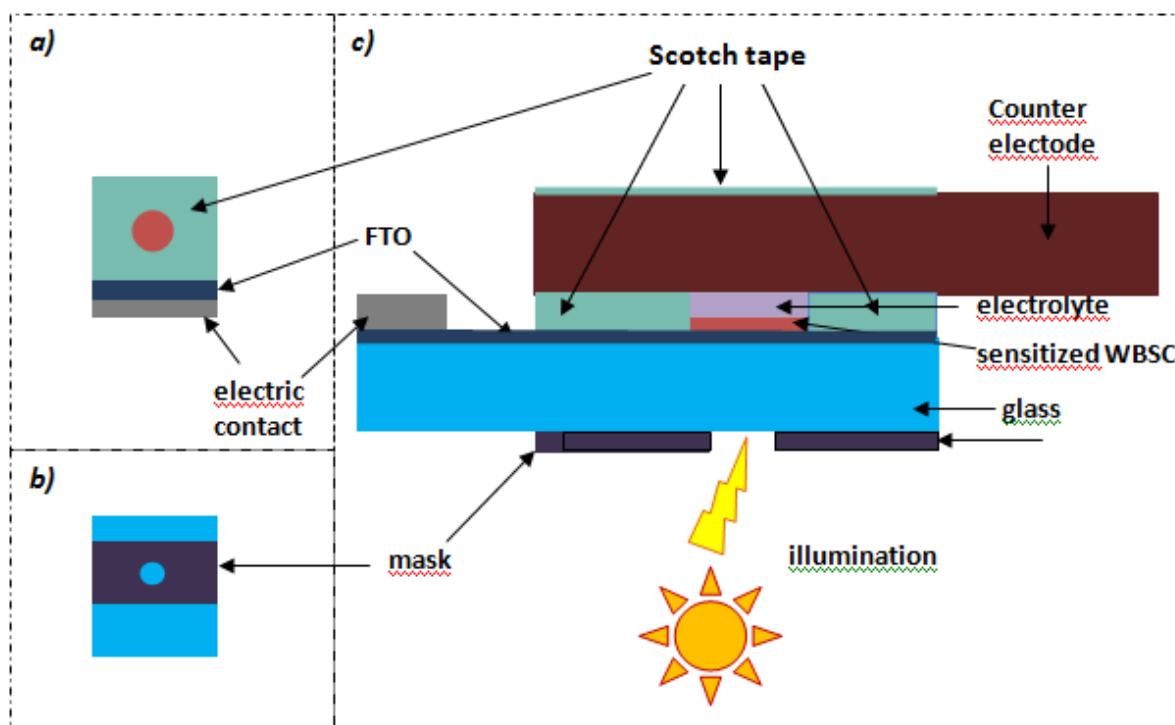


Figure II.15 a) Top-view of the photoanode, masked by the Scotch tape on the conducting side. b) The non-conducting side of the photoanode covered by a mask with a 0.07 cm^2 circular hole. c) Cross-sectional view of the assembled complete solar cell.

The solar cells containing a liquid electrolyte were fabricated following the steps:

1. The photoanode, which had the size of $1.5 \text{ cm} \cdot 1.5 \text{ cm}$, was masked by a Scotch tape except for a circular area of 5 millimeters of diameter (as shown in *Figure II.15 a*). A 5 mm wide edge strip was also let uncovered..
2. The non-conducting side of the photoanodes was masked using a metallic mask, leaving a circular area of 0.07 cm^2 free for illumination during solar cell tests, as illustrated in *Figure II.15. b*).
3. A metallic contact was soldered on the FTO edge strip.
4. The brass/ Cu_2S counter electrode, which had the same size as the photoanode, was coated on its backside by an insulating scotch tape, except a 5 mm wide edge.
5. The photoanode and the counter electrode (both of the size of $1.5 \cdot 1.5 \text{ cm}$) were placed on each other with a shift of 5 mm, leaving the electric contact uncovered.
6. $20 \mu\text{l}$ of the liquid electrolyte was injected between the two electrodes spaced out by the Scotch tape, and reaches the unmasked circular area by capillarity.

Chapter II. Theoretical and experimental methods

7. The electrodes were held together using two paper clip binders. The contact between the metallic parts of the paper clip binder and the brass/Cu₂S cathode was hindered by the Scotch tape on the outer side of the cathode.

This setup ensured a fast solar cell assembly. However, because of the electrolyte leakage, the as-made solar cells worked only for a few minutes.

II.2.7. Characterization methods

The absorption spectra of the CdSe.SH nanoplatelets dispersed in NMF were measured using a UV-VIS Varian Cary-5^E spectrophotometer. The absorption spectra of the NPL-sensitized ZnO NR layers were obtained from the total transmittance and total reflectance spectra measured by a Cary 5000 UV-VIS spectrometer equipped with an integrating sphere.

Raman spectra of the substrates were obtained at ambient temperature (20 °C) in air using a confocal Renishaw inVia Reflex Raman spectroscopy equipped with a 100x objective and a 473 nm blue laser. The samples were scanned 15 times at a laser power attenuation of 10% for an accumulation time of 30 seconds/scan. The data were collected and analyzed using the Renishaw's WiRE software.

For the film structural characterizations, a PANalytical X'pert high-resolution X-ray diffractometer with a Cu K_α radiation with $\lambda = 1.5406 \text{ \AA}$ was used, operated at a voltage 40 kV and a current of 45 mA.

For the solar cell characterization, the current-voltage characteristics were recorded with a Keithley 2400 sourcemeter using a voltage sweep rate of 0.01 V s⁻¹. The solar cells were illuminated with a solar simulator (Abet Technology Sun 2000) filtered to mimic air mass AM 1.5G conditions. The power density was calibrated to 100 mW·cm⁻² with the help of a reference silicon solar cell. The illuminated surface was delimited to 0.07 cm² by a black mask.

References

- (1) Koopmans, T. Über Die Zuordnung von Wellenfunktionen Und Eigenwerten Zu Den Einzelnen Elektronen Eines Atoms. *Physica* **1934**, *1*, 104.
- (2) Roothaan, C. C. J. New Developments in Molecular Orbital Theory. *Rev. Mod. Phys.* **1951**, *23*, 69.
- (3) Thomas, L. H. The Calculation of Atomic Fields. *Proc. Camb. Philol. Soc.* **1927**, *23*, 542–548.
- (4) Fermi, E. No Title. *Zeitschrift für Phys.* **1928**, *48*, 73.
- (5) Dirac, P. A. M. Note on Exchange Phenomena in the Thomas Atom. *Math. Proc. Cambridge Philos. Soc.* **1930**, *26* (03), 376.
- (6) Hohenberg, P.; Kohn, W. Inhomogeneous Electron Gas. *Phys. Rev.* **1964**, *136*, B864–B871.
- (7) Kohn, W.; Sham, L. J. Self-Consistent Equations Including Exchange and Correlation Effects. *Phys. Rev.* **1965**, *140*, A1133–A1138.
- (8) Xiao, H.; Tahir-Kheli, J.; Goddard, W. A. Accurate Band Gaps for Semiconductors from Density Functional Theory. *J. Phys. Chem. Lett.* **2011**, *2*, 212.
- (9) Martsinovich, N.; Jones, D. R.; Troisi, A. Electronic Structure of TiO₂ Surfaces and Effect of Molecular Adsorbates Using Different DFT Implementations. *J. Phys. Chem.* **2010**, *114*, 22659–22670.
- (10) Cora, F.; Alfredsson, M.; Mallia, G.; Middlemiss, D. S.; Mackrodt, W. C.; Dovesi, R.; Orlando, R. The Performance of Hybrid Density Functionals in Solid State Chemistry. In *Struct. Bonding*; Springer Berlin / Heidelberg: Berlin, 2004; p 171.
- (11) Csonka, G. I.; Perdew, J. P.; Ruzsinszky, A. Global Hybrid Functionals: A Look at the Engine under the Hood. *J. Chem. Theory Comput.* **2010**, *6* (12), 3688–3703.
- (12) Becke, A. D. No Title. *Phys. Rev. A* **1988**, *38*, 3098–3100.
- (13) Lee, C.; Yang, W.; Parr, R. G. No Title. *Phys. Rev. B* **1988**, *37*, 785–789.
- (14) Perdew, J. P.; Wang, Y. No Title. *Phys. Rev. B* **1992**, *45*, 13244.
- (15) Perdew, J. P.; Burke, K.; Ernzerhof, M. Generalized Gradient Approximation Made Simple. *Phys. Rev. Lett.* **1996**, *77*, 3865–3868.
- (16) Adamo, C.; Barone, V. Toward Reliable Density Functional Methods without Adjustable Parameters: The PBE0 Model. *J. Chem. Phys.* **1999**, *110* (13), 6158.
- (17) Becke, A. D. Density-Functional Thermochemistry. III. The Role of Exact Exchange. *J. Chem. Phys.* **1993**, *7*, 5648–5652.
- (18) Lee, C.; Yang, W.; Parr, R. G. Development of the Colle-Salvetti Correlation-Energy Formula into a Functional of the Electron Density. *Phys. Rev. B* **1988**, *37* (2), 785–789.
- (19) Perdew, J.; Chevary, J.; Vosko, S.; Jackson, K.; Pederson, M.; Singh, D.; Fiolhais, C. Erratum: Atoms, Molecules, Solids, and Surfaces: Applications of the Generalized Gradient Approximation for Exchange and Correlation. *Phys. Rev. B* **1993**, *48* (7), 4978–4978.
- (20) Cohen, A. J.; Handy, N. C. Dynamic Correlation. *Mol. Phys.* **2001**, *99* (7), 607–615.
- (21) Xu, X.; Goddard, W. A. The X3LYP Extended Density Functional for Accurate Descriptions of Nonbond Interactions, Spin States, and Thermochemical Properties. *Proc. Natl. Acad. Sci. U. S. A.* **2004**, *101* (9), 2673–2677.
- (22) Krukau, A. V.; Vydrov, O. A.; Izmaylov, A. F.; Scuseria, G. E. Influence of the Exchange Screening Parameter on the Performance of Screened Hybrid Functionals. *J. Chem. Phys.* **2006**, *125* (22).
- (23) Henderson, T. M.; Izmaylov, A. F.; Scuseria, G. E.; Savin, A. The Importance of Middle-Range Hartree-Fock-Type Exchange for Hybrid Density Functionals. *J. Chem. Phys.* **2007**, *127* (22), 0–4.
- (24) Henderson, T. M.; Izmaylov, A. F.; Scuseria, G. E.; Savin, A. Assessment of a Middle-Range Hybrid Functional. *J. Chem. Theory Comput.* **2008**, *4* (8), 1254–1262.
- (25) Weintraub, E.; Henderson, T. M.; Scuseria, G. E. Long-Range-Corrected Hybrids Based on a New Model Exchange Hole Long-Range-Corrected Hybrids Based on a New Model Exchange Hole. *J. Chem. Theory Comput.* **2009**, *5* (March), 754–762.
- (26) Marsman, M.; Paier, J.; Stroppa, A.; Kresse, G. Hybrid Functionals Applied to Extended Systems. *J. physics. Condens. matter* **2008**, *20* (6), 064201.
- (27) Towler, M. D.; Zupan, A.; Causa, M. Density Functional Theory in Periodic Systems Using Local Gaussian Basis Sets. *Comput. Phys. Commun.* **1996**, *98*, 181.
- (28) Corà, F.; Alfredsson, M.; Mallia, G.; Middlemiss, D. S.; Mackrodt, W. C.; Dovesi, R.; Orlando, R. The Performance of Hybrid Density Functionals in Solid State Chemistry. In *Structure and Bonding*; Springer-Verlag Berlin Heidelberg, 2004; Vol. 113, p 171.

Chapter II. Theoretical and experimental methods

- (29) Delle Piane, M.; Corno, M.; Orlando, R.; Dovesi, R.; Ugliengo, P. Elucidating the Fundamental Forces in Protein Crystal Formation: The Case of Crambin. *Chem. Sci.* **2016**, *7*, 1496–1507.
- (30) Tasker, P. W. The Stability of Ionic Crystal Surfaces. *J. Phys. C Solid State Phys.* **1979**, *12*, 4977–4984.
- (31) Liu, L.; Zhuang, Z.; Xie, T.; Wang, Y.-G.; Li, J.; Peng, Q.; Li, Y. Shape Control of CdSe Nanocrystals with Zinc Blende Structure. *J. Am. Chem. Soc.* **2009**, *131* (45), 16423–16429.
- (32) Dovesi, R.; Saunders, V. R.; Roetti, C.; Orlando, R.; Zicovich-Wilson, C. M.; Pascale, F.; Civalleri, B.; Doll, K.; Harrison, N. M.; Bush, I. J.; et al. Crystal09 User's Manual. Università di Torino: Torino 2013.
- (33) Dovesi, R.; Orlando, R.; Civalleri, B.; Roetti, C.; Saunders, V. R.; Zicovich-Wilson, C. M. CRYSTAL : A Computational Tool for the Ab Initio Study of the Electronic Properties of Crystals. *Zeitschrift für Krist. - Cryst. Mater.* **2005**, *220*, 571–573.
- (34) Dovesi, R.; Saunders, V. R.; Roetti, C.; Orlando, R.; Zicovich-Wilson, C. M.; Pascale, F.; Civalleri, B.; Doll, K.; Harrison, N. M.; Bush, I. J.; et al. CRYSTAL14 - User's Manual. **2014**.
- (35) Hamann, D.; Schlüter, M.; Chiang, C. Norm-Conserving Pseudopotentials. *Phys. Rev. Lett.* **1979**, *43* (20), 1494–1497.
- (36) Bachelet, G. B.; Hamann, D. R.; Schluter, M. Pseudopotentials That Work: From H to Pu. *Phys. Rev. B* **1982**, *26* (8), 4199.
- (37) Vanderbilt, D. Soft Self-Consistent Pseudopotentials in a Generalized Eigenvalue Formalism. *Phys. Rev. B* **1990**, *41* (11), 7892–7895.
- (38) Blöchl, P. E. Projector Augmented-Wave Method. *Phys. Rev. B* **1994**, *50* (24), 17953–17979.
- (39) Ithurria, S.; Bousquet, G.; Dubertret, B. Continuous Transition from 3D to 1D Confinement Observed during the Formation of CdSe Nanoplatelets. *J. Am. Chem. Soc.* **2011**, *133* (9), 3070–3077.
- (40) Ithurria Lhuillier, S. Synthèses et Caractérisations de Nanoparticules de Semiconducteurs II-VI de Géométries Contrôlées, Université Pierre et Marie Curie - Paris VI, 2010.
- (41) Ithurria, S.; Tessier, M. D.; Mahler, B.; Lobo, R. P. S. M.; Dubertret, B.; Efros, A. L. Colloidal Nanoplatelets with Two-Dimensional Electronic Structure. *Nat. Mater.* **2011**, *10* (12), 936–941.
- (42) Tessier, M. D.; Javaux, C.; Maksimovic, I.; Lorette, V.; Dubertret, B. Spectroscopy of Single CdSe Nanoplatelets. *ACS Nano* **2012**, *6* (8), 6751–6758.
- (43) Achtstein, A. W.; Schliwa, A.; Prudnikau, A.; Hardzei, M.; Artemyev, M. V.; Thomsen, C.; Woggon, U. Electronic Structure and Exciton-Phonon Interaction in Two-Dimensional Colloidal CdSe Nanosheets. *Nano Lett.* **2012**, *12* (6), 3151–3157.
- (44) Guzelturk, B.; Martinez, P. L. H.; Zhang, Q.; Xiong, Q.; Sun, H.; Sun, X. W.; Govorov, A. O.; Demir, H. V. Excitonics of Semiconductor Quantum Dots and Wires for Lighting and Displays. *Laser Photon. Rev.* **2014**, *8* (1), 73–93.
- (45) Li, M.; Zhi, M.; Zhu, H.; Wu, W.-Y.; Xu, Q.-H.; Jhon, M. H.; Chan, Y. Ultralow-Threshold Multiphoton-Pumped Lasing from Colloidal Nanoplatelets in Solution. *Nat. Commun.* **2015**, *6*, 8513.
- (46) Szemjonov, A.; Pauporté, T.; Ithurria, S.; Lequeux, N.; Dubertret, B.; Ciofini, I.; Labat, F. Ligand-Stabilized CdSe Nanoplatelet Hybrid Structures with Tailored Geometric and Electronic Properties. New Insights from Theory. *RSC Adv.* **2014**, *4* (99), 55980–55989.
- (47) Ithurria, S.; Dubertret, B. Quasi 2D Colloidal CdSe Platelets with Thicknesses Controlled at the Atomic Level. *J. Am. Chem. Soc.* **2008**, *130* (49), 16504–16505.
- (48) Ithurria, S.; Talapin, D. V. Colloidal Atomic Layer Deposition (c-ALD) Using Self-Limiting Reactions at Nanocrystal Surface Coupled to Phase Transfer between Polar and Nonpolar Media. *J. Am. Chem. Soc.* **2012**, *134* (45), 18585–18590.
- (49) Flamee, S.; Cirillo, M.; Abe, S.; De Nolf, K.; Gomes, R.; Aubert, T.; Hens, Z. Fast, High Yield, and High Solid Loading Synthesis of Metal Selenide Nanocrystals. *Chem. Mater.* **2013**, *25* (12), 2476–2483.
- (50) Sun, X.; Zhang, H.; Xu, J.; Zhao, Q.; Wang, R.; Yu, D. Shape Controllable Synthesis of ZnO Nanorod Arrays via Vapor Phase Growth. *Solid State Commun.* **2004**, *129* (12), 803–807.
- (51) Chen, J.; Zhang, H.; Liu, P.; Wang, Y.; Liu, X.; Li, G.; An, T.; Zhao, H. Vapor-Phase Hydrothermal Synthesis of Rutile TiO₂ Nanostructured Film with Exposed Pyramid-Shaped (111) Surface and Superiorly Photoelectrocatalytic Performance. *J. Colloid Interface Sci.* **2014**, *429*, 53–61.
- (52) Wu, J.-J.; Liu, S.-C. Low-Temperature Growth of Well-Aligned ZnO Nanorods by Chemical Vapor Deposition. *Adv. Mater.* **2002**, *14* (3), 215–218.
- (53) Wu, J. M.; Shih, H. C.; Wu, W. T.; Tseng, Y. K.; Chen, I. C. Thermal Evaporation Growth and the Luminescence Property of TiO₂ Nanowires. *J. Cryst. Growth* **2005**, *281* (2-4), 384–390.
- (54) Berhe, S. a; Nag, S.; Molinets, Z.; Youngblood, W. J. Influence of Seeding and Bath Conditions in Hydrothermal Growth of Very Thin (~20 Nm) Single-Crystalline Rutile TiO₂ Nanorod Films. *ACS Appl. Mater. Interfaces* **2013**, *5* (4), 1181–1185.

Chapter II. Theoretical and experimental methods

- (55) Sussha, A. S.; Lutich, A. a; Liu, C.; Xu, H.; Zhang, R.; Zhong, Y.; Wong, K. S.; Yang, S.; Rogach, A. L. Comparative Optical Study of Colloidal Anatase Titania Nanorods and Atomically Thin Wires. *Nanoscale* **2013**, 5 (4), 1465–1469.
- (56) Miao, L.; Tanemura, S.; Toh, S.; Kaneko, K.; Tanemura, M. Heating-Sol-Gel Template Process for the Growth of TiO₂ Nanorods with Rutile and Anatase Structure. *Appl. Surf. Sci.* **2004**, 238 (1-4 SPEC. ISS.), 175–179.
- (57) Shao, Z.; Zhu, W.; Li, Z.; Yang, Q.; Wang, G. One-Step Fabrication of CdS Nanoparticle-Sensitized TiO₂ Nanotube Arrays via Electrodeposition. *J. Phys. Chem. C* **2012**, 116 (3), 2438–2442.
- (58) Besra, L.; Liu, M. A Review on Fundamentals and Applications of Electrophoretic Deposition (EPD). *Prog. Mater. Sci.* **2007**, 52 (1), 1–61.
- (59) Liang, Y. C.; Wang, C. C.; Kei, C. C.; Hsueh, Y. C.; Cho, W. H.; Perng, T. P. Photocatalysis of Ag-Loaded TiO₂ Nanotube Arrays Formed by Atomic Layer Deposition. *J. Phys. Chem. C* **2011**, 115 (19), 9498–9502.
- (60) Sui, R.; Rizkalla, A. S.; Charpentier, P. A. Formation of Titania Nanofibers: A Direct Sol-Gel Route in Supercritical CO₂. *Langmuir* **2005**, 21 (14), 6150–6153.
- (61) Soleimanzadeh, R.; Mousavi, M. S. S.; Mehrfar, A.; Esfahani, Z. K.; Kolahdouz, M.; Zhang, K. Sequential Microwave-Assisted Ultra-Fast ZnO Nanorod Growth on Optimized Sol-gel Seedlayers. *J. Cryst. Growth* **2015**, 426, 228–233.
- (62) Li, D.; Xia, Y. Fabrication of Titania Nanofibers by Electrospinning. *Nano Lett.* **2003**, 3 (4), 555–560.
- (63) Chuangchote, S.; Sagawa, T.; Yoshikawa, S. Electrospun TiO₂ Nanowires for Hybrid Photovoltaic Cells. *J. Mater. Res.* **2011**, 26 (17), 2316–2321.
- (64) Öztürk, S.; Kılınç, N.; Öztürk, Z. Z. Fabrication of ZnO Nanorods for NO₂ Sensor Applications: Effect of Dimensions and Electrode Position. *J. Alloys Compd.* **2013**, 581 (2), 196–201.
- (65) Greene, L. E.; Law, M.; Tan, D. H.; Montano, M.; Goldberger, J.; Somorjai, G.; Yang, P. General Route to Vertical ZnO Nanowire Arrays Using Textured ZnO Seeds. *Nano Lett.* **2005**, 5 (7), 1231–1236.
- (66) Weintraub, B.; Zhou, Z.; Li, Y.; Deng, Y. Solution Synthesis of One-Dimensional ZnO Nanomaterials and Their Applications. *Nanoscale* **2010**, 2 (9), 1573–1587.
- (67) Kenanakis, G.; Vernardou, D.; Koudoumas, E.; Katsarakis, N. Growth of c-Axis Oriented ZnO Nanowires from Aqueous Solution: The Decisive Role of a Seed Layer for Controlling the Wires' Diameter. *J. Cryst. Growth* **2009**, 311 (23-24), 4799–4804.
- (68) Kumar, N.; Mittal, H.; Reddy, L.; Nair, P.; Ngila, J. C.; Parashar, V. Morphogenesis of ZnO Nanostructures: Role of Acetate (COO⁻) and Nitrate (NO₃⁻) Ligand Donors from Zinc Salt Precursors in Synthesis and Morphology Dependent Photocatalytic Properties. *RSC Adv.* **2015**, 5 (48), 38801–38809.
- (69) Xu, S.; Wang, Z. L. One-Dimensional ZnO Nanostructures: Solution Growth and Functional Properties. *Nano Res.* **2011**, 4 (11), 1013–1098.
- (70) Song, J.; Lim, S. Effect of Seed Layer on the Growth of ZnO Nanorods. *J. Phys. Chem. C* **2007**, 111 (2), 596–600.
- (71) Deng, J.; Wang, M.; Song, X.; Liu, J. Controlled Synthesis of Aligned ZnO Nanowires and the Application in CdSe-Sensitized Solar Cells. *J. Alloys Compd.* **2014**, 588, 399–405.
- (72) Chevalier-César, C.; Capochichi-Gnambodoe, M.; Leprince-Wang, Y. Growth Mechanism Studies of ZnO Nanowire Arrays via Hydrothermal Method. *Appl. Phys. A* **2014**, 115 (3), 953–960.
- (73) Xu, C.; Shin, P.; Cao, L.; Gao, D. Preferential Growth of Long ZnO Nanowire Array and Its Application in Dye-Sensitized Solar Cells. *J. Phys. Chem. C* **2010**, 114, 125–129.
- (74) Ru, S.; Yahav, S.; Greenwald, S.; Zaban, A. Importance of Recombination at the TCO / Electrolyte Interface for High Efficiency Quantum Dot Sensitized Solar Cells. *J. Phys. Chem. C* **2012**, 116, 17473–17478.
- (75) Law, M.; Greene, L. E.; Johnson, J. C.; Saykally, R.; Yang, P. Nanowire Dye-Sensitized Solar Cells. *Nat. Mater.* **2005**, 4 (6), 455–459.
- (76) Govender, K.; Boyle, D. S.; Kenway, P. B.; O'Brien, P. Understanding the Factors That Govern the Deposition and Morphology of Thin Films of ZnO from Aqueous Solution. *J. Mater. Chem.* **2004**, 14 (16), 2575–2591.
- (77) Wu, W.; Hu, G.; Cui, S.; Zhou, Y.; Wu, H. Epitaxy of Vertical ZnO Nanorod Arrays on Highly (001)-Oriented ZnO Seed Monolayer by a Hydrothermal Route. *Cryst. Growth Des.* **2008**, 8 (11), 4014–4020.
- (78) Khun, K.; Ibupoto, Z. H.; Willander, M. Development of Fast and Sensitive Ultraviolet Photodetector Using P-Type NiO/n-Type TiO₂ Heterostructures. *Phys. Status Solidi* **2013**, 210 (12), 2720–2724.
- (79) Liu, B.; Aydil, E. S. Growth of Oriented Single-Crystalline Rutile TiO₂ Nanorods on Transparent Conducting Substrates for Dye-Sensitized Solar Cells. *J. Am. Chem. Soc.* **2009**, 131 (11), 3985–3990.

Chapter II. Theoretical and experimental methods

- (80) Huang, H.; Pan, L.; Lim, C. K.; Gong, H.; Guo, J.; Tse, M. S.; Tan, O. K. Hydrothermal Growth of TiO₂ Nanorod Arrays and in Situ Conversion to Nanotube Arrays for Highly Efficient Quantum Dot-Sensitized Solar Cells. *Small* **2013**, *9* (18), 3153–3160.
- (81) Bang, J. H.; Kamat, P. V. Solar Cells by Design: Photoelectrochemistry of TiO₂ Nanorod Arrays Decorated with CdSe. *Adv. Funct. Mater.* **2010**, *20* (12), 1970–1976.
- (82) Liao, M. Y.; Fang, L.; Xu, C. L.; Wu, F.; Huang, Q. L.; Saleem, M. Effect of Seed Layer on the Growth of Rutile TiO₂ Nanorod Arrays and Their Performance in Dye-Sensitized Solar Cells. *Mater. Sci. Semicond. Process.* **2014**, *24*, 1–8.
- (83) Kumar, A.; Madaria, A. R.; Zhou, C. Growth of Aligned Single-Crystalline Rutile TiO₂ Nanowires on Arbitrary Substrates and Their Application in Dye-Sensitized Solar Cells. *J. Phys. Chem. C* **2010**, *114* (17), 7787–7792.
- (84) Huang, Q.; Gao, L. A Simple Route for the Synthesis of Rutile TiO₂ Nanorods. *Chem. Lett.* **2003**, *32* (7), 638–639.
- (85) Li, J.; Ishigaki, T.; Sun, X. Anatase, Brookite, and Rutile Nanocrystals via Redox Reactions under Mild Hydrothermal Conditions: Phase-Selective Synthesis and Physicochemical Properties. *J. Phys. Chem. C* **2007**, *111*, 4969–4976.
- (86) Wells, A. F. *Structural Inorganic Chemistry*, 4th editio.; Clarendon Press: Oxford, 1975.
- (87) Kim, H.-S.; Lee, C.-R.; Im, J.-H.; Lee, K.-B.; Moehl, T.; Marchioro, A.; Moon, S.-J.; Humphry-Baker, R.; Yum, J.-H.; Moser, J. E.; et al. Lead Iodide Perovskite Sensitized All-Solid-State Submicron Thin Film Mesoscopic Solar Cell with Efficiency Exceeding 9%. *Sci. Rep.* **2012**, *2*, 591.
- (88) Kim, H.-S.; Lee, J.-W.; Yantara, N.; Boix, P. P.; Kulkarni, S. a; Mhaisalkar, S.; Grätzel, M.; Park, N.-G. High Efficiency Solid-State Sensitized Solar Cell-Based on Submicrometer Rutile TiO₂ Nanorod and CH₃NH₃PbI₃ Perovskite Sensitizer. *Nano Lett.* **2013**, *13* (6), 2412–2417.
- (89) Colvin, V. L.; Goldstein, A. N.; Alvisatos, P. Semiconductor Nanocrystals Covalently Bound to Metal Surfaces with Self-Assembled Monolayers. *J. Am. Chem. Soc.* **1992**, *114*, 5221–5230.
- (90) Blackburn, J. L.; Selmarten, D. C.; Nozik, A. J. Electron Transfer Dynamics in Quantum Dot/Titanium Dioxide Composites Formed by in Situ Chemical Bath Deposition. *J. Phys. Chem. B* **2003**, *107* (51), 14154–14157.
- (91) Yashar, A. K.; Muradov, M. B.; Mammedov, R. K.; Khodayari, A. Growth Process and Investigation of Some Physical Properties of CdS Nanocrystals Formed in Polymer Matrix by Successive Ionic Layer Adsorption and Reaction (SILAR) Method. *J. Cryst. Growth* **2007**, *305* (1), 175–180.
- (92) Lee, Y. H.; Im, S. H.; Lee, J.-H.; Seok, S. Il. Porous CdS-Sensitized Electrochemical Solar Cells. *Electrochim. Acta* **2011**, *56* (5), 2087–2091.
- (93) Zhu, L.; An, W.-J.; Springer, J. W.; Modesto-Lopez, L. B.; Gullapalli, S.; Holten, D.; Wong, M. S.; Biswas, P. Linker-Free Quantum Dot Sensitized TiO₂ Photoelectrochemical Cells. *Int. J. Hydrogen Energy* **2012**, *37*, 6422–6430.
- (94) Guijarro, N.; Lana-Villarreal, T.; Mora-Sero, I.; Bisquert, J.; Gomez, R. CdSe Quantum Dot-Sensitized TiO₂ Electrodes: Effect of Quantum Dot Coverage and Mode of Attachment. *J. Phys. Chem. C* **2009**, *113*, 4208–4214.
- (95) Fuke, N.; Hoch, L. B.; Koposov, A. Y.; Manner, V. W.; Werder, D. J.; Fukui, A.; Koide, N.; Katayama, H.; Sykora, M. CdSe Quantum-Dot-Sensitized Solar Cell with Similar to 100% Internal Quantum Efficiency. *ACS Nano* **2010**, *4* (11), 6377–6386.
- (96) Mora-Seró, I.; Giménez, S.; Moehl, T.; Fabregat-Santiago, F.; Lana-Villareal, T.; Gómez, R.; Bisquert, J. Factors Determining the Photovoltaic Performance of a CdSe Quantum Dot Sensitized Solar Cell: The Role of the Linker Molecule and of the Counter Electrode. *Nanotechnology* **2008**, *19* (424007), 1–7.
- (97) Jun, H. K.; Careem, M. a.; Arof, a. K. Quantum Dot-Sensitized Solar Cells—perspective and Recent Developments: A Review of Cd Chalcogenide Quantum Dots as Sensitizers. *Renew. Sustain. Energy Rev.* **2013**, *22*, 148–167.
- (98) Robel, I.; Subramanian, V.; Kuno, M.; Kamat, P. V. Quantum Dot Solar Cells. Harvesting Light Energy with CdSe Nanocrystals Molecularly Linked to Mesoscopic TiO₂ Films. *J. Am. Chem. Soc.* **2006**, *128* (7), 2385–2393.
- (99) Bakkers, E. P. a. M.; Roest, a. L.; Marsman, a. W.; Jenneskens, L. W.; de Jong-van Steensel, L. I.; Kelly, J. J.; Vanmaekelbergh, D. Characterization of Photoinduced Electron Tunneling in Gold/SAM/Q-CdSe Systems by Time-Resolved Photoelectrochemistry. *J. Phys. Chem. B* **2000**, *104* (31), 7266–7272.
- (100) Adams, D. M.; Brus, L.; Chidsey, C. E. D.; Creager, S.; Creutz, C.; Kagan, C. R.; Kamat, P. V.; Lieberman, M.; Lindsay, S.; Marcus, R. a.; et al. Charge Transfer on the Nanoscale: Current Status. *J. Phys. Chem. B* **2003**, *107* (28), 6668–6697.

Chapter II. Theoretical and experimental methods

- (101) Dibbell, R. S.; Watson, D. F. Distance-Dependent Electron Transfer in Tethered Assemblies of CdS Quantum Dots and TiO₂ Nanoparticles. *J. Phys. Chem. C* **2009**, *113* (22), 13511–13519.
- (102) Marcus, R. A.; Sutin, N. Electron Transfers in Chemistry and Biology. *Biochim. Biophys. Acta - Rev. Bioenerg.* **1985**, *811*, 265–322.
- (103) Yun, H. J.; Paik, T.; Edley, M. E.; Baxter, J. B.; Murray, C. B. Enhanced Charge Transfer Kinetics of CdSe Quantum Dot-Sensitized Solar Cell by Inorganic Ligand Exchange Treatments. *ACS Appl. Mater. Interfaces* **2014**, *6* (5), 3721–3728.
- (104) Zhang, X.; Zhang, Y.; Wu, H.; Yan, L.; Wang, Z.; Zhao, J.; Yu, W. W.; Rogach, A. L. PbSe Quantum Dot Films with Enhanced Electron Mobility Employed in Hybrid Polymer/nanocrystal Solar Cells. *RSC Adv.* **2016**, *6* (21), 17029–17035.
- (105) Li, H.; Zhitomirsky, D.; Dave, S.; Grossman, J. C. Towards the Ultimate Limit of Connectivity in Quantum Dots with High Mobility and Clean Gaps. *ACS Nano* **2016**, *10*, 606–614.
- (106) Zhang, Z.; Yang, J.; Wen, X.; Yuan, L.; Shrestha, S.; Stride, J. A.; Conibeer, G. J.; Patterson, R. J.; Huang, S. Effect of Halide Treatments on PbSe Quantum Dot Thin Films: Stability, Hot Carrier Lifetime, and Application to Photovoltaics. *J. Phys. Chem. C* **2015**, *119* (42), 24149–24155.
- (107) Bryant, G. W.; Jaskolski, W. Surface Effects on Capped and Uncapped Nanocrystals. *J. Phys. Chem. B* **2005**, *109* (42), 19650–19656.
- (108) Leschkes, K. S.; Divakar, R.; Basu, J.; Enache-Pommer, E.; Boercker, J. E.; Carter, C. B.; Kortshagen, U. R.; Norris, D. J.; Aydil, E. S. Photosensitization of ZnO Nanowires with CdSe Quantum Dots for Photovoltaic Devices. *Nano Lett.* **2007**, *7* (6), 1793–1798.
- (109) Nag, A.; Kovalenko, M. V.; Lee, J.-S.; Liu, W.; Spokoyny, B.; Talapin, D. V. Metal-Free Inorganic Ligands for Colloidal Nanocrystals : S²⁻, HS⁻, Te²⁻, HTe⁻, TeS₃²⁻, OH⁻ and NH₂⁻ as Surface Ligands. *J. Am. Chem. Soc.* **2011**, *133*, 10612–10620.
- (110) Pan, Z.; Mora-Seró, I.; Shen, Q.; Zhang, H.; Li, Y.; Zhao, K.; Wang, J.; Zhong, X.; Bisquert, J. High-Efficiency “green” quantum Dot Solar Cells. *J. Am. Chem. Soc.* **2014**, *136* (25), 9203–9210.
- (111) Ahmed, R.; Zhao, L.; Mozer, A. J.; Will, G.; Bell, J.; Wang, H. Enhanced Electron Lifetime of CdSe/CdS Quantum Dot (QD) Sensitized Solar Cells Using ZnSe Core-Shell Structure with Efficient Regeneration of Quantum Dots. *J. Phys. Chem. C* **2015**, *119* (5), 2297–2307.
- (112) Alberio, J.; Clifford, J. N.; Palomares, E. Quantum Dot Based Molecular Solar Cells. *Coord. Chem. Rev.* **2014**, *263-264* (1), 53–64.
- (113) Lee, H.; Wang, M.; Chen, P.; Gamelin, D. R.; Zakeeruddin, S. M.; Grätzel, M.; Nazeeruddin, M. K. Efficient CdSe Quantum Dot-Sensitized Solar Cells Prepared by an Improved Successive Ionic Layer Adsorption and Reaction Process. *Nano Lett.* **2009**, *9* (12), 4221–4227.
- (114) Zhang, R.; Luo, Q.-P.; Chen, H.-Y.; Yu, X.-Y.; Kuang, D.-B.; Su, C.-Y. CdS/CdSe Quantum Dot Shell Decorated Vertical ZnO Nanowire Arrays by Spin-Coating-Based SILAR for Photoelectrochemical Cells and Quantum-Dot-Sensitized Solar Cells. *Chemphyschem* **2012**, *13* (6), 1435–1439.
- (115) Senthamilselvi, V.; Saravanakumar, K.; Jabena Begum, N.; Anandhi, R.; Ravichandran, A. T.; Sakthivel, B.; Ravichandran, K. Photovoltaic Properties of Nanocrystalline CdS Films Deposited by SILAR and CBD Techniques-a Comparative Study. *J. Mater. Sci. Mater. Electron.* **2012**, *23* (1), 302–308.
- (116) Rühle, S.; Shalom, M.; Zaban, A. Quantum-Dot-Sensitized Solar Cells. *Chemphyschem* **2010**, *11*, 2290–2304.
- (117) Klayman, D. L.; Griffin, T. S. Reaction of Selenium with Sodium Borohydride in Protic Solvents. A Facile Method for the Introduction of Selenium into Organic Molecules. *J. Am. Chem. Soc.* **1973**, *2* (1), 197–199.
- (118) Snaith, H. J.; Grätzel, M. Enhanced Charge Mobility in a Molecular Hole Transporter via Addition of Redox Inactive Ionic Dopant: Implication to Dye-Sensitized Solar Cells. *Appl. Phys. Lett.* **2006**, *89* (26), 2004–2007.
- (119) Snaith, H. J.; Humphry-Baker, R.; Chen, P.; Cesar, I.; Zakeeruddin, S. M.; Grätzel, M. Charge Collection and Pore Filling in Solid-State Dye-Sensitized Solar Cells. *Nanotechnology* **2008**, *19* (42), 424003.
- (120) Krüger, J.; Plass, R.; Cevey, L.; Piccirelli, M.; Grätzel, M.; Bach, U. High Efficiency Solid-State Photovoltaic Device due to Inhibition of Interface Charge Recombination. *Appl. Phys. Lett.* **2001**, *79* (13), 2085–2087.
- (121) Jennings, J. R.; Wang, Q. Influence of Lithium Ion Concentration on Electron Injection, Transport, and Recombination in Dye-Sensitized Solar Cells. *J. Phys. Chem. C* **2010**, *114* (3), 1715–1724.
- (122) Cappel, U. B.; Smeigh, A. L.; Plogmaker, S.; Johansson, E. M. J.; Rensmo, H.; Hammarström, L.; Hagfeldt, A.; Boschloo, G. Characterization of the Interface Properties and Processes in Solid State Dye-Sensitized Solar Cells Employing a Perylene Sensitizer. *J. Phys. Chem. C* **2011**, *115* (10), 4345–4358.
- (123) Jiao, S.; Shen, Q.; Mora-Sero, I.; Wang, J.; Pan, Z.; Zhao, K.; Kuga, Y.; Zhong, X.; Bisquert, and J. Band

Chapter II. Theoretical and experimental methods

Engineering in Core / Shell ZnTe / CdSe for Photovoltage and Efficiency Enhancement in Exciplex Quantum Dot Sensitized Solar Cells. *ACS Nano* **2015**, 9 (1), 908–915.

III.1. Context

Before building theoretical models of CdSe sensitizers and calculating their relevant properties for photovoltaic applications, it was necessary to define a computational protocol that accurately describes its bulk and surface structural and electronic properties, at a reasonable computational cost. Concerning previous theoretical works on CdSe, Wang et al gave a detailed description of the relaxation and the electronic structure of CdSe bulk crystals in both wurtzite and zinc blende phases, as well as the (10-10) and (11-20) cleavage surfaces¹ using an sp^3 semi-empirical tight-binding model, and validated their theoretical investigation by comparing their results to bulk optical and X-ray photoemission data. Later, the same systems were examined at different approximations within the density functional theory (DFT) framework.²⁻⁵ Although these studies provided an accurate geometric description, band gaps were severely underestimated in most of the cases. Indeed, it is well-known that local density approximation (LDA) and generalized gradient approximation (GGA) functionals such as those applied in these early studies significantly underestimate band gaps due to the self-interaction problem.⁶ However, hybrid functionals containing a portion of exact Hartree-Fock exchange give a substantially better estimation,⁷ even though they are computationally more expensive than GGAs.⁸ Goddard et al demonstrated on a range of semiconductors, including CdSe that the global hybrid B3PW91 functional gives accurate band gaps with the chosen Gaussian-type orbital (GTO) basis set, and performs better than other popular hybrid functionals like B3LYP.⁹ It is noteworthy that although hybrid functionals can be used with plane-wave (PW) basis sets as well, calculations remain so far computationally much more expensive.¹⁰ On the other hand, when combined with Gaussian-type basis sets, hybrids can efficiently be applied to periodic systems,^{11,12} even to very large ones.¹³

In this chapter, several combinations of GTO basis sets and exchange-correlation functional, (both GGAs and hybrids) are tested with the CRYSTAL09 coded^{14,15} in order to define the best performing computational protocol based on the comparison of geometrical and electronic properties to available experimental data for the bulk crystal of CdSe. In selected

Chapter III. Bulk and surface properties of CdSe

cases, for further validation of the calculations using GTO basis sets, additional projector-augmented wave (PAW) calculations were carried out. Next, we show the ability of the so-defined method to simulate not only the bulk properties, but also wurtzite nanocrystals exposing their nonpolar (10-10) surface.

III.2. Computational details

Three types of GTO basis sets have been mainly used. As previously described for CdSe,⁹ when needed, basis sets were modified by setting exponents inferior to 0.10 to this value.

- The first basis set, denoted as AE, is an all-electron basis set with a (27s,18p,10d)→[6s,5p,3d] contraction scheme for Cd¹⁶ and a (27s,18p,6d)→[6s,5p,2d] one for Se atoms.¹⁷
- The second one (SBKJC) applies the SBKJC small-core effective core potential (ECP) with double-zeta valence basis set for Cd¹⁸ and the SBKJC large-core ECP with double-zeta basis set¹⁸ augmented by one d polarization function¹⁹ for Se. The following electrons are treated explicitly: 4s² 4p⁶ 4d¹⁰ 5s² for Cd and 4s² 4p⁴ for Se.
- The third one (RSC) uses small-core relativistic effective core potentials (RECP) with modified (abbreviated as m-) double zeta valence basis sets: m-Stuttgart RSC 1997 ECP for Cd and m-cc-pVDZ-pp for Se, as detailed in ref. 20. The 4s² 4p⁶ 4d¹⁰ 5s² electrons are treated explicitly for Cd and the 3s² 3p⁶ 3d¹⁰ 4s² 4p⁴ electrons for Se.

To further validate these double-zeta plus polarization basis sets, in some selected bulk cases, we also performed additional calculations with: (i) modified def2-TZVP basis sets, following the strategy mentioned above for exponents lower than 0.10; (ii) a PAW basis set with a 500 eV energy cut-off, and pseudopotentials with 12 and 6 explicit electrons for Cd and Se, respectively, using VASP.^{21–24} These calculations are referred to as def2 and PAW in the following.

Several density functional theory (DFT) approaches with exchange-correlation functionals based on the generalized gradient approximation, (PBE, BLYP, BPW91), as well as some global hybrid HF/KS functionals (PBE0, B3LYP, B3PW91) have been tested. Dispersion forces may play an important role in the packing of crystals, and they are expected to be relevant

Chapter III. Bulk and surface properties of CdSe

when comparing the relative stability of different phases.^{25,26} However, a drawback of common functionals, such as GGAs and hybrids, is that they do not correctly describe long-range electron correlation that is responsible for these interactions.^{27,28} In order to study the effect of dispersion forces on the results obtained, an empirical London-type correction was introduced in the calculations (according to the DFT-D2 scheme, as proposed by Grimme²⁹) in the case of hybrid functionals, for which we expect the most accurate description of electronic properties. This modification of the selected functionals is denoted as PBE0-D, B3LYP-D and B3PW91-D.

An extra-large DFT integration grid, consisting of 75 radial and 974 angular points, was applied in order to provide accurate results for calculations on CdSe compounds. The following truncation criteria (ITOL parameters)¹⁴ were set for the accuracy of the Coulomb and exchange series: 10^{-7} as the overlap threshold for Coulomb integrals, 10^{-7} as the penetration threshold for Coulomb integrals, 10^{-7} as the overlap threshold for HF exchange integrals, and 10^{-9} and 10^{-20} as the pseudo-overlap for HF exchange series. For both bulk and surface calculations, a Monkhorst-Pack shrinking factor³⁰ of 6 has been applied, which corresponds to 28 (16) k points in the irreducible Brillouin zone (IBZ) of the wurtzite (zinc blende) phase of the bulk, and 16 k points in the IBZ of the wurtzite (10-10) surface.

For surface properties calculations, we adopted the slab model, which was described in **Chapter II**. Only atoms were allowed to relax during geometry optimization. The convergence of calculated properties (structure, energy and electronic properties) as a function of the slab thickness has been monitored. Surface formation energy was calculated according to *Equation III.1*:

$$E_{n,s} = \frac{E_n - n \cdot (E_n - E_{n-1})}{2A} \quad \text{III.1.}$$

where n is the number of layers in the slab, $E_{n,s}$ is the calculated surface formation energy for an n -layer slab, A is the area of the primitive surface unit cell, and E_n and E_{n-1} are the total energies of an n - and $(n-1)$ -layer slab, respectively. As the number of layers increases, $(E_n - E_{n-1})$ converges to the total energy of a one layer thick part of the bulk crystal (E_{bulk}), and $E_{n,s}$ converges to the surface formation energy per unit area.

III.3. Bulk properties of CdSe

III.3.1. Structural features

Under atmospheric conditions, CdSe exists in two phases: the hexagonal wurtzite structure and the cubic zinc blende structure.³¹ Cd and Se are tetraordinated in both structures. The hexagonal wurtzite structure, belonging to the $P6_3mc$ space group, is characterized by alternating layers positioned directly above each other in an A, B, A, B... arrangement along the [001] axis. In the face-centered cubic zinc blende structure, which belongs to the $Fm\bar{3}m$ space group, every fourth layer is positioned above each other in an A, B, C, A, B, C ... arrangement along the [111] axis (see *Figure III.1.*). This subtle structural difference, which appears only from the second coordination sphere, results in different physical properties of the two polytypes.

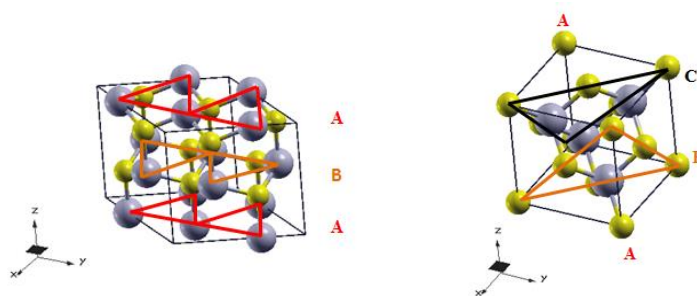


Figure III.1. Packing of layers in the primitive cell of the wurtzite (left) and zinc blende (right) crystal structures. Cd and Se atoms are shown as grey and yellow spheres, respectively.

The optimized geometrical parameters of the CdSe wurtzite and zinc blende crystals obtained with our calculations, compared with previously published experimentally and computationally obtained data are reported in *Table III.1*. It can be seen that nearly all combinations of exchange-correlation functionals and basis sets (except for some of the methods containing dispersion corrections) slightly overestimate the lattice constants but they provide very similar u wurtzite internal parameters that approximate the ideal value of $3/8 = 0.375^3$ in each case.

Chapter III. Bulk and surface properties of CdSe

method	basis set	wurtzite			zinc blende
		<i>a</i>	<i>c</i>	<i>u</i>	<i>a</i>
PBE	AE	4.482	7.245	0.377	6.313
	SBKJC	4.426	7.204	0.376	6.252
	RSC	4.392	7.160	0.376	6.207
	RSC	4.392	7.160	0.376	6.207
	def2	4.393	7.159	0.376	6.211
	PAW	4.388	7.169	0.375	6.205
BLYP	AE	4.546	7.376	0.376	6.411
	SBKJC	4.499	7.341	0.376	6.360
	RSC	4.475	7.313	0.375	6.327
BPW91	AE	4.482	7.268	0.377	6.317
	SBKJC	4.432	7.210	0.376	6.259
	RSC	4.396	7.165	0.376	6.212
PBE0	AE	4.447	7.182	0.377	6.263
	SBKJC	4.391	7.135	0.376	6.199
	RSC	4.348	7.083	0.376	6.148
PBE0-D	AE	4.380	6.996	0.378	6.148
	SBKJC	4.312	6.949	0.377	6.072
	RSC	4.263	6.904	0.376	6.011
B3LYP	AE	4.500	7.297	0.376	6.345
	SBKJC	4.452	7.256	0.376	6.290
	RSC	4.418	7.220	0.375	6.249
B3LYP-D	AE	4.429	7.134	0.377	6.232
	SBKJC	4.369	7.090	0.376	6.165
	RSC	4.331	7.043	0.376	6.115
B3PW91	AE	4.457	7.205	0.377	6.278
	SBKJC	4.404	7.256	0.376	6.218
	RSC	4.365	7.112	0.376	6.167
B3PW91-D	AE	4.388	7.024	0.378	6.162
	SBKJC	4.323	6.979	0.377	6.090
	RSC	4.277	6.930	0.376	6.033
CA/GTO ³²		4.21	6.86		
CA/FP-LAPW ³³					6.018
PBE/PAW ³		4.299	7.012	0.376	6.077
EV-GGA/FP-LAPW ³⁴		4.34	7.27		
PBE/FP-LAPW ³³					6.197
HSE/GTO ³⁵					6.152
experimental		4.300 ³⁶	7.011 ³⁶	0.375 ³⁷	6.052 ³⁶

Table III.1. Experimental and computed lattice and internal (*u*, the fractional coordinate of the Se atoms along the *c* axis) parameters (in Å) of the CdSe wurtzite and zinc blende phases calculated with different exchange-correlation functionals and basis sets. For each functional, the best results (with respect to experimental data) are given in bold.

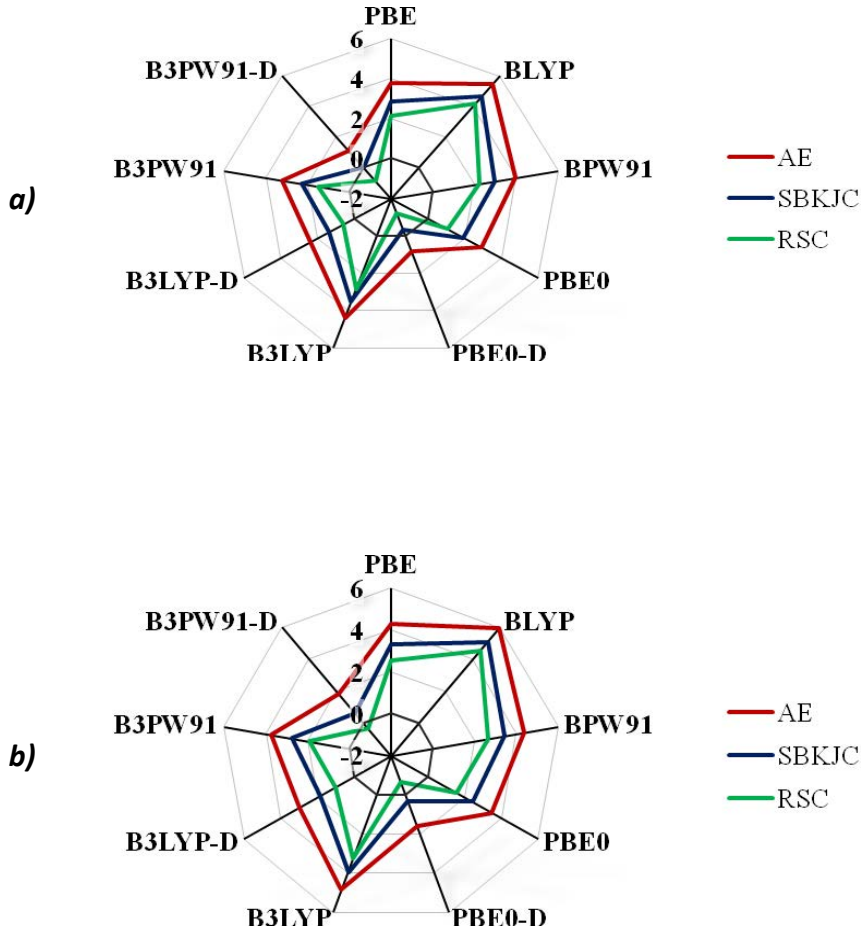


Figure III.2. Computed average deviation (in %) of CdSe bulk lattice parameters with respect to experimental data: a) wurtzite a and c parameters and b) zinc blende a parameter.

In order to visualize the the differences (in %) between computed GTO lattice parameters and experimental data for the two CdSe polytypes, radar charts are reported in *Figure III.2*. It can be seen from the charts that results obtained with the RSC basis set are the closest to the experimental values in each case, followed by the SBKJC and the AE, although we have to stress that the differences between these offsets are very small (for example, 0.85% between the AE and SBKJC and 0.65% between the SBKJC and RSC basis sets in the case of the B3LYP functional for the wurtzite polytype). In addition, we note that computed def2-TZVP data are very close to the RSC and PAW values, the discrepancy with the SBKJC data being only slightly larger. This further validates our choice of double-zeta plus polarization quality GTO basis sets for the bulk study.

Chapter III. Bulk and surface properties of CdSe

Regarding the exchange-correlation functionals, it is known that LDA functionals underestimate lattice parameters, while GGA functionals overestimate them,^{38,39} which is reflected by the comparison between our computed results and previously published theoretical and experimental data reported in *Table III.1* and *Figure III.2*. Regarding the performance of hybrid functionals, it has already been shown for the description of the properties of the cubic CdSe bulk crystal that the B3PW91 functional considerably outperforms the most popular B3LYP.⁹ Our investigation confirms this result, and shows that the same holds for the hexagonal phase. Also, we should note that the PBE0 functional performs very similarly to B3PW91. The inclusion of dispersion forces improved the accuracy of all the hybrid functionals as it decreased the overestimated lattice parameters. Overall, it should be noted that all methods tested in this study provide a fairly good geometrical description of the bulk crystal of CdSe, with lattice parameters never exceeding or underestimating the experimental data by more than 6%.

III.3.2. Energetic and electronic properties

Experimentally, the total energy per unit cell of the wurtzite and zinc blende phases of bulk CdSe are very close. Indeed, depending on experimental parameters, any of the two phases can be prepared at ambient pressure.^{40–42} Several theoretical works predict that the zinc blende phase is slightly more stable (by 1.4–2.9 meV/atom),^{3,43} although wurtzite has also been reported to be the more stable phase.^{2,44} Experimentally, the zinc blende phase is more stable at low temperatures, and it transforms into wurtzite above a critical temperature (95±5 °C).⁴⁵ Nevertheless, to our knowledge, no experimental reference on their relative total energies exists. In this study, we computed the difference between the total energy per unit cell of the CdSe bulk crystal in the wurtzite and in the zinc blende phases with all basis set-DFT functional combinations. These values defined as:

$$\Delta E_{\text{wz-zb}} = E_{\text{wz}}(\text{total}) - E_{\text{zb}}(\text{total}) \quad (\text{III.2.})$$

are reported in *Table III.2*. It is observed that while the hybrid functionals including dispersion corrections predicted higher stability for the wurtzite phase in each case, the other methods gave variable results on the relative stability of the two polytypes, the absolute value of the $\Delta E_{\text{wz-zb}}$ energy differences being always very small, in the order of less than 9 meV/atom.

Chapter III. Bulk and surface properties of CdSe

method	basis set	$E_{gap}(\text{wurtzite})$	$E_{gap}(\text{zinc blende})$	$\Delta E_{\text{Wz-zb}}$
PBE	AE	1.171	1.164	-3.35
	SBKJC	0.776	0.714	0.10
	RSC	0.538	0.458	0.10
	RSC	0.538	0.458	0.10
	def2	0.759	0.700	0.10
	PAW	1.000	1.170	1.00
BLYP	AE	0.966	0.961	-2.64
	SBKJC	0.575	0.524	1.20
	RSC	0.309	0.263	1.01
BPW91	AE	1.169	1.161	-3.48
	SBKJC	0.767	0.705	-0.07
	RSC	0.520	0.767	0.03
PBE0	AE	2.775	2.780	0.46
	SBKJC	2.277	2.216	-1.47
	RSC	2.170	2.014	-0.45
PBE0-D	AE	2.913	2.937	-8.78
	SBKJC	2.457	2.384	-3.59
	RSC	2.194	2.122	-4.15
B3LYP	AE	2.216	2.210	-4.39
	SBKJC	1.745	1.694	0.19
	RSC	1.445	1.416	1.01
B3LYP-D	AE	2.392	2.402	-6.69
	SBKJC	1.938	1.877	-1.17
	RSC	1.649	1.601	-0.69
B3PW91	AE	2.412	2.415	-0.27
	SBKJC	1.920	1.862	-1.04
	RSC	1.761	1.719	-0.09
B3PW91-D	AE	2.552	2.568	-7.12
	SBKJC	2.100	2.027	-2.37
	RSC	1.911	1.834	-3.50
CA/GTO ³²		0.60		
CA/LAPW ⁴³				1.40
WC-GGA/FP-LAPW+lo ⁴⁶			0.40	
PBE/PAW ³		0.99	0.97	2.90
B3LYP/GTO ⁹			1.68	
HSE/GTO ⁹			1.39	
mBJ/FP-LAPW ⁴⁷		2.10		
experimental ¹³⁶		1.83	1.90	

Table III.2. Calculated and experimental band gaps (in eV) for the CdSe wurtzite and zinc blende structures and total energy difference (in meV/atom) between the wurtzite and zinc blende phases of bulk CdSe, obtained with different Hamiltonians and basis sets. For each Hamiltonian, the best results for band gaps (with respect to experimental value) are given in bold.

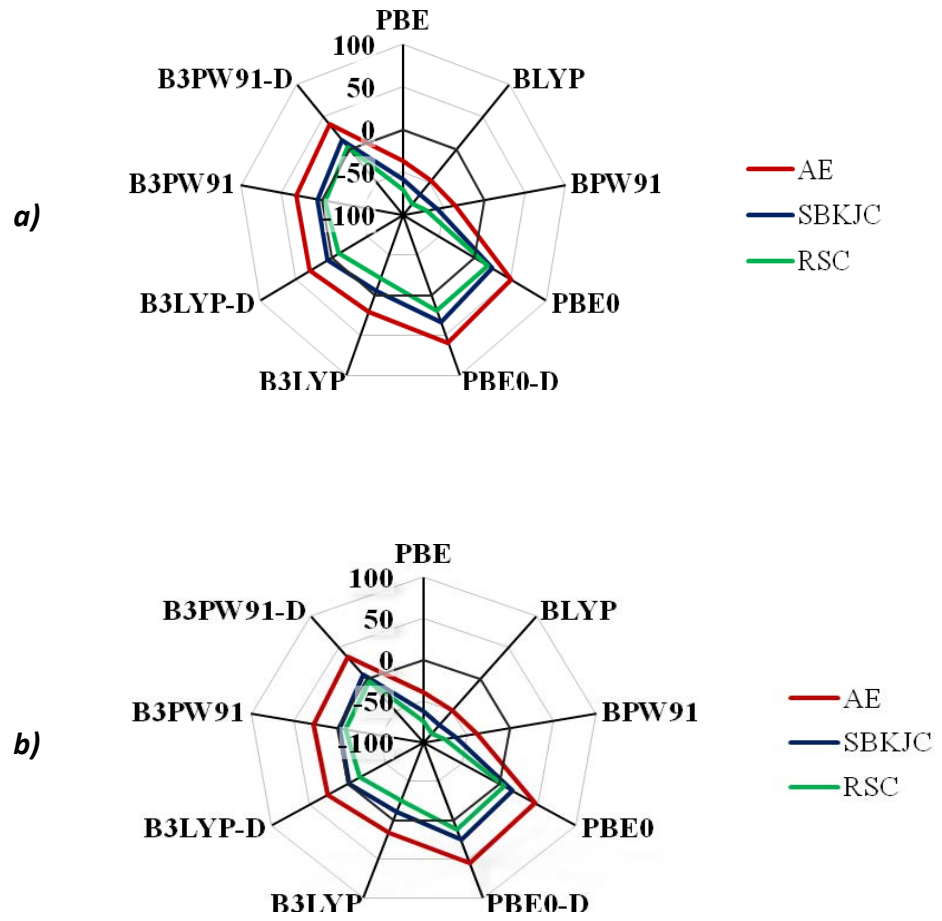


Figure III.3. Computed deviation (in %) of CdSe wurtzite (a) and zinc blende (b) bulk band gaps with respect to experimental data.

Table III.2 also lists the band gaps calculated with different methods, compared to previously published experimental and theoretical results. Figure III.2 shows radar charts of the computed differences between calculated and experimental band gaps of the two CdSe polytypes.³⁶ The general conclusions that can be drawn from Table III.2 and Figure III.3 are in line with previous theoretical studies on semiconductor band gaps. While LDA and GGA functionals underestimate band gaps^{9,32,48}, hybrid functionals give significantly better results.^{7,49} In addition, the PBE/SBKJC band gaps are in nice agreement with the def2-TZVP data, the discrepancy with PAW results being small, further outlining the quality of the SBKJC basis sets for CdSe bulk investigation.

Chapter III. Bulk and surface properties of CdSe

From the results collected in *Table III.2*, it can be noted that the London-type corrections increase the computed band gaps when comparing to the data obtained without the inclusion of dispersion forces. This leads to the high accuracy of band gaps calculated with the B3LYP-D/SBKJC and B3PW91-D/RSC methods. The first one differs only by 6.0% and -1.2% from the experimental band gap of wurtzite and zinc blende bulk crystals, respectively, while the latter gives corresponding deviations of 4.5% and -3.5%. Regarding the computational protocols not including any dispersion corrections, the B3PW91 functional combined with the SBKJC basis set gives the most accurate band gaps for both phases, with errors of 5.0% with respect to the experimental wurtzite and -2.0% with respect to the zinc blende values, which is comparable to the results obtained with the B3LYP-D/SBKJC and B3PW91-D/RSC methods. Of note, the B3PW91/SBKJC method is also extremely accurate in the prediction of geometrical parameters. For this reason, although the inclusion of dispersion forces globally improves the geometrical parameters, and in some cases, gives accurate band gaps, we did not use the empirical D2 correction scheme in further investigations, since an already satisfactory precision for both the geometrical and electronic properties is obtained with the B3PW91/SBKJC method. It was thus decided to use this protocol for calculations of surface properties, with two main points in mind: (i) the overall nice agreement of SBKJC data both with larger def2-TZVP basis sets and PAW results; (ii) the additional computational cost associated to the RSC and def2-TZVP basis sets, when compared to SBKJC. Indeed, although the SBKJC, RSC and def2-TZVP basis sets all have 20 explicit electrons for Cd, they correspond respectively to 6, 24 and 34 explicit electrons for Se. If we aim at modeling CdSe nanoparticles of realistic sizes for QDSC application (about 500 atoms are needed for spherical stoichiometric clusters for instance), compared to the SBKJC basis set, the RSC and def2-TZVP basis sets correspond to an increase in the number of explicit electrons to be treated of 4500 and 7000, respectively, making at least def2-TZVP calculations on large systems intractable. The use of the SBKJC basis set is therefore particularly appealing, especially if we focus on absorption spectra calculation with TD-DFT techniques, which are going to be particularly computationally-demanding for such large systems. In addition, a recent benchmark carried out on small (CdSe)₆ clusters with different DFT methods and basis sets⁵⁰ revealed that the SBKJC basis set was the best one in terms of accuracy and computational cost for geometrical parameters, vibrational normal modes and low-lying excitation energies, validating the use of the SBKJC basis set.

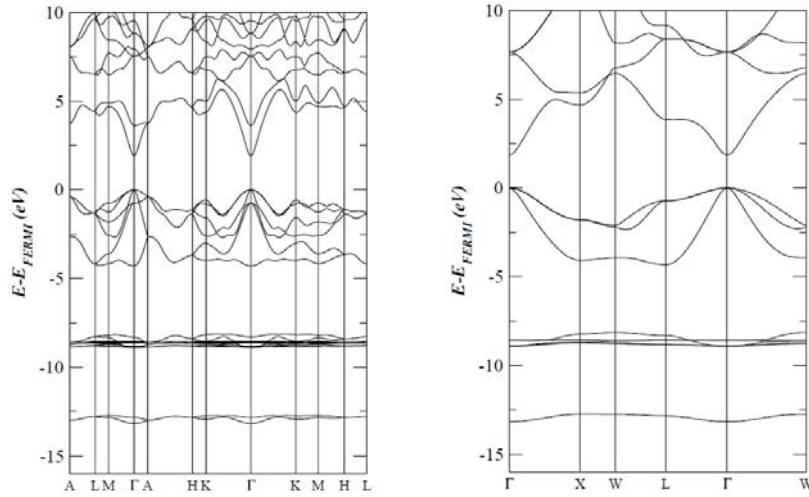


Figure III.4. Calculated band structure of the CdSe bulk wurtzite (left) and zinc blende (right) phase obtained with the B3PW91/SBKJC method. The Fermi level was set at 0 eV.

Band structures of both phases of the bulk crystal of CdSe were computed at the B3PW91/SBKJC level, as reported in *Figure III.4*. The overall band profiles and the observable direct band gap at the Γ point of the Brillouin zone agree well with previous theoretical results obtained with the DFT^{5,51,52} and the GW⁵³ methods. The valence bands have a globally flat structure, which is typical to partially ionic compounds, although the observable energy dispersion indicates a non-negligible covalent character, which is approximately equal in case of the hexagonal and the cubic phases.

Analyzing the total density of states (DOS) reported in *Figure III.5*, one can note that its overall shape for the wurtzite and the zinc blende phases are very similar. It can be observed that the sharp and large contribution of the Cd_{4d} orbitals between -8 and -9 eV significantly overlaps with the Se_{4sp}, revealing the partially covalent character of the Cd-Se bond in the bulk crystal. Both the Cd_{4d} and the Se_{4sp} bands are split into two peaks in this structure; which is attributed to the tetrahedral environment of the Cd atoms, causing the Cd_{4d} orbitals to split into t_{2g} and e_g states that couple with the Se_{4p} orbitals.⁵ The further contributions of Se_{4sp} are a sharp peak at around -13 eV, an approximately 4 eV wide band below the Fermi level, and they are also present in the conduction band, where they overlap with the Cd_{sp} orbitals. These observations agree well with other theoretical works^{5,51,54} and previously published X-ray photoelectron spectra⁵⁵, although the low resolution of experimental spectra allows only a qualitative comparison.

Chapter III. Bulk and surface properties of CdSe

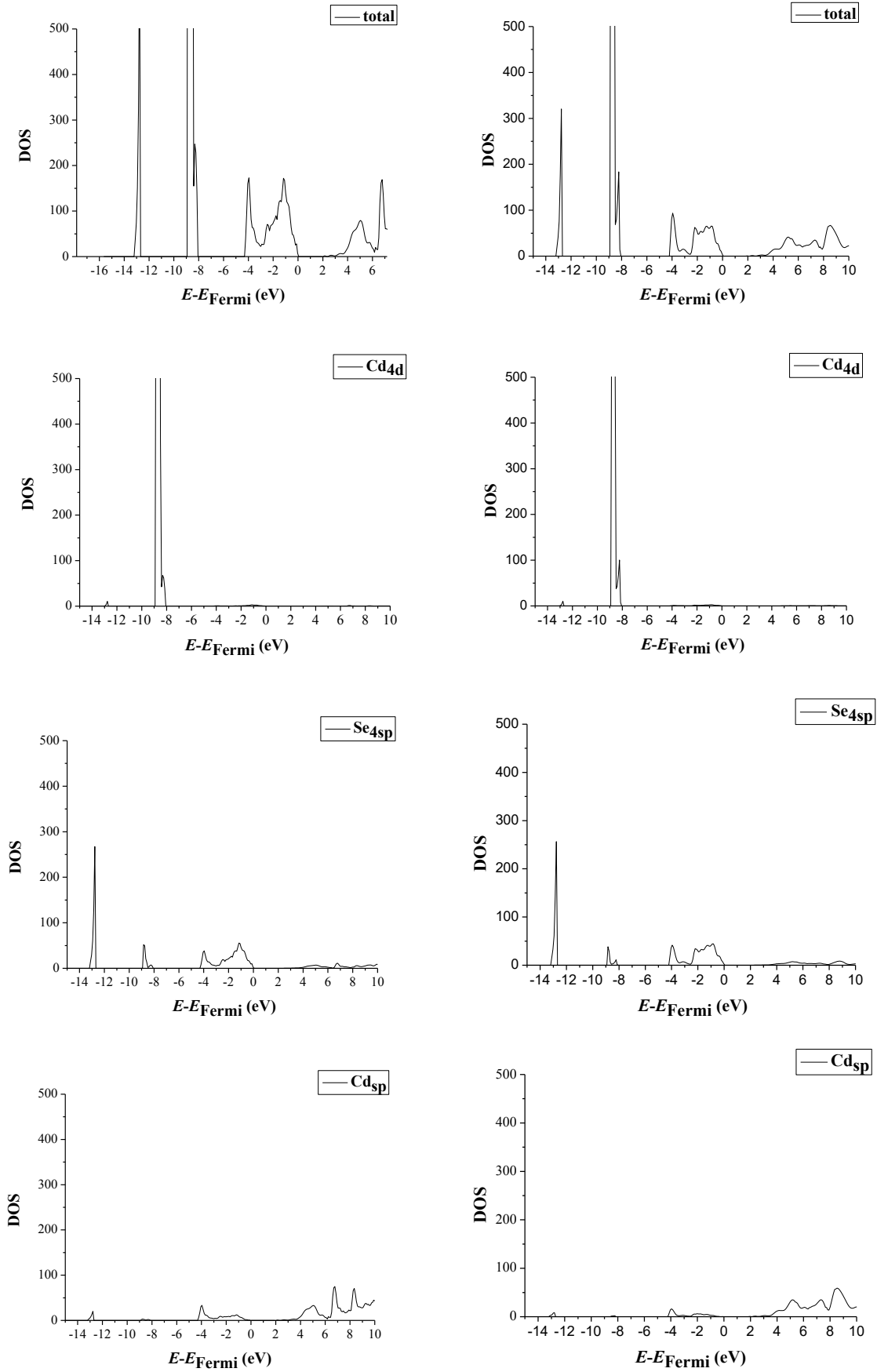


Figure III.5. Calculated total and orbital-projected density of states of the CdSe wurtzite (left) and zinc blende (right) bulk crystals. Fermi level was set at 0 eV.

Chapter III. Bulk and surface properties of CdSe

The Mulliken population analysis shows nearly equal results for the two polytypes in terms of atomic charges: $q_{\text{Cd}} = + 0.425 \text{ |e|}$, $q_{\text{Se}} = - 0.425 \text{ |e|}$ for wurtzite, and $q_{\text{Cd}} = + 0.424 \text{ |e|}$ and $q_{\text{Se}} = - 0.424 \text{ |e|}$, for zinc blende. The relatively small atomic charges and high bond overlap populations ($b_{\text{CdSe}} = 0.366$ for wurtzite and 0.368 for zinc blende, similarly to $b_{\text{CdSe,zb}} = 0.38$ in ref. 5), in agreement with the band structure, suggest the significant covalent character of the bulk system.

III.4. Surface properties of CdSe

III.4.1. Geometrical properties

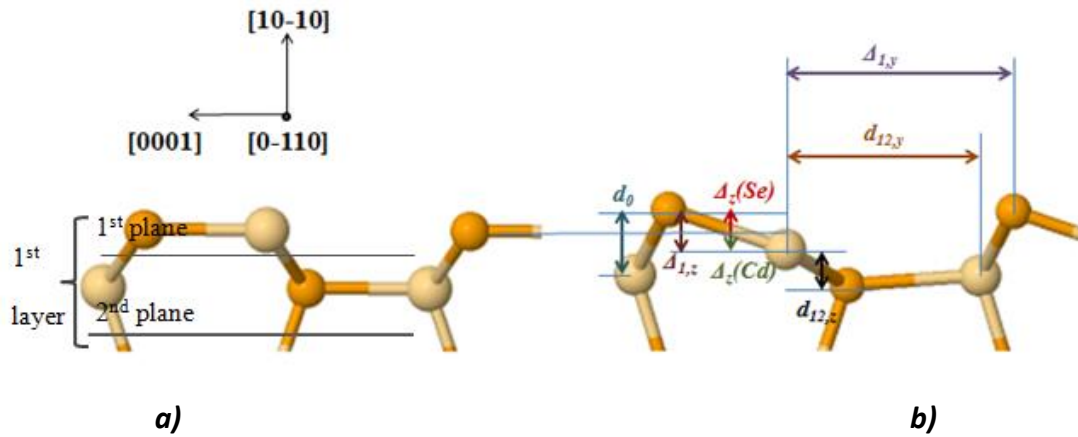


Figure III.6. Side views of the unrelaxed (a) and relaxed (b) structures of the CdSe wurtzite (10-10) surface. The definitions of the structural parameters of the relaxed surface are shown in (b). Cd atoms shown as larger white spheres, Se atoms as smaller yellow spheres.

The (10-10) surface of the wurtzite structure is a neutral, stable and nonpolar Tasker type I surface,⁵⁶ consisting of an equal number of cations and anions. It is one of the cleavage surfaces of the wurtzite structure, besides the (11-20) surface, and has been studied extensively both at the experimental^{57,58} and theoretical levels.^{59,60} The experimental measurement of two dimensional energetic properties like the surface formation energy is difficult. It can give ambiguous results because extremely clean materials with uniform exposed surface are needed and it is often not the case.⁵⁸ Therefore, theoretical investigations are of high relevance in this case. Using the previously selected computational protocol (that is the B3PW91 functional combined with the SBKJC basis set), a detailed

Chapter III. Bulk and surface properties of CdSe

investigation of the geometrical and electronic properties of the CdSe (10-10) wurtzite surface was thus performed.

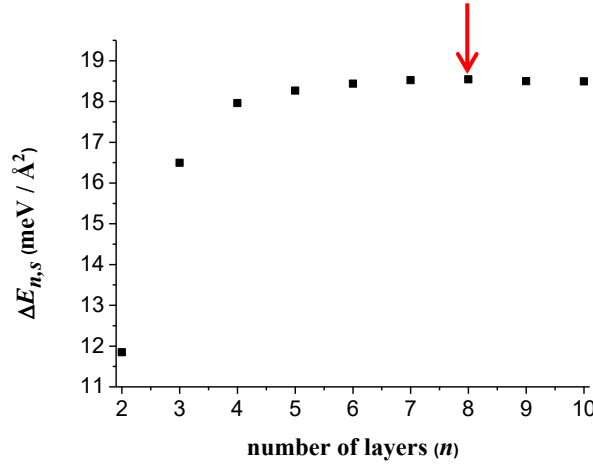


Figure III.7. Calculated surface formation energies for the (10-10) surface as a function of the number of layers of CdSe wurtzite slabs. Convergence (indicated by a red arrow) is reached at 8 layers.

First, the convergence of slab properties was investigated by calculating surface formation energies of slabs with increasing thickness. In this study, one slab layer stands for a unit containing two cadmium-selenium pairs per primitive cell, the two pairs being situated in two <10-10> planes as depicted on *Figure III.6*. The calculated surface formation energies as a function of slab thickness are reported in *Figure III.7*. Convergence is reached at 8 layers, after which the difference between the surface formation energies does not exceed 0.02 meV / Å² if the slab thickness is increased by one layer. The converged surface formation energy is 18.5 meV / Å², which is close to the 21.11 meV / Å² estimated by Sarkar et al⁴ and the 23.59 meV / Å² value obtained by Li et al,² both calculated at the GGA level.

Next, the structural parameters upon relaxation were computed for the 8 and 9 layers thick slabs, in order to confirm the convergence at 8 layers of thickness. In agreement with previous results for the CdSe wurtzite (10-10) surface,^{1,60} we have found that cations of the uppermost layer move inwards as a result of relaxation, while anions move outwards with respect to their unrelaxed positions, as described in *Figure III.6*. The computed geometric parameters of the relaxed structures are collected and compared to available data from other experimental and theoretical works in *Table III.3*. As we can see from *Table III.3*, the

Chapter III. Bulk and surface properties of CdSe

geometrical parameters do not differ significantly in case of 8 and 9 layers, which confirms the convergence of slab properties at 8 layers of thickness. Furthermore, our computed results are in very good agreement with previously reported experimental data, which justifies our choice of surface model.

	<i>present work</i>		<i>LEPD</i> ⁵⁷	<i>LEED</i> ⁵⁷	<i>Semiemp. Tight-binding</i> ⁶⁰	<i>Emp. Tight-binding</i> ¹	<i>LDA/PW</i> ⁵⁹
<i>n</i>	8	9	238-atom cluster			8	10
$\Delta_z(\text{Se})$	0.596	0.587	<i>nd</i>	<i>nd</i>	0.616	<i>nd</i>	<i>nd</i>
$\Delta_z(\text{Cd})$	0.225	0.216	<i>nd</i>	<i>nd</i>	0.299	<i>nd</i>	<i>nd</i>
$\Delta_{1,z}$	0.821	0.802	0.68	0.96	0.914	0.775	0.92
$d_{12,z}$	0.720	0.719	0.65	0.45	<i>nd</i>	0.639	0.46
d_0	1.347	1.346	<i>nd</i>	<i>nd</i>	<i>nd</i>	1.241	1.38
$d_{12,y}$	4.050	4.050	3.96	4.07	<i>nd</i>	4.036	<i>nd</i>
$\Delta_{1,y}$	4.725	4.724	4.48	4.57	<i>nd</i>	4.593	4.34

Table III.3. Structural parameters (in Å) of the CdSe wurtzite (10-10) surface after relaxation for 8 and 9 layers thick slabs, computed in the present study, in comparison with experimental (LEED and LEPD) and other theoretical data. (*nd*: no data available)

III.4.2. Electronic properties

The Mulliken atomic charges and overlap populations for an 8 layer thick CdSe wurtzite (10-10) slab are reported in *Table III.4*. The overall tendency is the increase of atomic charges and the decrease of overlap populations when moving from the surface towards the center of the slab. Defining $\Delta q = q^{\text{slab}} - q^{\text{bulk}}$ and $\Delta b = b^{\text{slab}} - b^{\text{bulk}}$ as the difference between the slab and bulk atomic charges and overlap populations, respectively, one can conclude from the computed Δq and Δb values that the upper surface layers are characterized by a significant decrease of ionicity compared to the bulk system, and these differences attenuate from the surface to the innermost layers of the slab. This is in line with the previously described phenomena that the surface redistributes the occupied anion-derived dangling bond charge density into bonding orbitals upon relaxation,⁶¹ which is reflected by the computed band structure reported in *Figure III.8*. Indeed, the S surface state typically observed for cadmium chalcogenide crystals in scanning tunneling microscopy (STM) experiments,⁶² which originates from the occupied surface anionic dangling bonds, lowers upon relaxation

Chapter III. Bulk and surface properties of CdSe

towards the rest of the valence band, and thus contributes to the stabilization of the structure. In accordance with these observations, the $\text{Se}_{4\text{sp}}$ states corresponding to the undercoordinated atoms in the uppermost plane are shifted towards the Fermi level with respect to the second plane DOS contribution of $\text{Se}_{4\text{sp}}$ orbitals, as reported *Figure III.9*. Although more slowly than surface formation energies, band gaps also converge towards the bulk value as the slab thickness is increased. For an 8 layers thick slab for instance, the band gap is 2.06 eV compared to the computed bulk value of 1.92 eV. This confirms the reliability of the model to describe the CdSe wurtzite (10-10) surface.

n	q_{Cd}	Δq_{Cd}	q_{Se}	Δq_{Se}	b_{CdSe}	Δb_{CdSe}
1	0.375	-0.050	-0.263	0.162	0.540	0.174
	0.361	-0.064	-0.418	0.007	0.540	0.174
2	0.371	-0.054	-0.440	-0.015	0.448	0.082
	0.437	0.012	-0.419	0.006	0.386	0.020
3	0.421	-0.004	-0.426	-0.001	0.380	0.014
	0.427	0.002	-0.423	0.002	0.370	0.004
4	0.423	-0.002	-0.425	0.000	0.370	0.004
	0.425	0.000	-0.424	0.001	0.370	0.014

Table III.4. Mulliken atomic charges (q) and overlap populations (b) for the CdSe wurtzite (10-10) surface, obtained at 8 layers, each layer containing two Cd-Se pairs/primitive cell (see *Figure III.6.*). n refers to the number of layers, $n=1$ being the outermost one with respect to the [10-10] direction indicated by an arrow. All data in $|e^-|$.

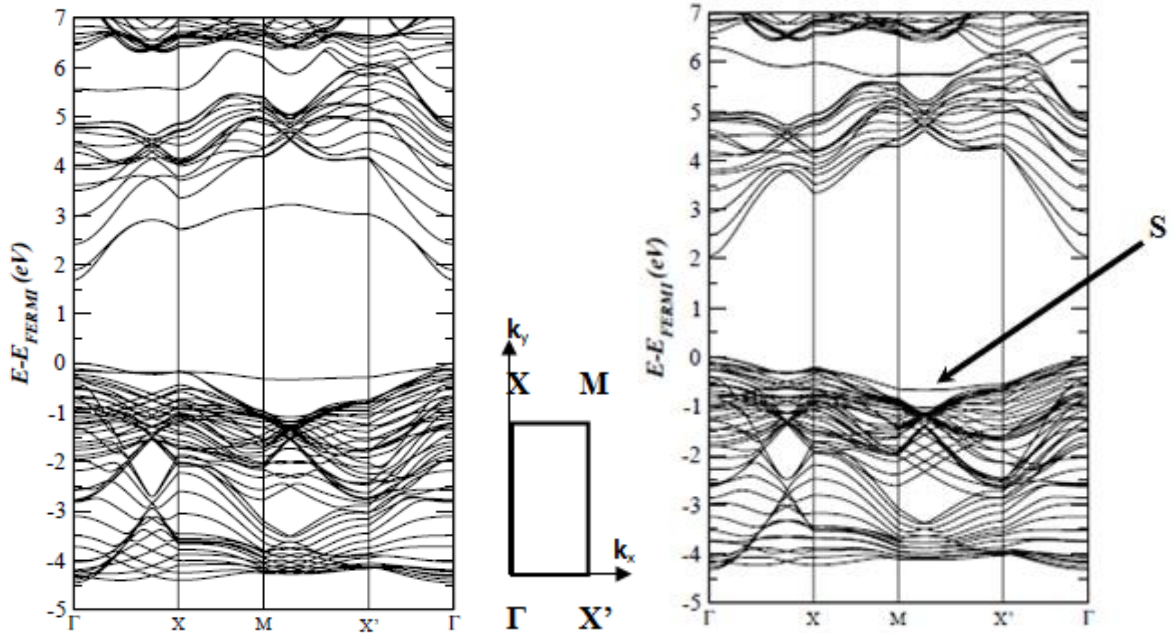


Figure III.8. Calculated band structure of the unrelaxed (left) and relaxed (right) CdSe wurtzite (10-10) surface obtained for an 8 layer thick slab. Corresponding Brillouin zone with high-symmetry points are indicated between the two band structures.

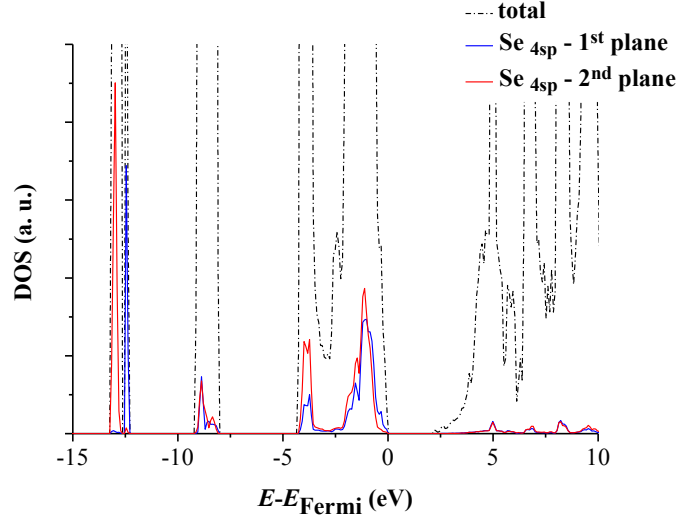


Figure III.9. Computed total and orbital-projected density of states of the CdSe wurtzite (10-10) surface obtained for an 8 layer thick slab. Fermi level was set at 0 eV.

III.5. Conclusion

In this chapter, a comprehensive DFT investigation of the geometrical and electronic properties of CdSe bulk crystals has been performed. We combined three main types of Gaussian-type orbital basis sets with six exchange-correlation functionals (three GGA-based and three global hybrids) within the density functional theory framework in order to find the computational protocol that gives the most accurate description both in terms of geometrical parameters and electronic structure for the two (wurtzite and zinc blende) CdSe bulk phases in comparison to available experimental data, data as well as in reference to def2-TZVP and PAW results. *We found that the global hybrid B3PW91 functional combined with small- and large-core effective pseudopotentials for Cd and Se, respectively, provides the best description considering the overall accuracy on several parameters.* Next, the nonpolar CdSe wurtzite (10-10) surface was modeled with the as-defined method. After reaching convergence on surface properties with slab thickness, we performed a detailed geometrical and electronic investigation of this surface. The relaxation induced changes in atomic positions and electronic structure have been described and compared to available experimental and theoretical data. The overall good agreement found justifies the choice of the model, and shows encouraging performance for an accurate modeling of quantum dot-based systems at low computational cost. In the next chapter, this computational protocol is

Chapter III. Bulk and surface properties of CdSe

used to simulate the sensitizers that we chose for this thesis: quasi-2D CdSe nanoplatelets of different thicknesses, passivated by various ligands.

Chapter III. Bulk and surface properties of CdSe

References

- (1) Wang, Y. R.; Duke, C. B. Cleavage Faces of Wurtzite CdS and CdSe: Surface Relaxation and Electronic Structure. *Phys. Rev. B* **1988**, *37* (11), 6417–6424.
- (2) Li, S.; Yang, G. W. Phase Transition of II - VI Semiconductor Nanocrystals. *J. Phys. Chem. C* **2010**, *114*, 15054–15060.
- (3) Datta, S.; Saha-Dasgupta, T.; Sarma, D. D. Wannier Function Study of the Relative Stability of Zinc-Blende and Wurtzite Structures in the CdX (X = S, Se, Te) Series. *J. Phys. Condens. Matter* **2008**, *20* (44), 445217.
- (4) Sarkar, S.; Pal, S.; Sarkar, P.; Rosa, A. L.; Frauenheim, T. Self-Consistent-Charge Density-Functional Tight-Binding Parameters for Cd-X (X = S, Se, Te) Compounds and Their Interaction with H, O, C, and N. *J. Chem. Theory Comput.* **2011**, *7*, 2262–2276.
- (5) Guo, L.; Zhang, S.; Feng, W.; Hu, G.; Li, W. A First-Principles Study on the Structural, Elastic, Electronic, Optical, Lattice Dynamical, and Thermodynamic Properties of Zinc-Blende CdX (X=S, Se, and Te). *J. Alloys Compd.* **2013**, *579*, 583–593.
- (6) Cora, F.; Alfredsson, M.; Mallia, G.; Middlemiss, D. S.; Mackrodt, W. C.; Dovesi, R.; Orlando, R. The Performance of Hybrid Density Functionals in Solid State Chemistry. In *Struct. Bonding*; Springer Berlin / Heidelberg: Berlin, 2004; p 171.
- (7) Muscat, J.; Wander, A.; Harrison, N. M. On the Prediction of Band Gaps from Hybrid Functional Theory. *Chem. Phys.* **2001**, *342*, 397–401.
- (8) Martsinovich, N.; Jones, D. R.; Troisi, A. Electronic Structure of TiO₂ Surfaces and Effect of Molecular Adsorbates Using Different DFT Implementations. *J. Phys. Chem.* **2010**, *114*, 22659–22670.
- (9) Xiao, H.; Tahir-Kheli, J.; Goddard, W. A. Accurate Band Gaps for Semiconductors from Density Functional Theory. *J. Phys. Chem. Lett.* **2011**, *2*, 212.
- (10) Marsman, M.; Paier, J.; Stroppa, A.; Kresse, G. Hybrid Functionals Applied to Extended Systems. *J. physics. Condens. matter* **2008**, *20* (6), 064201.
- (11) Towler, M. D.; Zupan, A.; Causa, M. Density Functional Theory in Periodic Systems Using Local Gaussian Basis Sets. *Comput. Phys. Commun.* **1996**, *98*, 181.
- (12) Corà, F.; Alfredsson, M.; Mallia, G.; Middlemiss, D. S.; Mackrodt, W. C.; Dovesi, R.; Orlando, R. The Performance of Hybrid Density Functionals in Solid State Chemistry. In *Structure and Bonding*; Springer-Verlag Berlin Heidelberg, 2004; Vol. 113, p 171.
- (13) Orlando, R.; Delle Piane, M.; Bush, I. J.; Ugliengo, P.; Ferrabone, M.; Dovesi, R. A New Massively Parallel Version of CRYSTAL for Large Systems on High Performance Computing Architectures. *J. Comput. Chem.* **2012**, *33* (28), 2276–2284.
- (14) Dovesi, R.; Saunders, V. R.; Roetti, C.; Orlando, R.; Zicovich-Wilson, C. M.; Pascale, F.; Civalleri, B.; Doll, K.; Harrison, N. M.; Bush, I. J.; et al. Crystal09 User's Manual. Università di Torino: Torino 2013.
- (15) Dovesi, R.; Orlando, R.; Civalleri, B.; Roetti, C.; Saunders, V. R.; Zicovich-Wilson, C. M. CRYSTAL : A Computational Tool for the Ab Initio Study of the Electronic Properties of Crystals. *Zeitschrift für Krist. - Cryst. Mater.* **2005**, *220*, 571–573.
- (16) Dou, Y.; Egdel, R. G.; Law, D. S. L.; Harrison, N. M.; Searle, B. G. An Experimental and Theoretical Investigation of the Electronic Structure of CdO. *J. Phys. Condens. Matter* **1998**, *10*, 8447–8458.
- (17) Towler, M. D.; Zicovich-Wilson, C. Mike Towler's CRYSTAL resources page <http://www.tcm.phy.cam.ac.uk/~mdt26/crystal.html> (accessed Feb 9, 2014).
- (18) Stevens, W. J.; Krauss, M.; Basch, H.; Jasien, P. G. Relativistic Compact Effective Potentials and Efficient, Shared-Exponent Basis Sets for the Third-, Fourth-, and Fifth-Row Atoms. *Can. J. Chem.* **1992**, *70* (2), 612–630.
- (19) Labello, N. P.; Ferreira, A. M.; Kurtz, H. a. An Augmented Effective Core Potential Basis Set for the Calculation of Molecular Polarizabilities. *J. Comput. Chem.* **2005**, *26* (14), 1464–1471.
- (20) Heyd, J.; Peralta, J. E.; Scuseria, G. E.; Martin, R. L. Energy Band Gaps and Lattice Parameters Evaluated with the Heyd-Scuseria-Ernzerhof Screened Hybrid Functional. *J. Chem. Phys.* **2005**, *123*, 174101.
- (21) Kresse, G.; Hafner, J. Ab Initio Molecular Dynamics for Liquid Metals. *Phys. Rev. B* **1993**, *47* (1), 558.
- (22) Kresse, G.; Hafner, J. Ab Initio Molecular-Dynamics Simulation For the Liquid-Metal-Amorphous-Semiconductor Transition in Germanium. *Phys. Rev. B* **1994**, *49* (20), 14251.

Chapter III. Bulk and surface properties of CdSe

- (23) Kresse, G.; Furthmüller, J. Efficient Iterative Schemes for Ab Initio Total-Energy Calculations Using a Plane-Wave Basis Set. *Phys. Rev. B* **1996**, *54* (16), 11169.
- (24) Kresse, G.; Furthmüller, J. Efficiency of Ab-Initio Total Energy Calculations for Metals and Semiconductors Using a Plane-Wave Basis Set. *Comput. Mater. Sci.* **1996**, *6*, 15.
- (25) Moellmann, J.; Ehrlich, S.; Tonner, R.; Grimme, S. A DFT-D Study of Structural and Energetic Properties of TiO₂ Modifications. *J. Phys. Condens. Matter* **2012**, *24* (42), 424206.
- (26) Conesa, J. C. The Relevance of Dispersion Interactions for the Stability of Oxide Phases. *J. Phys. Chem. C* **2010**, *114* (51), 22718–22726.
- (27) Kristyan, S.; Pulay, P. Can (Semi)local Density Functional Theory Account for the London Dispersion Forces ? *Chem. Phys. Lett.* **1994**, *229*, 175–180.
- (28) Hobza, P.; Sponer, J.; Reschel, T. Density Functional Theory and Molecular Clusters. *J. Comput. Chem.* **1995**, *16* (11), 1315–1325.
- (29) Grimme, S. Semiempirical GGA-Type Density Functional Constructed with a Long-Range Dispersion Correction. *J. Comput. Chem.* **2006**, *27*, 1787–1799.
- (30) Monkhorst, H. J.; Pack, J. D. Special Points for Brillouin-Zone Integrations. *Phys. Rev. B* **1976**, *13* (12), 5188–5192.
- (31) Zakharov, O.; Rubio, A.; Cohen, M. L. Calculated and Electronic Properties of CdSe under Pressure. *Phys. Rev. B* **1995**, *51*, 4926–4930.
- (32) Schröer, P.; Krüger, P.; Pollmann, J. Ab Initio Calculations of the Electronic Structure of the Wurtzite Compounds CdS and CdSe. *Phys. Rev. B* **1993**, *48* (24), 18264–18267.
- (33) Schowalter, M.; Lamoén, D.; Rosenauer, a.; Kruse, P.; Gerthsen, D. First-Principles Calculations of the Mean Inner Coulomb Potential for Sphalerite Type II–VI Semiconductors. *Appl. Phys. Lett.* **2004**, *85* (21), 4938.
- (34) Reshak, A. H.; Kityk, I. V.; Khenata, R.; Auluck, S. Effect of Increasing Tellurium Content on the Electronic and Optical Properties of Cadmium Selenide Telluride Alloys CdSe_{1-x}Te_x: An Ab Initio Study. *J. Alloys Compd.* **2011**, *509* (24), 6737–6750.
- (35) Heyd, J.; Scuseria, G. E.; Ernzerhof, M. Hybrid Functionals Based on a Screened Coulomb Potential. *J. Chem. Phys.* **2003**, *118* (18), 8207–8215.
- (36) Madelung, O. *Semiconductors - Basic Data*; Springer: Berlin, 1996.
- (37) Xu, Y.-N.; Ching, W. Y. Electronic, Optical and Structural Properties of Some Wurtzite Crystals. *Phys. Rev. B* **1993**, *48* (7), 4335–4351.
- (38) Zhuravlev, K. K. PbSe vs. CdSe: Thermodynamic Properties and Pressure Dependence of the Band Gap. *Phys. B Condens. Matter* **2007**, *394* (1), 1–7.
- (39) Meyer, B.; Marx, D. Density-Functional Study of the Structure and Stability of ZnO Surfaces. *Phys. Rev. B* **2003**, *67* (3), 035403.
- (40) Nag, A.; Hazarika, A.; Shanavas, K. V.; Sharma, S. M.; Dasgupta, I.; Sarma, D. D. Crystal Structure Engineering by Fine-Tuning the Surface Energy: The Case of CdE (E = S/Se) Nanocrystals-Supporting Information. *J. Phys. Chem. Lett.* **2011**, *2*.
- (41) Rivera-Marquez, A.; Rubin-Falfan, M.; Lozada-Morales, R.; Portillo-Moreno, O.; Zelaya-Angel, O.; Luyo-Alvarado, J.; Melendez-Lira, M.; Banos, L. Quantum Confinement and Crystalline Structure of CdSe Nanocrystalline Films. *Phys. Status Solidi* **2001**, *188* (3), 1059–1064.
- (42) Kale, R. B.; Lokhande, C. D. Systematic Study on Structural Phase Behavior of CdSe Thin Films. *J. Phys. Chem. B* **2005**, *109* (43), 20288–20294.
- (43) Yeh, C.; Lu, Z. W.; Froyen, S.; Zunger, A. Zinc-Blende-Wurtzite Polytypism in Semiconductors. *Phys. Rev. B* **1992**, *46* (16), 10086–10097.
- (44) Zunger, A.; Cohen, M. L. Density-Functional Pseudopotential Approach to Crystal Phase Stability and Electronic Structure. *Phys. Rev. Lett.* **1978**, *41* (1), 53–56.
- (45) Fedorov, V. A.; Ganshin, V. A.; Korkishko, Y. N. Determination of the Point of the Zincblende-to-Wurtzite Structural Phase Transition in Cadmium Selenide Crystals. *Phys. Status Solidi* **1991**, *126*, K5–K7.
- (46) Noor, N. a.; Tahir, W.; Aslam, F.; Shaukat, a. Ab Initio Study of Structural, Electronic and Optical Properties of Be-Doped CdS, CdSe and CdTe Compounds. *Phys. B Condens. Matter* **2012**, *407* (6), 943–952.
- (47) Alahmed, Z. a. Effects of in-Plane Tensile Strains on Structural, Electronic, and Optical Properties of CdSe. *Solid State Sci.* **2013**, *21*, 11–18.
- (48) Sham, L. J.; Schluter, M. Density-Functional Theory of the Energy Gap. *Phys. Rev. Lett.* **1983**, *51* (20), 1888–1891.

Chapter III. Bulk and surface properties of CdSe

- (49) Labat, F.; Ciofini, I.; Adamo, C. Modeling ZnO Phases Using a Periodic Approach: From Bulk to Surface and Beyond. *J. Chem. Phys.* **2009**, *131* (4), 044708.
- (50) Azpiroz, J. M.; Ugalde, J. M.; Infante, I. Benchmark Assessment of Density Functional Methods on Group II–VI MX (M = Zn, Cd; X = S, Se, Te) Quantum Dots. *J. Chem. Theory Comput.* **2014**, *10* (1), 76–89.
- (51) Noor, N. A.; Shaukat, A. Ab Initio Study of Structural, Electronic and Optical Properties of Mg X Cd 1-X X (X = S, Se, Te) Alloys. *Int. J. Mod. Phys. B* **2012**, *26* (30), 1250168.
- (52) Huang, M.-Z.; Ching, W. Y. A Minimal Basis Semi-Ab Initio Approach to the Band Structures of Semiconductors. *J. Phys. Chem. Solids* **1985**, *46* (8), 977–995.
- (53) Zakharov, O.; Rubio, A.; Blase, X.; Cohen, M. L.; Louie, S. G. Quasi-Particle Band Structures of Six II-VI Compounds: ZnS, ZnSe, ZnTe, CdS, CdSe, and CdTe. *Phys. Rev. B* **1994**, *50* (15), 780–787.
- (54) Wei, S.; Lu, J.; Qian, Y. Density Functional Study of 2D Semiconductor CdSe·Hda 0.5 (Hda = 1,6-Hexanediamine) and Its Excitonic Optical Properties. *Chem. Mater.* **2008**, *20*, 7220–7227.
- (55) Ley, L.; Pollak, A.; McFeely, F. R.; Kowalczyk, S. P.; Shirley, D. A. Total Valence-Band Densities of States of III-V and II-VI Compounds from X-Ray Photoemission Spectroscopy. *Phys. Rev. B* **1973**, *9* (2), 600–621.
- (56) Tasker, P. W. The Stability of Ionic Crystal Surfaces. *J. Phys. C Solid State Phys.* **1979**, *12*, 4977–4984.
- (57) Horsky, T. N.; Brandes, G. R.; Canter, K. F.; Duke, C. B.; Paton, A.; Lessor, D. L.; Kahn, A.; Horng, S. F.; Stevens, K.; Stiles, K.; et al. Analysis of the Atomic Geometries of the (10-10) and (11-20) Surfaces of CdSe by Low-Energy-Electron Diffraction and Low-Energy-Positron Diffraction. *Phys. Rev. B* **1992**, *46* (11), 7011–7026.
- (58) Xu, F.; Zhou, W.; Navrotsky, A. Cadmium Selenide: Surface and Nanoparticle Energetics. *J. Mater. Res.* **2011**, *26* (05), 720–725.
- (59) Csik, I.; Russo, S. P.; Mulvaney, P. Density Functional Study of Non-Polar Surfaces of Wurtzite CdSe. *Chem. Phys. Lett.* **2005**, *414*, 322–325.
- (60) Leung, K.; Whaley, K. B. Surface Relaxation in CdSe Nanocrystals. *J. Chem. Phys.* **1999**, *110*, 11012.
- (61) LaFemina, J. P. Total-Energy Calculations of Semiconductor Surface Reconstructions. *Surf. Sci. Rep.* **1992**, *16* (4-5), 137–260.
- (62) Siemens, B.; Domke, C.; Ebert, P.; Urban, K. Electronic Structure of Wurtzite II-VI Compound Semiconductor Cleavage Surfaces Studied by Scanning Tunneling Microscopy. *Phys. Rev. B* **1997**, *56* (19), 12321–12326.

IV.1. Context

As discussed in **Chapter I**, quasi-two dimensional CdSe nanoplatelets with a well-controlled thickness exhibit several advantageous properties for optical and opto-electronic applications, such as in quantum dot sensitized solar cells (QDSCs). Typically, CdSe zinc blende nanoplatelets are capped with fatty acids,^{1,2,3} which cannot be used as bifunctional ligands, and are too long to ensure charge transfer between the sensitizer and the wide band gap semiconductor. Organic capping agents of spherical CdSe quantum dots have been efficiently replaced by inorganic ligands (S^{2-} , SH^- , OH^- , Te^{2-} , TeH^-) by ligand exchange reactions. These inorganic ligands have been shown to facilitate charge transfer compared to long-chain organic ones.⁴ Therefore, the use of inorganic ligands can open interesting possibilities for QDs of other shapes, such as the quasi-2D nanoplatelets. In this chapter, a theoretical study of CdSe zinc blende nanoplatelets of different thicknesses in the (100) direction is presented. Three cases have been studied: 1) nanoplatelets stabilized by fatty acids, 2) thiols (SH^-) and 3) hydroxide groups (OH^-). A theoretical model of these ligand-nanocrystal hybrid systems has been built, and the geometric and electronic properties of these nanocrystals have been in-depth investigated within the DFT framework. The theoretical results obtained were validated by experimental measurements. More precisely, the band gaps of the synthesized nanoplatelets were measured by absorption spectroscopy.

IV.2 Experimental details

The synthesis of 5, 7, 9 atomic layers thick nanoplatelets was based on ref. 1, and was described in detail in **Chapter II**, section **II.2.1**. TEM images of these nanoplatelets are reported in *Figure IV.1 a)* and *b)*. The definition of one monolayer (ML), standing for an atomic layer composed exclusively of cadmium or selenium atoms in the same $\langle 100 \rangle$ plane, is illustrated in *Figure IV.1 c)*. The details of ligand exchange reactions based on ref. 4 can be found in **Chapter II**, section **II.2.3. b)**, as well as those of the UV-VIS absorption measurements. The band gap of the NPLs was determined at the maximum of their first absorption peak.

Chapter IV. Cadmium selenide nanoplatelets

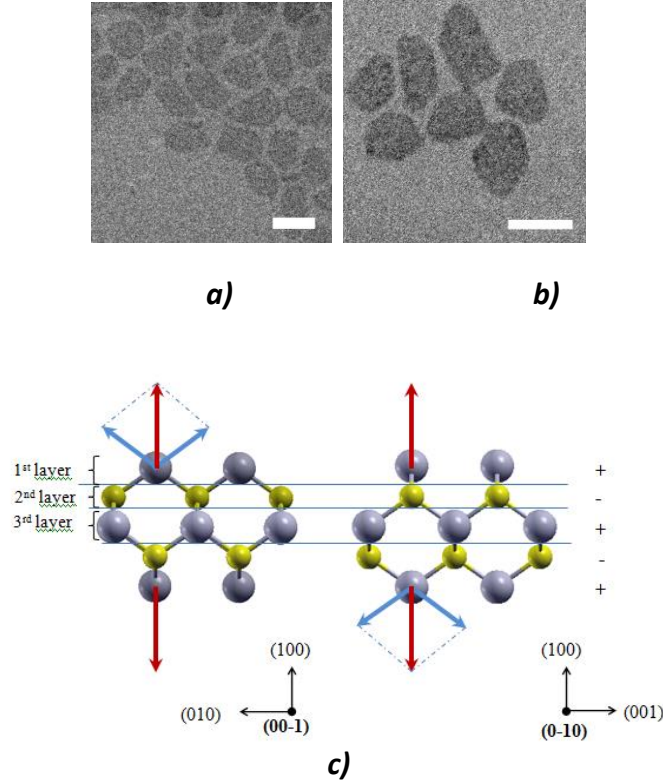


Figure IV.1. TEM views of a) 9 and b) 13 atomic layers thick CdSe nanoplatelets. The scale bar length is 20 nm. c) Side views of the alternate stacking of positively (+ sign) and negatively (- sign) charged planes in a CdSe zinc blende five layers thick slab exposing its Cd-terminated (100) surface. Cd atoms are presented as grey spheres, Se atoms as yellow spheres. Blue arrows show the dipole momenta arising from the dangling bonds of the surface Cd atoms, the vector sum of which is represented by a red arrow.

IV.3. Computational details

Similarly to the previous chapter, all calculations in this work were carried out with the *ab initio* Crystal09^{5,6} code. Following the results obtained in the previous chapter,⁷ our investigations were carried out using the global hybrid B3PW91 functional.⁸ For CdSe, we used a Gaussian-type orbital (GTO) double-zeta basis set, and replaced the core electrons by effective core potentials (ECPs) including scalar relativistic effects, as described in ref. 9. In more detail, the SBKJC small-core ECP¹⁰ was applied for Cd and the SBKJC large-core ECP¹⁰ with a basis set augmented by one d polarization function¹¹ for Se. As a consequence, the following electrons were treated explicitly: $4s^2 4p^6 4d^{10} 5s^2$ for Cd and $4s^2 4p^4$ for Se. As previously described for CdSe,⁹ basis sets were modified by setting exponents inferior to 0.10. It is to note that although hybrid functionals can be also used with plane-wave (PW)

Chapter IV. Cadmium selenide nanoplatelets

basis sets, calculations remain computationally much more expensive in that case.¹² On the other hand, when combined with Gaussian-type basis sets, hybrids can efficiently be applied to periodic systems,^{13,14} even to very large ones like the nanoplatelets studied here.¹⁵ To simplify calculations, HCOO⁻ served as a model for fatty acids, keeping in mind that it is only through the carboxylate functional group that fatty acids bind to the surface, and the alkyl chain has no influence on the changes induced in the surface electronic states upon adsorption of the ligand. All-electron GTO basis sets taken from ref. 16 were applied for the modeling of the C, O and H atoms of the adsorbed species with the following contractions: (9s,3p,1d)→[3s,2p,1d] for C atoms, (14s,6p,1d)→[4s,3p,1d] for O atoms, (7s,1p)→[3s,1p] for H atoms, and (14s,8p,1d)→[5s,4p,1d] contraction for S atoms.¹⁷

An extra-large DFT integration grid, consisting of 75 radial and 974 angular points, was applied in order to provide accurate results for calculations. The following truncation criteria (ITOL parameters)⁵ were set for the accuracy of the Coulomb and exchange series: 10⁻⁷ as the overlap threshold for Coulomb integrals, 10⁻⁷ as the penetration threshold for Coulomb integrals, 10⁻⁷ as the overlap threshold for HF exchange integrals, and 10⁻⁹ and 10⁻²⁰ as the pseudo-overlap for HF exchange series. A Monkhorst-Pack shrinking factor¹⁸ of 6 has been applied, which corresponds to 20 k points in the irreducible Brillouin zone (IBZ) of the stabilized zinc blende (100) surfaces. For the calculations of surface properties, we adopted a slab model: a slice of material with a thickness of several atomic layers, terminated by two free surfaces, for which two dimensional periodic boundary conditions were imposed. Only atoms were allowed to relax during geometry optimization in the stabilised CdSe zinc blende slabs. All of the slabs studied here are non-stoichiometric, and are terminated by Cd atoms on both basal planes like the CdSe zinc blende nanoplatelets previously synthesized by Ithurria et al.¹ Two adsorption modes of formate and one adsorption mode of hydroxide and sulfide ions on CdSe (100) surface were considered. In the following, the studied systems are abbreviated as CdSe.HCOO, CdSe.OH and CdSe.SH, respectively.

In general, the adsorption energy of an X ligand on the surface of Y can be calculated as:

$$E_{ads} = E_{tot}(Y.X) - E_{tot}(X) - E_{tot}(Y) \quad (IV.1.)$$

Chapter IV. Cadmium selenide nanoplatelets

Where E_{ads} is the calculated adsorption energy, $E_{tot}(Y.X)$ is the total energy of Y with the X ligand adsorbed on its surface, $E_{tot}(X)$ is the total energy of the X ligand, and $E_{tot}(Y)$ is the total energy of the bare Y. In case of the systems studied here, this equation cannot be directly applied. Instead, the zinc blende (100) surface is a polar, unstable Tasker type 3 surface, that is characterized by a divergent surface energy originating from the permanent dipole momenta perpendicular to its surface,¹⁹ as illustrated in *Figure IV.1 c*). The third term (the energy of the clean slab) in *Equation IV.1* is therefore approximated as the total energy of a part of the bulk crystal which contains a number of atoms equal to that of the slab. Furthermore, since the Cd-terminated (100) slab is nonstoichiometric, the first term of *Equation IV.1* is replaced by the average of the total energies of a slab terminated by Cd atoms and stabilized with anionic ligands on both basal planes and that of a CdSe zinc blende slab terminated by Se atoms and stabilized by Na^+ ions on its basal planes. This approach is similar to the one proposed for the calculations of non-stoichiometric perovskite slabs by Evarestov et al.²⁰ Next, the total energy of both the anion and the Na^+ should be subtracted from this term. To sum up, in this chapter, the adsorption energies of $HCOO^-$, OH^- and SH^- ligands on the CdSe zinc blende (100) surface were thus calculated according to the following equation:

$$E_{ads} = (E_{tot}(CdSe.X) + E_{tot}(CdSe.Na)) / 2 - E_{tot}(X^-) - E_{tot}(Na^+) - n \cdot E_{tot}(CdSe_{bulk}) \quad (IV.2.)$$

where n is the ratio of the number of atoms per unit cell in the slab and in the bulk, and X^- stands either for $HCOO^-$, OH^- or SH^- . In the following, CdSe.X means a slab terminated by Cd and stabilized by X^- on both (100) surfaces, while CdSe.Na is a slab terminated by Se and stabilized by Na^+ on both (100) surfaces.

IV.4. Theoretical model of the CdSe zinc blende (100) surface

Under atmospheric conditions, two stable phases are found for CdSe: the hexagonal wurtzite structure and the face-centered cubic zinc blende structure,²¹ the latter belonging to the Fm3m space group. The zinc blende (100) surface consists of alternately charged planes,¹⁹ as

Chapter IV. Cadmium selenide nanoplatelets

also shown on *Figure IV.1*. In this structure, the dipole moments originating from the two dangling bonds of the under-coordinated Cd atoms in the uppermost layer of the (100) basal planes sum up as a dipole moment perpendicular to the (100) surface (as illustrated in *Figure IV.1 c*)), which results in a divergent surface energy. In order to stabilize this kind of surfaces, a substantial surface reconstruction or the adsorption of additional species is needed. Because of their instability, polar semiconductor surfaces are less investigated than cleavage surfaces like the wurtzite (10-10) and (11-20) of CdSe.^{22–24} In theoretical studies, polar CdSe surfaces have been passivated by phosphines,^{25,26} amines,^{25,27} thiols,²⁵ and fatty acids.^{28,29} These organic ligands are commonly used during and after the synthesis of CdSe quantum dots.^{1,30,31} Atomic reconstructions of the polar zinc blende (111) and (001) surfaces of CdSe have also been investigated,³² the latter surface being equivalent to the (100) surface of our interest.

Carefully chosen ligands can influence the shape of the nanocrystal.^{33–35} The CdSe zinc blende crystal structure has an isotropic unit cell structure, which facilitates the growth of isotropic structures like cubes. In order to produce quasi-two-dimensional (2D) zinc blende nanocrystals, one needs to suppress the high reactivity of polar surfaces.^{28,36} This is commonly done by using ligands that specifically bind to these planes, such as oleic acid (OA). As these ligands link to cations, a thin quasi-2D (100) nanocrystal whose synthesis is based on the passivation of polar surfaces should be terminated by Cd atoms on both (100) basal planes, as in previously studied CdSe zinc blende nanoplatelets.^{37,28} However, this results in a non-stoichiometric structure and excess positive charges due to the additional Cd plane which should be compensated by negative charges. Li et al²⁸ proposed a structure in which onefold negatively charged ligands are adsorbed on both basal planes of a nanocrystal. Indeed, in this case, in a purely ionic picture, the additional +2 charge per unit cell due to the excess of Cd planes is neutralized by the 2·(-1) charge of the ligands on the two basal planes, as long as each surface Cd is bound to a ligand. The appropriately chosen ligands also serve as a model of different capping agents of the synthesized nanoplatelets, which influence their charge transfer properties,⁴ therefore this way of stabilizing the zinc blende (100) surface leads to a model that is better adapted to simulate the synthesized nanoplatelets than the surface atomic reconstructions. In the present work, calculations were performed only on slabs with selected thicknesses: 5, 9 and 13 atomic layers.

IV.5. Geometrical investigation

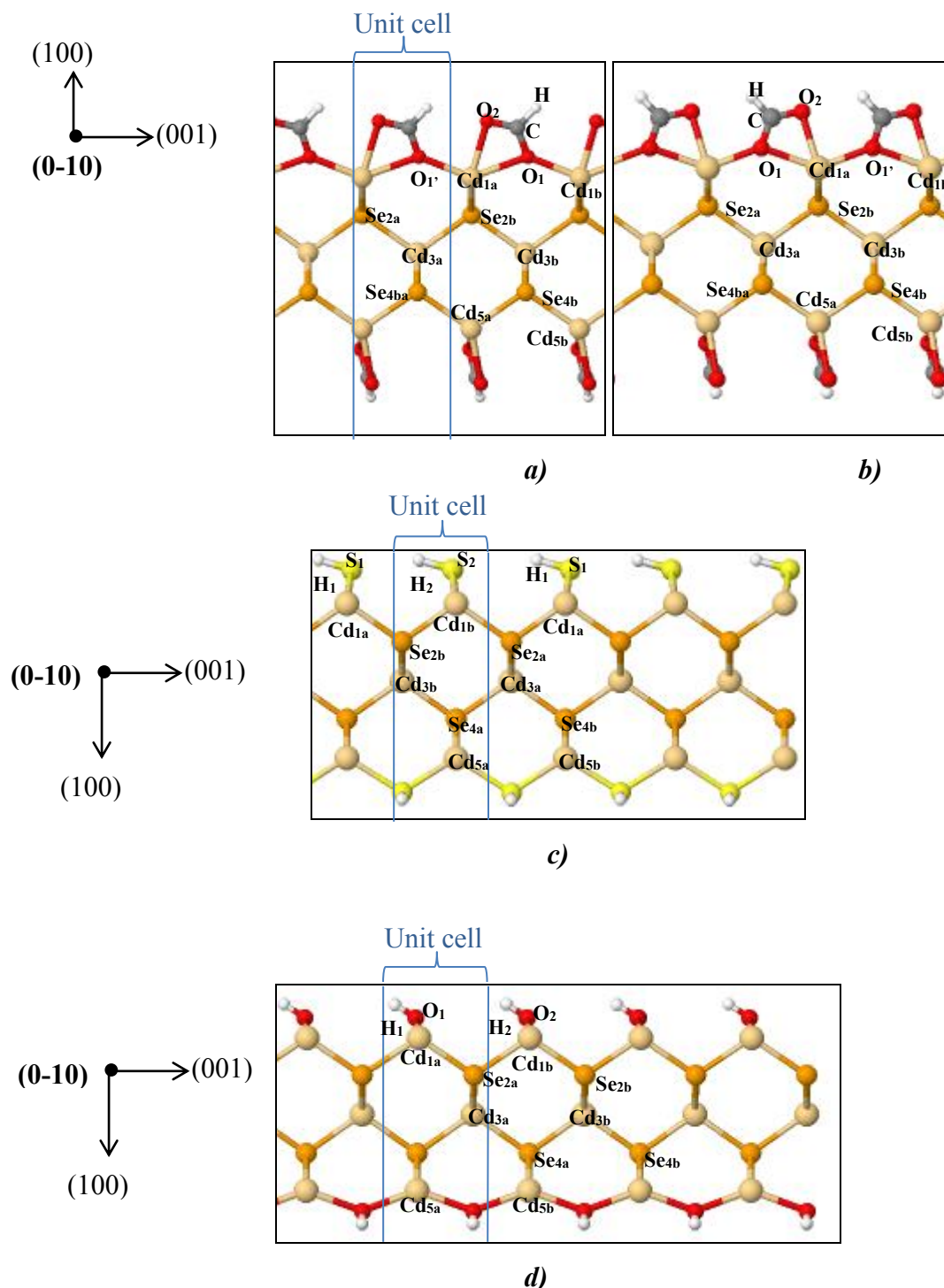


Figure IV.2. Optimized structures of stabilized five layers thick slabs: the CdSe.HCOO system in the a) bidentate and b) monodentate adsorption mode of the formate ligand, and those of the c) CdSe.SH and d) CdSe.OH systems. Cd, Se, O, C, H and S atoms are presented as beige, orange, red, grey, white and yellow spheres, respectively.

Chapter IV. Cadmium selenide nanoplatelets

Figure IV.2 represents the optimized geometries of five layers thick slabs stabilized with different ligands. With the chosen orientation, the ligands on the two basal planes are turned by 90° with respect to each other, following the relative positions of tetracoordinated Cd and Se atoms in the bulk crystal. The optimized geometrical parameters are reported in Table IV.1. It is to note that the interatomic distances characterizing the optimized adsorption geometries of the ligands on the CdSe zinc blende (100) surface do not change with slab thickness.

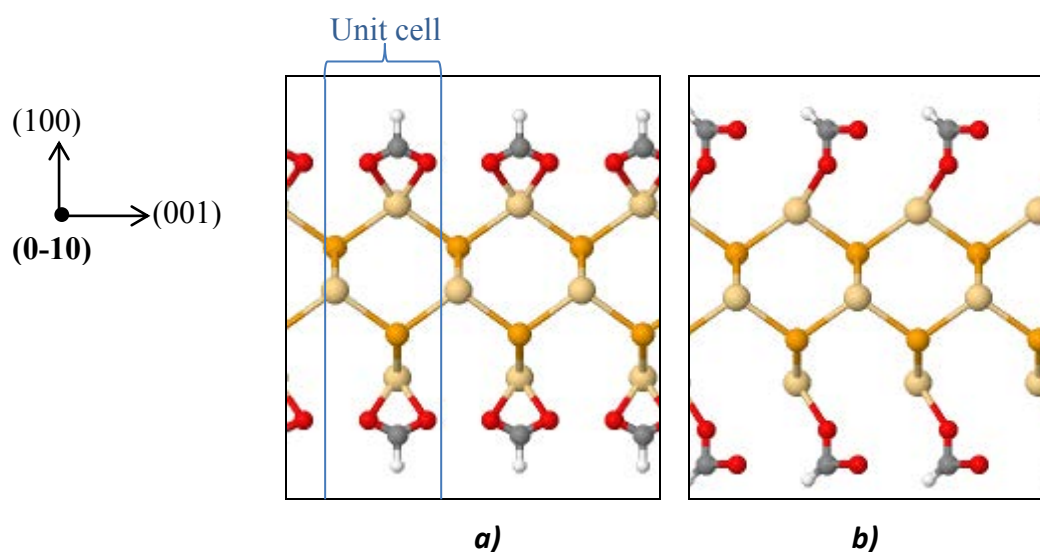


Figure IV.3. Initial geometries of CdSe.HCOO with a) bidentate and b) monodentate adsorption mode of the HCOO⁻ ligand.

CdSe.HCOO		CdSe.SH		CdSe.OH	
$d(\text{C-O}_1)$	2.43	$d(\text{Cd}_{1a}\text{-S}_1)$	2.60	$d(\text{Cd}_{1a}\text{-O})$	2.34
$d(\text{C-O}_2)$	2.37	$d(\text{Cd}_{1b}\text{-S}_2)$	2.61	$d(\text{Cd}_{1b}\text{-O})$	2.34
$d(\text{C-O}_{1'})$	2.27	$d(\text{S}_1\text{-H}_1)$	1.37	$d(\text{O}_1\text{-H}_1)$	0.96
$d(\text{Cd}_{1a}\text{-C})$	2.75	$d(\text{S}_1\text{-H}_2)$	3.58	$d(\text{O}_1\text{-H}_2)$	3.62
$d(\text{Cd}_{1b}\text{-C})$	2.75	$d(\text{S}_2\text{-H}_2)$	1.37	$d(\text{O}_2\text{-H}_2)$	0.96
$d(\text{C-H})$	1.10	$d(\text{S}_2\text{-H}_1)$	2.75	$d(\text{O}_2\text{-H}_1)$	3.62

Table IV.1. Relaxed geometrical parameters (in Å) of the bidentate CdSe.HCOO, the CdSe.SH and the CdSe.OH slabs.

Chapter IV. Cadmium selenide nanoplatelets

In the present study, the mono- and bidentate adsorption geometries of the formate ion (*Figures IV.3. a) and b)*, respectively) were considered on the CdSe zinc blende (100) surface. As mentioned above, the excess +2 charge per unit cell (see *Figure IV.2.*) of the additional Cd layer is compensated in these cases, as one HCOO^- anion is attached to each Cd atom on both basal planes, which means that $2 \cdot (-1) = -2$ charge is introduced upon ligand adsorption. A test optimization on five layer slabs showed that the two optimized structures actually converge on the same minimum. Starting either with a mono- or with a bidentate adsorption mode resulted in a geometry in which the formate group is tilted in a way that one of its O atoms (O_1) forms a bridge between two neighboring Cd atoms and the other O atom (O_2) stays connected to one single Cd atom, resulting in pentacoordinated Cd atoms, as shown on *Figures IV.2 a) and b)*. As a consequence, only the bidentate adsorption mode has been considered as initial geometry for investigations on thicker slabs,.

Also, in the case of SH^- ligands, the initial configuration was chosen to be a bridging one (see *Figure IV.2 c)*). This structure can be regarded as a result of a surface treatment of the CdSe zinc blende (100) surface with sulfide ions that occupy the same positions as selenide ions in a bulk zinc blende CdSe crystal. This ensures the tetrahedral coordination of the surface Cd atoms. Each surface Cd atom is linked to 2 Se and 2 S atoms, and each S atom is linked to two Cd atoms and one H atom. In this arrangement, the negative charges introduced by the so formed S^{2-} layers (-2 per unit cell) are compensated by H^+ counter ions ($2 \cdot (+1)$ per unit cell), in a manner similar to that described above for CdSe.HCOO. As a result of the optimization, S atoms are displaced closer to H atoms of the neighbouring bridges, possibly forming a network of S-H hydrogen bonds. Regarding the distance between S and H atoms of the neighbouring bridges, alternating rows are formed on the (100) basal planes, characterized by small but remarkable differences in the relative positions of the atoms (*Table IV.1*). Finally, the initial structure for the OH^- stabilized CdSe zinc blende (100) slabs was constructed based on the relaxed CdSe.SH geometry: the S atoms of the relaxed SH^- stabilized slabs were simply replaced by O atoms. Upon optimization, the O atoms got closer to the surface than S atoms (*Figure IV.2. d)*), and instead of alternating rows, all optimized O-H distances were equal (*Table IV.1*).

IV.6. Adsorption energies

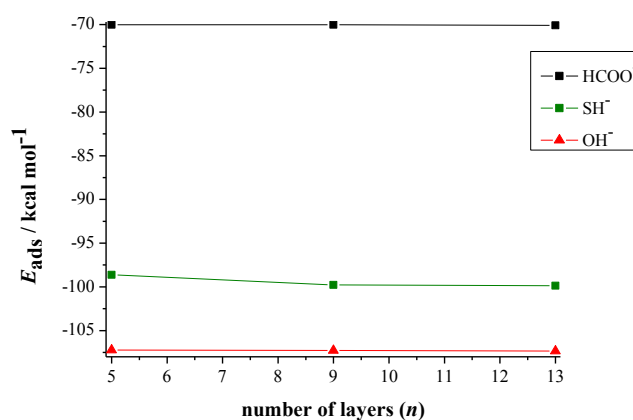


Figure IV.4. Adsorption energies of HCOO^- , OH^- and SH^- ligands on the CdSe zinc blende (100) surface (in kcal mol^{-1}) calculated according to Equation IV.2 for 5; 9 and 13 atomic layers thick slabs.

The adsorption energies of the studied ligands on slabs of different thickness have been calculated based on Equation IV.2. Bifunctional linkers that are used to attach CdSe quantum dots to wide band gap semiconductors such as ZnO and TiO_2 are typically mercaptoalcanoic acids, e.g. mercaptopropionic acid (MPA, $\text{HS-CH}_2\text{-CH}_2\text{-COOH}$).^{38–40} These molecules link to the QD with their sulfide functional group, and their carboxylate group links to the wide band gap oxide. This is in line with the reported average adsorption energies in Figure IV.4: the absolute value of the obtained adsorption energy of the SH^- ligand on the CdSe zinc blende (100) surface is higher than that of the HCOO^- ligand. One can also see in Figure IV.4 that according to the established theoretical model, the OH^- ligand is attached even more strongly to the CdSe zinc blende (100) surface than the SH^- ligand. In contrary to this result, as mentioned above, Nag et al previously observed that unlike SH^- ligands, OH^- ligands cannot be completely exchanged with the fatty acids used as capping agents during the synthesis of colloidal CdSe quantum dots,⁴ from which one could conclude that the adsorption energy of SH^- on CdSe QDs is superior to that of OH^- . However, it should be noted that the spherical quantum dots used in their study expose several different surfaces⁴¹ to which the adhesion of ligands can be different.^{42,43} Most importantly, one can remark from Figure IV.4 that the adsorption energy of the studied ligands is practically independent of the

Chapter IV. Cadmium selenide nanoplatelets

slab thickness, confirming the convergence of results on the overall of the chosen thicknesses.

IV.7. Electronic properties

Mulliken population analysis performed for 5 and 13 atomic layers thick CdSe zinc blende slabs stabilized with different ligands on their (100) surfaces is reported in *Table IV.2*. One can conclude that the difference between the charges of corresponding atoms in the uppermost layers of the slabs is negligible in case of 5 and 13 layers thick slabs with the same ligands, which indicates that increasing the thickness of these CdSe nanoplatelets does not significantly change the electronic properties of the zinc blende (100) - ligand interface, in line with the practically constant adsorption energies of the different ligands on this surface as a function of slab thickness (see before). In case of 13 layers thick slabs, regarding the evolution of the absolute values of the atomic charges of Cd and Se from the (100) surface towards the innermost layers in the [100] direction, they both converge to a value of around 0.42-0.43 $|e^-|$ (where $|e^-|$ is the elementary electron charge), close to the previously obtained 0.424 $|e^-|$ value for bulk CdSe.⁷ This shows that the ions in the innermost layers of a 13 layers thick CdSe zinc blende slab already possess bulk like charges.

The total charge of the adsorbed hydroxide ligand (-0.644 $|e^-|$) is close to that of the adsorbed formate ligand (-0.663 $|e^-|$). The relatively high atomic charges of the surface Cd (0.880-0.882 $|e^-|$) and the O atoms involved in the binding of the OH⁻ (-0.950 $|e^-|$) and HCOO⁻ ligands ($q_{O1} = -0.485 |e^-|$ and $q_{O2} = -0.610 |e^-|$) and the low bond overlap populations between them ($b_{Cd-O} = 0.150 |e^-|$ for CdSe.OH, $b_{Cd-O1} = 0.038 |e^-|$, $b_{Cd-O2} = 0.130 |e^-|$ and $b_{Cd-O1'} = 0.018 |e^-|$ for CdSe.HCOO) suggest a significant ionic character of the Cd-O bonding. On the other hand, in case of the surfaces stabilized with SH⁻ ligands, both S and corresponding Cd atoms exhibit much weaker charges ($q_{Cd} = 0.341-0.348 |e^-|$, $q_{S1} = -0.098 |e^-|$ and $q_{S2} = -0.116 |e^-|$), and one can observe a significantly higher bond overlap population between the surface Cd and S atoms ($b_{Cd-S} = 0.452 |e^-|$), suggesting the strong covalent character of the Cd-S bond.

Chapter IV. Cadmium selenide nanoplatelets

Indeed, from the computed charges it seems that a pronouncedly effective charge transfer mechanism from the SH⁻ to the CdSe slab surface takes place, the SH⁻ moiety being only very marginally negatively charged when adsorbed on the surface (of the order of -0.1 |e⁻|). Furthermore, as a consequence to the not fully symmetric arrangement of the two SH⁻ ligands, the H₁ and S₂ atoms, that are closer to each other are more negatively charged than the H₂ and S₁ atoms. This pattern of charges induced by ligands with alternate configurations is observable until the third layer in the CdSe.SH slabs.

<i>CdSe.HCOO</i>			
	<i>5 layers</i>		<i>13 layers</i>
Cd_{1a} (Cd_{5a})	+0.882	Cd_{1a} (Cd_{13a})	+0.880
Cd_{1b} (Cd_{5b})	+0.882	Cd_{1b} (Cd_{13b})	+0.880
Se_{2a} (Se_{4a})	-0.434	Se_{2a} (Se_{12a})	-0.430
Se_{2b} (Se_{4b})	-0.434	Se_{2b} (Se_{12b})	-0.430
Cd_{3a}	+0.430	Cd_{3a} (Cd_{11a})	+0.426
Cd_{3a}	+0.430	Cd_{3a} (Cd_{11a})	+0.426
O₁	-0.485	Se_{4a} (Se_{10a})	-0.427
O₂	-0.610	Se_{4a} (Se_{10a})	-0.427
C	+0.293	Cd₅ (Cd₉)	+0.424
H	+0.140	Se₆ (Se₈)	-0.427
		Cd₇	+0.423
		O₁	-0.485
		O₂	-0.611
		C	+0.293
		H	+0.140
<i>CdSe.SH</i>			
	<i>5 layers</i>		<i>13 layers</i>
Cd_{1a} (Cd_{5a})	+0.342	Cd_{1a} (Cd_{13a})	+0.341
Cd_{1b} (Cd_{5b})	+0.348	Cd_{1b} (Cd_{13b})	+0.348
Se_{2a} (Se_{4a})	-0.436	Se_{2a} (Se_{12a})	-0.435
Se_{2b} (Se_{4b})	-0.448	Se_{2b} (Se_{12b})	-0.446
Cd_{3a}	+0.448	Cd_{3a} (Cd_{11a})	+0.431
Cd_{3b}	+0.448	Cd_{3b} (Cd_{11b})	+0.440
S₁	-0.098	Se_{4a} (Se_{10a})	-0.423
S₂	-0.116	Se_{4a} (Se_{10a})	-0.423
H₁	-0.052	Cd₅ (Cd₉)	+0.423
H₂	+0.013	Se₆ (Se₈)	-0.424
		Cd₇	+0.422
		S₁	-0.097
		S₂	-0.118
		H₁	-0.049
		H₂	+0.013
<i>CdSe.OH</i>			
	<i>5 layers</i>		<i>13 layers</i>

Chapter IV. Cadmium selenide nanoplatelets

Cd_{1a} (Cd_{5a})	+0.857	Cd_{1a} (Cd_{13a})	+0.856
Cd_{1b} (Cd_{5b})	+0.857	Cd_{1b} (Cd_{13b})	+0.856
Se_{2a} (Se_{4a})	-0.434	Se_{2a} (Se_{12a})	-0.429
Se_{2b} (Se_{4b})	-0.434	Se_{2b} (Se_{12b})	-0.429
Cd_{3a}	+0.441	Cd_{3a} (Cd_{11a})	+0.432
Cd_{3b}	+0.441	Cd_{3b} (Cd_{11b})	+0.432
O	-0.949	Se_{4a} (Se_{10a})	-0.427
H	+0.306	Se_{4a} (Se_{10a})	-0.427
		Cd₅ (Cd₉)	+0.424
		Se₆ (Se₈)	-0.422
		Cd₇	+0.422
		O	-0.950
		H	+0.306

Table IV.2. Computed Mulliken atomic charges (in $|e^-|$) for 5 and 13 layers thick CdSe zinc blende slabs with HCOO⁻, OH⁻ or SH⁻ ligands adsorbed on both of its [100] basal planes. Cd and Se atoms are indicated as Cd_n and Se_n where n=1-13 and n is the number of atomic layers, n=1 and n=5 (13) being the outermost layer of the slab. The atoms in equivalent positions with respect to the (100) surfaces are shown in parentheses.

CdSe.HCOO							
Cd₁	4sp	4d	5sp	5d	6sp	6d	7sp
	4.171	5.820	0.908	3.224	0.248	0.998	3.750
O₁	1sp	2sp	3sp	3d	4sp		
	1.998	2.715	2.660	0.024	1.087		
O₂	1sp	2sp	3sp	3d	4sp		
	1.999	2.714	2.698	0.020	1.179		
CdSe.SH							
Cd_{1a}	4sp	4d	5sp	5d	6sp	6d	7sp
	4.181	5.797	0.851	3.204	0.852	1.031	3.742
Cd_{1b}	4sp	4d	5sp	5d	6sp	6d	7sp
	4.181	5.797	0.862	3.203	0.835	1.032	3.742
S₁	1s	2s+2p	3s+3p	3d	4s+4p	5s+5p	
	2.010	4.759	3.313	0.049	5.295	0.672	
S₂	1s	2s+2p	3s+3p	3d	4s+4p	5s+5p	
	2.010	4.759	3.313	0.049	5.293	0.692	
CdSe.OH							
Cd₁	4sp	4d	5sp	5d	6sp	6d	7sp
	4.171	5.815	0.826	3.223	0.365	0.993	3.750
O	1sp	2sp	3sp	3d	4sp		
	1.998	2.682	2.737	0.016	1.516		

Table IV.3. Computed Mulliken atomic orbital populations for 5 layers thick CdSe zinc blende slab with HCOO⁻, OH⁻ or SH⁻ ligands adsorbed on both of its [100] basal planes. All values are expressed in $|e^-|$.

Chapter IV. Cadmium selenide nanoplatelets

<i>CdSe.HCOO</i>							
Cd₁	4sp	4d	5sp	5d	6sp	6d	7sp
	4.17	5.82	0.90	3.22	0.25	0.9	3.75
	1	0	8	4	0	98	0
O₁	1sp	2sp	3sp	3d	4sp		
	1.99	2.71	2.66	0.02	1.08		
	8	5	0	4	7		
O₂	1sp	2sp	3sp	3d	4sp		
	1.99	2.71	2.69	0.02	1.18		
	9	5	8	0	0		
<i>CdSe.SH</i>							
Cd_{1a}	4sp	4d	5sp	5d	6sp	6d	7sp
	4.18	5.79	0.85	3.20	0.85	1.03	3.74
	1	7	1	4	3	1	2
Cd_{1b}	4sp	4d	5sp	5d	6sp	6d	7sp
	4.18	5.79	0.86	3.20	0.83	1.03	3.74
	1	7	2	3	5	2	2
S₁	1s	2s+2	3s+3	3d	4s+4	5s+5	
		p	p		p	p	
	2.01	4.75	3.31	0.04	5.29	0.67	
	0	9	3	9	4	7	
S₂	1s	2s+2	3s+3	3d	4s+4	5s+5	
		p	p		p	p	
	2.01	4.75	3.31	0.04	5.29	0.69	
	0	9	3	9	2	5	
<i>CdSe.OH</i>							
Cd₁	4sp	4d	5sp	5d	6sp	6d	7sp
	4.17	5.81	0.82	3.22	0.36	0.99	3.75
	1	5	6	3	7	3	0
O	1sp	2sp	3sp	3d	4sp		
	1.99	2.68	2.73	0.01	1.51		
	8	2	7	6	6		

Table IV.4. Computed Mulliken atomic orbital populations for 13 layers thick CdSe zinc blende slabs with HCOO⁻, OH⁻ or SH⁻ ligands adsorbed on both of its [100] basal planes. All values are expressed in |e⁻|.

In more detail, the Mulliken atomic orbital populations for Cd, O and S atomic orbitals of the CdSe-ligand interface is reported in *Table IV.3* for 5 and in *Table IV.4* for 13 layers thick slabs. One can remark that in case of the CdSe.SH system, the 6sp orbital of surface Cd atoms is filled with more electrons (0.835 or 0.853) than in the CdSe.OH (0.367) and CdSe.HCOO systems (0.250), while the other corresponding orbitals of these systems are filled with nearly the same amount of electrons. This indicates that the above mentioned charge transfer from the ligands towards the CdSe zinc blende slab is directed to the 6 sp orbitals of the surface Cd atoms. The total and orbital-projected density of states (DOS) together with the corresponding band structures are shown in *Figure IV.5*. The reported figures correspond

Chapter IV. Cadmium selenide nanoplatelets

to 13 layers thick slabs, for which the atomic charges of the innermost layers are already converged to the bulk value, as previously discussed in *Table IV.4*. The overall flat structure of the bands with the nonetheless observable energy dispersion shows that the compounds studied here have a partially ionic, partially covalent character. It is also important to note that none of the ligands introduce electronic states in the band gap.

As regards the Cd atoms of the (100) surfaces of the systems studied here, their 4d orbitals mainly contribute to the valence band of the stabilized slabs. In the CdSe.HCOO and CdSe.OH, the 2sp of the O atoms also contribute to the DOS in the valence band. The overlap between these two orbitals suggests a partially covalent character of the Cd-O bond on the (100) surfaces of the slabs. Supposing an analogy with the CdSe.OH system, the S 3p orbital should overlap with the Cd 4d in the CdSe.SH system. However, it does not contribute to the total DOS, only the S 2p core orbital, which, on the other hand, overlaps with Cd 4d, showing the covalent character of the Cd-S bond as well. Also, in case of the Cd 6sp orbital, which is more negatively charged in the CdSe.SH than in the CdSe.OH and CdSe HCOO system, the peak at around -14 eV is significantly more intense than in the other two slabs. These observations confirm again the above described charge transfer from the SH⁻ ligand to the Cd terminated CdSe zinc blende (100) surface.

The computed band gaps as a function of slab thickness together with the experimental values are listed in *Table IV.5* and shown in *Figure IV.6*. Taken all together, the computed data are in very good agreement with the experimental ones both in terms of trend and absolute value. In more detail, the results show that the gap is slightly overestimated for the HCOO⁻ and SH⁻ ligands, while the reverse holds for OH⁻ ligands. It can also be noted that the experimental E_{gap} (CdSe.OH) > E_{gap} (CdSe.SH) order is inversed in case of the computed results. It must be kept in mind however, that as it has previously been shown by FTIR spectroscopy,⁴ the ligand exchange reaction is not complete for OH⁻ ligands, contrary to SH⁻ ligands. Therefore, the synthesized, OH⁻ passivated CdSe zinc blende 2D nanocrystals are, in reality, covered by a mixture of hydroxide ligands and, in an inferior proportion, fatty acids, which can indeed increase their band gap compared to a purely OH⁻ capped nanoplatelet, such as the here established CdSe.OH model.

Chapter IV. Cadmium selenide nanoplatelets

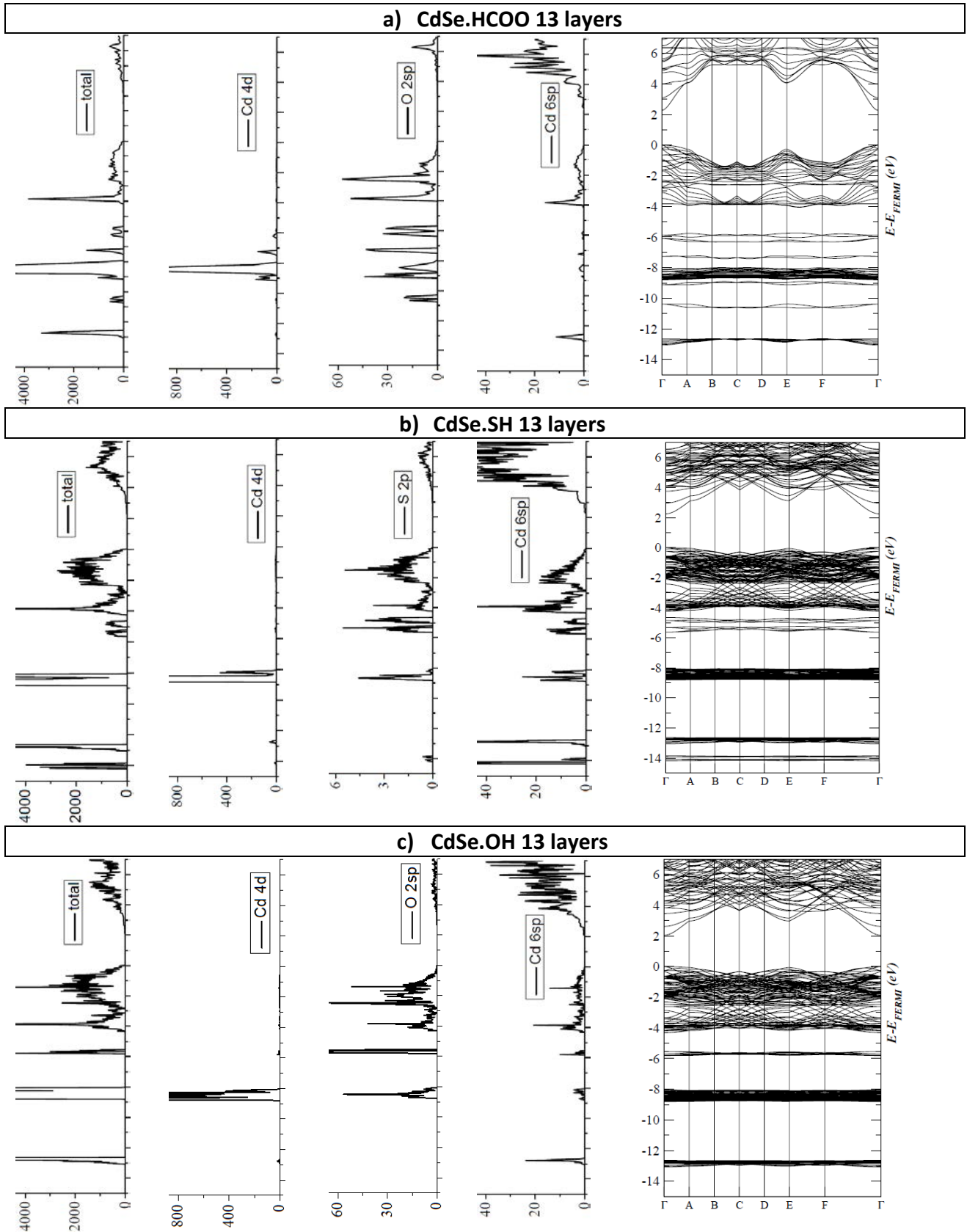


Figure IV.5. Total and orbital-projected density of states of the S and O atoms of the ligands and of the Cd atoms of the (100) surface and band structures of the a) CdSe.HCOO, b) CdSe.SH and c) CdSe.OH systems. Fermi level was set at 0 eV.

Chapter IV. Cadmium selenide nanoplatelets

	<i>n</i>	5	7	9	11	13
HCOO^-	computed	3.31	nd	2.57	nd	2.29
	experimental	3.13	2.68	2.42	2.25	2.16
SH^-	computed	3.00	nd	2.48	nd	2.25
	experimental	nd	2.46	2.29	2.15	nd
OH^-	computed	2.50	nd	2.17	nd	2.05
	experimental	nd	2.50	2.39	2.21	nd

Table IV.5. Computed and experimental band gaps (in eV) of CdSe zinc blende slabs stabilized with HCOO^- , SH^- and OH^- ligands on their (100) basal planes. nd: no data available

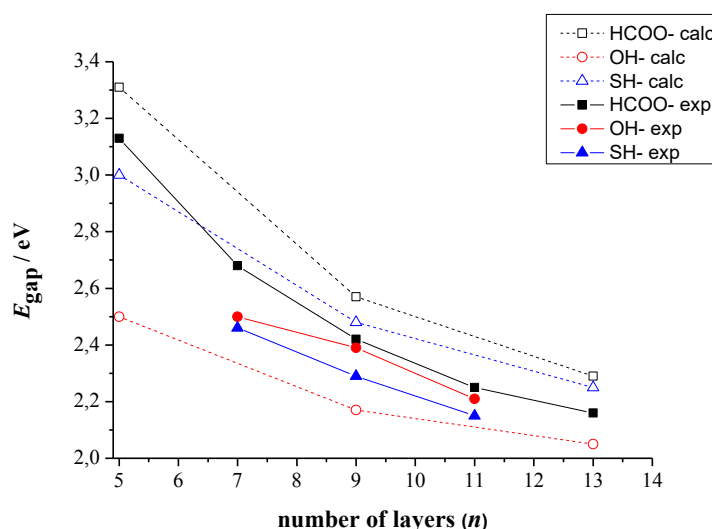


Figure IV.6. Calculated and experimental band gaps as a function of slab thickness for CdSe zinc blende slabs stabilized with HCOO^- , SH^- and OH^- ligands on their (100) basal planes. Note for the experimental values that the ligand exchange for OH^- is not complete.⁴

IV.8. Conclusions

We have performed a comprehensive density functional theory investigation of non-stoichiometric CdSe zinc blende nanoplatelets of various thicknesses and stabilized by different ligands (HCOO^- , SH^- and OH^-) on their polar (100) surface. A theoretical model has been established for these hybrid ligand-nanocrystal systems. The global hybrid B3PW91 functional was used for all calculations, combined with the SBKJC small- and large-core effective pseudopotentials for Cd and Se, respectively, and all-electron basis sets for H, C, S and O atoms. The relaxation parameters of the ligands adsorbed on the (100) surface of the

Chapter IV. Cadmium selenide nanoplatelets

nanoplatelets have been calculated, along with their adsorption energies. We found that these parameters do not change with the thickness of the nanoplatelets, confirming the convergence of these properties on the overall of the chosen thicknesses. Regarding the electronic properties, the band gaps, band structures and orbital-projected density of states of the stabilized nanoplatelets have been calculated, along with a detailed Mulliken analysis of the atomic and orbital charges. The latter revealed a major electron transfer from the SH⁻ ligands towards the surface of the nanocrystals, in line with what can be inferred from the density of states. CdSe zinc blende nanoplatelets of various thicknesses, stabilized by fatty acids, SH⁻ and OH⁻ ligands have also been synthesized, and their band gaps have been measured by absorption spectroscopy. A nice agreement is found between the experimental and calculated band gaps, especially concerning the evolution of the band gaps with the thickness of the nanoplatelets. We can thus conclude that the chosen theoretical model and computational protocol together can serve as a powerful tool for the qualitative and quantitative description of the geometrical and electronic properties of CdSe nanoplatelets, which can potentially be applied in solar cells and various advanced optoelectronic applications. In the next chapter, the potential photoanode of a solar cell is simulated as a CdSe.SH – ZnO heterostructure, using the same computational protocol and the same CdSe.SH model as in this chapter. The results of the theoretical investigation are confirmed and completed by experimental measurements.

Chapter IV. Cadmium selenide nanoplatelets

References

- (1) Ithurria, S.; Tessier, M. D.; Mahler, B.; Lobo, R. P. S. M.; Dubertret, B.; Efros, A. L. Colloidal Nanoplatelets with Two-Dimensional Electronic Structure. *Nat. Mater.* **2011**, *10*, 936–941.
- (2) Kunne, L. T.; Tessier, M. D.; Heuclin, H.; Dubertret, B.; Aulin, Y. V.; Grozema, F. C.; Schins, J. M.; Siebbeles, L. D. A. Bimolecular Auger Recombination of Electron–Hole Pairs in Two-Dimensional CdSe and CdSe/CdZnS Core/Shell Nanoplatelets. *J. Phys. Chem. Lett.* **2013**, *4*, 3574–3578.
- (3) Bouet, C.; Mahler, B.; Nadal, B.; Abecassis, B.; Tessier, M. D.; Ithurria, S.; Xu, X.; Dubertret, B. Two-Dimensional Growth of CdSe Nanocrystals, from Nanoplatelets to Nanosheets. *Chem. Mater.* **2013**, *25*, 639–645.
- (4) Nag, A.; Kovalenko, M. V.; Lee, J.; Liu, W.; Spokoyny, B.; Talapin, D. V. Metal-Free Inorganic Ligands for Colloidal Nanocrystals: S²⁻, HS⁻, Se²⁻, HSe⁻, Te²⁻, HTe⁻, TeS₃²⁻, OH⁻, and NH₂⁻ as Surface Ligands. *J. Am. Chem. Soc.* **2011**, *133*, 10612–10620.
- (5) Dovesi, R.; Saunders, V. R.; Roetti, C.; Orlando, R.; Zicovich-Wilson, C. M.; Pascale, F.; Civalieri, B.; Doll, K.; Harrison, N. M.; Bush, I. J.; et al. Crystal09 User's Manual, 2013.
- (6) Dovesi, R.; Orlando, R.; Civalieri, B.; Roetti, C.; Saunders, V. R.; Zicovich-Wilson, C. M. CRYSTAL: A Computational Tool for the Ab Initio Study of the Electronic Properties of Crystals. *Zeitschrift für Krist. - Cryst. Mater.* **2005**, *220*, 571–573.
- (7) Szemjonov, A.; Pauporté, T.; Ciofini, I.; Labat, F. Investigation of the Bulk and Surface Properties of CdSe: Insights from Theory. *Phys. Chem. Chem. Phys.* **2014**, *16*, 23251–23259.
- (8) Becke, A. D. Density-Functional Thermochemistry. III. The Role of Exact Exchange. *J. Chem. Phys.* **1993**, *7*, 5648–5652.
- (9) Xiao, H.; Tahir-Kheli, J.; Goddard, W. A. Accurate Band Gaps for Semiconductors from Density Functional Theory. *J. Phys. Chem. Lett.* **2011**, *2*, 212.
- (10) Stevens, W. J.; Krauss, M.; Basch, H.; Jasien, P. G. Relativistic Compact Effective Potentials and Efficient, Shared-Exponent Basis Sets for the Third-, Fourth-, and Fifth-Row Atoms. *Can. J. Chem.* **1992**, *70*, 612–630.
- (11) Labello, N. P.; Ferreira, A. M.; Kurtz, H. a. An Augmented Effective Core Potential Basis Set for the Calculation of Molecular Polarizabilities. *J. Comput. Chem.* **2005**, *26*, 1464–1471.
- (12) Marsman, M.; Paier, J.; Stroppa, A.; Kresse, G. Hybrid Functionals Applied to Extended Systems. *J. physics. Condens. matter* **2008**, *20*, 064201.
- (13) Towler, M. D.; Zupan, A.; Causa, M. Density Functional Theory in Periodic Systems Using Local Gaussian Basis Sets. *Comput. Phys. Commun.* **1996**, *98*, 181.
- (14) Corà, F.; Alfredsson, M.; Mallia, G.; Middlemiss, D. S.; Mackrodt, W. C.; Dovesi, R.; Orlando, R. The Performance of Hybrid Density Functionals in Solid State Chemistry. In *Structure and Bonding*; Springer-Verlag Berlin Heidelberg, 2004; Vol. 113, p. 171.
- (15) Orlando, R.; Delle Piane, M.; Bush, I. J.; Ugliengo, P.; Ferrabone, M.; Dovesi, R. A New Massively Parallel Version of CRYSTAL for Large Systems on High Performance Computing Architectures. *J. Comput. Chem.* **2012**, *33*, 2276–2284.
- (16) Labat, F.; Ciofini, I.; Adamo, C. Modeling ZnO Phases Using a Periodic Approach: From Bulk to Surface and Beyond. *J. Chem. Phys.* **2009**, *131*, 044708.
- (17) Peintinger, M. F.; Oliveira, D. V.; Bredow, T. Consistent Gaussian Basis Sets of Triple-Zeta Valence with Polarization Quality for Solid-State Calculations. *J. Comput. Chem.* **2013**, *34*, 451–459.
- (18) Monkhorst, H. J.; Pack, J. D. Special Points for Brillouin-Zone Integrations. *Phys. Rev. B* **1976**, *13*, 5188–5192.
- (19) Tasker, P. W. The Stability of Ionic Crystal Surfaces. *J. Phys. C Solid State Phys.* **1979**, *12*, 4977–4984.
- (20) Evarestov, R. a.; Kotomin, E. a.; Fuks, D.; Felsteiner, J.; Maier, J. Ab Initio Calculations of the LaMnO₃ Surface Properties. *Appl. Surf. Sci.* **2004**, *238*, 457–463.
- (21) Zakharov, O.; Rubio, A.; Cohen, M. L. Calculated and Electronic Properties of CdSe under Pressure. *Phys. Rev. B* **1995**, *51*, 4926–4930.
- (22) Siemens, B.; Domke, C.; Ebert, P.; Urban, K. Electronic Structure of Wurtzite II-VI Compound Semiconductor Cleavage Surfaces Studied by Scanning Tunneling Microscopy. *Phys. Rev. B* **1997**, *56*, 12321–12326.
- (23) Wang, Y. R.; Duke, C. B. Cleavage Faces of Wurtzite CdS and CdSe: Surface Relaxation and Electronic

Chapter IV. Cadmium selenide nanoplatelets

- Structure. *Phys. Rev. B* **1988**, 37, 6417–6424.
- (24) Csik, I.; Russo, S. P.; Mulvaney, P. Density Functional Study of Non-Polar Surfaces of Wurtzite CdSe. *Chem. Phys. Lett.* **2005**, 414, 322–325.
- (25) Schapotschnikow, P.; Hommersom, B.; Vlugt, T. J. H. Adsorption and Binding of Ligands to CdSe Nanocrystals. *J. Phys. Chem. C* **2009**, 113, 12690–12698.
- (26) Rabani, E. Structure and Electrostatic Properties of Passivated CdSe Nanocrystals. *J. Chem. Phys.* **2001**, 115, 1493.
- (27) Manna, L.; Wang, L. W.; Cingolani, R.; Alivisatos, A. P. First-Principles Modeling of Unpassivated and Surfactant-Passivated Bulk Facets of Wurtzite CdSe: A Model System for Studying the Anisotropic Growth of CdSe Nanocrystals. *J. Phys. Chem. B* **2005**, 109, 6183–6192.
- (28) Li, Z.; Peng, X. Size/shape-Controlled Synthesis of Colloidal CdSe Quantum Disks: Ligand and Temperature Effects. *J. Am. Chem. Soc.* **2011**, 133, 6578–6586.
- (29) Liu, L.; Zhuang, Z.; Xie, T.; Wang, Y.-G.; Li, J.; Peng, Q.; Li, Y. Shape Control of CdSe Nanocrystals with Zinc Blende Structure. *J. Am. Chem. Soc.* **2009**, 131, 16423–16429.
- (30) Yu, K.; Singh, S.; Patrito, N.; Chu, V. Effect of Reaction Media on the Growth and Photoluminescence of Colloidal CdSe Nanocrystals. *Langmuir* **2004**, 20, 11161–11168.
- (31) Cooper, J. K.; Franco, A. M.; Gul, S.; Corrado, C.; Zhang, J. Z. Characterization of Primary Amine Capped CdSe, ZnSe, and ZnS Quantum Dots by FT-IR: Determination of Surface Bonding Interaction and Identification of Selective Desorption. *Langmuir* **2011**, 27, 8486–8493.
- (32) Zhu, L.; Yao, K. L.; Liu, Z. L.; Li, Y. B. First-Principles Studies of the Atomic Reconstructions of CdSe (001) and (111) Surfaces. *J. Phys. Condens. Matter* **2009**, 21, 095001.
- (33) Manna, L.; Milliron, D. J.; Meisel, A.; Scher, E. C.; Alivisatos, A. P. Controlled Growth of Tetrapod-Branched Inorganic Nanocrystals. *Nat. Mater.* **2003**, 2, 382–385.
- (34) Talapin, D. V.; Rogach, A. L.; Kornowski, A.; Haase, M.; Weller, H. Highly Luminescent Monodisperse CdSe and CdSe/ZnS Nanocrystals Synthesized in a Hexadecylamine–Trioctylphosphine Oxide–Trioctylphosphine Mixture. *Nano Lett.* **2001**, 1, 207–211.
- (35) Benchamekh, R.; Gippius, N. A.; Even, J.; Nestoklon, M. O.; Jancu, J.-M.; Ithurria, S.; Dubertret, B.; Efros, A. L.; Voisin, P. Tight-Binding Calculations of Image-Charge Effects in Colloidal Nanoscale Platelets of CdSe. *Phys. Rev. B* **2014**, 89, 035307.
- (36) Benchamekh, R.; Even, J.; Jancu, J.; Nestoklon, M.; Ithurria, S.; Dubertret, B.; Voisin, P. Electronic and Optical Properties of Colloidal CdSe Nanoplatelets. In *Nanosstructures: Physics and Technology*; Nizhny Novgorod, Russia, 2012; p. 56.
- (37) Tessier, M. D.; Javaux, C.; Maksimovic, I.; Lorient, V.; Dubertret, B. Spectroscopy of Single CdSe Nanoplatelets. *ACS Nano* **2012**, 6, 6751–6758.
- (38) Mora-Seró, I.; Giménez, S.; Moehl, T.; Fabregat-Santiago, F.; Lana-Villareal, T.; Gómez, R.; Bisquert, J. Factors Determining the Photovoltaic Performance of a CdSe Quantum Dot Sensitized Solar Cell: The Role of the Linker Molecule and of the Counter Electrode. *Nanotechnology* **2008**, 19, 424007.
- (39) Robel, I.; Subramanian, V.; Kuno, M.; Kamat, P. V. Quantum Dot Solar Cells. Harvesting Light Energy with CdSe Nanocrystals Molecularly Linked to Mesoscopic TiO₂ Films. *J. Am. Chem. Soc.* **2006**, 128, 2385–2393.
- (40) Dibbell, R. S.; Watson, D. F. Distance-Dependent Electron Transfer in Tethered Assemblies of CdS Quantum Dots and TiO₂ Nanoparticles. *J. Phys. Chem. C* **2009**, 113, 3139.
- (41) Yang, Y. A.; Wu, H.; Williams, K. R.; Cao, Y. C. Synthesis of CdSe and CdTe Nanocrystals without Precursor Injection. *Angew. Chem. Int. Ed. Engl.* **2005**, 44, 6712–6715.
- (42) Peng, Z. A.; Peng, X. Mechanisms of the Shape Evolution of CdSe Nanocrystals. *J. Am. Chem. Soc.* **2001**, 123, 1389.
- (43) Owen, J. S.; Park, J.; Trudeau, P.-E.; Alivisatos, A. P. Reaction Chemistry and Ligand Exchange at Cadmium-Selenide Nanocrystal Surfaces. *J. Am. Chem. Soc.* **2008**, 130, 12279.

V.1. Context

The first challenge in fabricating QDSCs is the preparation of the photoanode. The WBSC substrate with a high surface area is expected to be generously and homogeneously covered with QDs. It can be demanding to fulfill these requirements when combining pre-synthesized, bifunctional ligand-capped nanocrystals with ZnO/TiO₂ nanorods for photovoltaic application. In the literature, pre-synthesized sensitizers are typically attached to mesoporous ZnO or TiO₂ substrates made of spherical nanoparticles.¹⁻⁴ Very few articles can be found about ligand-capped QDs being attached to ZnO or TiO₂ nanorods, and these studies reported low QD loading and solar cell efficiency.⁵⁻⁷ As what concerns nanoplatelets, the main focus of this thesis, up to this date, no articles have reported their photovoltaic application, and not even their attachment to ZnO and TiO₂ nanorods.

As detailed in **Chapter II** section **II.2.3. a)**, the first step of the linker-assisted attachments was to exchange the oleic acid (OA) passivating ligands of the CdSe nanocrystals (nanoplatelets of various thicknesses and spherical QDs) to smaller bifunctional ligands (SH⁻, OH⁻ and MPA). Next, the nanocrystals were linked to ZnO and TiO₂ nanorod arrays (resumed as WBSC in the following) *via* bifunctional ligands. Likewise, the coming subsections start with the characterization of the CdSe nanocrystals before and after ligand exchange. This is followed by the analysis of the CdSe-ligand-WBSC heterostructures. The samples studied in this chapter were characterized by UV-VIS absorption and Raman spectroscopy.

Quasi-2D nanostructures have a step function-like absorption spectra with a high-intensity peak at each tread of a stair. As the latter is due to the creation of excitons in these quantum confined systems, these peaks are known as *excitonic peaks*. The absorption spectra of 3D-confined quantum dots also feature an *excitonic peak* structure due to the widening of discrete spectral lines, which is caused by heterodisperse QD size distribution and phonon-photon coupling. Changes in the shape and the position of *excitonic peaks* indicate structural changes in the nanocrystals, therefore their absorption spectra provides interesting insights into the functionalization of the nanocrystals, and their subsequent attachment to ZnO/TiO₂

Chapter V. Hybrid semiconductor heterostructures

nanorods. In the following, we will only concentrate on the position of the first excitonic peak, which corresponds to the lowest energy electron excitation,⁸ the energy of which we associated with the band gap of these nanocrystals. It is to note that although the spectra of dispersions and solid thin layers were recorded with different spectrophotometers, they are all reported on the same figure in order to compare peak positions. For clarity, all spectra were scaled to the same order of magnitude.

Raman spectroscopy can efficiently identify crystal phases, since the frequency of lattice vibrations (*phonons*) is specific to crystal geometry. The shape, width and the position of peaks in a crystal's Raman spectra are very sensitive to structural changes. In more particular, Raman spectroscopy has been demonstrated to be a useful method for characterizing semiconductor surfaces and interfaces, since the surface (interface) formation gives rise to characteristic Raman modes which reflect the surface (interfacial) geometry and strain.⁹ In this study, we were interested to see how Raman spectroscopy reflects the structural changes induced by sensitization in the semiconductors.

V.2. ZnO and TiO₂ nanorod arrays

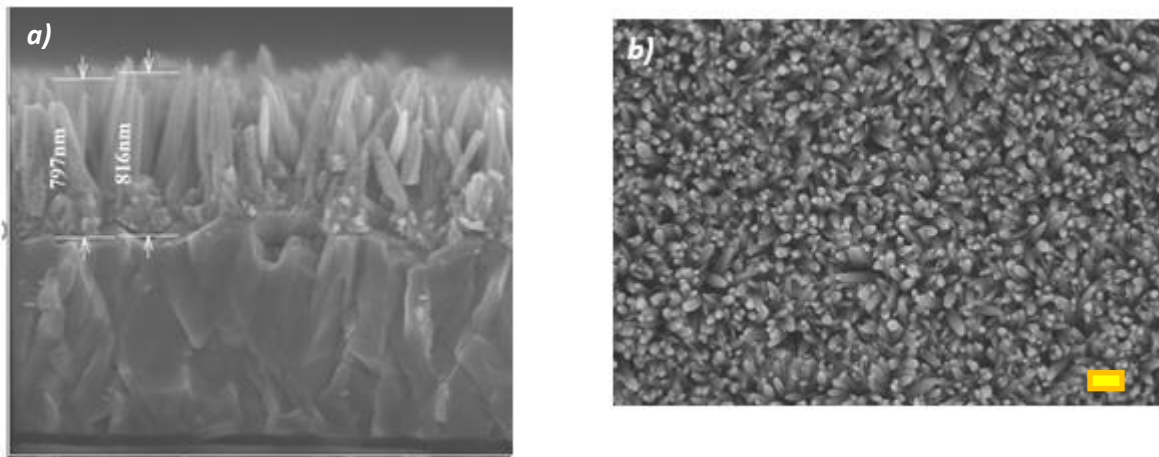


Figure V.1. a) Cross-sectional and b) top-view SEM images of ZnO NRs. The yellow scale bar is 1 μm long.

The SEM images (Figure V.1), reveal that the synthesized ZnO nanorod arrays are vertically aligned along the *c* axis, and are around 800 nm long. The vertical alignment is also

Chapter V. Hybrid semiconductor heterostructures

confirmed by X-ray diffraction (XRD) analysis (*Figure V.2*), as the peak corresponding to the (002) facet of the nanorods has significantly higher intensity than the other ones. *Figure V.2* also reveals that the resulting ZnO nanorods are of the hexagonal wurtzite phase. In agreement with XRD, the Raman spectra of the ZnO NR substrate (*Figure V.3*) also features peaks corresponding to vibrations of the ZnO wurtzite lattice.^{10,11}

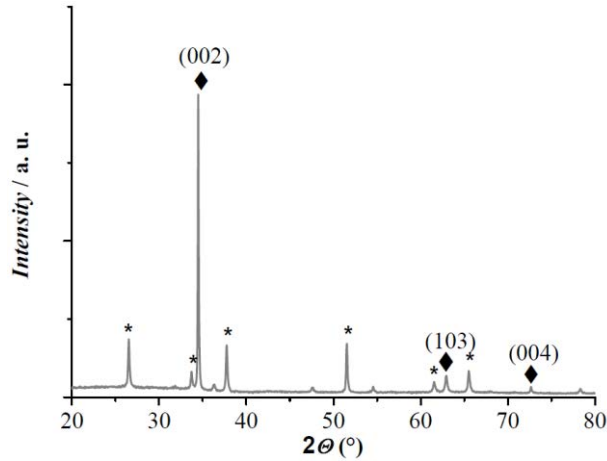


Figure V.2. XRD analysis of ZnO NRs. Peaks marked with an asterisk correspond to the cubic phase of SnO_2 on the TCO glass substrate (standard JCPDS card N°04-008-8130), while those marked with a diamond correspond to the different crystal planes of wurtzite ZnO (standard JCPDS N° 01-070-8072)

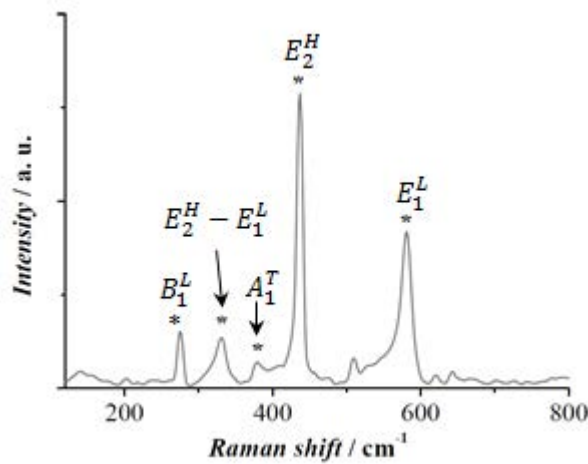


Figure V.3. Raman spectra of ZnO NRs with characteristic ZnO wurtzite peaks.

The SEM images of the synthesized TiO_2 nanorods are reported in *Figure V.4*. The nanorods are well-aligned along the c axis, and are stuck together in bunches. The XRD patterns reported in *Figure V.5* and the Raman spectra in *Figure V.6* show that the nanorods are of the rutile phase of TiO_2 .¹²

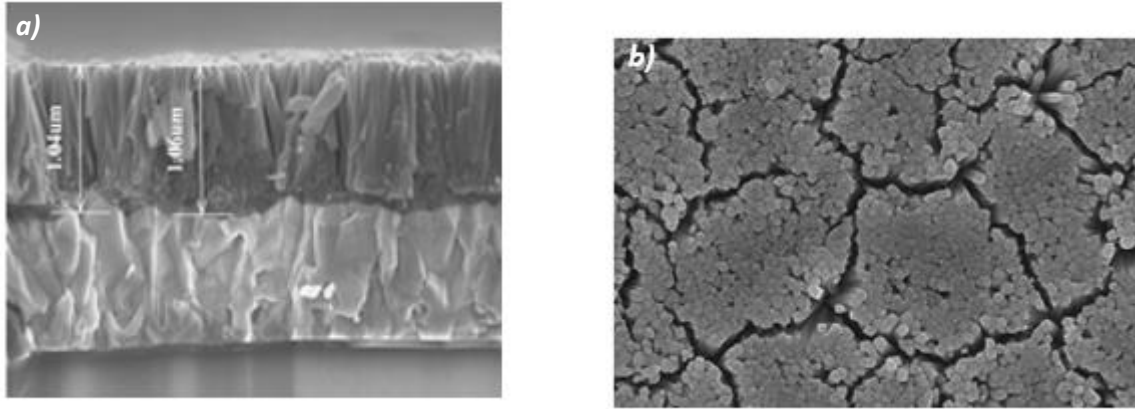


Figure V.4. a) Cross-sectional and b) top-view SEM images of TiO_2 nanorods arrays. The yellow scale bar is 1 μm long.

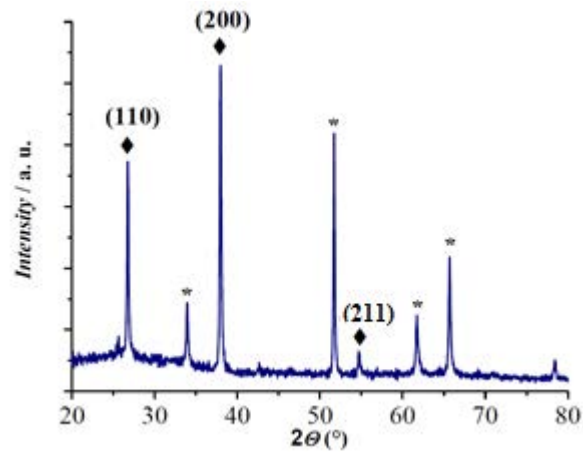


Figure V.5. XRD patterns of TiO_2 nanorod arrays. Peaks marked with an asterisk correspond to the cubic phase of SnO_2 on the TCO glass substrate (standard JCPDS card N° 04-008-8130), while those marked with a diamond correspond to the different crystal planes of the rutile phase of TiO_2 (standard JCPDS N° 04-005-4692).

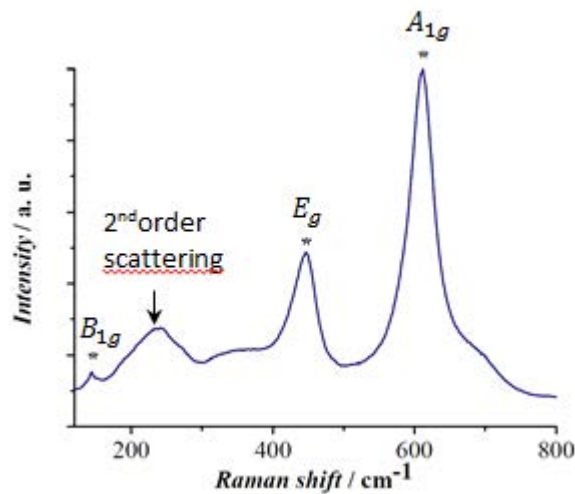


Figure V.6. Raman spectra of TiO_2 nanorod arrays with characteristic TiO_2 rutile peaks. Peaks corresponding to first-order scattering are marked with an asterisk.

V.3. Attachment of CdSe nanoplatelets to WBSC *via* SH⁻ ligands

The $\text{OA} \leftrightarrow \text{SH}^-$ ligand exchange changes the color of the NPL dispersions, which manifests in the redshift of the NPL excitonic peaks in the UV-VIS absorption spectra, as illustrated in *Figure V.7*. As discussed in previous chapters, due to the quantum confinement effects, the band gap of the NPLs (associated with the position of the first excitonic peak in this work) varies with NPL thickness. Hence, the redshift is explained by the fact that ligand exchange results in the addition of a sulfide layer on the two Cd-rich (100) facets of the nanoplatelets.^{13,14} The resulting sulfide-passivated NPLs can thus be regarded as *quasi-(n+2)* layers thick nanocrystals if they originally consisted of *n* atomic layers. This hypothesis is confirmed by the observation that the first excitonic peak of *n* layers thick CdSe.SH NPLs is approximately at the same wavelength as that of (*n*+2) layers thick CdSe.OA NPLs, indicating a similar degree of quantum confinement in the two systems. Other observable feature of the CdSe.SH absorption spectra is that its peaks are wider and less structured than those of the CdSe.OA peaks, which suggests that the addition of sulfide layers distorts the CdSe NPL crystal structure.

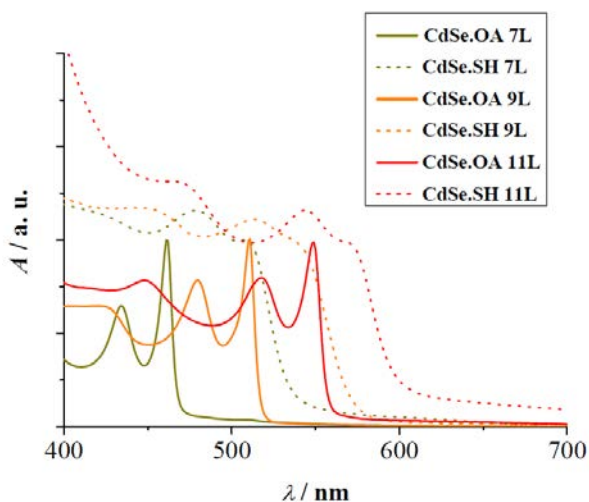


Figure V.7. UV-VIS absorption spectra of CdSe NPLs of different thicknesses (7, 9 and 11 layers). NPLs passivated by oleic acid (OA) are indicated as full, while NPLs after ligand exchange with SH⁻ are shown as dotted lines.

When attached to ZnO nanorods, the dispersion of CdSe.SH NPLs of all thicknesses formed a homogeneous colored layer on the ZnO substrate, as demonstrated by the SEM views in

Chapter V. Hybrid semiconductor heterostructures

Figure V.8. The UV-VIS absorption spectra of these heterostructures are reported in *Figure V.9*, along with the UV-VIS absorption spectra of the bare NPLs for comparison. A redshift of the CdSe.SH NPLs excitonic peaks could be observed for all NPL thicknesses considered in this study. This suggests that significant structural changes took place in the NPLs upon attachment to the ZnO nanorod arrays. In order to make sure that this shift was not the result of the aggregation of the NPLs on the ZnO substrate, the absorption spectrum of a sample prepared with 7 layers thick NPLs, rinsed with ethanol after sensitization, was also recorded and shown in *Figure V.9*. Although the peaks in its UV-VIS absorption spectra (indicated by a dotted line *Figure V.9*) were less structured, the sensitization still resulted in a redshift of the excitonic peaks confirming the attachment of the nanostructures.

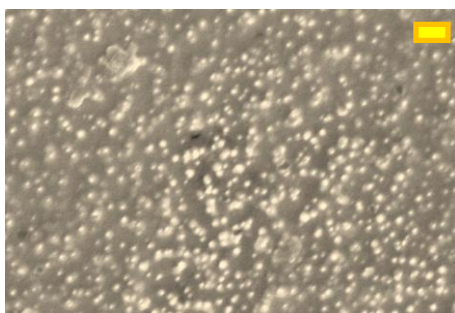


Figure V.8. Top SEM view of ZnO nanorod arrays sensitized by 9 layers thick CdSe.SH nanoplatelets. The length of the yellow scalebar is 1 μm .

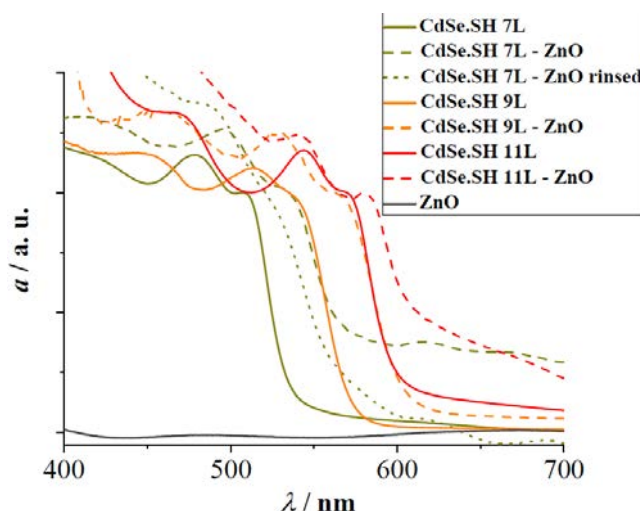


Figure V.9. UV-VIS absorption spectra of ZnO nanorod arrays and 7, 9 and 11 layers thick CdSe.SH NPLs in dispersion (indicated by green, orange and red full lines, respectively) and after attachment to ZnO nanorod arrays (indicated by dashed lines of the corresponding color, and by a dotted line after consequent washing with ethanol).

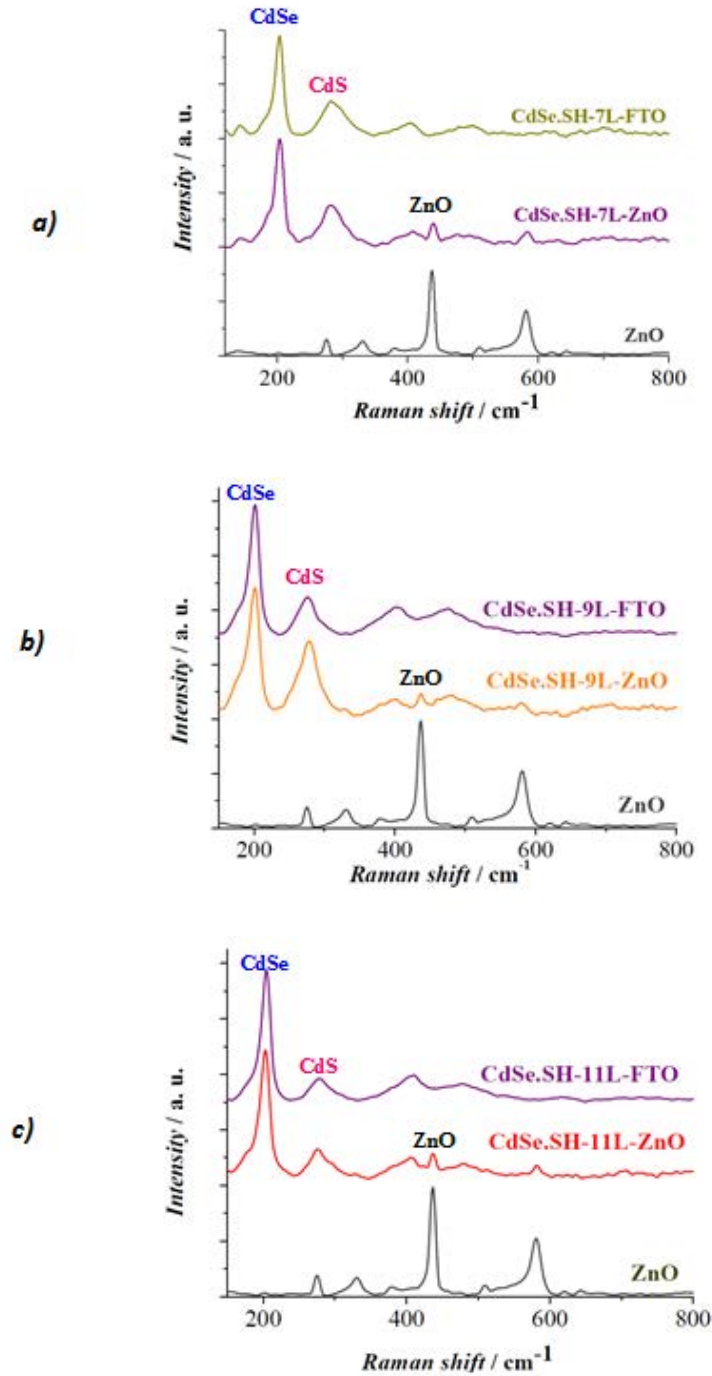
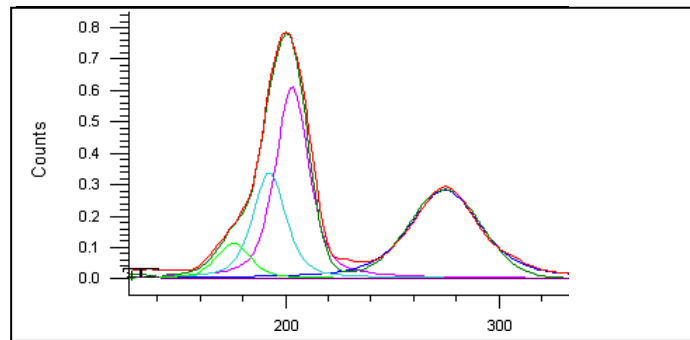


Figure V.10. Raman spectra of a) 7, b) 9 and c) 11 layers thick CdSe.SH NPLs, of ZnO nanorod arrays sensitized by the same NPLs and of bare ZnO nanorod arrays.

In Figure V.10, the Raman spectra of CdSe.SH NPLs of different thicknesses on FTO glasses is compared to the spectra of CdSe.SH-ZnO heterostructures and that of the bare ZnO nanorod arrays (which had already been in Figure V.3). The experimental Raman spectra of the isolated CdSe.SH NPLs of different thicknesses on the bare FTO-coated glass (represented as purple curves in Figure V.10) features peaks related to the zinc blende phase of CdSe and

Chapter V. Hybrid semiconductor heterostructures

CdS. The reported spectra are globally very similar to previously published spectra of zinc blende CdSe/CdS core shell quantum dots^{15,16}. The first peak at around 200 cm^{-1} is attributed to the CdSe zinc blende longitudinal optical (LO) mode. Its broadening towards the lower frequencies can be explained by the presence of interface and surface optical phonons,¹⁵ as shown in *Figure V.11*. The peak at around 280 cm^{-1} is attributed to the LO mode of the zinc blende phase of CdS, although redshifted from its bulk position near 300 cm^{-1} . It is due to the large strain that the single CdS layer suffers at the interface, as observed previously for CdSe/CdS core/shell QDs with a thin CdS shell.^{15–18} The other modes observed for Raman shifts above 400 cm^{-1} correspond to overtones and mixed modes.^{15,18} On the experimental Raman spectra of the CdSe.SH NPL-sensitized ZnO nanorod arrays (reported in *Figure V.10*), we can observe the superposition of peaks characteristic of the bare NPLs and of the bare ZnO substrate, although the latter has a low intensity compared to the NPL peaks. Therefore, only the highest intensity ZnO peak, E_2^H is observable in these spectra at 438 cm^{-1} . In *Figure V.10.*, we did not observe a significant shift of the Raman peaks of the semiconductor components after they are linked. In order to account for the changes that the CdSe.SH – ZnO interface formation induces in the Raman shifts, or the eventual formation of interface modes, a more refined measurement is needed.



Curve name	Centre (nm)	Width (nm)	Height (counts)	% Gaussian
CdS interface	274.6	39.66	0.2839	100
CdSe bulk LO	202.9	18.30	0.6198	100
CdSe SO	192.3	18.30	0.3399	50
CdSe TO	175.4	18.30	0.1147	50

Figure V.11. Decomposition of the CdSe- and CdS-related peaks in the experimental Raman spectra of 9 layers thick CdSe.SH NPLs. Surface optical modes are denoted as SO, transverse optical mode as TO.

Chapter V. Hybrid semiconductor heterostructures

When attached to TiO_2 nanorods, the dispersion of CdSe.SH NPLs of all thicknesses formed a homogeneous colored layer on the TiO_2 substrate, as illustrated in *Figure V.12*. The UV-VIS absorption spectra of these heterostructures are reported in *Figure V.13*, along with the UV-VIS absorption spectra of the bare NPLs for comparison. It can be observed for all NPL thicknesses that the NPL excitonic peaks are redshifted after the NPLs attachment to the oxide. However, they are far less structured in case of 7 layers thick NPLs than for 9 and 11 layers thick NPLs, suggesting that the original NPL structure is more distorted upon attachment to TiO_2 NRs if the nanocrystals are thinner.

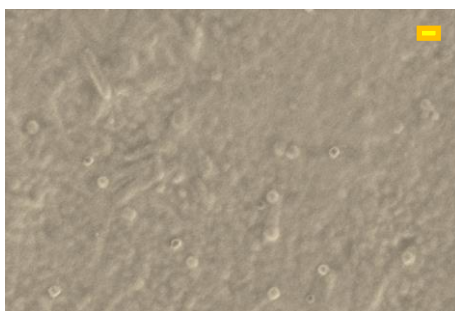


Figure V.12. Top SEM view of TiO_2 nanorod arrays sensitized by 9 layers thick CdSe.SH nanoplatelets. The length of the yellow scalebar is 1 μm .

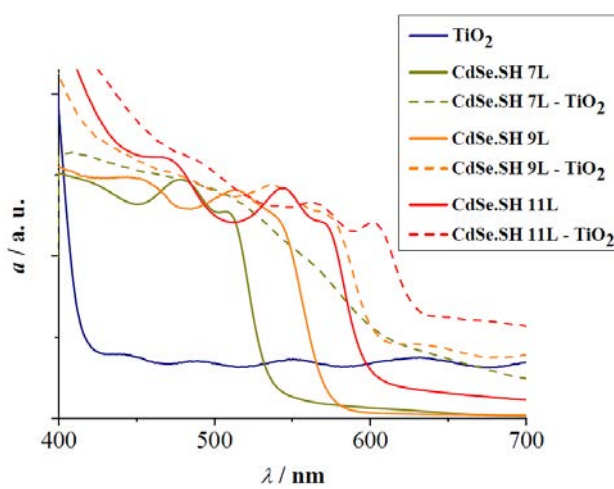


Figure V.13. UV-VIS absorption spectra of TiO_2 nanorod arrays and 7, 9 and 11 layers thick CdSe.SH NPLs in dispersion (indicated by green, orange and red full lines, respectively) and after attachment to TiO_2 nanorod arrays (indicated by dashed lines of the corresponding color)

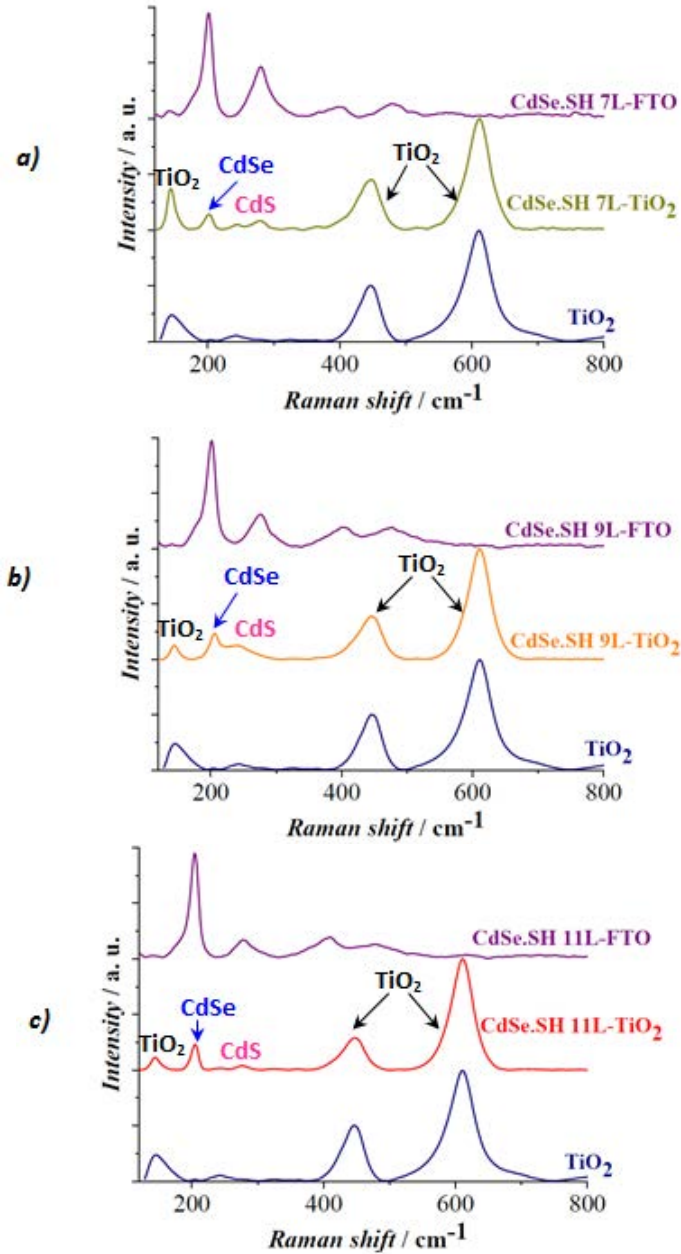


Figure V.14. Raman spectra of a) 7, b) 9 and c) 11 layers thick CdSe.SH NPLs, of TiO₂ nanorod arrays sensitized by the same NPLs and of bare TiO₂ nanorod arrays.

On the experimental Raman spectra of the CdSe.SH NPL-sensitized TiO₂ nanorod arrays (reported in Figure V.14), we can observe the superposition of the characteristic peaks of the bare NPLs and of the bare TiO₂ substrate, although the latter has a very high intensity compared to the NPL peaks. Similarly to what was observed in the Raman spectra CdSe.SH – ZnO systems reported in Figure V.10, the NPL- and TiO₂-related peaks observed in the Raman spectra of the CdSe.SH – TiO₂ heterostructures are found at the same Raman shift as in the Raman spectra of the bare NPLs and of the TiO₂ nanorod substrate.

V.4. Attachment of CdSe nanoplatelets to WBSC *via* OH⁻ ligands

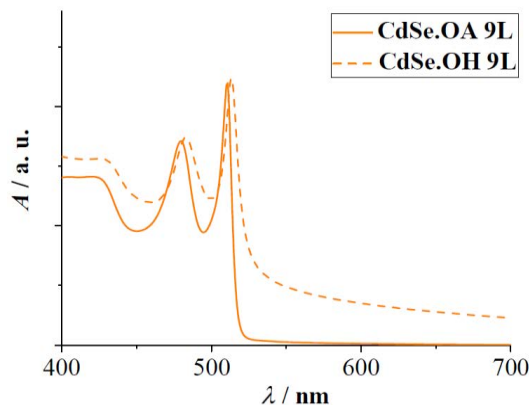


Figure V.15. UV-VIS absorption spectra of 9 layers thick CdSe NPLs before and after ligand exchange with OH⁻ (indicated by full and dotted lines, respectively).

In case of 7 and 11 L thick NPLs, the ligand exchange reaction with OH⁻ resulted in the aggregation of the NPLs, and no homogeneous solution could be obtained. This observation is in accordance with a previous study in which it was demonstrated by FTIR that the OA \leftrightarrow OH⁻ exchange on CdSe.QDs is only partial, in contrary to the OA \leftrightarrow SH⁻ exchange.¹⁹ However, in case of 9 L thick NPLs, it was possible to obtain a homogeneous NPL dispersion after the biphasic OA \leftrightarrow OH⁻ ligand exchange. The UV-VIS absorption spectra of 9 L thick CdSe.OA and CdSe.OH NPLs are compared in Figure V.15. Only a very slight redshift of the excitonic peaks can be observed as the OA ligands are exchanged to OH⁻.

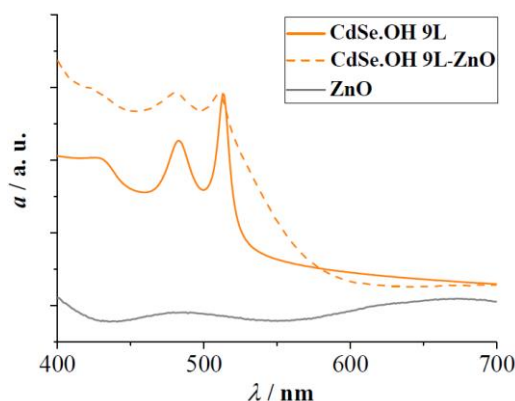


Figure V.16. UV-VIS absorption spectra of ZnO nanorod arrays and 9 layers thick CdSe.OH NPLs in dispersion (indicated by orange full lines) and after attachment to ZnO nanorod arrays (indicated by orange dashed lines)

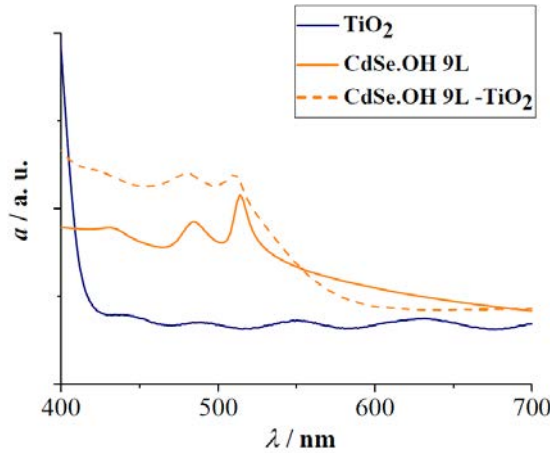


Figure V.17. UV-VIS absorption spectra of TiO_2 nanorod arrays and 9 layers thick CdSe.OH NPLs in dispersion (indicated by orange full lines) and after attachment to TiO_2 nanorod arrays (indicated by orange dashed lines)

It can be observed on the corresponding UV-VIS absorption spectra presented in *Figures V.16. and V.17.* that after sensitization, the NPL excitonic peaks are only slightly blueshifted with respect to their position in the spectra of the bare NPL, and this effect is more enhanced when they are attached to TiO_2 nanorods. This blueshift indicates a slight decrease in their thickness upon sensitization (presumably due to compressive strain along the thickness), in contrary to what was observed in case of CdSe.SH NPLs. The compression of lattice constants in the c direction results in the lateral expansion of lattice parameters according to Poisson's law. Indeed, this horizontal lattice expansion is manifested in the slight redshift of NPL-related CdSe LO Raman peak, as reported in *Figures V.18. and V.19.* and *Table V.1.* The ZnO or TiO_2 related peaks stay in the same position as in the Raman spectra of the bare ZnO or TiO_2 NR arrays.

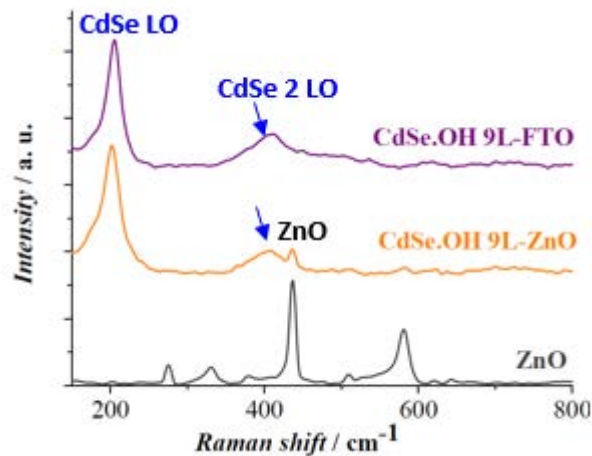


Figure V.18. Raman spectra of 9 layers thick CdSe.SH NPLs, of ZnO nanorod arrays sensitized by the same NPLs and of bare ZnO nanorod arrays.

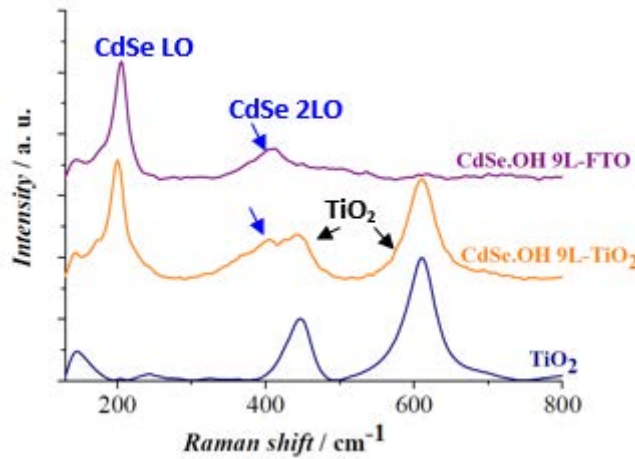


Figure V.19. Raman spectra of 9 layers thick CdSe.SH NPLs, of TiO₂ nanorod arrays sensitized by the same NPLs and of bare TiO₂ nanorod arrays.

sample	Raman shift of the CdSe LO peak (cm ⁻¹)
CdSe.OH 9L - FTO	205
CdSe.OH 9L - ZnO	201
CdSe.OH 9L - TiO ₂	200

Table V.1. Raman shift of the CdSe LO peak before and after the CdSe.OH NPLs are attached to ZnO or TiO₂ nanorods

V.5. Attachment of CdSe nanoplatelets to WBSC via MPA ligands

Similarly to $\text{OA} \leftrightarrow \text{SH}^-$ ligand exchange reactions on CdSe NPLs, their passivation by MPA also resulted in the redshift of excitonic peaks, which became less structured than those of CdSe.OA NPLs, as reported in Figure V.20. As MPA ligands are known to link to the Cd-rich $\langle 100 \rangle$ NPL facets with their SH functional groups, it can be assumed that they also form a quasi-CdS shell on the CdSe NPLs. The sensitization of WBSC substrates by CdSe.MPA NPLs was successful only in case of 9 layers thick NPLs. 7 and 11 layers thick NPLs aggregated and did not form a homogeneous colored layer on the WBSC substrates. When attached to ZnO and TiO₂ NR arrays, the excitonic peaks of 9 layers thick CdSe. MPA NPLs do not significantly change their positions, they only become less structured, as illustrated in Figures V.21 and V.22. This indicates that the sensitization-induced structural changes in the CdSe.MPA NPLs are less important than in the CdSe.SH NPLs, which is intuitively explained by the fact that the MPA ligands increase the sensitizer-WBSC distance, the NPLs are thus not affected by strain caused by the lattice mismatch between the NPLs and the WBSC.

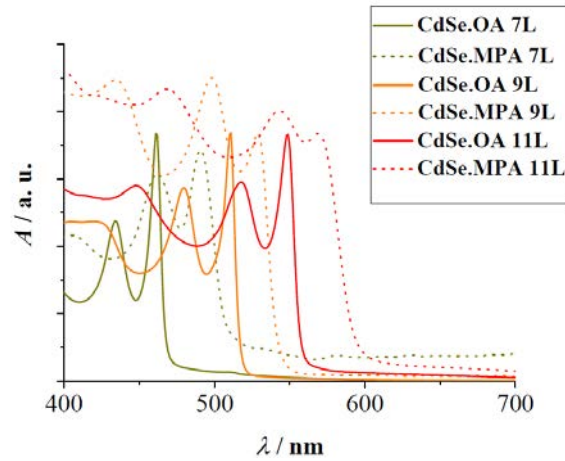


Figure V.20. UV-VIS absorption spectra of 7, 9 and 11 layers thick CdSe NPLs before and after ligand exchange with MPA (indicated by green, orange and red full and dotted lines, respectively).

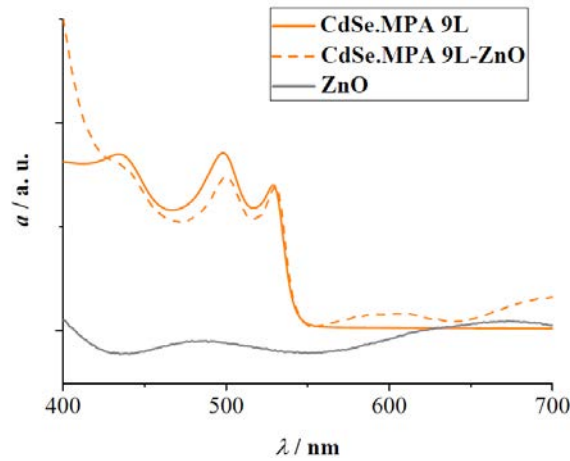


Figure V.21. UV-VIS absorption spectra of ZnO nanorod arrays and 9 layers thick CdSe.MPA NPLs in dispersion (indicated by orange full lines) and after attachment to ZnO nanorod arrays (indicated by orange dashed lines)

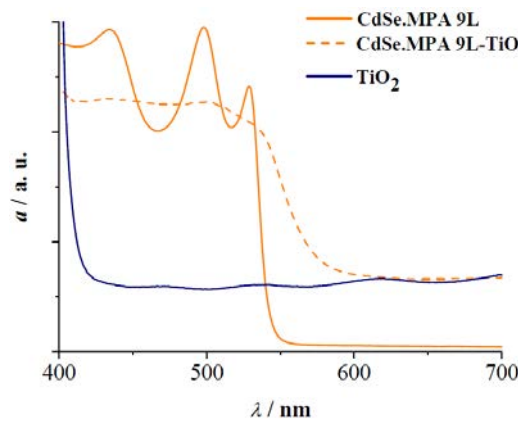


Figure V.22. UV-VIS absorption spectra of TiO₂ nanorod arrays and 9 layers thick CdSe.MPA NPLs in dispersion (indicated by orange full lines) and after attachment to TiO₂ nanorod arrays (indicated by orange dashed lines)

Chapter V. Hybrid semiconductor heterostructures

On the Raman spectra of the CdSe.MPA-ZnO and of the CdSe.MPA TiO₂ systems reported in *Figures V.23 and V.24*, one can mainly observe peaks corresponding to its two components. A significant redshift of the CdSe LO peaks can be observed after the NPLs are attached to the ZnO and TiO₂ nanorods, as reported in *Table V.2*, which suggests that in contrary to what we could observe from the UV-VIS absorption spectra reported in *Figures V.21 and V.22*, the sensitization does alter the structure of CdSe.MPA NPLs.

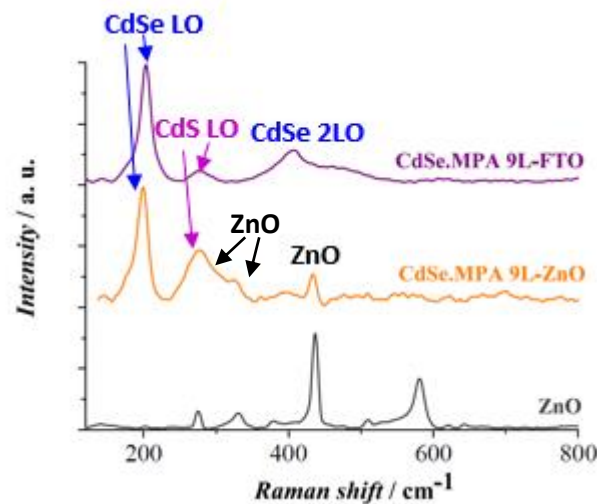


Figure V.23. Raman spectra of 9 layers thick CdSe.MPA NPLs, of ZnO nanorod arrays sensitized by the same NPLs and of bare ZnO nanorod arrays.

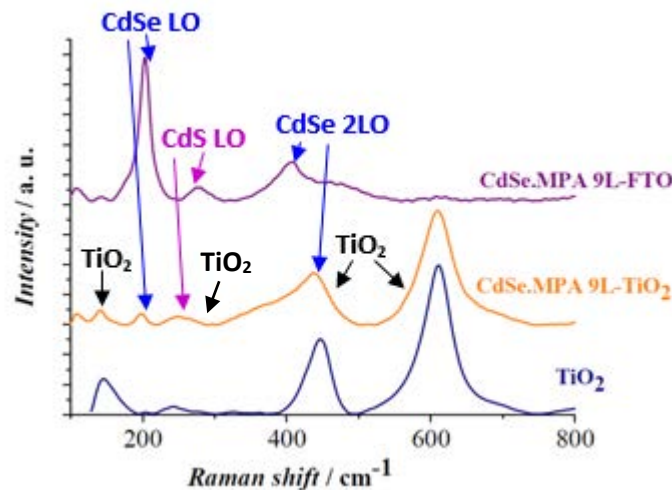


Figure V.24. Raman spectra of 9 layers thick CdSe.MPA NPLs, of TiO₂ nanorod arrays sensitized by the same NPLs and of bare TiO₂ nanorod arrays.

sample	CdSe LO Raman shift (cm ⁻¹)
CdSe.MPA - FTO	203
CdSe.MPA - ZnO	200
CdSe.MPA – TiO ₂	198

Table V.2. Raman shifts of the CdSe LO peaks before and after the CdSe.MPA NPLs are attached to ZnO or TiO₂ nanorods

V.6. Attachment of CdSe quantum dots to WBSC

Ligand exchange reactions on CdSe QDs resulted only in a slight shift of excitonic peaks, as shown in *Figure V.25*. This is explained by the fact that the spherical quantum dots expose several different surfaces²⁰ to which the adhesion of ligands can be different.^{21,22}. Therefore, a large area of the QD surface can still remain passivated by oleic acid after ligand exchange.

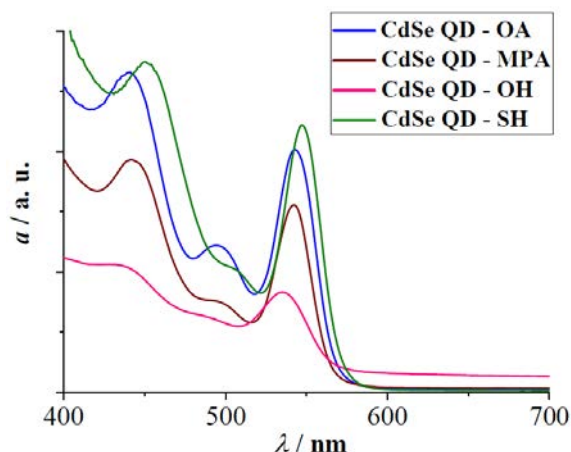


Figure V.25. UV-VIS absorption spectra of CdSe.OA QDs before and after ligand exchange with MPA, SH⁻ and OH⁻.

Among the ligand-passivated QDs, only the attachment of the CdSe.SH QDs to ZnO nanorod arrays was successful. The sensitization using other linkers or a TiO₂ substrate resulted in the aggregation of QDs with an inhomogeneous coverage. The UV-VIS absorption spectra of the CdSe.SH-ZnO system is compared to that of its components in *Figure V.26*. No significant change in the QD excitonic peak positions is observed after sensitization, the spectra only became less structured. We can thus conclude that in contrary to CdSe.SH NPLs, the

Chapter V. Hybrid semiconductor heterostructures

quantum confinement effects in CdSe.SH QDs did not change dramatically after attachment to a WBSC surface, although their structural distortion is observable upon sensitization.

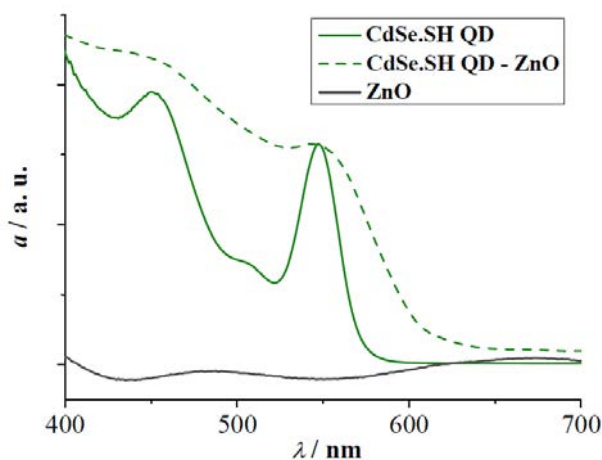


Figure V.26. UV-VIS absorption spectra of ZnO nanorod arrays and CdSe.SH QDs in dispersion (indicated by green full lines) and after attachment to ZnO nanorod arrays (indicated by green dashed lines)

V.7. Conclusion

In this chapter, CdSe nanocrystals (nanoplatelets of various thicknesses and spherical QDs) Next, the nanocrystals were linked to ZnO and TiO₂ nanorod arrays (referred to as WBSC) *via* bifunctional ligands (SH⁻, OH⁻ and MPA). The as-prepared nanocrystal-ligand-WBSC heterostructures were characterized by UV-VIS absorption and Raman spectroscopy.

In case of OH⁻ and MPA ligand exchange reactions on CdSe NPLs or QDs, some ligand exchanges or the attachment of ligand-passivated CdSe nanocrystals to ZnO/TiO₂ nanorods resulted in the aggregation of nanocrystals, and were thus regarded as unsuccessful. Therefore, these systems were not suitable for examining the effect of NPL thickness on the physical chemical properties of these systems.

On the other hand, all OA \leftrightarrow SH⁻ ligand exchange reactions on NPLs of various thicknesses, as well as QDs resulted in homogeneous CdSe nanocrystal dispersions. Subsequently, ZnO nanorod arrays could be homogeneously coated by CdSe.SH NPLs of all thicknesses, as well as CdSe.SH QDs, while TiO₂ nanorod arrays could only be sensitized by NPLs. Comparing the

Chapter V. Hybrid semiconductor heterostructures

UV-VIS absorption spectra of the CdSe.SH-ZnO and CdSe.SH-TiO₂ heterostructures and that of the bare NPLs, it can be concluded that the NPL attachment to a ZnO or a TiO₂ substrate induces structural changes in the nanocrystals. The Raman spectra of the mixed CdSe.SH-ZnO and CdSe.SH-TiO₂ systems features peaks of both of its components. While the NPL-related peaks have low intensity compared to the TiO₂-related ones, they have high intensity with respect to the ones associated with the ZnO NRs. In the latter case, it would thus be possible to analyze the shape of these NPL-related peaks in detail and decompose them into surface or interface modes. *Hence, a more refined analysis of the Raman modes of the latter system would make it possible to study the peak structure in detail, and in consequence to obtain interesting insights on the structural changes that the sensitization induces in the CdSe nanocrystals.*

*To sum up, SH⁻ ligands can be regarded as the best-working linkers for the goals of this thesis, especially when they are used to attach CdSe nanocrystals to ZnO substrates. We thus concluded that CdSe.SH - ZnO systems are worth studying in more detail, and conducted a mixed theoretical/experimental investigation on their interface properties, which is presented in **Chapter 6**.*

References

- (1) Yun, H. J.; Paik, T.; Edley, M. E.; Baxter, J. B.; Murray, C. B. Enhanced Charge Transfer Kinetics of CdSe Quantum Dot-Sensitized Solar Cell by Inorganic Ligand Exchange Treatments. *ACS Appl. Mater. Interfaces* **2014**, 6 (5), 3721–3728.
- (2) Pan, Z.; Mora-Seró, I.; Shen, Q.; Zhang, H.; Li, Y.; Zhao, K.; Wang, J.; Zhong, X.; Bisquert, J. High-Efficiency “green” quantum Dot Solar Cells. *J. Am. Chem. Soc.* **2014**, 136 (25), 9203–9210.
- (3) Wang, J.; Mora-Sero, I.; Pan, Z.; Zhao, K.; Zhang, H.; Feng, Y.; Yang, G.; Zhong, X.; Bisquert, J. Core/shell Colloidal Quantum Dot Exciplex States for the Development of Highly Efficient Quantum-Dot-Sensitized Solar Cells. *J. Am. Chem. Soc.* **2013**, 135 (42), 15913–15922.
- (4) Pan, Z.; Zhao, K.; Wang, J.; Zhang, H.; Feng, Y.; Zhong, X. Near Infrared Absorption of CdSe X Te 1-X Alloyed Quantum Dot Sensitized Solar Cells with More than 6% Efficiency and High Stability. *ACS Nano* **2013**, 7 (6), 5215–5222.
- (5) Luan, C.; Vaneski, A.; Susha, A. S.; Xu, X.; Wang, H.-E.; Chen, X.; Xu, J.; Zhang, W.; Lee, C.-S.; Rogach, A. L.; et al. Facile Solution Growth of Vertically Aligned ZnO Nanorods Sensitized with Aqueous CdS and CdSe Quantum Dots for Photovoltaic Applications. *Nanoscale Res. Lett.* **2011**, 6 (1), 340.
- (6) Sun, X. W.; Chen, J.; Song, J. L.; Zhao, D. W.; Deng, W. Q.; Lei, W. Ligand Capping Effect for Dye Solar Cells with a CdSe Quantum Dot Sensitized ZnO Nanorod Photoanode. *Opt. Express* **2010**, 18 (2), 1296–1301.
- (7) Kumar, A.; Li, K.; Madaria, A. R.; Zhou, C. Sensitization of Hydrothermally Grown Single Crystalline TiO₂ Nanowire Array with CdSeS Nanocrystals for Photovoltaic Applications. *Nano Res.* **2011**, 4 (12), 1181–1190.
- (8) Ithurria, S.; Tessier, M. D.; Mahler, B.; Lobo, R. P. S. M.; Dubertret, B.; Efros, A. L. Colloidal Nanoplatelets with Two-Dimensional Electronic Structure. *Nat. Mater.* **2011**, 10 (12), 936–941.
- (9) Geurts, J. Raman Spectroscopy from Buried Semiconductor Interfaces: Structural and Electronic Properties. *Phys. Status Solidi* **2015**, 252 (1), 19–29.
- (10) Marie, M.; Mandal, S.; Manasreh, O. An Electrochemical Glucose Sensor Based on Zinc Oxide Nanorods. *Sensors* **2015**, 15 (8), 18714–18723.
- (11) Venkatesh, P. S.; Purushothaman, V.; Muthu, S. E.; Arumugam, S.; Ramakrishnan, V.; Jeganathan, K.; Ramamurthi, K. Role of Point Defects on the Enhancement of Room Temperature Ferromagnetism in ZnO Nanorods. *CrystEngComm* **2012**, 14 (14), 4713.
- (12) Selman, A. M.; Hassan, Z. Structural and Photoluminescence Studies of Rutile TiO₂ Nanorods Prepared by CBD Method on Si Substrates. *Am. J. Mater. Sci.* **2015**, 5 (3B), 16–20.
- (13) Nag, A.; Kovalenko, M. V.; Lee, J.-S.; Liu, W.; Spokoyny, B.; Talapin, D. V. Metal-Free Inorganic Ligands for Colloidal Nanocrystals : S²⁻, HS⁻, Te²⁻, HTe⁻, TeS₃²⁻, OH⁻ and NH₂⁻ as Surface Ligands. *J. Am. Chem. Soc.* **2011**, 133, 10612–10620.
- (14) Ithurria, S.; Talapin, D. V. Colloidal Atomic Layer Deposition (c-ALD) Using Self-Limiting Reactions at Nanocrystal Surface Coupled to Phase Transfer between Polar and Nonpolar Media. *J. Am. Chem. Soc.* **2012**, 134 (45), 18585–18590.
- (15) Tschirner, N.; Lange, H.; Schliwa, A.; Biermann, A.; Thomsen, C.; Lambert, K.; Gomes, R.; Hens, Z. Interfacial Alloying in CdSe/CdS Heteronanocrystals: A Raman Spectroscopy Analysis. *Chem. Mater.* **2012**, 24 (2), 311–318.
- (16) Lin, C.; Gong, K.; Kelley, D. F.; Kelley, A. M. Electron-Phonon Coupling in CdSe/CdS Core/Shell Quantum Dots. *ACS Nano* **2015**, 9 (8), 8131–8141.
- (17) Dzhagan, V. M.; Valakh, M. Y.; Milekhin, A. G.; Yeryukov, N. a.; Zahn, D. R. T.; Cassette, E.; Pons, T.; Dubertret, B. Raman- and IR-Active Phonons in CdSe/CdS Core/Shell Nanocrystals in the Presence of Interface Alloying and Strain. *J. Phys. Chem. C* **2013**, 117 (35), 18225–18233.
- (18) Lu, L.; Xu, X.-L.; Liang, W.-T.; Lu, H.-F. Raman Analysis of CdSe/CdS Core-Shell Quantum Dots with Different CdS Shell Thickness. *J. physics. Condens. matter* **2007**, 19 (40), 406221.
- (19) Nag, A.; Kovalenko, M. V.; Lee, J.; Liu, W.; Spokoyny, B.; Talapin, D. V. Metal-Free Inorganic Ligands for Colloidal Nanocrystals : S²⁻, HS⁻, Se²⁻, HSe⁻, Te²⁻, HTe⁻, TeS₃²⁻, OH⁻, and NH₂⁻ as Surface Ligands. *J. Am. Chem. Soc.* **2011**, 133, 10612–10620.

Chapter V. Hybrid semiconductor heterostructures

- (20) Yang, Y. A.; Wu, H.; Williams, K. R.; Cao, Y. C. Synthesis of CdSe and CdTe Nanocrystals without Precursor Injection. *Angew. Chemie* **2005**, *44* (41), 6712–6715.
- (21) Peng, Z. A.; Peng, X. Mechanisms of the Shape Evolution of CdSe Nanocrystals. *J. Am. Chem. Soc.* **2001**, *123*, 1389–1395.
- (22) Owen, J. S.; Park, J.; Trudeau, P.-E.; Alivisatos, A. P. Reaction Chemistry and Ligand Exchange at Cadmium-Selenide Nanocrystal Surfaces. *J. Am. Chem. Soc.* **2008**, *130* (37), 12279–12281.

Chapter VI. Towards the modeling of QDSCs: sensitizer-oxide heterostructures

VI.1. Context

A deep understanding of the structure-property interplay is essential for the design of complex devices such as quantum dot solar cells (QDSCs), in which interfacial recombinations are a major source of performance loss. This requires an accurate characterization of semiconductor interfaces from both the experimental and theoretical point of view, which remains problematic especially in case of lattice-mismatched compounds. It is particularly difficult to account for the inter-diffusion and bond distortions at the interfaces that appear in case of high lattice mismatch between the QDs and the substrate.^{1,2} Previous computational studies focused on TiO_2 surfaces sensitized by Sb_2S_3 nanoribbons with nearly matching lattice parameters³ or on the modelling of PbSe ,⁴ CdS ⁵ and CdSe ⁶ QDs which do not form a laterally extended interface with the substrate. Only very few examples of computational studies of semiconductor interfaces formed between compounds with a significant lattice-mismatch can be found in the literature.^{7–11} These calculations were mostly limited to an interface made between a single^{7–9} or a double adsorbate layer¹⁰ and a substrate surface. Moreover, DFT was applied using local density and generalized gradient approximations which severely underestimate band gaps.¹² Furthermore, an accurate model will have to reproduce the vibrational properties of the heterostructure and interface which depend in a large extent to compositional changes⁹ and bond lengths.¹³

Raman spectroscopy is a very sensitive characterization method of semiconductor interfaces. The formation of the interface gives rise to characteristic Raman modes whose frequencies reflect the interfacial geometry and strain.¹⁴ Moreover, phonon properties are known to influence the material electron mobility and thus the performance of opto-electronic devices. Moreover, simulations have shown that certain vibrations can promote charge recombination⁴ or electron transfer¹⁵ at the QD- TiO_2 interface by varying the electronic density distribution between donor and acceptor species. Hence, Raman spectra

Chapter VI. Towards the modeling of QDSCs: sensitizer-oxide heterostructures

of these systems provide valuable information that can be related to the device functioning. Since the experimental measurement of the Raman spectra of nanostructures can be rather challenging with traditional instrumental setups, and might demand special techniques,^{16–18} computational methods to simulate the vibrational properties of these systems can be very helpful to understand the vibrational behavior of heterointerfaces.

In this chapter, we combine theoretical and experimental methods to address the challenge of characterizing a lattice mismatched interface formed between a QDSC sensitizer and a wide band gap semiconductor surface. As an interesting alternative to spherical quantum dots (QDs), the quasi two-dimensional CdSe nanoplatelets (NPLs) of different thicknesses have been linked to ZnO nanorods using SH⁻ functional group as a simple linker. The general advantages and the synthesis of these CdSe NPLs have been discussed in **Chapters I** and **II**, and their geometric and electronic properties have been studied in detail in **Chapter IV**.

This chapter is organized as follows. First, a consistent model of the interface is built and its Raman spectrum is computed and analyzed. Secondly, results of the electronic property calculations of the NPL/ZnO heterostructure are shown (including the band gaps, the band structures, the density of states (DOS), the crystalline orbitals (CO)). Then the electron injection efficiency from the NPL towards the ZnO surface is computed. In order to examine the effect of NPL thickness on these properties, all calculations were performed on a ZnO surface sensitized by 5 and 9 layers thick CdSe NPLs with SH⁻ linkage (denoted by CdSe.SH NPLs in the following).

VI.2. Experimental details

The synthesis of ZnO nanorods, as well as that of 7, 9 and 11 layers thick CdSe NPLs and the ligand exchange reactions replacing oleic acid ligands to SH⁻ have been described in **Chapter II**, section **II.2.1**. The details of the characterization of the samples by UV-VIS and Raman spectroscopy are also provided in **Chapter II** section **II.2.7**. In order to sensitize the ZnO nanorods by CdSe NPLs, a droplet of 100 μ l of CdSe.SH NPL dispersion in N-methyl

Chapter VI. Towards the modeling of QDSCs: sensitizer-oxide heterostructures

formamide (NMF) was cast on the ZnO NR arrays, and heated at 150°C on a hot plate for 5 minutes in order to evaporate the solvent.

VI.3. Computational details

All calculations were carried out with the ab initio CRYSTAL14^{19,20} code. Following the results obtained in **Chapters II** and **III**, our investigations were carried out using the global hybrid B3PW91 functional.²³ As the interface formation between two, largely lattice-mismatched semiconductors is assumed to alter the atomic distances significantly even in atomic layers that are far from the actual interface, long-range interactions including dispersion forces are expected to be relevant for the present study. Since hybrid functionals do not describe them satisfactorily,^{24,25} an empirical London-type correction was also taken into account (according to the DFT-D2 scheme, as described by Grimme et al²⁶). Following standard notation, this approach is denoted as B3PW91-D. These corrections altered the atomic positions compared to the B3PW91 functional,²² and provided us an accurate description of the electronic properties of the semiconductor heterostructures.

For CdSe, we used a double-zeta basis set, in which core electrons were replaced by effective core potentials (ECPs) including scalar relativistic effects, as described in ref 27. SBKJC small-core ECP²⁸ was applied with a (8s, 8p, 5d)→[4s, 4p, 3d] contraction for Cd, and the SBKJC large-core ECP²⁸ with a basis set augmented by one d polarization function,²⁹ with a (5s, 5p, 2d)→[2s, 2p, 1d] contraction for Se. As a consequence, 4s² 4p⁶ 4d¹⁰ 5s² and 4s² 4p⁴ electrons were treated explicitly for Cd and for Se, respectively. As previously described for CdSe,³⁰ basis sets were modified by setting exponents inferior to 0.10 to this value. The suitability of this modified SBKJC basis set to describe CdSe, both in its bulk and surface forms, has already been discussed in a previous work.⁵⁰ In order to reduce the computational burden, pseudopotentials were applied for S, Zn and O atoms as well. Durand and Barthelat large-core pseudopotentials with a (4s, 4p)→[2s, 2p] contraction were used for the O atoms^{31,32}, while large core Hay and Wadt pseudopotentials with a (3s, 3p, 5d)→[3s, 3p, 2d] contraction were retained for Zn atoms.³³ The sp and d polarization functions of Zn and O atoms were reoptimized in a previous work.³⁴ The core electrons of S

Chapter VI. Towards the modeling of QDSCs: sensitizer-oxide heterostructures

were described using Durand and Barthelat large-core pseudopotentials as well^{31,32}. For the valence electrons of S, a split valence basis set optimized for periodic systems and completed with a 3d polarization function was applied with a (4s, 4p, 1d)→[2s, 2p, 1d] contraction.³⁵ As a consequence, the following electrons were treated explicitly: 2s² 2p⁴ for O, 3d¹⁰ 4s² for Zn and 3s² 3p⁴ for S. An all-electron basis set with a (7s, 1p)→[3s, 1p] contraction was used for H.

An extra-large DFT integration grid, consisting of 75 radial and 974 angular points, was applied in order to provide accurate results for calculations. The following truncation criteria^{19,20} were set for the accuracy of the Coulomb and exchange series: 10⁻⁷ as the overlap threshold for Coulomb integrals, 10⁻⁷ as the penetration threshold for Coulomb integrals, 10⁻⁷ as the overlap threshold for HF exchange integrals, and 10⁻⁹ and 10⁻²⁰ as the pseudo-overlap for HF exchange series.

For the calculations of surface and interface properties, we adopted a slab model described in **Chapter II**, section **II.1.6. b)**. As illustrated in *Figure VI.1*, the ZnO surface was modeled as a wurtzite (10-10) slab at a converged thickness of 8 ZnO layers (with one layer containing a row of Zn and O atoms in the same <10-10> plane).³⁴ CdSe.SH NPLs were modeled as CdSe zinc blende slabs cut along the <100> plane, and passivated by SH⁻ ligands at the (100) surfaces.⁴⁴ The thickness of the CdSe NPLs was defined as in **Chapter II** section **II.2.1.**, that is one layer corresponds to an atomic layer composed exclusively of cadmium or selenium atoms in the same <100> plane (*Figure VI.1*). As explained in more detail in the following section, in order to form an interface between the CdSe.SH and the ZnO slabs, we placed a CdSe.SH unit cell with altered lattice parameters on top of a 3x2 supercell of a ZnO wurtzite (10-10) slab. The lateral dimension of the resulting heterostructure was 9.86 Å x 10.34 Å. We applied a Monkhorst–Pack shrinking factor of 2 for this system, which corresponds to 4 independent k points in the irreducible Brillouin zone (IBZ) of the CdSe.SH-ZnO slab heterostructure. In the present work, heterostructures based on 5 and 9 layers thick CdSe.SH NPL have been modeled. Since the obtained results are qualitatively similar in both cases, we only comment the results obtained for the system containing the 5 layers thick NPL, except

Chapter VI. Towards the modeling of QDSCs: sensitizer-oxide heterostructures

for the band gap data. The results obtained for the heterostructure with 9 layers thick NPL are provided in the **Annexe I**.

The calculation of harmonic vibrational frequencies at the Γ point, as implemented in the CRYSTAL14 code,^{36,37} was carried out on the same fragment. Raman intensities were calculated via the Coupled-Perturbed Hartree-Fock/Kohn-Sham (CPHF) approach.^{38–42} The threshold of the self-consistent field energy for the frequency calculations was set to 10^{-12} hartree. Experimental conditions (temperature of measurement: 293.15 K, laser wavelength: 473 nm) were taken into account for the calculation of Raman intensities as described in ref. 20.

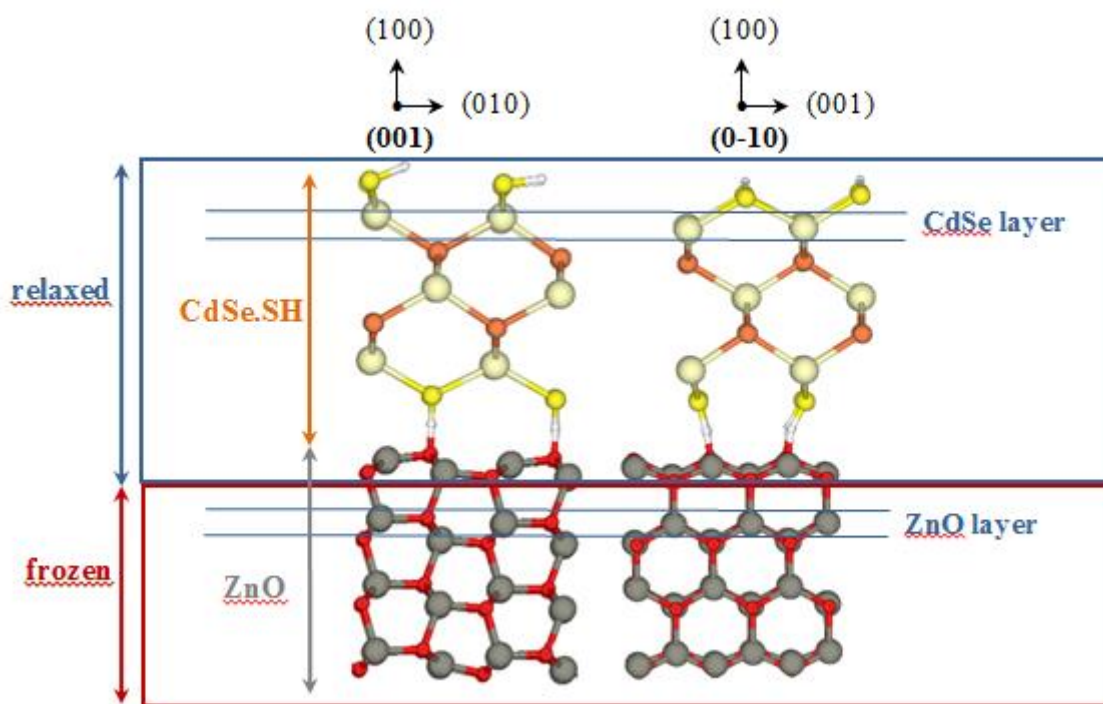


Figure VI.1. Initial structural model of 5 layers thick CdSe.SH nanoplatelets attached to the ZnO (10-10) surface via SH ligands. Zn atoms are represented by grey, O by red, H by white, S by yellow, Cd by beige and Se by orange spheres.

VI.4. Structural features of the CdSe.SH – ZnO system

The efficient sensitization of wide band gap semiconductors by nanostructures for QDSC application requires the actual bonding between the sensitizer and the electron transport material. This bonding allows the charge transfer between the two components after the

Chapter VI. Towards the modeling of QDSCs: sensitizer-oxide heterostructures

excitation of the absorber material by solar light and exciton generation. In the present case, the absorber is composed of CdSe NPLs whereas ZnO, in the form of nanorods, was used as the oxide substrate. Both components were supposed to be connected through SH⁻ surface linkers. In order to experimentally evaluate the structural interactions between the two semiconductors and the modifications induced by the formation of the NPL-ZnO interfaces, the CdSe.SH – ZnO systems were firstly characterized by UV-VIS absorption measurements. NPLs described in **Chapter II** section II.2.1. were attached to the ZnO NRs presented in **Chapter II** section II.2.2 a).

Figure VI.2 shows that, when linked to the ZnO NR substrate, a redshift of the CdSe.SH NPLs excitonic peaks was observed for all NPL thicknesses considered in this study. This suggests that significant structural changes took place in the NPL upon attachment to the ZnO nanorod arrays. In order to make sure that this shift was not the result of the aggregation of the NPLs on the ZnO substrate, the absorption spectrum of a sample prepared with 7 layer thick NPLs, rinsed with ethanol after sensitization, was recorded and shown in Figure VI.2. Although the peaks in its UV-VIS absorption spectrum (indicated by a dotted line in Figure VI.2) were less structured, the sensitization still results in a redshift of the excitonic peak, confirming the attachment of the nanostructures.

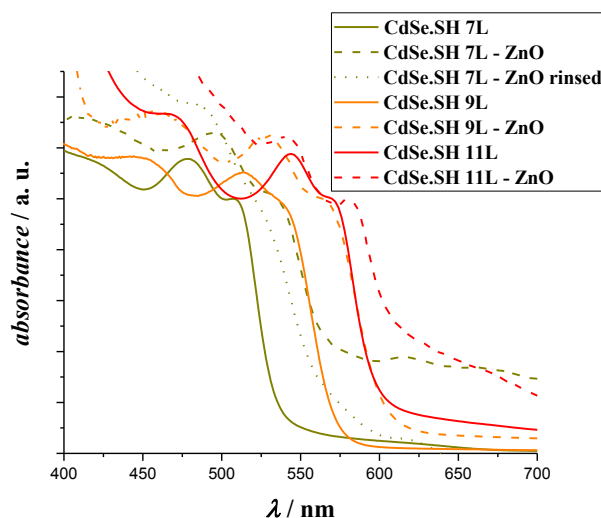


Figure VI.2. Experimental UV-VIS absorption spectra of 7, 9 and 11 layers thick CdSe.SH NPLs in dispersion (indicated by green, orange and red full lines, respectively) and after attachment to ZnO nanorod arrays (indicated by dashed lines of the corresponding colour, and by a dotted line after subsequent washing with ethanol).

Chapter VI. Towards the modeling of QDSCs: sensitizer-oxide heterostructures

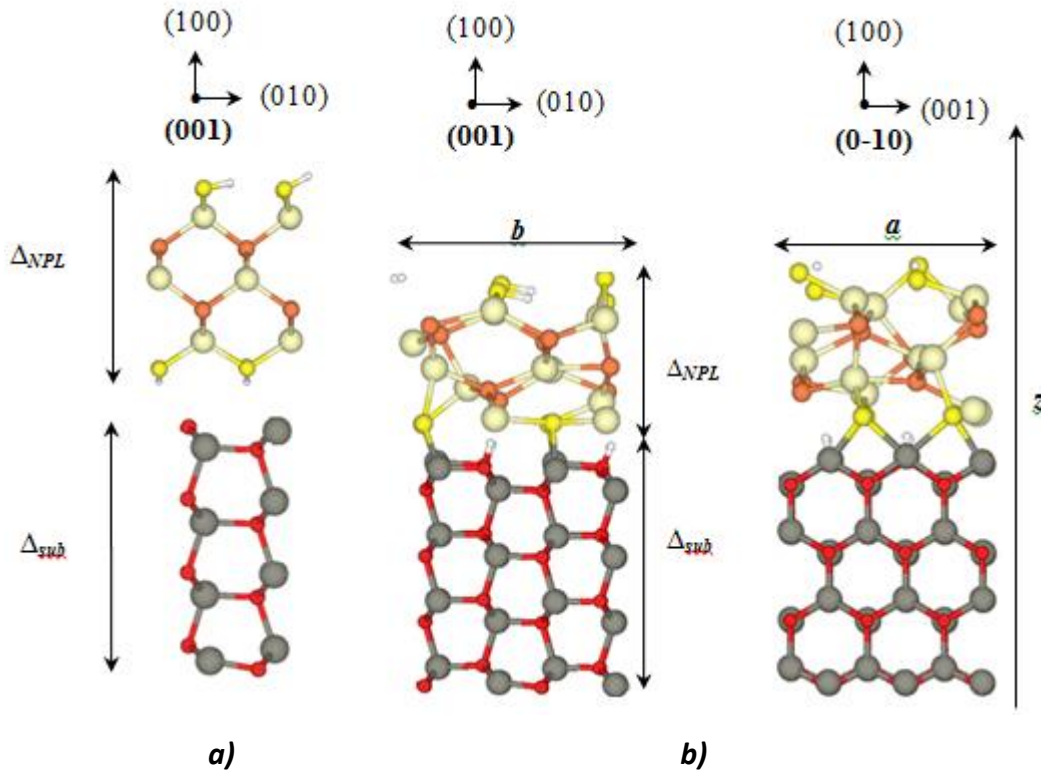


Figure VI.3. a) Structure of the isolated subsystems: 5 layers thick (5L) CdSe.SH and 8 layers thick (8L) ZnO slabs. b) Optimized geometry of the CdSe.SH (5L) – ZnO (8L) heterostructure, viewed along the (001) and (0-10) directions.

	CdSe.SH NPL	ZnO slab	Optimized CdSe.SH – ZnO interface
a	8.79	9.93	9.86
b	8.79	10.50	10.34
Δ_{NPL}	10.23	--	7.32
Δ_{Sub}	--	9.42	9.89
γ	90.00	90.00	90.02
d (Cd-Se)	2.69	--	2.64-2.90
d (Cd-S)	2.60	--	2.49-2.65
d (Zn-S)	--	--	2.39-2.69
d (O-H)	--	--	0.98-1.00
d^1 (Zn-O)	--	1.86	2.05-2.08
d^2 (Zn-O)	--	2.00	2.00
δ_z^1 (Zn)	--	--	0.78
δ_z^1 (O)	--	--	0.33

Table VI.1. Lattice parameters (a , b in Å and γ in degrees) and relevant interatomic distances (d (Cd-Se), d (Cd-S), d (Zn-S), d (O-H)) of the isolated subsystems and of the optimized heterostructure. d^1 (Zn-O) and d^2 (Zn-O) correspond to Zn-O distances in the first and in the second ZnO slab layer, respectively. δ_z^1 (Zn) and δ_z^1 (O) are the shifts, upon optimization, of Zn and O atoms along the z axis compared to their initial positions in the uppermost layer of the ZnO slab.

Chapter VI. Towards the modeling of QDSCs: sensitizer-oxide heterostructures

The next step was to actually model the formed heterostructures and to better understand the structural relationship between the CdSe NPLs and ZnO. In the periodic approach applied here, the large lattice mismatch between the CdSe.SH NPL ($a=b=8.79 \text{ \AA}$, $\alpha=\beta=\gamma=90.00^\circ$)²¹ and the ZnO wurtzite slab ($a=3.31 \text{ \AA}$, $b=5.25 \text{ \AA}$, $\alpha=\beta=\gamma=90.00^\circ$)³⁴ made the modeling of the adsorption of nanoplatelets on the substrate difficult. Based on the above detailed UV-VIS absorption spectroscopic data, we chose to alter the structural parameters of the CdSe.SH NPL rather than those of the ZnO slab. In particular, the lattice parameters of a CdSe.SH slab unit cell were enlarged to match those of a 3x2 supercell of a ZnO wurtzite (10-10) slab. Then, the slab representing the CdSe.SH nanoplatelet was positioned on top of the ZnO slab, and the above described fragment let to relax. The resulting optimized structure is shown in *Figure VI.3 b*), and its lattice parameters are compared to those of the isolated subsystems in *Table VI.1*. The optimized geometry is greatly distorted with respect to the isolated subsystems, especially the CdSe.SH fragment. The thickness of the CdSe.SH slab in the (100) direction (denoted as Δ_{NPL} in *Table VI.1*) drastically decreases upon optimization. Moreover, the symmetric tetrahedral organization of Cd, Se and S atoms is lost in the optimized structure. This latter effect is indeed characterized by a range of different Cd-S and Cd-Se atomic distances. For the ZnO slab, the atomic positions in its uppermost layer are slightly altered. The $\delta_z(\text{Zn})$ and $\delta_z(\text{O})$ values in *Table VI.1* show that upon the interface formation, the atoms of the uppermost ZnO layer are shifted upwards along the z axis with respect to their position in the isolated ZnO slab. This also causes a slight increase in the thickness of the substrate as indicated by the Δ_{sub} value. At the interface, the bottom H atoms of the SH groups are bound to the oxygens of the ZnO surface, and the S atoms are horizontally shifted towards bridging positions between Zn atoms, to form almost a ZnS layer at the NPL-ZnO interface. The optimized Zn-S atomic distances are ranging between 2.39 and 2.69 \AA , close to the 2.36 \AA value of the interatomic distance observed in zinc blende ZnS, or to 2.58 \AA , corresponding to the sum of the ionic radii of the two compounds.⁴³ These data indicate the emergence of a strong and iono-covalent bonding between CdSe.SH and ZnO upon interface formation.

Chapter VI. Towards the modeling of QDSCs: sensitizer-oxide heterostructures

VI.5. Vibrational features

The modeled optimal heterostructure is characterized by vibrational modes which can be efficiently explored by Raman spectroscopy. Therefore, a computational protocol was developed for the calculation of the Raman spectrum of the heterostructure. First, the accuracy of the protocol was validated by calculating the Raman modes of the bulk phases of zinc blende CdSe and ZnO. The data reported in *Table VI.2* agree globally well with the experimental data available from the literature.

	mode	Computed (this work)	Experimental
CdS	TO	230	230 ⁴⁴
	LO	303	305 ⁴⁵
CdSe	TO	160	170 ⁴⁶
	LO	206	211 ⁴⁷
ZnO	E ₂ (low)	114	99 ⁴⁸
	A ₁ (TO)	391	379 ⁴⁸
	E ₁ (TO)	434	410 ⁴⁸
	E ₂ (high)	462	437 ⁴⁸

Table VI.2. Computed and experimental Raman shifts (in cm^{-1}) of the bulk modes of CdS, CdSe, ZnO. TO and LO correspond to the transverse and longitudinal optical modes, respectively.

An important point on the calculation of vibrational spectra is that the splitting between longitudinal optical (LO) and transverse optical (TO) modes experimentally observed for ionic compounds is not straightforwardly obtained in our calculations, as a consequence of imposing periodic boundary conditions.²⁰ In more detail, the eigenvalues obtained by the diagonalization of the mass-weighted W matrix correspond to the TO frequencies. W is then corrected with a term W^{NA} that depends on the cell volume, the dynamic dielectric tensor and the Born effective charges, as described in ref.⁴⁹, and the LO frequencies correspond to the eigenvalues obtained by the diagonalization of the $W+W^{\text{NA}}$ matrix. The correspondence between the LO and TO modes is established based on the maximum overlap between LO and TO modes. However, the TO and LO vectors originate from independent diagonalizations, and do not belong to the same orthonormal set. Therefore, a TO mode from one orthonormal set of vectors and the corresponding LO mode from another one might not have a mutual maximum overlap with each other, preventing us from making a

Chapter VI. Towards the modeling of QDSCs: sensitizer-oxide heterostructures

one-to-one correspondence between the two. Due to the high symmetry of bulk compounds, it was possible to compute the LO/TO splitting in their Raman spectra with the chosen computational protocol. This was not the case for the low-symmetry slabs, therefore we deduced their LO frequencies by adding the corresponding bulk LO/TO splitting values to their TO frequencies.

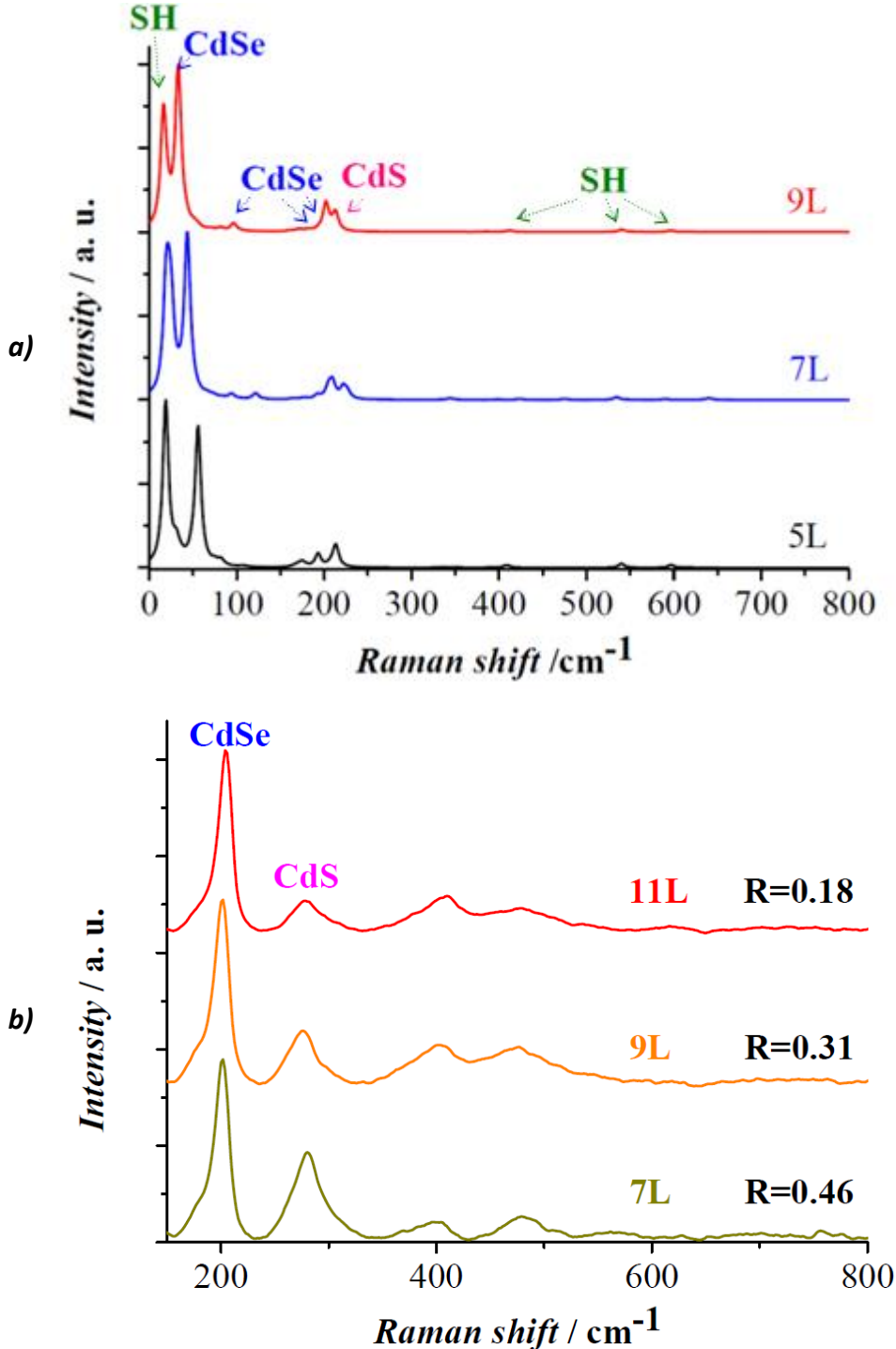


Figure VI.4. a) Computed Raman spectra of 5, 7 and 9 layers thick CdSe.SH NPLs. b) Experimental Raman spectra of 7, 9 and 11 layers thick CdSe.SH nanoplatelets dropcasted

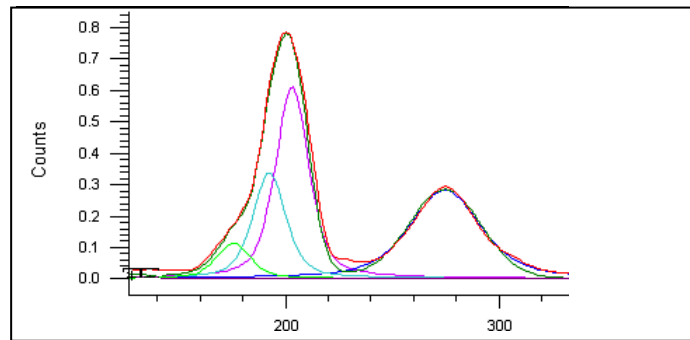
Chapter VI. Towards the modeling of QDSCs: sensitizer-oxide heterostructures

on FTO/glass substrates. $R = I_{CdS} / I_{CdSe}$. The spectra was normalized to the highest intensity peak for each curve.

Next, the Raman modes of 5, 7 and 9 layers thick CdSe.SH NPLs were computed, as reported in *Figure VI.4 a)*. In all cases we found:

- i. - High intensity peaks at 17-22 cm^{-1} assigned to ligand-related S-H vibrations.
- ii. Low intensity peaks between 98 and 184 cm^{-1} related to CdSe- vibrations of the inner part of the NPL.
- iii. Large intensity peaks at 33-55 cm^{-1} and peaks between 184 and 200 cm^{-1} corresponding to vibrations delocalized on the whole slab.
- iv. .
- v. Vibrations from 212 cm^{-1} to 224 cm^{-1} clearly localized on the outermost, quasi-CdS layers of the NPLs.
- vi. Low intensity peaks computed above 300 cm^{-1} are ligand-related S-H vibrations.

Considering an LO/TO splitting of 46 cm^{-1} for CdSe and 73 cm^{-1} for CdS, both derived from the differences between the Raman shifts of LO and TO bulk modes shown in *Table VI.2*, we obtained that CdSe-related LO peaks are at 144-230 cm^{-1} and CdS-related LO peaks are in the interval of 285-297 cm^{-1} in the computed spectra of the NPL. These values are relatively close to the experimentally measured ones reported in *Figure VI.4 b)*.



Curve name	Centre (nm)	Width (nm)	Height (counts)	% Gaussian
CdS interface	274.6	39.66	0.2839	100
CdSe bulk LO	202.9	18.30	0.6198	100
CdSe SO	192.3	18.30	0.3399	50
CdSe TO	175.4	18.30	0.1147	50

Figure VI.5. Decomposition of the CdSe- and CdS-related peaks in the experimental Raman spectra of 9 layers thick CdSe.SH NPLs.

Chapter VI. Towards the modeling of QDSCs: sensitizer-oxide heterostructures

Similarly to the theoretical one, the experimental Raman spectra of the isolated CdSe.SH NPLs of different thicknesses (*Figure VI.4 b*) also features CdSe and CdS-related peaks. The reported spectra are globally very similar to previously published spectra of zinc blende CdSe/CdS core shell quantum dots^{50,51}. The first peak at around 200 cm^{-1} is attributed to the CdSe zinc blende longitudinal optical (LO) mode. Its broadening towards the lower frequencies can be explained by the presence of interface and surface optical phonons,⁵⁰ as shown by the band deconvolution detailed in *Figure VI.5*. The peak at around 280 cm^{-1} is attributed to the LO mode of the zinc blende phase of CdS, although redshifted from its bulk position near 300 cm^{-1} . It can be due to the large strain that the single CdS layer suffers at the interface, as also observed previously for CdSe/CdS core/shell QDs with a thin CdS shell.⁵⁰⁻⁵³ The other modes observed for Raman shifts above 400 cm^{-1} correspond to overtones and mixed modes.^{50,53} Since the NPLs of various thicknesses were all passivated by a single layer of SH⁻, the ratio of CdS layers with respect to CdSe layers decreased with the increase of NPL thickness. This structural feature was qualitatively reflected on the experimental spectra shown in *Figure VI.4 b*): the ratio R of the intensity of the CdS-related peak (near 280 cm^{-1}) to the CdSe-related peak (near 200 cm^{-1}) decreases with the increase of the nanoplatelet thickness. A similar effect was observed in several works on the Raman spectroscopy of CdSe/CdS core/shell structures where the authors grew CdS shells of different thicknesses on a CdSe core of the same diameter.^{50,52} In line with the present work, they observed that the decrease of CdS shell thickness with respect to the CdSe core size results in the decrease of R .

Finally, the Raman spectra of the CdSe.SH-ZnO system was computed. The spectra of this system reported in *Figure VI.6 a*) features a dense array of peaks. This is clearly a consequence of the symmetry lowering when moving from the isolated subsystems towards the interface. Generally speaking, one can distinguish:

- i- A group of peaks at low frequencies ($<50\text{ cm}^{-1}$) corresponding to the entire CdSe.SH part of the heterostructure.
- ii- A ligand (S-H)-related peak at 100 cm^{-1} .
- iii- Between around 150 and 200 cm^{-1} , the lattice vibrations are localized on the uppermost CdS layer of the adsorbate.

Chapter VI. Towards the modeling of QDSCs: sensitizer-oxide heterostructures

iv- Peaks between 200 and 300 cm^{-1} are assigned to vibrations related to the interface CdS and ZnS layer.

v- Frequencies above 300 cm^{-1} correspond to ligand- (S-H) and ZnO-related modes.

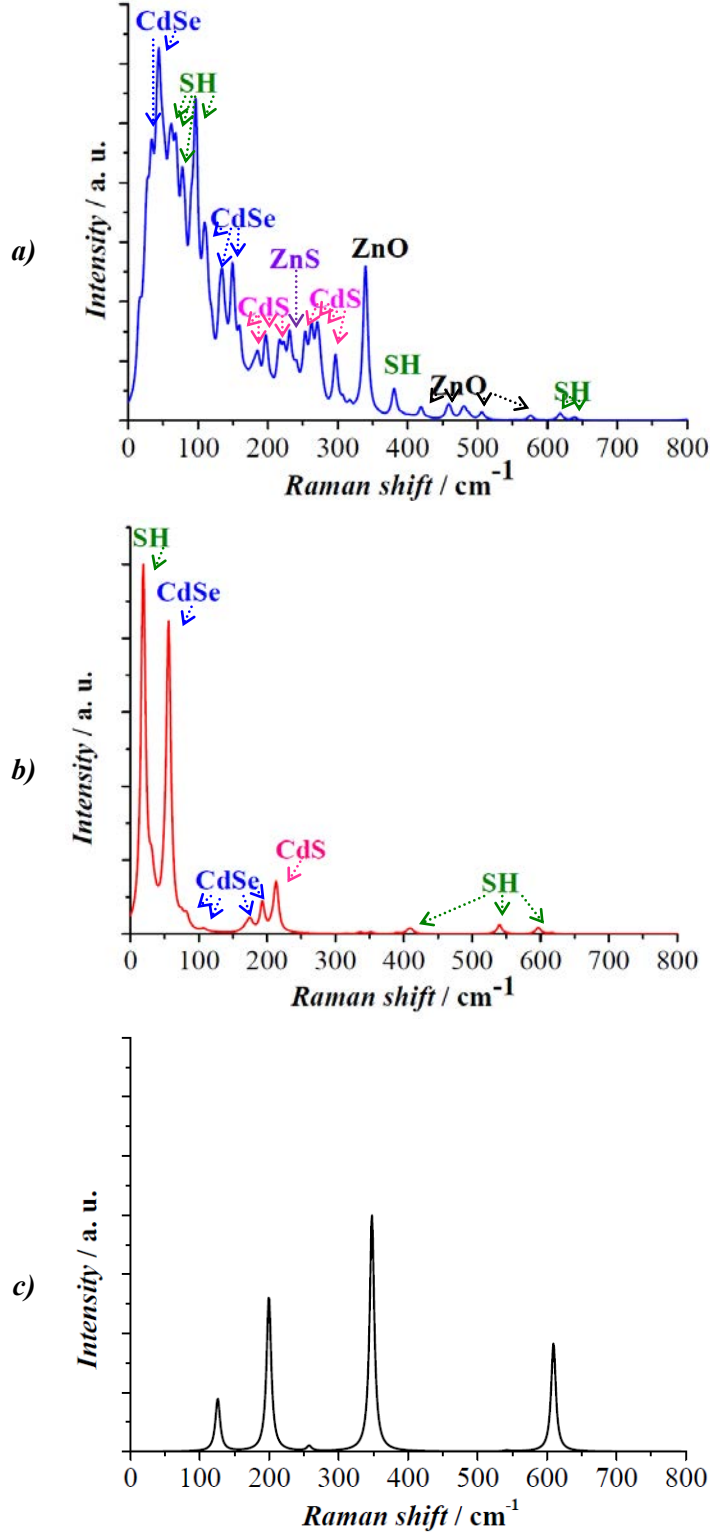


Figure VI.6. Computed Raman spectra of a) the CdSe.SH (5L) - ZnO heterostructure, b) a 5 layers thick CdSe.SH slab and c) the uppermost layer of a ZnO wurtzite (10-10) slab.

Chapter VI. Towards the modeling of QDSCs: sensitizer-oxide heterostructures

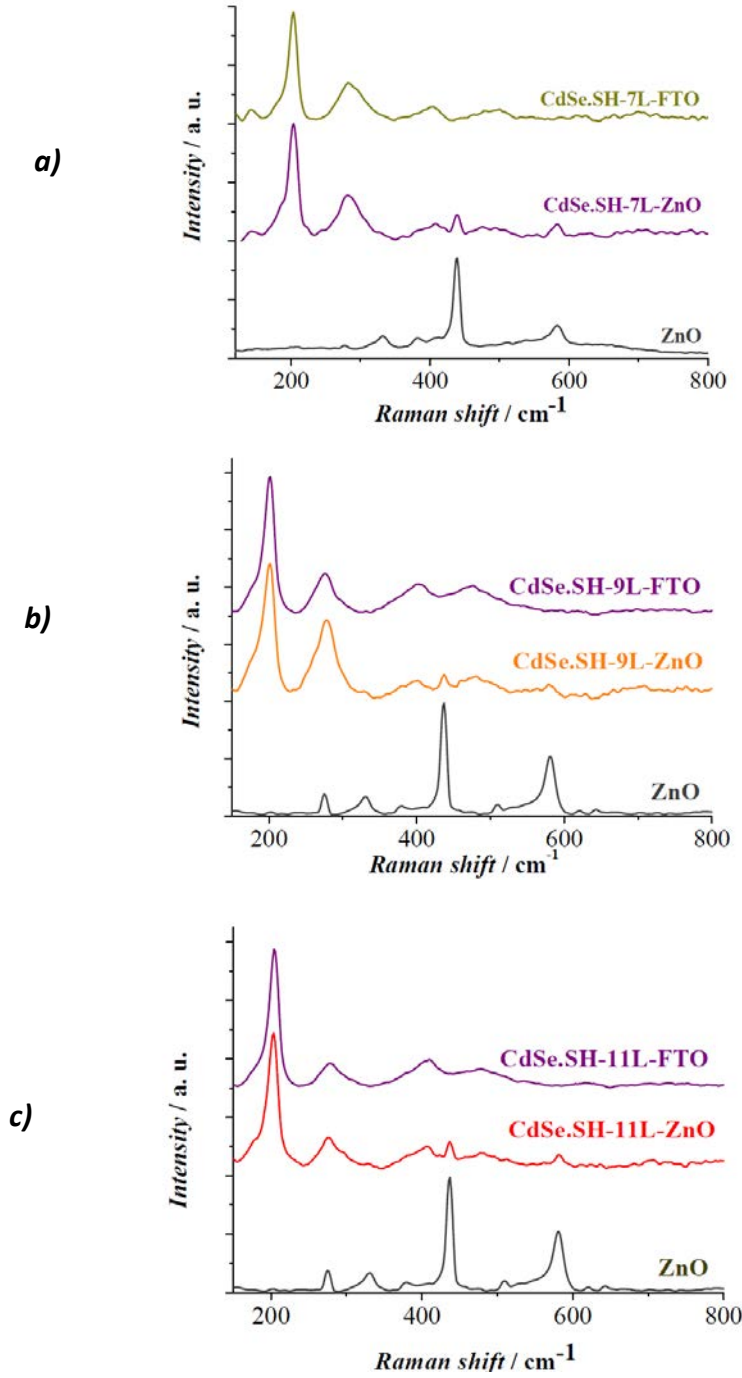


Figure VI.7. Experimental Raman spectra of a) 7, b) 9 and c) 11 layers thick CdSe.SH NPLs, of ZnO nanorod arrays sensitized by the same NPLs and of bare ZnO nanorod arrays.

In comparison to the Raman spectra of the isolated subsystems, it is worth to note that most peaks are redshifted with respect to their equivalent in bare CdSe.SH and ZnO slabs. In the case of CdSe.SH, this can be explained by the greater lattice parameters, while in the case of the ZnO fragment, it is attributed to the formation of an additional quasi-ZnS layer upon the

Chapter VI. Towards the modeling of QDSCs: sensitizer-oxide heterostructures

ZnO surface. Also, as a result of the structural disorder in the final optimized geometry of the CdSe-SH-ZnO system, all bands are split into several ones.

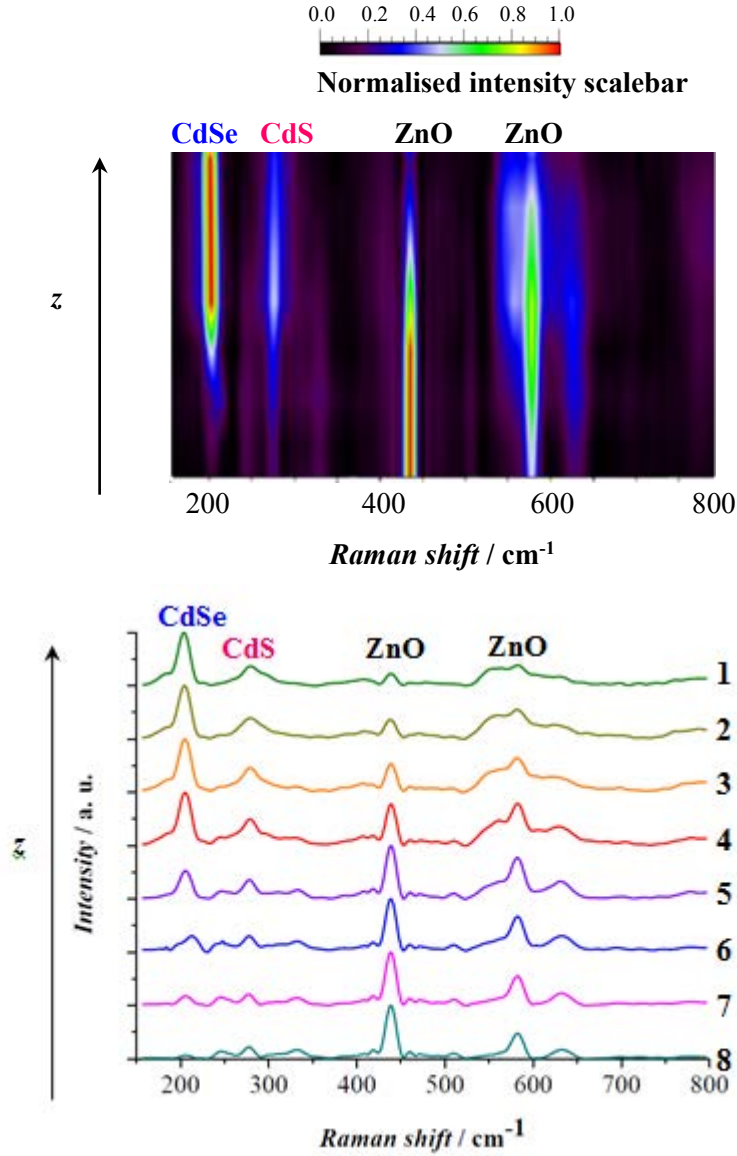


Figure VI.8. Two representations of the depth Raman profile of ZnO nanorod arrays sensitized by 7 layers thick CdSe.SH NPLs. The arrow indicating the z direction points towards the CdSe.SH nanoplatelet-coated surface of the sample.

On the experimental Raman spectra of the CdSe.SH NPL-sensitized ZnO nanorod arrays reported in Figure VI.7.a), b) and c) for 7, 9 and 11 layers thick CdSe.SH NPLs, respectively, we can observe the superposition of peaks characteristic of the bare NPLs and of the bare ZnO substrate, although the latter have a low intensity compared to the NPL peaks. Therefore, only the highest intensity ZnO peak, E_2^{high} is observable in these spectra at 438

Chapter VI. Towards the modeling of QDSCs: sensitizer-oxide heterostructures

cm^{-1} . This is explained by the fact that the ZnO nanorod substrate is buried under a thick CdSe.SH layer, as revealed by the depth profile reported in *Figure VI.8* and *Figure VI.9*. As the incident light is focalized deeper and deeper in the sensitized substrate (towards decreasing z on *Figure VI.8*), ZnO-related peaks appear besides the CdSe.SH-related ones, and the intensities of the former increase compared to the intensities of the NPL peaks. Similar trends were observed in a previous study by Drews et al,⁵⁴ who deposited a CdTe layer on a InSb (110) surface by molecular beam epitaxy growth, and performed *in situ* Raman monitoring of the growth process.

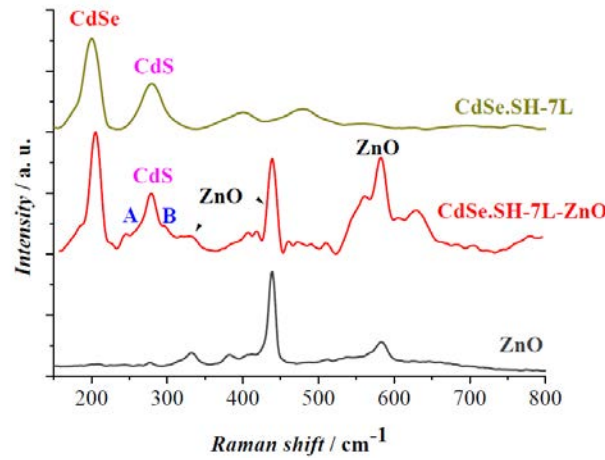


Figure VI.9. Comparison of the experimental Raman spectra of 7 layers thick CdSe.SH NPLs, of bare ZnO nanorod arrays and of ZnO nanorod arrays sensitized by the same NPLs. The latter is an inset from the 4th acquisition of the depth Raman profile reported in more detail in *Figure VI.8*.

	CdSe.SH 7L	CdSe.SH 7L - ZnO	ZnO
CdSe LO	200	206	
A		245	
CdS LO	278	279	
B		293	
ZnO $E_2^{high} - E_2^{low}$		332	332
ZnO E_2^{high}		438	438
ZnO A_1^{low}		582	582

Table VI.3. Experimental Raman shifts (in cm^{-1}) of notable modes in the Raman spectra of the 7 layers thick CdSe.SH NPLs, of ZnO nanorods sensitized by the same NPLs, and of the bare ZnO nanorods

Further details could be observed on the Raman spectra acquired deeper inside the sample, near the NPL-ZnO interface. In the 4th acquisition (red curve) of *Figure VI.9*, the intensity of

Chapter VI. Towards the modeling of QDSCs: sensitizer-oxide heterostructures

the ZnO-related peak at around 438 cm^{-1} became comparable to those of the CdSe and CdS-related peaks at around 200 and 280 cm^{-1} , respectively. By focusing even deeper inside the sample, the intensity of ZnO peaks became higher with respect to the NPL-related ones. Therefore, the spectrum obtained in the 4th acquisition was chosen to be analyzed in more detail and compared to the computed Raman spectra. The Raman shifts of the most notable peaks are gathered for clarity in *Table VI.3*.

It can be observed in *Table VI.3* that the ZnO-related peaks were not shifted with respect to their position in the spectra of the bare ZnO nanorods. A significant redshift of the ZnO-related peak was on the contrary observed in the computed Raman spectra upon the interface formation. In this respect, it should be underlined that the frequencies were computed only on a single ZnO layer, due to the high computational cost associated with Raman spectra calculation with periodic boundary conditions. On the other hand, the experimental spectrum is not limited to one atomic layer, and the Raman spectra of the ensemble of ZnO nanorods are expected to be similar to that of the bulk.⁵⁵ However, the peaks attributed to the ZnO substrate in *Figure VI.8* became wider, and surrounded by several smaller intensity peaks, as reported in *Figure VI.9*. The latter was also observed in the computed Raman spectra in *Figure VI.6 a)*, and can be explained by the structural distortions related to the interface formation, especially in the upper atomic layers of ZnO.

The experimentally observed CdSe and CdS LO peaks are both slightly blueshifted with respect to their position in the Raman spectra of the bare nanoplatelets, which can be a sign of the compressive strain that the NPLs suffer upon interface formation. Two additional peaks appear in partial overlap with the CdS LO mode that were not present in the spectra of the bare nanoplatelet: **A** at 245 cm^{-1} and **B** at 293 cm^{-1} . Based on previous works that reported the LO mode of $\text{Cd}_x\text{Zn}_{(1-x)}\text{S}$ nanostructures at around 300 cm^{-1} ,^{56,57} and their surface optical (SO) mode at around $250\text{-}270\text{ cm}^{-1}$,^{56,57} **A** and **B** peaks are assigned to the nanoplatelet-oxide interface formed via Cd-S-Zn bonds. The equivalent of **A** and **B** modes in the theoretical spectra are the interface modes appearing between 200 and 300 cm^{-1} .

Chapter VI. Towards the modeling of QDSCs: sensitizer-oxide heterostructures

To summarize, we can point out that we observed the same groups of peaks in the experimental and in the computed spectra in the same frequency order, corresponding to characteristic vibrations of the single components of these heterostructures and of the interface they formed. This qualitative agreement mutually validates the two approaches to characterize the nanostructures studied in this work, and, besides, our model.

VI.6. Electronic properties

Considering the basic working principle of QDSCs, illumination promotes an electron to a QD excited state, from which it is injected into the conduction band (CB) of a wide band gap semiconductor (WBSC), typically TiO_2 or ZnO . The electrons are then transported through the WBSC layer until they reach the front contact. They are then transferred through an external load to the counter-electrode. An appropriate description of the electronic structure of solar cell components is thus crucial for optimizing the performance of these devices. Due to the difficulties related to obtaining an experimentally accurate description of the electronic properties at an atomistic scale, the use of computational approaches is highly relevant. The band structure, especially band gaps, the top of VB and the bottom of CB levels, density of states (DOS) and the electronic structure of surfaces and interfaces are actually all essential parameters for the quantification of electron excitation and injection processes.

Band structures, as well as density of states (DOS) of the CdSe.SH NPL and the CdSe.SH-ZnO system have been computed, and are shown in *Figure VI.10*, in which the top of VB of the CdSe.SH NPL was chosen as the zero of energy in each case. The comparison of the DOS computed for the optimized CdSe.SH-ZnO structure and that of the CdSe.SH NPL, highlights significant differences due to the formation of the interface. Adsorbate (CdSe.SH)-projected DOS are shifted towards higher energy with respect to the DOS of the bare NPL, causing a lowering of the band gap of the heterostructure compared to that of the bare NPL, as also reported in *Table VI.4*. This is qualitatively in line with the experimental observation that the band gap of CdSe.SH NPLs decreased by 0.1-0.2 eV upon adsorption onto the ZnO nanorod arrays (*Table VI.4*). This decrease is overestimated by the theoretical model. It can also be

Chapter VI. Towards the modeling of QDSCs: sensitizer-oxide heterostructures

observed in *Figure VI.10 b*) that the adsorbate- and substrate-projected DOS overlap in a large interval below the Fermi level and also in the conduction band (CB) of the CdSe.SH-ZnO structure, which indicates a strong interaction between the NPL and the ZnO substrate. As shown in *Figure VI.10 b*), the top of valence bands (VB) of the heterostructure is dominated by NPL-projected states with low ZnO-projected contribution. On the other hand, the bottom of CB is dominated by ZnO-projected states with low NPL contribution. These findings indicate that the electron transfer from the excited CdSe.SH NPL towards the ZnO surface should be possible, in line with the basic operating principles of QDSCs, in which a photoexcited electron localized on the quantum dot is injected to the CB of a wide band gap semiconductor.

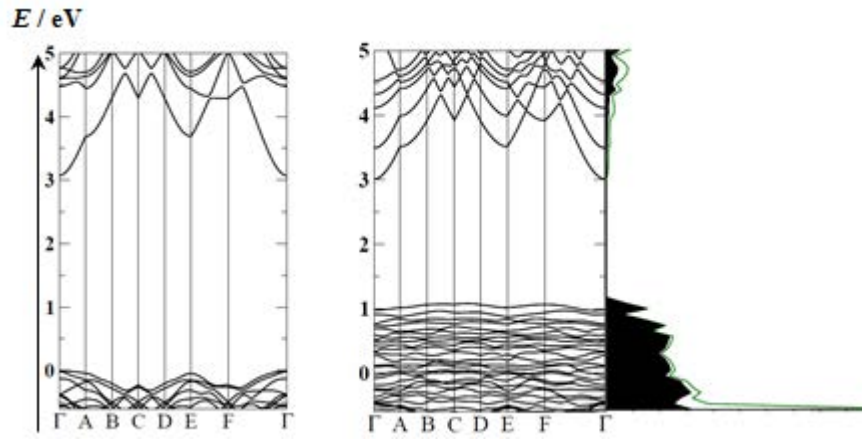


Figure VI.10. Band structures and density of states (DOS) of a) the bare CdSe.SH slab and b) the CdSe.SH (5L) – ZnO (8L) heterostructure. The Fermi energy of the bare CdSe.SH slab was chosen to be the zero of energy in each figure. The k points in the reciprocal space are defined as Γ (0 0 0), A $\left(0 \frac{1}{3} 0\right)$, B $\left(\frac{1}{3} \frac{1}{3} \frac{1}{3}\right)$, C $\left(\frac{2}{3} \frac{1}{3} \frac{2}{3}\right)$, D $\left(\frac{2}{3} \frac{2}{3} \frac{2}{3}\right)$, E $\left(\frac{3}{3} \frac{2}{3} 0\right)$, F $\left(\frac{2}{3} \frac{1}{3} 0\right)$.

	CdSe.SH 5L	CdSe.SH 7L	CdSe.SH 9L	CdSe.SH 11L
E_{gap} (eV)	3.07 (d) ^{theo}	2.45 (d) ^{exp}	2.53 (d) ^{theo} ; 2.29 (d) ^{exp}	2.18 (d) ^{exp}
	CdSe.SH 5L - ZnO	CdSe.SH 7L - ZnO	CdSe.SH 9L - ZnO	CdSe.SH 11L - ZnO
E_{gap} (eV)	1.93 (i) ^{theo}	2.25 (i) ^{exp}	1.83 (i) ^{theo} ; 2.19 (i) ^{exp}	2.02 (i) ^{exp}

Table VI.4. Computed band gaps of the isolated CdSe.SH NPLs and CdSe.SH – ZnO heterostructures. Experimental and theoretical band gaps referred to as “exp” and “theo”. The nature of band gaps (direct (d) and indirect (i)) is also indicated.

To better clarify this point, the highest occupied and lowest unoccupied crystalline orbitals at the Γ point (HOCO and the LUCO, respectively) are reported in *Figure VI.11*. It can be

Chapter VI. Towards the modeling of QDSCs: sensitizer-oxide heterostructures

observed that although the HOCO is dominated by adsorbate contributions and the LUCO is mainly localized on the substrate, there are significant contributions from the other subsystem in both cases. This qualitatively suggests that the electron injection from the NPL towards the ZnO surface is partial.

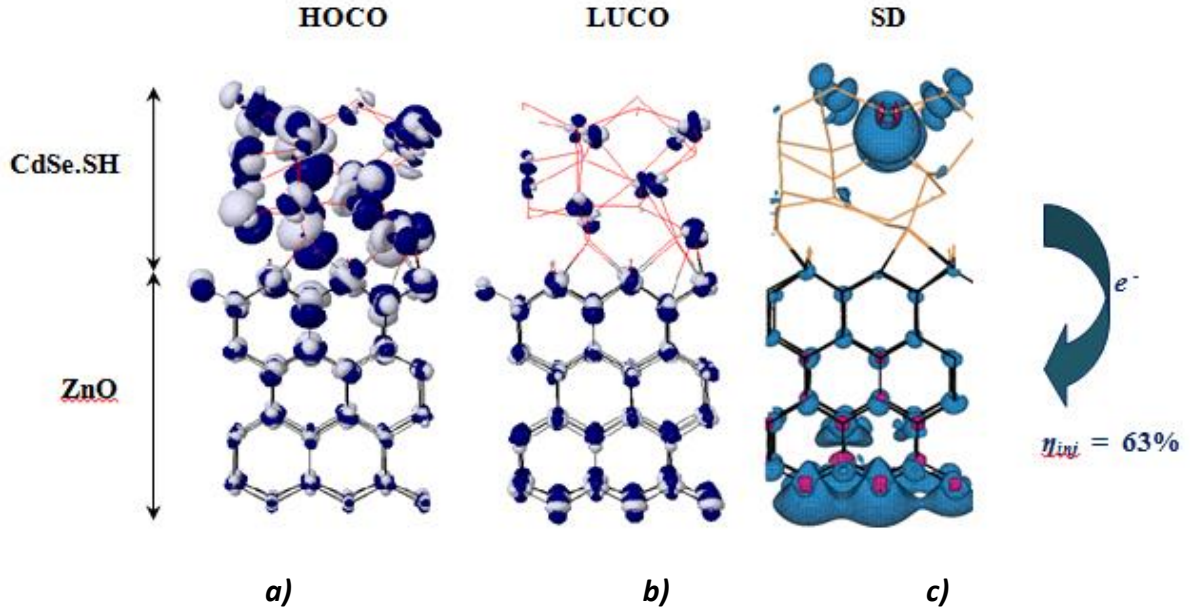


Figure VI.11. a) Γ -point HOCO and b) Γ -point LUCO of the CdSe.SH-ZnO heterostructure. Isosurface level at 0.02 a.u. Spin densities (SD) of the reduced CdSe.SH (5L)-ZnO system (excess of alpha electron is indicated in blue) isosurface level at 0.00034 a.u.

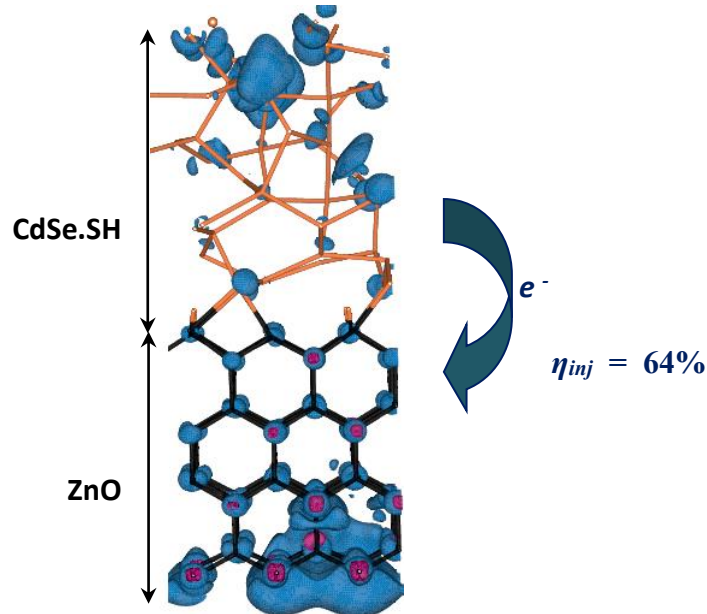


Figure V.12. Spin densities (SD) of the reduced CdSe.SH (9L)-ZnO system (excess of alpha electron is indicated in blue) isosurface level at 0.00034 a.u.

Chapter VI. Towards the modeling of QDSCs: sensitizer-oxide heterostructures

In order to model the electron injection from the CdSe.SH NPL to the ZnO surface, the corresponding one-electron reduced system was studied. This approach is analogous to experimental spectro-electrochemical studies that mimic excited states resulting from photo-induced electron transfer processes via the reduced system.^{58,59} Besides, it has also been shown to be particularly efficient for predicting electron injection rates in dye sensitized solar cells (DSSCs).^{60–62} In order to analyze the electronic structure of the reduced system, its spin density map (corresponding to the difference between alpha- and beta-spin electron densities) was computed and reported in *Figure VI.11. c) for 5 layers thick CdSe.SH NPLs*. The computed spin density is delocalized over the whole system, and by integration of the spin density over the ZnO slab, we obtained that only 63% of the electron is injected from the sensitizer to the substrate in case of the heterostructure with 5 layers thick CdSe.SH NPLs.

We have also shown that the injection efficiency is not sensitive to the slab thickness, since a value of 64% for the system with 9 layers thick NPLs has been computed (*Figure VI.12.*). This partial electron injection is in line with the analysis of the DOS and the Γ -point frontier crystalline orbitals and highlights the delocalized nature of the reduced state, which predicts a high probability of electron-hole recombinations between the sensitizer and the substrate.

VI.6. Conclusions

We developed a combined theoretical and experimental approach to characterize a semiconductor heterostructure consisting of CdSe nanoplatelets linked to a ZnO surface by SH⁻ ligands, and paid a special attention on the interface properties of this system. Experimentally, ZnO wurtzite nanorods were grown by a hydrothermal method, and quasi two-dimensional CdSe nanoplatelets of different thicknesses were bounded to them through SH⁻ ligands. The attachment of NPLs to the ZnO substrate caused a redshift of the excitonic peaks in their UV-VIS absorption spectra, which suggests that structural modifications took place upon sensitization, especially in the NPLs. The Raman spectra of the nanoplatelet-nanorod heterostructures featured the peaks of both bare components, with the additional

Chapter VI. Towards the modeling of QDSCs: sensitizer-oxide heterostructures

presence of interface related peaks. Applying a computationally affordable but accurate periodic DFT-based computational protocol, we were able to characterize the nature of the heterostructure that contains the CdSe.SH part and the uppermost ZnO layer. The obtained results suggest that the CdSe.SH nanoplatelet is covalently bound to the ZnO surface through sulphur atoms. In agreement with the experimental findings, the formation of this semiconductor interface resulted in significant structural modifications, especially in case of the CdSe.SH subsystem whose atoms were largely displaced with respect to their initial position, and lost their tetrahedrally symmetric coordination. The computed Raman spectra reflected this loss of symmetry, as the peaks of the initial subsystems were split into several ones. The computed frequencies were in qualitative agreement with the experimental data. Moreover, the interface formation through Cd-S-Zn bonds was demonstrated by peaks related to vibrations specific to the Cd-S and Zn-S bonds at the interface of this heterostructure. The electronic properties of the system, including band gaps, density of states and crystalline orbitals were also calculated. In line with the experimental results, the computed band gap of the heterostructure was also found smaller than that of the bare NPL, although the computed band gap decrease was superior to the experimental one. Finally, we calculated the electron injection efficiency from the nanoplatelet towards the ZnO, an important parameter for solar cell applications. In agreement with the density of states and the crystalline orbitals investigation, this charge injection turned out to be possible, although only partial: a 63% efficiency was obtained for the heterostructure with 5 layers thick CdSe.SH NPLs, and 64% for the one with 9 layers thick NPLs. The delocalized nature of the electronic states indicated that electron-hole recombinations between the CdSe.SH NPL and the ZnO substrate are highly probable.

From these results, we can thus conclude that the here presented system is less advantageous for photovoltaic applications but can be used to draw guidelines for designing more efficient systems. In particular, replacing atomic linkers such as the here studied SH⁻, by longer molecular linkers such as mercaptopropionic acid (MPA) should result in a less distorted nanoplatelet-oxide interface (as it can actually be deduced from the UV-VIS absorption spectra of CdSe.MPA – ZnO systems reported in **Chapter V Figure V.19**), and

Chapter VI. Towards the modeling of QDSCs: sensitizer-oxide heterostructures

eventually in electronic states that are more localized on either of the components, making it possible to obtain a more complete electron injection.

In the next chapter, the CdSe.SH – ZnO systems will be incorporated into solar cells, and the as-made devices tested. Their performance will be compared to those based on CdSe.SH – TiO₂ photoanodes, as well as ZnO and TiO₂ nanorods sensitized with in situ grown CdSe QDs, instead of pre-synthesized nanoplatelets.

Chapter VI. Towards the modeling of QDSCs: sensitizer-oxide heterostructures

References

- (1) Xu, S. J.; Wang, H.; Li, Q.; Xie, M. H.; Wang, X. C.; Fan, W. J.; Feng, S. L. X-Ray Diffraction and Optical Characterization of Interdiffusion in Self-Assembled InAs/GaAs Quantum-Dot Superlattices. *Appl. Phys. Lett.* **2000**, 77 (14), 2130.
- (2) Pagès, O.; Ajjoun, M.; Tite, T.; Bormann, D.; Tournié, E.; Rustagi, K. C. Long-Wave Phonons in ZnSe – BeSe Mixed Crystals: Raman Scattering and Percolation Model. *Phys. Rev. B* **2004**, 70 (15), 155319.
- (3) Patrick, C. E.; Giustino, F. Structural and Electronic Properties of Semiconductor-Sensitized Solar-Cell Interfaces. *Adv. Funct. Mater.* **2011**, 21, 4663–4667.
- (4) Long, R.; English, N. J.; Prezhdo, O. V. Minimizing Electron – Hole Recombination on TiO₂ Sensitized with PbSe Quantum Dots: Time-Domain Ab Initio Analysis. *J. Phys. Chem. Lett.* **2014**, 5, 2941.
- (5) Dong, C.; Li, X.; Qi, J. First-Principles Investigation on Electronic Properties of Quantum Dot-Sensitized Solar Cells Based on Anatase TiO₂ Nanotubes. *J. Phys. Chem. C* **2011**, 115, 20307–20315.
- (6) Tafen, D. N.; Prezhdo, O. V. Size and Temperature Dependence of Electron Transfer between CdSe Quantum Dots and a TiO₂ Nanobelt. *J. Phys. Chem. C* **2015**, 119 (10), 5639–5647.
- (7) Gómez Díaz, J.; Ding, Y.; Koitz, R.; Seitsonen, A. P.; Iannuzzi, M.; Hutter, J. Hexagonal Boron Nitride on Transition Metal Surfaces. *Theor. Chem. Acc.* **2013**, 132 (4), 1350.
- (8) Mohn, C. E.; Stein, M. J.; Allan, N. L. Oxide and Halide Nanoclusters on Ionic Substrates: Heterofilm Formation and Lattice Mismatch. *J. Mater. Chem.* **2010**, 20 (46), 10403.
- (9) Muck, T.; Wagner, J. W.; Hansen, L.; Wagner, V.; Geurts, J.; Ivanov, S. V. Vibration Dynamics and Interfacial Chemistry of the CdSe / BeTe Interface. *Phys. Rev. B* **2004**, 69 (24), 245314.
- (10) Rache Salles, B.; Kunc, K.; Eddrief, M.; Etgens, V. H.; Finocchi, F.; Vidal, F. Hexagon-on-Cube versus Cube-on-Cube Epitaxy: The Case of ZnSe(111) on SrTiO₃ (001). *Phys. Rev. B* **2009**, 79 (15), 155312.
- (11) Trejo, O.; Roelofs, K. E.; Xu, S.; Logar, M.; Sarangi, R.; Nordlund, D.; Dadlani, A. L.; Kravec, R.; Dasgupta, N. P.; Bent, S. F.; et al. Quantifying Geometric Strain at the PbS QD-TiO₂ Anode Interface and Its Effect on Electronic Structures. *Nano Lett.* **2015**, 15 (12), 7829–7836.
- (12) Corà, F.; Alfredsson, M.; Mallia, G.; Middlemiss, D. S.; Mackrodt, W. C.; Dovesi, R.; Orlando, R. The Performance of Hybrid Density Functionals in Solid State Chemistry. In *Structure and Bonding*; Springer-Verlag Berlin Heidelberg, 2004; Vol. 113, p 171.
- (13) Han, P.; Bester, G. Heavy Strain Conditions in Colloidal Core-Shell Quantum Dots and Their Consequences on the Vibrational Properties from Ab Initio Calculations. *Phys. Rev. B* **2015**, 92, 125438.
- (14) Geurts, J. Raman Spectroscopy from Buried Semiconductor Interfaces: Structural and Electronic Properties. *Phys. Status Solidi* **2015**, 252 (1), 19–29.
- (15) Long, R.; Prezhdo, O. V. Ab Initio Nonadiabatic Molecular Dynamics of the Ultrafast Electron Injection from a PbSe Quantum Dot into the TiO₂ Surface. *J. Am. Chem. Soc.* **2011**, 133, 19240–19249.
- (16) Sigle, D. O.; Hugall, J. T.; Ithurria, S.; Dubertret, B.; Baumberg, J. J. Probing Confined Phonon Modes in Individual CdSe Nanoplatelets Using Surface-Enhanced Raman Scattering. *Phys. Rev. Lett.* **2014**, 113 (8), 087402.
- (17) Zardo, I.; Conesa-Boj, S.; Peiro, F.; Morante, J. R.; Arbiol, J.; Uccelli, E.; Abstreiter, G.; Fontcuberta i Morral, a. Raman Spectroscopy of Wurtzite and Zinc-Blende GaAs Nanowires: Polarization Dependence, Selection Rules, and Strain Effects. *Phys. Rev. B* **2009**, 80 (24), 245324.
- (18) Rumyantseva, A.; Kostcheev, S.; Adam, P.-M.; Gaponenko, S. V.; Vaschenko, S. V.; Kulakovich, O. S.; Ramanenka, A. A.; Guzatov, D. V.; Korbutyak, D.; Dzhagan, V.; et al. Nonresonant Surface-Enhanced Raman Scattering of ZnO Quantum Dots with Au and Ag Nanoparticles. *ACS Nano* **2013**, 7 (4), 3420–3426.
- (19) Dovesi, R.; Orlando, R.; Civalieri, B.; Roetti, C.; Saunders, V. R.; Zicovich-Wilson, C. M. CRYSTAL : A Computational Tool for the Ab Initio Study of the Electronic Properties of Crystals. *Zeitschrift für Krist. - Cryst. Mater.* **2005**, 220, 571–573.
- (20) Dovesi, R.; Saunders, V. R.; Roetti, C.; Orlando, R.; Zicovich-Wilson, C. M.; Pascale, F.; Civalieri, B.; Doll, K.; Harrison, N. M.; Bush, I. J.; et al. CRYSTAL14 - User's Manual. **2014**.
- (21) Szemjonov, A.; Pauporté, T.; Ithurria, S.; Lequeux, N.; Dubertret, B.; Ciofini, I.; Labat, F. Ligand-Stabilized CdSe Nanoplatelet Hybrid Structures with Tailored Geometric and Electronic Properties. New Insights

Chapter VI. Towards the modeling of QDSCs: sensitizer-oxide heterostructures

-
- from Theory. *RSC Adv.* **2014**, 4 (99), 55980–55989.
- (22) Szemjonov, A.; Pauporté, T.; Ciofini, I.; Labat, F. Investigation of the Bulk and Surface Properties of CdSe: Insights from Theory. *Phys. Chem. Chem. Phys.* **2014**, 16 (42), 23251–23259.
- (23) Becke, A. D. Density-Functional Thermochemistry. III. The Role of Exact Exchange. *J. Chem. Phys.* **1993**, 7, 5648–5652.
- (24) Kristyan, S.; Pulay, P. Can (Semi)local Density Functional Theory Account for the London Dispersion Forces ? *Chem. Phys. Lett.* **1994**, 229, 175–180.
- (25) Hobza, P.; Sponer, J.; Reschel, T. Density Functional Theory and Molecular Clusters. *J. Comput. Chem.* **1995**, 16 (11), 1315–1325.
- (26) Grimme, S. Semiempirical GGA-Type Density Functional Constructed with a Long-Range Dispersion Correction. *J. Comput. Chem.* **2006**, 27, 1787–1799.
- (27) Becke, A. D. Density-Functional thermochemistry.III. The Role of Exact Exchange. *J. Chem. Phys.* **1993**, 98 (7), 5648.
- (28) Stevens, W. J.; Krauss, M.; Basch, H.; Jasien, P. G. Relativistic Compact Effective Potentials and Efficient, Shared-Exponent Basis Sets for the Third-, Fourth-, and Fifth-Row Atoms. *Can. J. Chem.* **1992**, 70 (2), 612–630.
- (29) Labello, N. P.; Ferreira, A. M.; Kurtz, H. a. An Augmented Effective Core Potential Basis Set for the Calculation of Molecular Polarizabilities. *J. Comput. Chem.* **2005**, 26 (14), 1464–1471.
- (30) Xiao, H.; Tahir-Kheli, J.; Goddard, W. A. Accurate Band Gaps for Semiconductors from Density Functional Theory. *J. Phys. Chem. Lett.* **2011**, 2, 212.
- (31) Durand, P.; Barthelat, J.-C. NEW ATOMIC PSEUDOPOTENTIALS FOR ELECTRONIC STRUCTURE CALCULATIONS OF MOLECULES AND SOLIDS. *Chem. Phys. Lett.* **1974**, 27, 191–194.
- (32) Durand, P.; Barthelat, J.-C. A Theoretical Method to Determine Atomic Pseudopotentials for Electronic Structure Calculations of Molecules and Solids. *Theor. Chim. Acta* **1975**, 38, 283–302.
- (33) Hay, P. J.; Wadt, W. R. Ab Initio Effective Core Potentials for Molecular Calculations. Potentials for the Transition Metal Atoms Sc to Hg. *J. Chem. Phys.* **1985**, 82 (1), 270.
- (34) Labat, F.; Ciofini, I.; Adamo, C. Modeling ZnO Phases Using a Periodic Approach: From Bulk to Surface and Beyond. *J. Chem. Phys.* **2009**, 131 (4), 044708.
- (35) Ouazzani, T.; Lichanot, A.; Pisani, C.; Roetti, C. RELAXATION AND ELECTRONIC STRUCTURE OF SURFACES IN LITHIUM SULPHIDE : A HARTREE-FOCK A13 INITIO APPROACH. *J. Phys. Chem. Solids* **1993**, 54 (11), 1603–1611.
- (36) Pascale, F.; Zicovich-Wilson, C. M.; Lopez Gejo, F.; Civalieri, B.; Orlando, R.; Dovesi, R. The Calculation of the Vibrational Frequencies of Crystalline Compounds and Its Implementation in the CRYSTAL Code. *J. Comput. Chem.* **2004**, 25, 888–897.
- (37) Zicovich-Wilson, C. M.; Pascale, F.; Roetti, C.; Saunders, V. R.; Orlando, R.; Dovesi, R. Calculation of the Vibration Frequencies of Alpha-Quartz: The Effect of Hamiltonian and Basis Set. *J. Comput. Chem.* **2004**, 25 (15), 1873–1881.
- (38) Maschio, L.; Kirtman, B.; Rérat, M.; Orlando, R.; Dovesi, R. Ab Initio Analytical Raman Intensities for Periodic Systems through a Coupled Perturbed Hartree-Fock/Kohn-Sham Method in an Atomic Orbital Basis. II. Validation and Comparison with Experiments. *J. Chem. Phys.* **2013**, 139 (16), 164102.
- (39) Maschio, L.; Kirtman, B.; Rérat, M.; Orlando, R.; Dovesi, R. Ab Initio Analytical Raman Intensities for Periodic Systems through a Coupled Perturbed Hartree-Fock/Kohn-Sham Method in an Atomic Orbital Basis. I. Theory. *J. Chem. Phys.* **2013**, 139 (16), 164101.
- (40) Ferrero, M.; Rérat, M.; Orlando, R.; Dovesi, R. Coupled Perturbed Hartree-Fock for Periodic Systems: The Role of Symmetry and Related Computational Aspects. *J. Chem. Phys.* **2008**, 128 (1), 014110.
- (41) Ferrero, M.; Rérat, M.; Kirtman, B.; Dovesi, R. Calculation of First and Second Static Hyperpolarizabilities of One- to Three-Dimensional Periodic Compounds. Implementation in the CRYSTAL Code. *J. Chem. Phys.* **2008**, 129 (24), 244110.
- (42) Ferrero, M.; Rérat, M.; Orlando, R.; Dovesi, R. The Calculation of Static Polarizabilities of 1-3D Periodic Compounds. the Implementation in the Crystal Code. *J. Comput. Chem.* **2008**, 29 (9), 1450–1459.
- (43) Buchanan, R. C.; Park, T. *Materials Crystal Chemistry*; CRC Press: New York, 1997.
- (44) Zuala, L.; Agarwal, P. Effect of Se Concentration on Mixed Phonon Modes and Spin Orbit Splitting in Thermally Evaporated CdS_xSe_{1-x} (0 ≤ x ≤ 1) Films Using CdS–CdSe Nano-Composites. *Mater. Chem. Phys.* **2015**, 162, 813–821.
- (45) Mitra, S. S.; Brafman, O.; Daniels, W. B.; Crawford, R. K. Pressure-Induced Phonon Frequency Shifts Measured by Raman Scattering. *Phys. Rev.* **1969**, 186 (3), 942–944.

Chapter VI. Towards the modeling of QDSCs: sensitizer-oxide heterostructures

- (46) Pejova, B. Phonon Confinement and Related Effects in Three-Dimensional Assemblies of Cubic Cadmium Selenide Quantum Dots Synthesized by Conventional Chemical and Sonochemical Routes. *J. Phys. Chem. C* **2013**, *117*, 19689–19700.
- (47) Behera, S. N.; Nayak, P.; Patnaik, K. A New Criterion for the Mixed Crystal Behaviour in the Diatomic Linear Chain Model. *Solids Pramana* **1977**, *8* (3), 255.
- (48) Cuscó, R.; Alarcón-Lladó, E.; Ibáñez, J.; Artús, L.; Jiménez, J.; Wang, B.; Callahan, M. J. Temperature Dependence of Raman Scattering in ZnO. *Phys. Rev. B* **2007**, *75* (16), 165202.
- (49) Zicovich-Wilson, C. M.; Torres, F. J.; Pascale, F.; Valenzano, L.; Orlando, R.; Dovesi, R. Ab Initio Simulation of the IR Spectra of Pyrope, Grossular, and Andradite. *J. Comput. Chem.* **2008**, *29*, 2268–2278.
- (50) Tschirner, N.; Lange, H.; Schliwa, A.; Biermann, A.; Thomsen, C.; Lambert, K.; Gomes, R.; Hens, Z. Interfacial Alloying in CdSe/CdS Heteronanocrystals: A Raman Spectroscopy Analysis. *Chem. Mater.* **2012**, *24* (2), 311–318.
- (51) Lin, C.; Gong, K.; Kelley, D. F.; Kelley, A. M. Electron-Phonon Coupling in CdSe/CdS Core/Shell Quantum Dots. *ACS Nano* **2015**, *9* (8), 8131–8141.
- (52) Dzhagan, V. M.; Valakh, M. Y.; Milekhin, A. G.; Yeryukov, N. a.; Zahn, D. R. T.; Cassette, E.; Pons, T.; Dubertret, B. Raman- and IR-Active Phonons in CdSe/CdS Core/Shell Nanocrystals in the Presence of Interface Alloying and Strain. *J. Phys. Chem. C* **2013**, *117* (35), 18225–18233.
- (53) Lu, L.; Xu, X.-L.; Liang, W.-T.; Lu, H.-F. Raman Analysis of CdSe/CdS Core-Shell Quantum Dots with Different CdS Shell Thickness. *J. physics. Condens. matter* **2007**, *19* (40), 406221.
- (54) Drews, D.; Sahm, J.; Richter, W.; Zahn, D. R. T. Molecular-Beam-Epitaxy Growth of CdTe on InSb (110) Monitored in Situ by Raman Spectroscopy. *J. Appl. Phys.* **1995**, *78* (6), 4060.
- (55) Yu, J. L.; Lai, Y. F.; Wang, Y. Z.; Cheng, S. Y.; Chen, Y. H. Polarized Raman Scattering of Single ZnO Nanorod. *J. Appl. Phys.* **2014**, *115* (3).
- (56) Kozytskiy, A. V.; Stroyuk, O. L.; Kuchmiy, S. Y.; Dzhagan, V. M.; Zahn, D. R. T.; Skoryk, M. a.; Moskalyuk, V. O. Morphology, Optical, and Photoelectrochemical Properties of Electrodeposited Nanocrystalline ZnO Films Sensitized with Cd X Zn1-x S Nanoparticles. *J. Mater. Sci.* **2013**, *48* (21), 7764–7773.
- (57) Azhniuk, Y. M.; Gomonnai, A. V.; Lopushansky, V. V.; Hutych, Y. I.; Turok, I. I.; Zahn, D. R. T. Resonant Raman Scattering Studies of Cd 1-X Zn X S Nanocrystals. *J. Phys. Conf. Ser.* **2007**, *92* (1), 012044.
- (58) Ciofini, I.; Laine, P. P.; Bedioui, F.; Adamo, C. Photoinduced Intramolecular Electron Transfer in Ruthenium and Osmium Polyads : Insights from Theory. *J. Am. Chem. Soc.* **2004**, *126*, 10763–10777.
- (59) Lainé, P. P.; Ciofini, I.; Ochsenbein, P.; Amouyal, E.; Adamo, C.; Bedioui, F. Photoinduced Processes within Compact Dyads Based on Triphenylpyridinium-Functionalized Bipyridyl Complexes of ruthenium(II). *Chem. -A Eur. J.* **2005**, *11* (12), 3711–3727.
- (60) Le Bahers, T.; Labat, F.; Pauporté, T.; Lainé, P. P.; Ciofini, I. Theoretical Procedure for Optimizing Dye-Sensitized Solar Cells: From Electronic Structure to Photovoltaic Efficiency. *J. Am. Chem. Soc.* **2011**, *133* (20), 8005–8013.
- (61) Le Bahers, T.; Pauporté, T.; Lainé, P. P.; Labat, F.; Adamo, C.; Ciofini, I. Modeling Dye-Sensitized Solar Cells : From Theory to Experiment. *J. Phys. Chem. Lett.* **2013**, *4*, 1044–1050.
- (62) Labat, F.; Ciofini, I.; Hratchian, H. P.; Frisch, M. J.; Raghavachari, K.; Adamo, C. Insights into Working Principles of Ruthenium Polypyridyl Dye-Sensitized Solar Cells from First Principles Modeling. *J. Phys. Chem. C* **2011**, *115*, 4297–4306.

Chapter VII. Quantum dot sensitized solar cells

In a final study of this thesis, photoanodes made with ex-situ grown nanoplatelets studied in **Chapters V** and **VI** have been implemented in solar cells. Both all-solid-state and liquid electrolyte-based configurations were tested and compared. Next, we have compared solar cells prepared with pre-synthesized nanocrystals and with *in situ* grown QDs. While photoanodes prepared with the former method were characterized and modeled in **Chapters V** and **VI**, the *in situ* growth of CdS and CdSe QDs on ZnO and TiO₂ NR arrays is studied in this chapter.

VII. 1. QDSCs based on *ex-situ* prepared CdSe NPLs

VII.1.1. All-solid-state QDSCs

The assembly of solar cells was described in detail in **Chapter II**. Briefly, ZnO NR arrays were sensitized with 9 layers thick CdSe.SH and CdSe.MPA NPLs. A spiro-OMeTAD-based solid-state hole transport material (HTM) was spin-coated on the top of the photoanodes, and a silver counter electrode was evaporated on the HTM. In the notation of the as-prepared solar cells, the first number corresponds to the NPL thickness (9 layers thick), the second character (**S** or **M**) is an abbreviation of the linker (SH⁻ or MPA), the third one (**Z** or **T**) corresponds to the ZnO or TiO₂ NR arrays, and the last one indicates that a solid-state electrolyte (**S**) was used. While **9MZS** and **9SZS** solar cells did not generate current, **9STS** solar cells worked, although their performance was poor, as reported in *Table VII.1*.

	V_{oc} / V	J_{sc} / mA	Fill factor / %	$\eta / \%$
9STS	0.426	0.052	34.8	0.008
9STS	0.136	0.014	28.8	0.006

Table VII.1. J-V characteristics of all-solid state QDSCs based on pre-synthesized CdSe.SH NPLs

The low performance is explained by the incomplete pore filling of the hole-transporting material within the WBSC film.¹ Hence, despite the presumed advantage of using solid HTM

Chapter VII. Quantum dot sensitized solar cells

for the long-term stability of the cells,² we did not continue testing all-solid-state QDSCs, and focused on solar cells made with a liquid redox electrolyte instead.

VII.1.2. QDSCs with liquid redox electrolytes

CdSe nanocrystals of different shapes (spherical QDs and quasi-2D NPLs of various thicknesses) have been linked to ZnO and TiO₂ nanorod arrays *via* SH⁻ ligands. The devices were completed by a S²⁻/Sn²⁻ liquid redox electrolyte and a brass/Cu₂S counter electrode, which preparation and composition are described in **Chapter II**. Similarly to the all-solid-state QDSCs, the different combinations of materials are denoted as follows. The first number or character corresponds to the CdSe nanocrystal shape. If NPLs were used, their thickness is denoted as **7**, **9** or **11** layers as defined in **Chapter II**, and the QDs are indicated as **Q**. In the following notations, **S** corresponds to the SH⁻ linker, **Z** and **T** to the ZnO and TiO₂ nanorod arrays, respectively, and **L** indicates that these QDSCs were prepared with a liquid redox electrolyte.

VII.1.2. a) ZnO-based QDSCs

As reported in *Table VII.2*, the efficiency parameters of QDSCs prepared with a ZnO substrate were very variable and irreproducible. A possible explanation is that the S²⁻/Sn²⁻ electrolyte washed off the majority of sensitizers from the ZnO or the TiO₂ substrate, as it was observed when the cells were disassembling after their characterization. Indeed, it has been reported in a previous study that CdSe.SH QD aggregates are easily solubilized in polar solvents containing an excess of SH⁻ ions.³ As it was deduced from our Raman depth profile study of the CdSe.SH-ZnO system (**Chapter V**), probably only a few of the NPLs were linked to the side facets of the nanorods, while most of them were stacked as a thick layer on top of the substrate. The nanoparticles in this layer could likely be dissolved by the liquid electrolyte. *Table VII.2* shows that in general, all the solar cells made with 7 and 11 L thick NPLs, as well as QDs performed poorly. However, in case of 9 layers thick CdSe.SH NPLs, it was possible to obtain a power conversion efficiency of up to 0.69%.

Chapter VII. Quantum dot sensitized solar cells

	V_{oc} / V	J_{sc} / mA	Fill factor / %	$\eta / \%$
7SZL	0.151	0.063	23.2	0.002
9SZL	0.175	0.835	56.8	0.08
9SZL	0.245	9.49	29.8	0.69
11SZL	0.123	0.192	34.5	0.01
11SZL	0.160	0.215	31.9	0.01
QSZL	0.247	0.319	25.9	0.02
QSZL	0.075	0.043	32.2	0.003
QSZL	0.241	1.66	25.3	0.09

Table VII.2. J-V curve parameters of QDSCs prepared with a liquid electrolyte and pre-synthesized CdSe.SH nanocrystals attached to ZnO nanorod arrays

VII.1.2. b) TiO₂-based QDSCs

Similarly, we have investigated QDSCs prepared with TiO₂ NRs. Poor performance and hardly reproducible results were obtained using pre-synthesized CdSe nanocrystals, as reported in Table VII.3. The power conversion efficiency of the studied TiO₂-based cells was generally higher than those with ZnO substrates reported in Table VII.2. $\eta = 0.65 \%$ was measured for the best performing QDSC with 7 L thick CdSe.SH NPLs, and $\eta = 1.90 \%$ with 9 L thick CdSe.SH NPLs.

	V_{oc} / V	J_{sc} / mA	Fill factor / %	$\eta / \%$
7STL	0.251	7.37	35.1	0.65
7STL	0.151	0.011	18.4	0.002
9STL	0.561	8.11	41.7	1.90
9STL	0.173	0.113	33.9	0.01
9STL	0.211	1.420	25.1	0.08

Table VII.3. J-V curve parameters of QDSCs prepared with a liquid electrolyte and pre-synthesized CdSe.SH NPLs attached to TiO₂ nanorod arrays

VII.2. QDSCs with *in-situ* prepared CdSe QDs

As a first step, we tested the SILAR procedure described in ref. 4 both on ZnO and TiO₂ nanorod arrays, and prepared solar cells with the same S^{2-}/S_n^{2-} liquid redox electrolyte and a brass/Cu₂S counter electrode as described above. We compared the performance of QDSCs prepared in 6 and 12 SILAR cycles. Moreover, we also constructed a system which was

Chapter VII. Quantum dot sensitized solar cells

comparable to the previously studied CdSe.SH-ZnO heterostructure. Accordingly, we incorporated a CdS layer by doing one CdS SILAR cycle first before to carry out the successive Cd and Se layers deposition for 12 cycles (see experimental details in **Chapter II** section II.2.3. b).

VII.2.1. QDSCs with a ZnO substrate

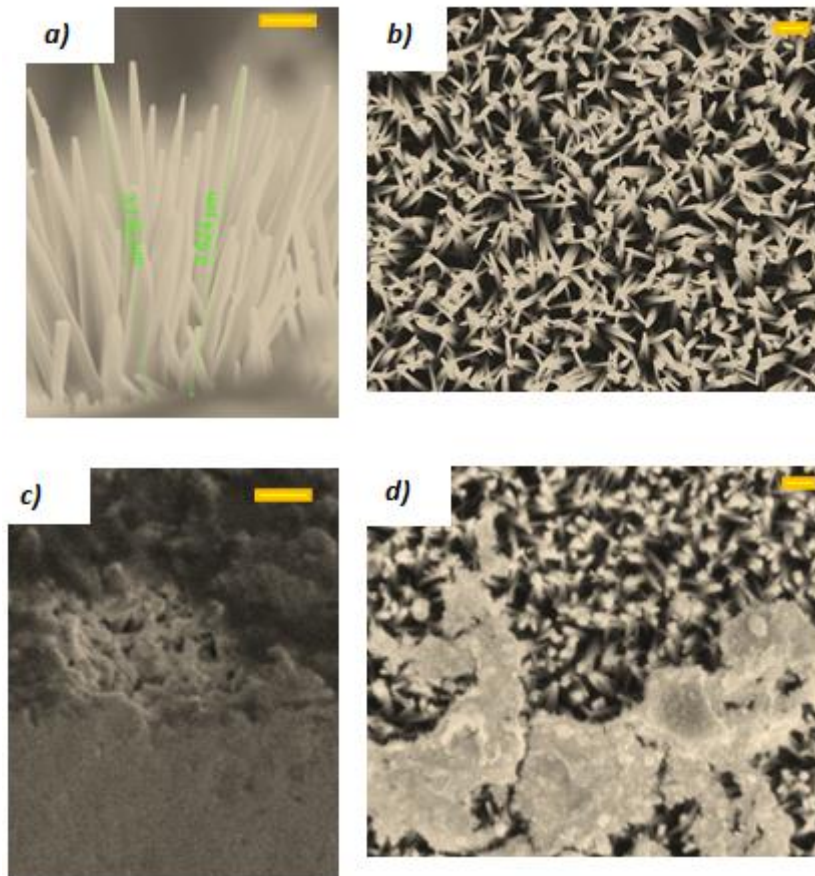


Figure VII.1. a) Cross-sectional and b) top SEM views of ZnO nanorods prepared as described in Chapter II. c) Cross-sectional and d) top SEM views of the same ZnO nanorods sensitized by CdSe QDs in 12 SILAR cycles. Scale bar length (indicated as a yellow bar) is 500 nm.

SEM images of the ZnO nanorod arrays before and after sensitization by 12 SILAR cycles are displayed in *Figure VII.1*. The cross-sectional images show that the voids between the 3.6-3.7 μm long NRs are filled with QDs. As demonstrated by the top-view SEM images, an excess of QDs is accumulated on top of the ZnO NR arrays. However, it does not form a thick

Chapter VII. Quantum dot sensitized solar cells

homogeneous layer on top of the substrate, in contrast to the samples with pre-synthesized CdSe nanocrystals presented in the *Figure V.8* of **Chapter V**.

The UV-VIS absorption spectra of the samples are reported in *Figure VII.2*. The spectra show a clear increase of the sample absorbance with the number of cycle. Also, it can be observed that the absorbance threshold is redshifted as the number of SILAR cycle is increased from 0 to 12.

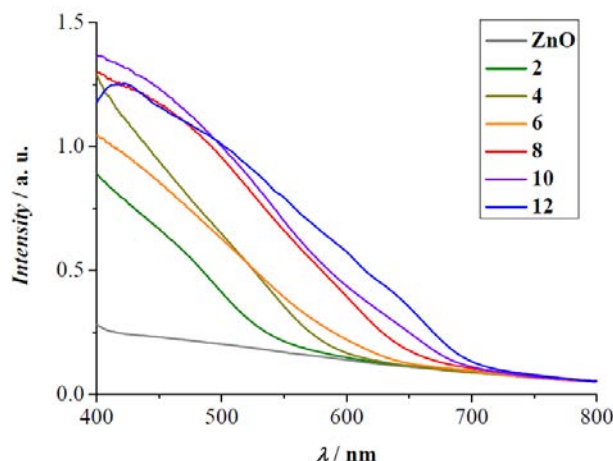


Figure VII.2. UV-VIS spectra of ZnO nanorod substrates sensitized with CdSe QDs in 2, 4, 6, 8, 10 and 12 SILAR cycles.

The Raman spectra of the samples are shown in *Figure VII.3*. The E_2^H peak of the ZnO wurtzite nanorod substrate at 437 cm^{-1} can be observed on the Raman spectra of all the CdSe QD-coated samples.⁵ However, with the increase in the number of SILAR cycles, its intensity gradually decreases compared to the CdSe zinc blende-related 1st and 2nd order LO peaks (LO and 2LO) at 208 cm^{-1} and at 420 cm^{-1} respectively.⁶ It is also observed that the characteristic CdSe LO peak at around 208 cm^{-1} becomes thinner and better defined as the number of SILAR cycles is increased. Initially, after 2-6 cycles, it is wide and presumably composed of several overlapping peaks corresponding to surface modes and a large range of Cd-Se bond distances. It is thus assumed that a lower number of SILAR cycles results in a structurally distorted CdSe layer, and the formation of a crystalline CdSe film on the ZnO surface with a more bulk-like character is observed only from 8 cycles.

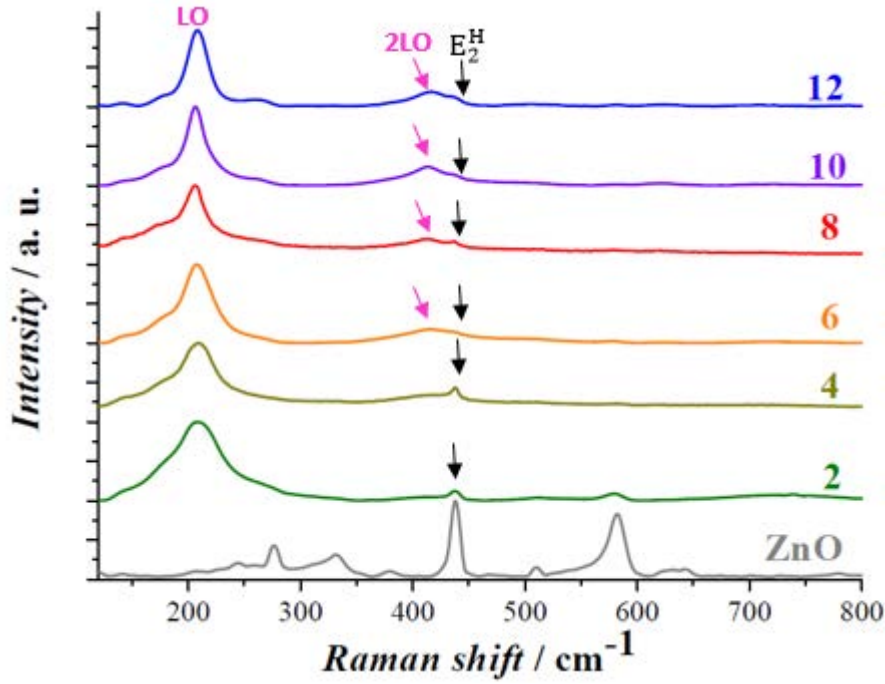


Figure VII.3. Raman spectra of ZnO nanorod substrates sensitized with CdSe QDs in 2, 4, 6, 8, 10 and 12 SILAR cycles. Intensities were normalized to the highest intensity peak in each curve.

The XRD patterns of ZnO NR arrays sensitized by CdSe QDs in 6 and 12 SILAR cycles are reported in *Figure VII.4*. After 6 cycles, only one peak at 43° is assigned to the zinc blende CdSe, and is identified as its (220) facet. After 12 cycles, one more CdSe zinc blende facet (111) becomes visible at 25°. Although these peaks are wide and their intensity is low (only visible on a logarithmic scale), it can be concluded that by increasing the number of SILAR cycles, the XRD CdSe peaks increase in intensity and that more zinc blende CdSe is deposited. The in situ made CdSe QD layer becomes more and more bulk-like with the number of SILAR cycles, This result is in agreement with the analysis of the UV-VIS absorption and the Raman spectra displayed in (*Figures VII.2.* and *VII.3.*, respectively). The crystallite size in the CdSe QD films was estimated from the full-width at half-maximum (FWHM) of the XRD peak at 43°, using the Scherrer's formula:⁷

$$d = \frac{K\lambda}{\beta \cos \Theta} \quad (\text{VII.1.})$$

Chapter VII. Quantum dot sensitized solar cells

In *Equation VII.1.*, d means the crystallite size in nm K is a shape factor that can be approximated as $K=0.89$ for the presumably spherical CdSe QD grains, $\lambda = 0.154060$ nm is the wavelength of the incident X-rays in nm, β is the peak width at half of the peak intensity maximum (expressed in radian), and θ is the Bragg angle of the peak. The values we plugged in the *Equation VII.1.* and the obtained results are summarized in *Table VII.4.* From this calculation, we obtained a CdSe crystallite size of 9.9 nm after 12 SILAR cycles.

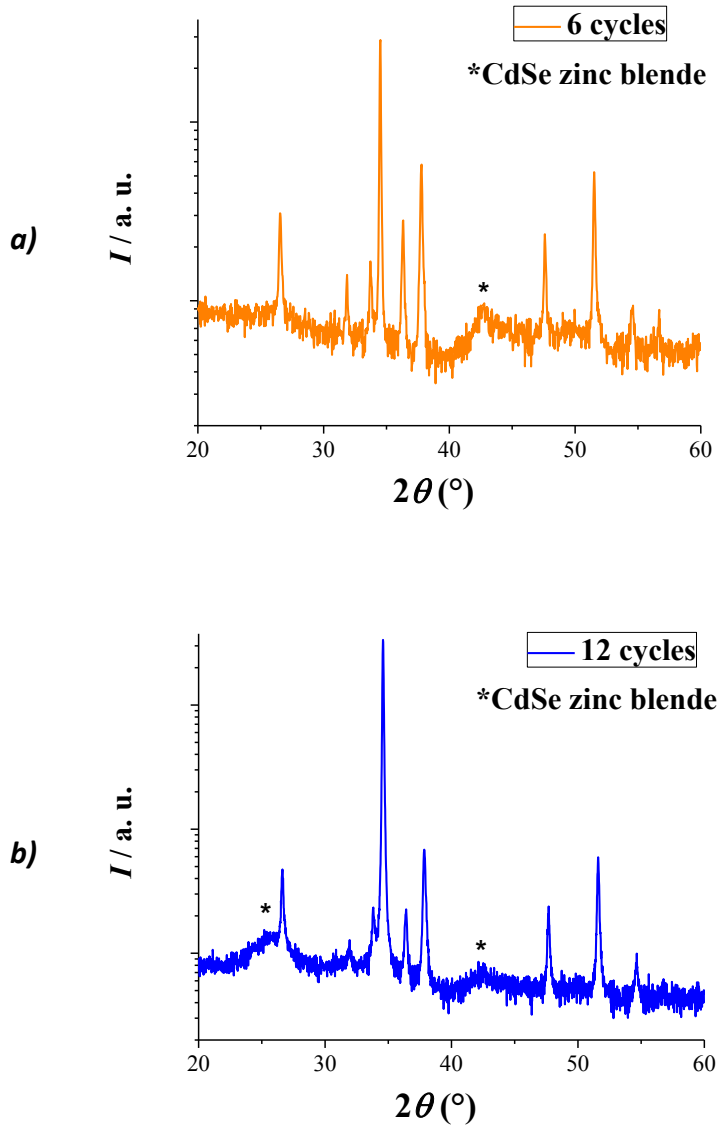


Figure VII.4. XRD patterns of ZnO nanorod substrates sensitized with CdSe QDs in 6 and in 12 SILAR cycles with logarithmic intensity scales. The peaks marked with an asterisk correspond to the zinc blende phase of CdSe, according to the JCPDS standard N° 04-004-5648.

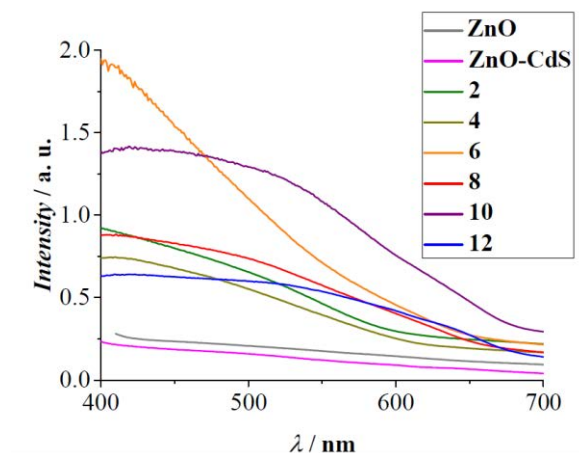


Figure VII. 5. UV-VIS absorption spectra of ZnO nanorod substrates sensitized with CdS QDs in 1 SILAR cycle, followed by CdSe QDs in 2, 4, 6, 8, 10 and 12 cycles.

In order to bring closer our ex-situ and in-situ sensitization experiments, we also studied samples prepared by sensitizing ZnO NR arrays with CdS QDs in 1 SILAR cycle, followed by CdSe QDs, denoted as ZnO-CdS-CdSe in the following. The UV-VIS absorption spectra of these samples are reported in *Figure VII. 5*. The addition of CdS in the 0th cycle results in the same spectra as that of the bare ZnO substrate. The slight difference in absorbance can be due to a measurement error. In the following SILAR cycles, we could not observe the same redshift and intensity growth tendencies by increasing the number of SILAR cycles as in case of the ZnO-CdSe samples shown in *Figure VII. 3*.

The Raman spectra of the ZnO-CdS-CdSe samples are reported in *Figure VII.6*. After the addition of a CdS QD layer, the Raman spectra of this sample did not feature new peaks with respect to that of the bare ZnO substrate. Although CdS and ZnS-related peaks would be expected at around 270-300 cm⁻¹, it appears that such a thin layer of CdS is not observable with this Raman setup. However, a low-intensity and wide peak is observable from the following cycles when CdSe QDs are deposited, which is attributed to CdS and /or ZnS.⁸ In order to explain why these peaks are observable only after starting to add CdSe QD layers, it can be supposed that interflowing layers are formed by the SILAR technique in this case, therefore some of the Cd²⁺ ions added in the subsequent cycles actually bond with the S²⁻ ions of the “0th” cycle.

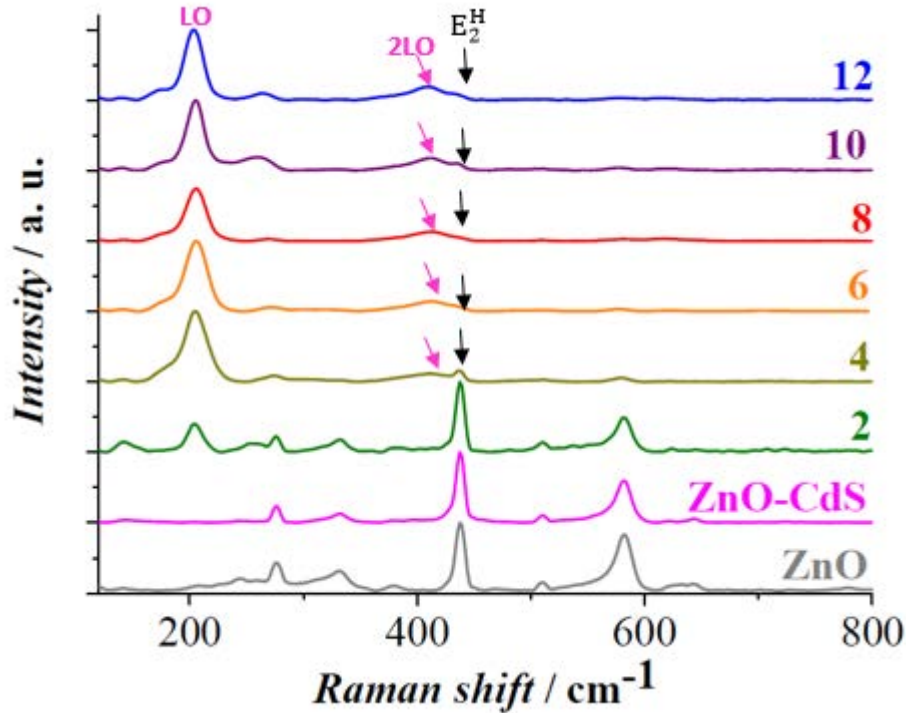


Figure VII.6. Raman spectra of ZnO nanorod substrates sensitized with CdS QDs in 1 SILAR cycle, followed by CdSe QDs in 2, 4, 6, 8, 10 and 12 cycles. Intensities were normalized to the highest intensity peak in each curve.

Similarly to the Raman spectra of these samples, *Figure VII.7* shows that the addition of a CdS layer in one SILAR cycle did not result in clearly identifiable ZnS or CdS peaks on the XRD patterns of the sample. When SILAR procedure was continued, CdSe zinc blende-related peaks became observable on the XRD patterns (*Figure VII.8*). After 6 SILAR cycles, the (220) plane of the CdSe zinc blende appeared at 43° , while a wide peak corresponding to the CdSe (110) plane also appeared at 25° . These peaks were poorly-defined, and it was not trivial to measure their width. The intensity of these peaks was significantly increased after 12 cycles. We used the Scherrer equation to estimate the crystalline size in the CdSe QD layer.⁷ We obtained that the intermediate sulfide layer between the CdSe QDs and the ZnO nanorods resulted in a smaller QD crystallite size of 4.2 nm a value approximately half of that obtained depositing solely CdSe QDs, (*Table VII. 4*). In accordance with what we observed from the UV-VIS absorption spectra reported in *Figure VII.5.*, this indicates an inferior crystalline quality with respect to the CdSe QD film deposited directly on the ZnO NR arrays.

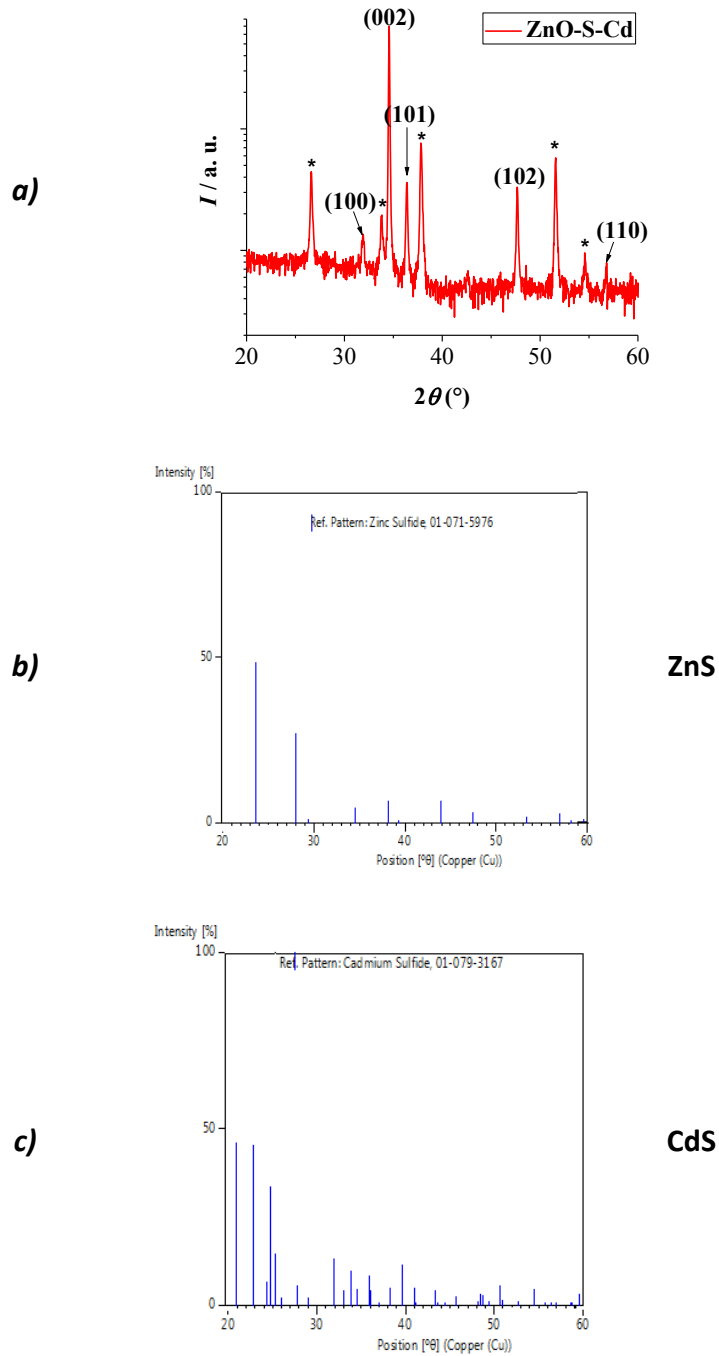


Figure VII.7. a) XRD patterns of ZnO substrates after the deposition of a CdS layer in one SILAR cycle in a logarithmic intensity scale. b) XRD patterns of ZnS sphalerite according to the JCPDS reference N° 01-071-5976. c) XRD patterns of CdS zinc blende according to the JCPDS reference N° 01-079-3167.

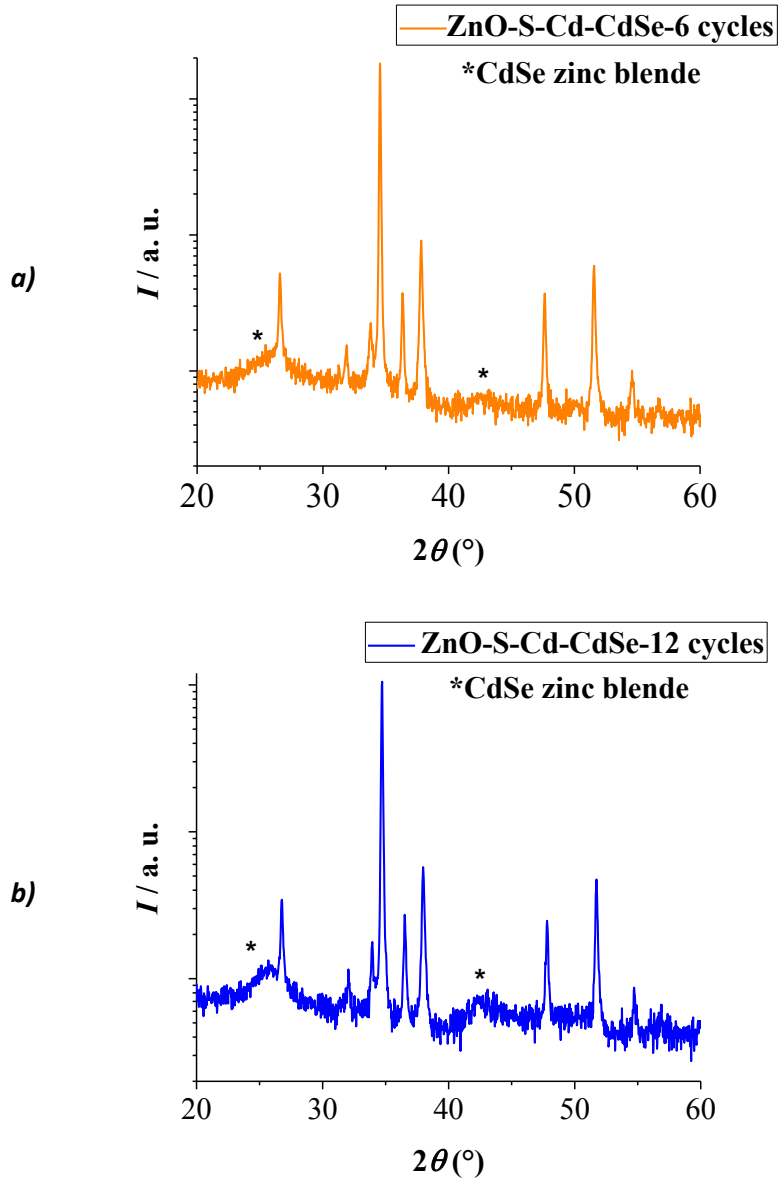


Figure VII.8. XRD patterns of ZnO nanorod substrates sensitized with CdS QDs in 1 SILAR cycle, followed by 6 and in 12 cycles of CdSe QD deposition (logarithmic intensity scales). The peaks marked with an asterisk correspond to the zinc blende phase of CdSe, according to the JCPDS standard N° 04-004-5648

Number of SILAR cycles	θ (rad)	$\cos \theta$	d (nm)
12	0.01484	0.9325	9.9
CdS+12	0.03491	0.9320	4.2

Table VII.4. Determination of the crystallite size in CdSe QD thin films from the Scherrer equation. CdS+12 corresponds to the sample sensitized with CdS QDs in 1 SILAR cycle, followed by CdSe QDs in 12 SILAR cycles.

Chapter VII. Quantum dot sensitized solar cells

The *J-V* characteristics of solar cells based on these systems are reported in *Table VII.5*. The first character **C** in the notation of the solar cells corresponds to the sensitization with CdSe QDs. In case the deposition of CdSe QDs on the WBSC substrate was preceded by the deposition of a CdS layer in SILAR cycle, the **C** character is followed by an **S**. Sensitization carried out in 6 (12) cycles is notated as **6 (12)**. Finally, the ZnO substrate is indicated as **Z**. It can be concluded from the data presented in *Table VII.5* that the SILAR method generally resulted in more reproducible solar cell performances than the *ex-situ* sensitization. 6 SILAR cycles appear to be insufficient to properly sensitize ZnO NRs, but the results are significantly better when applying 12 cycles. The addition of a CdS layer between the CdSe QDs and the ZnO NRs resulted in a lower but more reproducible solar cell performance.

	V_{oc} / V	J_{sc} / mA	Fill factor / %	$\eta / \%$
C6Z	0.154	1.43	26.4	0.06
C6Z	0.111	2.90	22.6	0.07
C6Z	0.012	1.13	20.5	0.01
C12Z	0.295	7.75	25.8	0.59
C12Z	0.338	11.66	31.6	1.25
C12Z	0.281	7.29	29.8	0.61
CS12Z	0.219	3.64	24.4	0.19
CS12Z	0.194	3.16	25.9	0.16
CS12Z	0.216	3.76	27.8	0.23

Table VII.5. *J-V* characteristics of QDSCs prepared with a liquid electrolyte and ZnO nanorod arrays in-situ sensitized with CdSe and CdS QDs

VII.2.2. QDSCs with a TiO₂ substrate

The absorbance spectra of TiO₂ NR sensitized by silar CdSe are shown in *Figure VII.9*. The absorbance was found to continuously increase with the number of SILAR cycles. On the contrary to the ZnO-based samples (*Figure VII.2*), the UV-VIS absorption spectra of the TiO₂-based ones demonstrated no redshift of the absorbance threshold as the number of SILAR cycles were increased. We also noted that the measured intensities were lower than those of the corresponding ZnO-based samples reported in *Figure VII.2*.

Chapter VII. Quantum dot sensitized solar cells

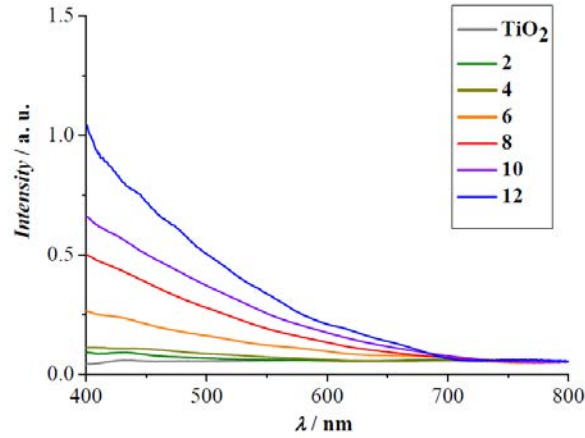


Figure VII.9. UV-VIS spectra of TiO_2 nanorod substrates sensitized with CdSe QDs in 2, 4, 6, 8, 10 and 12 SILAR cycles.

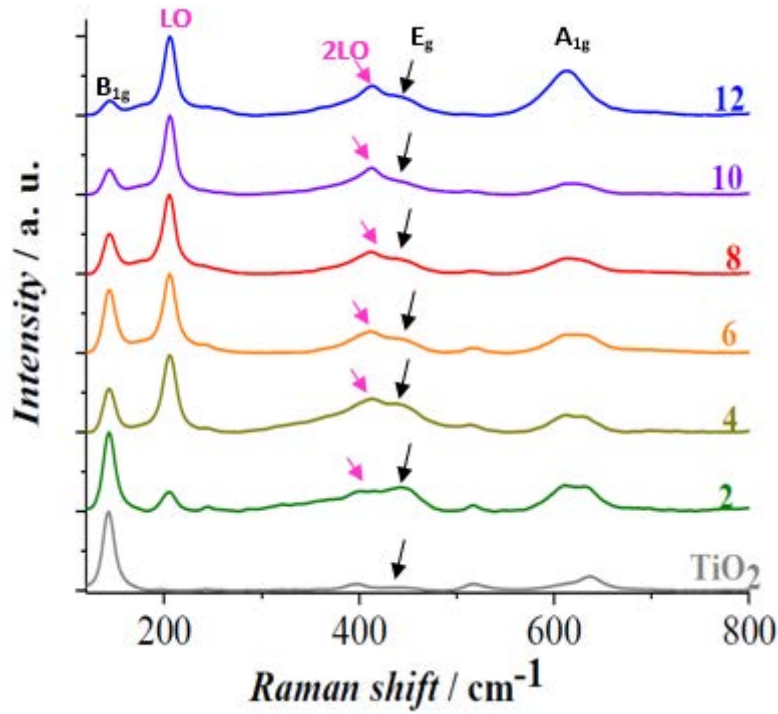


Figure VII.10. Raman spectra of TiO_2 nanorod substrates sensitized with CdSe QDs in 2, 4, 6, 8, 10 and 12 SILAR cycles. Intensities were normalized to the highest intensity peak in each curve.

The Raman spectra of the samples are shown in *Figure VII.10*. The LO and 2LO peaks of the zinc blende phase of CdSe (at around 210 and 420 cm^{-1} , respectively) can clearly be observed even after 2 SILAR cycles. The following vibrations of the TiO_2 rutile crystal are also measured: B_{1g} at around 140 cm^{-1} , E_g at around 440 cm^{-1} and A_{1g} at around 610 cm^{-1} .⁹ As the number of SILAR cycles increased, the intensity of the CdSe-related peaks increased with

Chapter VII. Quantum dot sensitized solar cells

respect to those of the TiO_2 -related peaks. However, the peak corresponding to the CdSe LO mode was thin and well-defined even after 4 cycles, and retains this shape in the following SILAR cycles. We can thus conclude that even at the lowest QD coverage, the CdSe QD are well-crystallized with a regular zinc blende structure on the TiO_2 NRs, which does not significantly change as more and more QDs are adsorbed on the substrate, in accordance with the observations of the UV-VIS absorbance measurement.

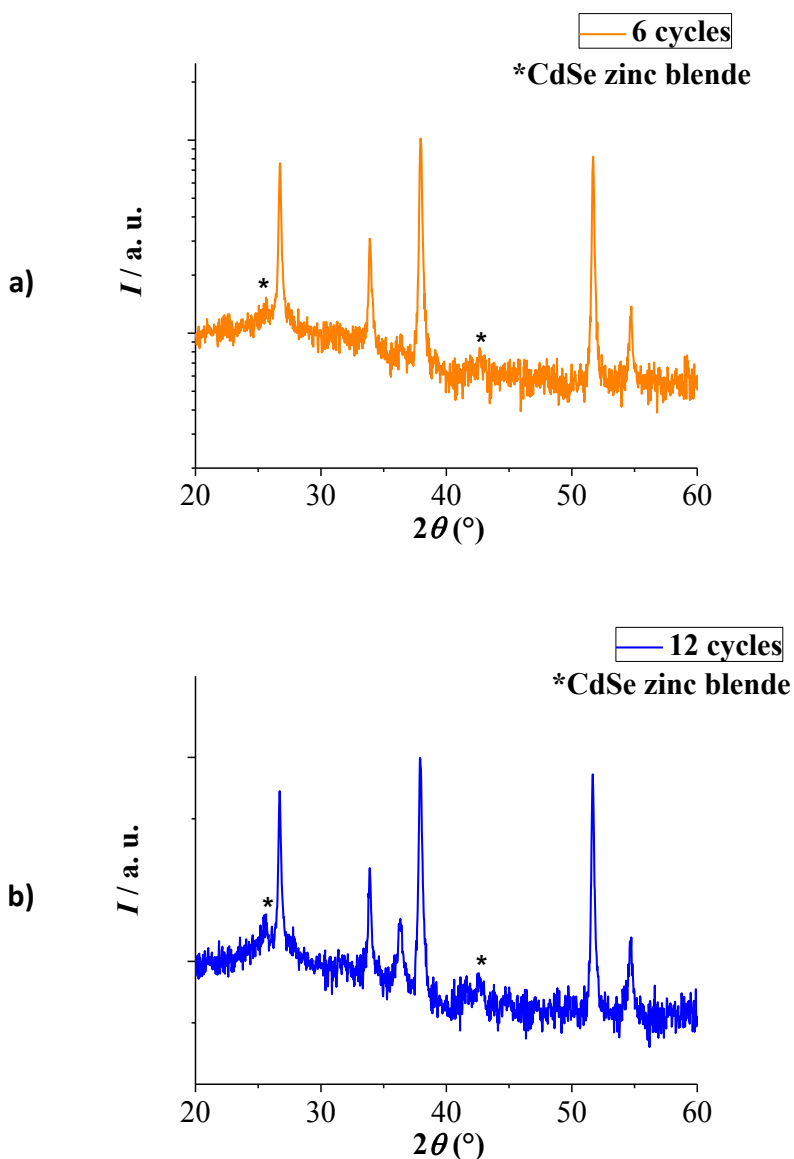


Figure VII.11. XRD patterns of TiO_2 nanorod arrays sensitized by CdSe QDs with the SILAR method in 6 and in 12 cycles with logarithmic intensity scales. The peaks marked with an asterisk correspond to the zinc blende phase of CdSe, according to the JCPDS standard N° 04-004-5648.

Chapter VII. Quantum dot sensitized solar cells

The XRD patterns of TiO₂ NR arrays sensitized by CdSe QDs in 6 and 12 SILAR cycles are reported in *Figure VII.11*. CdSe-related peaks at 25° and at 43° can be observed, although their intensity was lower than in case of ZnO-based samples. As the CdSe peaks on *Figure VII.11*. are poorly-defined, it was not possible to find their width, therefore we do not provide a Scherrer analysis of the sample crystallite size.

The *J-V* characteristics of the solar cells prepared with the above characterized TiO₂-based samples are reported in *Table VII.6*. We found that the performance of the TiO₂-based QDSCs were reproducible but inferior to the ZnO-based ones. Comparing the V_{oc} values, higher open-circuit voltages were measured for TiO₂- than for ZnO-based solar cells, which indicates a weaker dark current and less recombination. On the other hand, the short circuit current is lower for the latter than for the former cells, which indicates a less efficient sensitization by CdSe QDs. This is in accordance with the UV-VIS absorption spectra reported *Figure VII.9.*, where it was observed that the absorbance of the TiO₂ substrates is inferior to that of the ZnO nanorod arrays sensitized under the same experimental conditions.

	V_{oc} / V	J_{sc} / mA	Fill factor / %	$\eta / \%$
C6T	0.275	0.099	67.7	0.02
C6T	0.223	0.460	50.4	0.05
C6T	0.278	0.429	63.6	0.08
C12T	0.379	1.23	52.2	0.24
C12T	0.373	1.07	52.0	0.21
C12T	0.364	1.23	48.6	0.22

Table VII.6. *J-V* characteristics of QDSCs prepared with a liquid electrolyte and TiO₂ nanorod arrays in situ sensitized with CdSe QDs

VII.3. Conclusion

In summary, several QDSC configurations were tested in this chapter

1. with liquid or solid-state electrolyte
2. using ZnO or TiO₂ nanorod arrays
3. applying either an in-situ or an ex-situ protocol to attach CdSe nanocrystals to ZnO and TiO₂

Chapter VII. Quantum dot sensitized solar cells

- a. sensitizing the nanorods with CdSe QDs or NPLs of different thicknesses
- b. modifying the conditions of the SILAR growth procedure

1) Zero or hardly measurable photocurrent was generated in all-solid state QDSCs. On the other hand, many solar cells with a liquid electrolyte worked. *We thus propose the use of liquid electrolytes, rather than solid-state ones in solar cells with nanorod-based photoanodes because of their better pore filling in the samples studied in this thesis.*

2) It was interesting to compare the performance of ZnO and TiO₂ as a WBSC material, as the latter is much more commonly applied, despite the advantages of the former, as discussed in **Chapters I and II**. In case of *ex-situ* sensitized substrates, the use of TiO₂ nanorods resulted in higher power conversion efficiencies, while ZnO-based cells performed better than TiO₂-based ones if CdSe QDs were grown *in situ*. *Further structural investigations (both with experimental and computational approaches, as demonstrated in **Chapter V**) and probing electron lifetimes by photoluminescence spectroscopy could contribute to the rationalization of the results.*

3) Solar cells with pre-synthesized CdSe nanocrystals performed better but were less reproducible than those prepared by the SILAR method because the liquid electrolyte washed the nanocrystals off the substrate. As a continuation of this work of implementing CdSe NPLs in QDSCs, we propose *three possible approaches (or the combination them) to improve and to stabilize the solar cell performance: i) considering a less dense array of ZnO or TiO₂ nanostructures and ii) finding a liquid electrolyte that is less prone to solubilize CdSe nanocrystals, either by decreasing its polarity or the concentration of sulfide ions in the solution iii) sensitize the ZnO and TiO₂ nanorod arrays more slowly, allowing the NPLs to diffuse in the gaps between the nanorods.*

3. a) Although the performances of the NPL sensitized solar cells were hardly reproducible, we generally conclude from our data that the best results were obtained when applying CdSe NPLs of intermediate thickness (9 layers). *This is in accordance with the recent study of Bozyigit et al*

Chapter VII. Quantum dot sensitized solar cells

*discussed in **Chapter I** section **I.6.1**, in which the authors argued that after QDSC sensitizers of different sizes, the best electron injection efficiency was found for intermediate nanocrystal sizes. By optimizing the attachment of NPLs to ZnO and TiO₂ nanorods and by obtaining more reproducible solar cell characteristics, this interesting point could be experimentally investigated.*

3. b) QDSCs prepared in 6 SILAR cycles performed poorly both in the case of ZnO- and TiO₂-based photoanodes. Solar cell performance is significantly better for cells prepared in 12 SILAR cycles. In general, weaker but more reproducible results were obtained with TiO₂-based QDSCs. In the case of ZnO-based QDSC, it was demonstrated that the addition of a CdS layer between the ZnO nanorods and the CdSe QDs seems to alter the crystalline quality of the QDs and decreases solar cell performance, but the measured results were more reproducible.

References

- (1) Lee, H.; Leventis, H. C.; Moon, S.-J.; Chen, P.; Ito, S.; Haque, S. a.; Torres, T.; Nüesch, F.; Geiger, T.; Zakeeruddin, S. M.; et al. PbS and CdS Quantum Dot-Sensitized Solid-State Solar Cells: “Old Concepts, New Results.” *Adv. Funct. Mater.* **2009**, *19*, 2735–2742.
- (2) Lin, Y. D.; Ke, B. Y.; Lee, K. M.; Chang, S. H.; Wang, K. H.; Huang, S. H.; Wu, C. G.; Chou, P. T.; Jhulki, S.; Moorthy, J. N.; et al. Hole-Transporting Materials Based on Twisted Bimesitylenes for Stable Perovskite Solar Cells with High Efficiency. *ChemSusChem* **2016**, *9* (3), 274–279.
- (3) Nag, A.; Kovalenko, M. V.; Lee, J.-S.; Liu, W.; Spokoyny, B.; Talapin, D. V. Metal-Free Inorganic Ligands for Colloidal Nanocrystals : S²⁻ , HS⁻ , Te²⁻, HTe⁻, TeS₃²⁻, OH⁻ and NH₂⁻ as Surface Ligands. *J. Am. Chem. Soc.* **2011**, *133*, 10612–10620.
- (4) Deng, J.; Wang, M.; Song, X.; Liu, J. Controlled Synthesis of Aligned ZnO Nanowires and the Application in CdSe-Sensitized Solar Cells. *J. Alloys Compd.* **2014**, *588*, 399–405.
- (5) Lupan, O.; Guérin, V. M.; Tiginyanu, I. M.; Ursaki, V. V.; Chow, L.; Heinrich, H.; Pauporté, T. Well-Aligned Arrays of Vertically Oriented ZnO Nanowires Electrodeposited on ITO-Coated Glass and Their Integration in Dye Sensitized Solar Cells. *J. Photochem. Photobiol. A Chem.* **2010**, *211* (1), 65–73.
- (6) Kelley, A. M.; Dai, Q.; Jiang, Z. J.; Baker, J. A.; Kelley, D. F. Resonance Raman Spectra of Wurtzite and Zincblende CdSe Nanocrystals. *Chem. Phys.* **2013**, *422*, 272–276.
- (7) Patterson, A. L. The Scherrer Formula for X-Ray Particle Size Determination. *Phys. Rev.* **1939**, *56* (10), 978–982.
- (8) Dzhagan, V. M.; Valakh, M. Y.; Milekhin, A. G.; Yeryukov, N. a.; Zahn, D. R. T.; Cassette, E.; Pons, T.; Dubertret, B. Raman- and IR-Active Phonons in CdSe/CdS Core/Shell Nanocrystals in the Presence of Interface Alloying and Strain. *J. Phys. Chem. C* **2013**, *117* (35), 18225–18233.
- (9) Selman, A. M.; Hassan, Z. Structural and Photoluminescence Studies of Rutile TiO₂ Nanorods Prepared by CBD Method on Si Substrates. *Am. J. Mater. Sci.* **2015**, *5* (3B), 16–20.

Conclusions and perspectives

The general aim of this thesis was to contribute to a better understanding of the processes governing the performance of quantum dot sensitized solar cells. We used a mixed theoretical/experimental approach to analyze the semiconductor components of these devices and the interfaces formed between them. On one hand, we have checked the capacity of the used experimental and theoretical methods to characterize the systems studied in this thesis by their cross-validation. On the other hand, we have developed a mixed approach to provide a complementary picture of the semiconductor heterostructures and their elements, the characterization or testing of some physico-chemical properties being more feasible computationally, while others being more accessible experimentally.

Regarding the **computational part**, we first identified a computational protocol that accurately and efficiently describes the bulk and surface geometric and electronic properties of the chosen sensitizer material, CdSe both in the wurtzite and zinc blende structures. Then, we simulated zinc blende CdSe nanoplatelets of various thicknesses, passivated by different ligands. Next, a model of the sensitizer - wide band gap semiconductor heterostructure was built, and its properties were calculated. In the meantime, computational results were compared to experimental data, with an overall good agreement. **Experimentally**, both wide band gap semiconductors in the form of ZnO and TiO₂ nanorod arrays and sensitizer nanocrystals (CdSe nanoplatelets and quantum dots) were synthesized. The WBSC substrates were sensitized both by *ex situ* and *in situ* grown CdSe QDs. The semiconductor systems were characterized by UV-VIS absorption and Raman spectroscopy. Finally, solar cells based on these heterostructures were fabricated and tested.

In more detail, in **Chapter III**, a comprehensive DFT investigation of the geometric and electronic properties of CdSe bulk crystals has been performed. We combined three main types of Gaussian-type orbital basis sets (with and without the use of pseudopotentials) with GGA and global hybrid functionals in order to find the computational protocol that gives the most accurate description both in terms of geometric parameters and electronic structure for the two (wurtzite and zinc blende) CdSe bulk phases in comparison to available experimental data. We found that the global hybrid **functional B3PW91** combined with **small- and large-core effective pseudopotentials for Cd and Se, respectively**, (denoted as

Conclusions and perspectives

the **SBKJC** basis set) provides the best description considering the overall accuracy on several parameters. Next, the nonpolar CdSe wurtzite (10-10) surface was modeled with the as-defined method. The relaxation-induced changes in atomic positions and electronic structure have been described for a surface with a converged thickness, and compared to available experimental and theoretical data. *The overall good agreement found justified the choice of the model, and forecast an encouraging performance for an accurate modeling of quantum dot-based systems at low computational cost.*

In **Chapter IV**, a detailed DFT investigation has been performed on non-stoichiometric CdSe zinc blende nanoplatelets of various thicknesses, stabilized by different ligands (HCOO^- , SH^- and OH^-) on their polar (100) surface. A theoretical model has been established for these hybrid ligand-nanocrystal systems. Their properties were calculated using the computational protocol defined in **Chapter II** (B3PW91/SBKJC). First, the relaxation parameters of the ligands adsorbed on the (100) surface of the nanoplatelets have been computed, along with their adsorption energies. Regarding the electronic properties, the band gaps, band structures and orbital-projected density of states of the stabilized nanoplatelets have been calculated, along with a detailed Mulliken analysis of the atomic and orbital charges. The band gaps of CdSe zinc blende nanoplatelets of various thicknesses, stabilized by fatty acids, SH^- and OH^- ligands have also been measured by UV-VIS absorption spectroscopy. A good agreement was found between the experimental and calculated band gaps, especially concerning their evolution with the NPL thickness. *We could thus conclude that the chosen theoretical model and computational protocol together can serve as a powerful tool for the qualitative and quantitative description of the geometric and electronic properties of CdSe nanoplatelets that we intended to use as sensitizers in this thesis.*

In **Chapter V**, the initial oleic acid (OA) ligands on the CdSe nanocrystals (nanoplatelets of various thicknesses and spherical QDs) were first exchanged to smaller bifunctional ligands (SH^- , OH^- and MPA). Next, the nanocrystals were linked to ZnO and TiO_2 nanorod arrays (resumed as WBSC in the following) *via* bifunctional ligands. The as-prepared nanocrystal-ligand-WBSC heterostructures were characterized by UV-VIS absorption and Raman spectroscopy. Among the ligand exchange reactions, only the $\text{OA} \leftrightarrow \text{SH}^-$ exchange resulted in homogeneous CdSe nanocrystal dispersions for NPLs of all thicknesses, as well as for QDs.

Conclusions and perspectives

From the comparison of the UV-VIS absorption spectra of the CdSe.SH-ZnO and CdSe.SH-TiO₂ heterostructures and of the bare NPLs, it was concluded that the NPL attachment to the ZnO or TiO₂ substrate induces structural changes in the nanocrystals. The Raman spectra of the mixed CdSe.SH-ZnO and CdSe.SH-TiO₂ systems featured peaks of both of its components. While the NPL-related peaks had low intensity compared to the TiO₂-related ones, they had high intensity with respect to the ones associated with the ZnO NRs. *Hence, a more refined analysis of the latter system would make it possible to obtain interesting insights on the structural changes that the sensitization induces in the CdSe nanocrystals.*

Making a step towards the application of CdSe nanoplatelets in solar cells, the above mentioned deep analysis of the CdSe.SH – ZnO interface was performed in **Chapter VI**. A combined theoretical and experimental approach was used to characterize a semiconductor heterostructure consisting of CdSe nanoplatelets linked to a ZnO surface by SH⁻ ligands. The experimental characterization of these systems by Raman and by UV-VIS absorption spectroscopy suggested significant structural changes upon the formation of the interface. A theoretical investigation, performed using the computational protocol chosen in **Chapter III** enabled us to clarify the nature of these structural rearrangements, the characterization of the vibrational and electronic properties of this system, as well as to predict the electron injection efficiency from the NPLs to ZnO. In line with the working principles of QDSCs, the charge injection was proven to be possible, although only partial, which is explained by the delocalized nature of the electronic states at the interface. *This result forecasts that electron-hole recombinations in the CdSe.SH – ZnO system will be highly probable, causing a reduced solar cell performance for the devices that incorporate these systems. Therefore, we suggest that by replacing atomic linkers such as the here studied SH⁻, by longer molecular linkers such as mercaptopropionic acid (MPA) should result in a less distorted nanoplatelet-oxide interface, as could be deduced from the UV-VIS absorption spectra in **Chapter V**. Eventually, the electronic states in CdSe.MPA – ZnO systems should be more localized on either of the components, making it possible to obtain a more complete electron injection.*

The performance of solar cells made with ZnO or TiO₂ nanorods, sensitized either by pre-synthesized CdSe nanocrystals or *in situ* grown CdSe QDs, using either a solid-state or a

Conclusions and perspectives

liquid electrolyte were evaluated in **Chapter VII**. The following conclusions were made based on the results obtained in this chapter:

1. We suggest using liquid electrolytes instead of solid-state ones with nanorod-based photoanodes because of their better pore filling.
2. Comparing the performance of ZnO and TiO₂ as a WBSC material, we found that the use of TiO₂ nanorods resulted in higher power conversion efficiencies, while ZnO-based cells performed better than TiO₂-based ones if CdSe QDs were grown *in situ*. *Further experimental and computational investigations are suggested to rationalize these results. In more particular, the mixed approach presented in **Chapter VI** could provide interesting insights into the structural and electronic properties of these systems.*
3. The *in situ* sensitization resulted in more reproducible solar cell performances than the use of *ex situ* synthesized CdSe nanocrystals. Regarding the latter, three main approaches were proposed in order to improve their reproducibility:
 - a. *considering a less dense array of ZnO or TiO₂ nanostructures*
 - b. *finding a liquid electrolyte that is less prone to solubilize CdSe nanocrystals, either by decreasing its polarity or the concentration of sulfide ions in the solution*
 - c. *sensitize the ZnO and TiO₂ nanorod arrays more slowly, allowing the NPLs to diffuse in the gaps between the nanorods*
4. The low solar cell performance for devices based on CdSe.SH – ZnO systems forecast in **Chapter VI** was confirmed, which further validates the mixed theoretical/experimental approach presented in **Chapter VI**.

Based on the obtained results, this PhD thesis opens up the following perspectives:

- By validating the computational investigations by experimental data, the computational protocol identified in **Chapter III** (B3PW91/SBKJC) proved to be suitable for the modeling of more complex systems, such as quasi-2D CdSe nanoplatelets passivated by various ligands. Moreover, it was useful for modeling sensitizer-WBSC heterostructures based on these nanoplatelets. We can thus project that this protocol could be used to computationally screen potential candidate materials in QDSCs.

Conclusions and perspectives

- It was demonstrated that by simple physico-chemical characterization methods, such as UV-VIS absorption and Raman spectroscopy, we can provide valuable structural information that can be directly related to computational results. Hence, it is possible to cross-validate the capacity of the two approaches for the characterization of semiconductor heterostructures.
- The theoretical and experimental results obtained in this thesis made it possible to provide guidelines for the screening of QDSCs components.
- The here proposed mixed theoretical/experimental approach can be extended to the study of other semiconductor heterostructures present in a wide variety of optoelectronic applications, and it could contribute to better understand the working principle of these devices. In a broader perspective, it can contribute to the improvement of their performance.

Publications related to the thesis

Published

- Szemjonov, A.; Pauporté, T.; Ciofini, I.; Labat, F.; Investigation of the bulk and surface properties of CdSe: insights from theory, *Phys. Chem. Chem. Phys.*, 2014, 16, 23251-23259
- Szemjonov, A.; Pauporté, T.; Ithurria, S.; Lequeux, N.; Dubertret, B.; Ciofini, I.; Labat, F.; Ligand-stabilized CdSe nanoplatelet hybrid structures with tailored geometric and electronic properties. New insights from theory, *RSC Adv.*, 2014, 4, 55980-55989

Accepted

- Szemjonov, A.; Pauporté, T.; Ithurria, S.; Pedetti, S.; Lequeux, N.; Dubertret, B.; Ciofini, I.; Labat, F.; Towards the modeling of quantum dot sensitized solar cells: from structural and vibrational features to electron injection through lattice-mismatched interfaces (2016, accepted to *J Mater Chem A*)

Submitted

- Szemjonov, A.; Labat, F.; Ciofini, I.; Ithurria, S.; Dubertret, B.; Pauporté, T.; Ex situ and in situ sensitized quantum dot solar cells (2016, submitted to *Physica Status Solidi b*)

In preparation

- Szemjonov, A.; Pauporté, T.; Ithurria, S.; Pedetti, S.; Lequeux, N.; Dubertret, B.; Ciofini, I.; Labat, F.; Combined theoretical/experimental study of CdSe/CdS/ZnS core-shell nanocrystals (in preparation)
- Szemjonov, A.; Pauporté, T.; Ithurria, S.; Pedetti, S.; Lequeux, N.; Dubertret, B.; Ciofini, I.; Labat, F.; Linker-assisted attachment of CdSe nanoplatelets ZnO and TiO₂ nanorod arrays (in preparation)

Presentations at scientific events

1. Oral presentation: A. Szemjonov, F. Labat, I. Ciofini, S. Ithurria, S. Pedetti, N. Lequeux, B. Dubertret, T. Pauporté, “Combined theoretical and experimental analysis of lattice-mismatched semiconductor heterostructures in hybrid solar cells”, at the E-MRS Spring Meeting, Lille, France, 2-6 May 2016

2. Poster presentation: A. Szemjonov, F. Labat, I. Ciofini, S. Ithurria, S. Pedetti, N. Lequeux, B. Dubertret, T. Pauporté, “Complementary theoretical/experimental approach for characterizing nanoplatelet-oxide heterostructures in hybrid solar cells”, at the E-MRS Spring Meeting, Lille, France, 2-6 May 2016
3. Poster presentation: “DFT study of bulk and surface properties of CdSe: towards the modeling of nanocrystals”, A. Szemjonov, F. Labat, I. Ciofini, S. Ithurria, N. Lequeux, B. Dubertret, T. Pauporté, International Summer School on Nanosciences, Etolles, France, 22 June 2014-27 June 2014
4. Poster presentation: “DFT modeling of CdSe nanoparticles for QD application: investigation of bulk crystals and polar and nonpolar surfaces”, A. Szemjonov, F. Labat, I. Ciofini, S. Ithurria, N. Lequeux, B. Dubertret, T. Pauporté, 30 Years in Colloidal Quantum Dots, Paris, France, 26 May 2014-28 May 2014

List of figures

I.1.	a) Diffusion of free charge carriers between a p- and an n-type material. b) Formation of a depletion region with a built-in electric field in a p-n junction. c) Band energy levels in the p-n junction.....	3
I.2.	First, second and third generation photovoltaic cells.....	4
I.3.	Working principle of quantum dot sensitized solar cells. The inset zooms on the electron injection from the quantum dot to the metal oxide.....	7
I.4.	Main charge generation, transfer and recombination processes in a QDSC.....	7
I.5.	Solar irradiance spectra references according to the ASTM standards.....	15
I.6.	Current-voltage characteristics of a photovoltaic cell under illumination.....	16
II.1.	Schematic illustration of the creation of an 8 layers thick $\langle 10\bar{1}0 \rangle$ slab from the bulk form of wurtzite CdSe.....	47
II.2.	Schematic illustration of Tasker's classification of ionic crystal surfaces. q corresponds to the overall charge of the system, while μ to the dipole moment perpendicular to the crystal surface.....	48
II.3.	Structural model of a 5 layers thick CdSe zinc blende(100) nanoplatelet with the definition of one atomic monolayer (ML)	53
II.4.	Molecular structure of hexamethylene tetramine (HMTA).....	56
II.5.	Ramping program for the thermal treatment of seeded FTO glasses prepared with the spin-coating of $\text{Zn}(\text{Ac})_2$ solution with method 1).....	58
II.6.	Experimental setup for the ZnO NR growth.....	59
II.7.	Ramping program for the thermal treatment of hydrothermally grown ZnO NR arrays.....	59
II.8.	Ramping program the thermal treatment of seeded FTO glasses prepared with the spin-coating of $\text{Zn}(\text{Ac})_2$ solution with method 2).....	60
II.9.	Ramping program for the thermal treatment of seeded FTO glasses prepared with the spin-coating of TIPA solution.....	62
II.10	Ramping program for the thermal treatment of hydrothermally grown TiO_2 NR arrays.....	62
II.11.	3-Mercapto-propionic acid.....	64
II.12.	Schematic illustration of biphasic ligands exchange reactions on CdSe NPLs. The short polar bifunctional linker is denoted as L. CdSe.OA and CdSe.L stand for CdSe NPLs passivated by oleic acid and the L linker, respectively.....	62
II.13.	Schematic illustration of one SILAR cycle.....	66
II.14.	Molecular structure of spiro-OMeTAD.....	69
II.15.	a) Top-view of the photoanode, masked by the Scotch tape on the conducting side. b) The non-conducting side of the photoanode covered by a mask with a 0.33 cm^2 circular hole. c) Cross-sectional view of the complete solar cell assembly.....	70
III.1.	Packing of layers in the primitive cell of the wurtzite (left) and zinc blende (right) crystal structures. Cd and Se atoms are shown as grey and yellow spheres, respectively.....	81

III.2.	Computed average deviation (in %) of CdSe bulk lattice parameters with respect to experimental data: a) wurtzite a and c parameters and b) zinc blende a parameter.....	83
III.3.	Computed deviation (in %) of CdSe wurtzite (a) and zinc blende (b) bulk band gaps with respect to experimental data.....	86
III.4.	Calculated band structure of the CdSe bulk wurtzite (left) and zinc blende (right) phase obtained with the B3PW91/SBKJC method. The Fermi level was set at 0 eV.....	88
III.5.	Calculated total and orbital-projected density of states of the CdSe wurtzite (left) and zinc blende (right) bulk crystals. Fermi level was set at 0 eV.....	89
III.6.	Side views of the unrelaxed (a) and relaxed (b) structures of the CdSe wurtzite (10-10) surface. The definitions of the structural parameters of the relaxed surface are shown in (b). Cd atoms shown as larger white spheres, Se atoms as smaller yellow spheres.....	90
III.7.	Calculated surface formation energies for the (10-10) surface as a function of the number of layers of CdSe wurtzite slabs. Convergence (indicated by a red arrow) is reached at 8 layers.....	91
III.8.	Calculated band structure of the unrelaxed (left) and relaxed (right) CdSe wurtzite (10-10) surface obtained for an 8 layer thick slab. Corresponding Brillouin zone with high-symmetry points are indicated between the two band structures.....	93
III.9.	Computed total and orbital-projected density of states of the CdSe wurtzite (10-10) surface obtained for an 8 layer thick slab. Fermi level was set at 0 eV.....	94
IV.1.	TEM views of a) 9 and b) 13 atomic layers thick CdSe nanoplatelets. The scale bar length is 20 nm. c) Side views of the alternate stacking of positively (+ sign) and negatively (- sign) charged planes in a CdSe zinc blende five layers thick slab exposing its Cd-terminated (100) surface. Cd atoms are presented as grey spheres, Se atoms as yellow spheres. Blue arrows show the dipole momenta arising from the dangling bonds of the surface Cd atoms, the vector sum of which is represented by a red arrow.....	100
IV.2.	Optimized structures of stabilized five layers thick slabs: the CdSe.HCOO system in the a) bidentate and b) monodentate adsorption mode of the formate ligand, and those of the c) CdSe.SH and d) CdSe.OH systems. Cd, Se, O, C, H and S atoms are presented as beige, orange, red, grey, white and yellow spheres, respectively.....	104
IV.3.	Initial geometries of CdSe.HCOO with a) bidentate and b) monodentate adsorption mode of the HCOO ⁻ ligand.....	105
IV.4.	Adsorption energies of HCOO ⁻ , OH ⁻ and SH ⁻ ligands on the CdSe zinc blende (100) surface (in kcal mol ⁻¹) calculated according to Equation IV.2 for 5; 9 and 13 atomic layers thick slabs.....	107
IV.5.	Total and orbital-projected density of states of the S and O atoms of the ligands and of the Cd atoms of the (100) surface and band structures of the a) CdSe.HCOO, b) CdSe.SH and c) CdSe.OH systems. Fermi level was set at 0 eV.....	113
IV.6.	Calculated and experimental band gaps as a function of slab thickness for CdSe zinc blende slabs stabilized with HCOO ⁻ , SH ⁻ and OH ⁻ ligands on their (100) basal planes. Note for the experimental values that the ligand exchange for OH ⁻ is not complete.....	114
V.1.	a) Cross-sectional and b) top-view SEM images of ZnO NRs.....	119
V.2.	XRD analysis of ZnO NRs. Peaks marked with an asterisk correspond to the cubic phase of SnO ₂ on the TCO glass substrate (standard JCPDS card N°04-008-8130), while	120

	those marked with a diamond correspond to the different crystal planes of wurtzite ZnO (standard N° 01-070-8072).....	
V.3.	Raman spectra of ZnO NRs with characteristic ZnO wurtzite peaks.....	120
V.4.	a) Cross-sectional and b) top-view SEM images of TiO ₂ nanorods arrays.....	121
V.5.	XRD patterns of TiO ₂ nanorod arrays. Peaks marked with an asterisk correspond to the cubic phase of SnO ₂ on the TCO glass substrate (standard JCPDS card N° 04-008-8130), while those marked with a diamond correspond to the different crystal planes of the rutile phase of TiO ₂ (standard N° 04-005-4692).	121
V.6.	Raman spectra of TiO ₂ nanorod arrays with characteristic TiO ₂ rutile peaks.....	121
V.7.	UV-VIS absorption spectra of CdSe NPLs of different thicknesses (7, 9 and 11 layers). NPLs passivated by oleic acid (OA) are indicated as full, while NPLs after ligand exchange with SH ⁻ are shown as dotted lines.....	122
V.8.	Top SEM view of ZnO nanorod arrays sensitized by 9 layers thick CdSe.SH nanoplatelets. The length of the yellow scalebar is 1 µm.....	123
V.9.	UV-VIS absorption spectra of ZnO nanorod arrays and 7, 9 and 11 layers thick CdSe.SH NPLs in dispersion (indicated by green, orange and red full lines, respectively) and after attachment to ZnO nanorod arrays (indicated by dashed lines of the corresponding color, and by a dotted line after consequent washing with ethanol).....	123
V.10.	Raman spectra of a) 7, b) 9 and c) 11 layers thick CdSe.SH NPLs, of ZnO nanorod arrays sensitized by the same NPLs and of bare ZnO nanorod arrays.....	124
V.11.	Decomposition of the CdSe- and CdS-related peaks in the experimental Raman spectra of 9 layers thick CdSe.SH NPLs. Surface optical modes are denoted as SO, transverse optical mode as TO.....	125
V.12.	Top SEM view of TiO ₂ nanorod arrays sensitized by 9 layers thick CdSe.SH nanoplatelets. The length of the yellow scalebar is 1 µm.....	126
V.13.	UV-VIS absorption spectra of TiO ₂ nanorod arrays and 7, 9 and 11 layers thick CdSe.SH NPLs in dispersion (indicated by green, orange and red full lines, respectively) and after attachment to TiO ₂ nanorod arrays (indicated by dashed lines of the corresponding color).....	126
V.14.	Raman spectra of a) 7, b) 9 and c) 11 layers thick CdSe.SH NPLs, of TiO ₂ nanorod arrays sensitized by the same NPLs and of bare TiO ₂ nanorod arrays.....	127
V.15.	UV-VIS absorption spectra of 9 layers thick CdSe NPLs before and after ligand exchange with OH ⁻ (indicated by full and dotted lines, respectively).....	128
V.16.	UV-VIS absorption spectra of ZnO nanorod arrays and 9 layers thick CdSe.OH NPLs in dispersion (indicated by orange full lines) and after attachment to ZnO nanorod arrays (indicated by orange dashed lines).....	128
V.17.	UV-VIS absorption spectra of TiO ₂ nanorod arrays and 9 layers thick CdSe.OH NPLs in dispersion (indicated by orange full lines) and after attachment to TiO ₂ nanorod arrays (indicated by orange dashed lines.....	129
V.18.	Raman spectra of 9 layers thick CdSe.SH NPLs, of ZnO nanorod arrays sensitized by the same NPLs and of bare ZnO nanorod arrays.....	129
V.19.	Raman spectra of 9 layers thick CdSe.SH NPLs, of TiO ₂ nanorod arrays sensitized by the same NPLs and of bare TiO ₂ nanorod arrays.....	130
V.20.	UV-VIS absorption spectra of 7, 9 and 11 layers thick CdSe NPLs before and after ligand exchange with MPA (indicated by green, orange and red full and dotted lines, respectively).....	131
V.21.	UV-VIS absorption spectra of ZnO nanorod arrays and 9 layers thick CdSe.MPA NPLs in dispersion (indicated by orange full lines) and after attachment to ZnO nanorod	

	arrays (indicated by orange dashed lines).....	131
V.22.	UV-VIS absorption spectra of TiO ₂ nanorod arrays and 9 layers thick CdSe.MPA NPLs in dispersion (indicated by orange full lines) and after attachment to TiO ₂ nanorod arrays (indicated by orange dashed lines).....	131
V.23.	Raman spectra of 9 layers thick CdSe.MPA NPLs, of ZnO nanorod arrays sensitized by the same NPLs and of bare ZnO nanorod arrays.....	132
V.24.	Raman spectra of 9 layers thick CdSe.MPA NPLs, of TiO ₂ nanorod arrays sensitized by the same NPLs and of bare TiO ₂ nanorod arrays.....	132
V.25.	UV-VIS absorption spectra of CdSe.OA QDs before and after ligand exchange with MPA, SH ⁻ and OH ⁻	133
V.26.	UV-VIS absorption spectra of ZnO nanorod arrays and CdSe.SH QDs in dispersion (indicated by green full lines) and after attachment to ZnO nanorod arrays (indicated by green dashed lines).....	134
VI.1.	Initial structural model of 5 layers thick CdSe.SH nanoplatelets attached to the ZnO (10-10) surface via SH ligands. Zn atoms are represented by grey, O by red, H by white, S by yellow, Cd by beige and Se by orange spheres.....	142
VI.2.	Experimental UV-VIS absorption spectra of 7, 9 and 11 layers thick CdSe.SH NPLs in dispersion (indicated by green, orange and red full lines, respectively) and after attachment to ZnO nanorod arrays (indicated by dashed lines of the corresponding colour, and by a dotted line after consequent washing with ethanol).....	143
VI.3.	a) Structure of the isolated subsystems: 5 layers thick (5L) CdSe.SH and 8 layers thick (8L) ZnO slabs. b) Optimized geometry of the CdSe.SH (5L) – ZnO (8L) heterostructure, viewed along the (001) and (0-10) directions.....	144
VI.4.	a) Computed Raman spectra of 5, 7 and 9 layers thick CdSe.SH NPLs. b) Experimental Raman spectra of 7, 9 and 11 layers thick CdSe.SH nanoplatelets dropcasted on FTO/glass substrates. R = ICdS /ICdSe. The spectra was normalized to the highest intensity peak for each curve.....	147
VI.5.	Decomposition of the CdSe- and CdS-related peaks in the experimental Raman spectra of 9 layers thick CdSe.SH NPLs.....	148
VI.6.	Computed Raman spectra of a) the CdSe.SH (5L) - ZnO heterostructure, b) a 5 layers thick CdSe.SH slab and c) the uppermost layer of a ZnO wurtzite (10-10) slab.....	150
VI.7.	Experimental Raman spectra of a) 7, b)9 and c) 11 layers thick CdSe.SH NPLs, of ZnO nanorod arrays sensitized by the same NPLs and of bare ZnO nanorod arrays.....	151
VI.8.	Two representations of the depth Raman profile of ZnO nanorod arrays sensitized by 7 layers thick CdSe.SH NPLs. The arrow indicating the z direction points towards the CdSe.SH nanoplatelet-coated surface of the sample.....	152
VI.9.	Comparison of the experimental Raman spectra of 7 layers thick CdSe.SH NPLs, of bare ZnO nanorod arrays and of ZnO nanorod arrays sensitized by the same NPLs. The latter is an inset from the 4th acquisition of the depth Raman profile reported in more detail in Figure VI.8.....	153
VI.10.	Band structures and density of states (DOS) of a) the bare CdSe.SH slab and b) the CdSe.SH (5L) – ZnO (8L) heterostructure. The Fermi energy of the bare CdSe.SH slab was chosen to be the zero of energy in each figure. The k points in the reciprocal space are defined as as $\Gamma (0\ 0\ 0)$, A $\left(0\ \frac{1}{3}\ 0\right)$, B $\left(\frac{1}{3}\ \frac{1}{3}\ \frac{1}{3}\right)$, C $\left(\frac{2}{3}\ \frac{1}{3}\ \frac{2}{3}\right)$, D $\left(\frac{2}{3}\ \frac{2}{3}\ \frac{2}{3}\right)$, E $\left(\frac{3}{3}\ \frac{2}{3}\ 0\right)$, F $\left(\frac{2}{3}\ \frac{1}{3}\ 0\right)$	156

VI.11.	a) Γ -point HOCO and b) Γ -point LUCO of the CdSe.SH–ZnO heterostructure. Isosurface level at 0.02 a.u. Spin densities (SD) of the reduced CdSe.SH (5L)–ZnO system (excess of alpha electron is indicated in blue) isosurface level at 0.00034 a.u.....	157
VI.12.	Spin densities (SD) of the reduced CdSe.SH (9L)–ZnO system (excess of alpha electron is indicated in blue) isosurface level at 0.00034 a.u.....	157
VII.1.	Cross-sectional and b) top SEM views of ZnO nanorods prepared as described in reference 4 c) Cross-sectional and d) top SEM views of the same ZnO nanorods sensitized by CdSe QDs in 12 SILAR cycles. Scale bar length (indicated as a yellow bar) is 500 nm.....	167
VII.2.	UV-VIS spectra of ZnO nanorod substrates sensitized with CdSe QDs in 2, 4, 6, 8, 10 and 12 SILAR cycles.....	168
VII.3.	Raman spectra of ZnO nanorod substrates sensitized with CdSe QDs in 2, 4, 6, 8, 10 and 12 SILAR cycles. Intensities were normalized to the highest intensity peak in each curve.....	169
VII.4.	XRD patterns of ZnO nanorod substrates sensitized with CdSe QDs in 6 and in 12 SILAR cycles with logarithmic intensity scales. The peaks marked with an asterisk correspond to the zinc benede phase of CdSe, according to the JCPDS standard N° 04-004-5648.....	170
VII.5.	UV-VIS absorption spectra of ZnO nanorod substrates sensitized with CdS QDs in 1 SILAR cycle, followed by CdSe QDs in 2, 4, 6, 8, 10 and 12 cycles.....	171
VII.6.	Raman spectra of ZnO nanorod substrates sensitized with CdS QDs in 1 SILAR cycle, followed by CdSe QDs in 2, 4, 6, 8, 10 and 12 cycles. Intensities were normalized to the highest intensity peak in each curve.....	172
VII.7.	a) XRD patterns of ZnO substrates after the deposition of a CdS layer in one SILAR cycle in a logarithmic intensity scale. b) XRD patterns of ZnS sphalerite according to the JCPDS reference N° 01-071-5976. c) XRD patterns of CdS zinc blende according to the JCPDS reference N° 01-079-3167.....	173
VII.8.	XRD patterns of ZnO nanorod substrates sensitized with CdS QDs in 1 SILAR cycle, followed by CdSe QDs in 6 and in 12 cycles, with logarithmic intensity scales. The peaks marked with an asterisk correspond to the zinc benede phase of CdSe, according to the JCPDS standard N° 04-004-5648.....	174
VII.9.	UV-VIS spectra of TiO ₂ nanorod substrates sensitized with CdSe QDs in 2, 4, 6, 8, 10 and 12 SILAR cycles.....	176
VII.10.	Raman spectra of TiO ₂ nanorod substrates sensitized with CdSe QDs in 2, 4, 6, 8, 10 and 12 SILAR cycles. Intensities were normalized to the highest intensity peak in each curve.....	176
VII.11.	XRD patterns of TiO ₂ nanorod arrays sensitized by CdSe QDs with the SILAR method in 6 and in 12 cycles with logarithmic intensity scales. The peaks marked with an asterisk correspond to the zinc benede phase of CdSe, according to the JCPDS standard N° 04-004-5648.....	177
AI.1.	a) Structure of the isolated subsystems: 9 layers thick (9L) CdSe.SH and 8 layers thick (8L) ZnO slabs. b) Optimized geometry of the CdSe.SH (9L) – ZnO (8L) heterostructure, viewed along the (001) and (0-10) directions.....	197
AI.2.	Computed Raman spectra of a) the CdSe.SH (9L) - ZnO system b) a 9 layers thick CdSe.SH slab and c) the uppermost layer of a ZnO wurtzite (10-10) slab.....	199
AI.3.	Band structures and density of states (DOS) of a) the bare 9 layers thick CdSe.SH slab	

and b) the CdSe.SH (9L) – ZnO (8L) heterostructure. The Fermi energy of the bare 9 layers thick CdSe.SH slab was chosen to be the zero of energy in each figure. The k points in the reciprocal space were defined as Γ (0 0 0), A $\left(0 \frac{1}{3} 0\right)$, B $\left(\frac{1}{3} \frac{1}{3} \frac{1}{3}\right)$, C $\left(\frac{2}{3} \frac{1}{3} \frac{2}{3}\right)$, D $\left(\frac{2}{3} \frac{2}{3} \frac{2}{3}\right)$, E $\left(\frac{3}{3} \frac{2}{3} 0\right)$, F $\left(\frac{2}{3} \frac{1}{3} 0\right)$

200

AII.1.	QDSCs with <i>ex situ</i> prepared QDs.....	201
AII.1.1.	7SZL solar cell J-V curves.....	201
AII.1.2.	9SZL solar cell J-V curves.....	201
AII.1.3.	11SZL solar cell J-V curves.....	202
AII.1.4.	9STL solar cell J-V curves.....	202
AII.2.	QDSCs with <i>in situ</i> prepared QDs.....	203
AII.2.1.	C12Z solar cell J-V curves.....	203
AII.2.2.	CS12Z solar cell J-V curves.....	204
AII.2.3.	C6T solar cell J-V curves.....	204
AII.2.4.	C12T solar cell J-V curves.....	205

List of tables

III.1.	Experimental and computed lattice and internal (u , the fractional coordinate of the Se atoms along the c axis) parameters (in Å) of the CdSe wurtzite and zinc blende phases calculated with different exchange-correlation functionals and basis sets. For each functional, the best results (with respect to experimental data) are given in bold.	82
III.2.	Calculated and experimental band gaps (in eV) for the CdSe wurtzite and zinc blende structures and total energy difference (in meV/atom) between the wurtzite and zinc blende phases of bulk CdSe, obtained with different Hamiltonians and basis sets. For each Hamiltonian, the best results for band gaps (with respect to experimental value) are given in bold.....	85
III.3.	Structural parameters (in Å) of the CdSe wurtzite (10-10) surface after relaxation for 8 and 9 layers thick slabs, computed in the present study, in comparison with experimental (LEED and LEPD) and other theoretical data. (nd: no data available)	92
III.4.	Mulliken atomic charges (q) and overlap populations (b) for the CdSe wurtzite (10-10) surface, obtained at 8 layers, each layer containing two Cd-Se pairs/primitive cell (see Figure III.6.). n refers to the number of layers, $n=1$ being the outermost one with respect to the [10-10] direction indicated by an arrow. All data in $ e^- $	94
IV.1.	Relaxed geometrical parameters (in Å) of the bidentate CdSe.HCOO, the CdSe.SH and the CdSe.OH slabs.	105
IV.2.	Computed Mulliken atomic charges (in $ e^- $) for 5 and 13 layers thick CdSe zinc blende slabs with HCOO ⁻ , OH ⁻ or SH ⁻ ligands adsorbed on both of its [100] basal planes. Cd and Se atoms are indicated as Cd _{n} and Se _{n} where $n=1-13$ and n is the number of atomic layers, $n=1$ and $n=5$ (13) being the outermost layer of the slab. The atoms in equivalent positions with respect to the (100) surfaces are shown in parentheses.....	109
IV.3.	Computed Mulliken atomic orbital populations for 5 layers thick CdSe zinc blende slab with HCOO ⁻ , OH ⁻ or SH ⁻ ligands adsorbed on both of its [100] basal planes. All values are expressed in $ e^- $	110
IV.4.	Computed Mulliken atomic orbital populations for 13 layers thick CdSe zinc blende slabs with HCOO ⁻ , OH ⁻ or SH ⁻ ligands adsorbed on both of its [100] basal planes. All values are expressed in $ e^- $	111
IV.5.	Computed and experimental band gaps (in eV) of CdSe zinc blende slabs stabilized with HCOO ⁻ , SH ⁻ and OH ⁻ ligands on their (100) basal planes. nd: no data available.....	114
V.1.	Raman shift of the CdSe LO peak before and after the CdSe.OH NPLs are attached to ZnO or TiO ₂ nanorods.....	130
V.2.	Raman shifts of the CdSe LO peaks before and after the CdSe.MPA NPLs are attached to ZnO or TiO ₂ nanorods.....	133
VI.1.	Lattice parameters (a , b in Å and γ in degrees) and relevant interatomic distances (d (Cd-Se), d (Cd-S), d (Zn-S), d (O-H) of the isolated subsystems and of the optimized	144

	heterostructure. $d^1(\text{Zn-O})$ and $d^2(\text{Zn-O})$ correspond to Zn-O distances in the first and in the second ZnO slab layer, respectively. $\delta_z^1(\text{Zn})$ and $\delta_z^1(\text{O})$ are the shifts, upon optimization, of Zn and O atoms along the z axis compared to their initial positions in the uppermost layer of the ZnO slab.	
VI.2.	Computed and experimental Raman shifts (in cm^{-1}) of the bulk modes of CdS, CdSe, ZnO. TO and LO correspond to the transverse and longitudinal optical modes, respectively.	146
VI.3.	Experimental Raman shifts (in cm^{-1}) of notable modes in the Raman spectra of the 7 layers thick CdSe.SH NPLs, of ZnO nanorods sensitized by the same NPLs, and of the bare ZnO nanorods.....	153
VI.4.	Computed band gaps of the isolated CdSe.SH NPLs and CdSe.SH – ZnO heterostructures. Experimental and theoretical band gaps referred to as “exp” and “theo”. The nature of band gaps (direct (d) and indirect (i)) is also indicated.	156
VII.1.	J-V curve parameters of all-solid state QDSCs based on pre-synthesized CdSe.SH NPLs.....	164
VII.2.	J-V curve parameters of QDSCs prepared with a liquid electrolyte and pre-synthesized CdSe.SH nanocrystals attached to ZnO nanorod arrays.....	166
VII.3.	J-V curve parameters of QDSCs prepared with a liquid electrolyte and pre-synthesized CdSe.SH NPLs attached to TiO_2 nanorod arrays.....	166
VII.4.	Determination of the crystallite size in CdSe QD thin films from the Scherrer equation CdS+12 corresponds to the sample sensitized with CdS QDs in 1 SILAR cycle, followed by CdSe QDs in 12 SILAR cycles.	174
VII.5.	J-V curve parameters of QDSCs prepared with a liquid electrolyte and ZnO nanorod arrays in situ sensitized with CdSe and CdS QDs.....	175
VII.6.	J-V curve parameters of QDSCs prepared with a liquid electrolyte and TiO_2 nanorod arrays in situ sensitized with CdSe QDs.....	178
AI.1.	Lattice parameters (a, b in Å and γ in degrees) and interatomic distances of the isolated subsystems and the optimized CdSe.SH (9L) – ZnO (8L) heterostructure. d^1 and d^2 correspond to Zn-O distances in the uppermost ZnO slab layer and in the second layer, respectively. $\delta_z^1(\text{Zn})$ and $\delta_z^1(\text{O})$ are the shifts, upon optimization, of Zn and O atoms along the z axis compared to their initial positions in the uppermost layer of the ZnO slab.	198
AI.2.	Characteristics of the computed band gaps of the isolated subsystems and the constructed heterostructure.....	200

Annexe I. Geometrical and electronic properties of the CdSe.SH (9L) – ZnO system

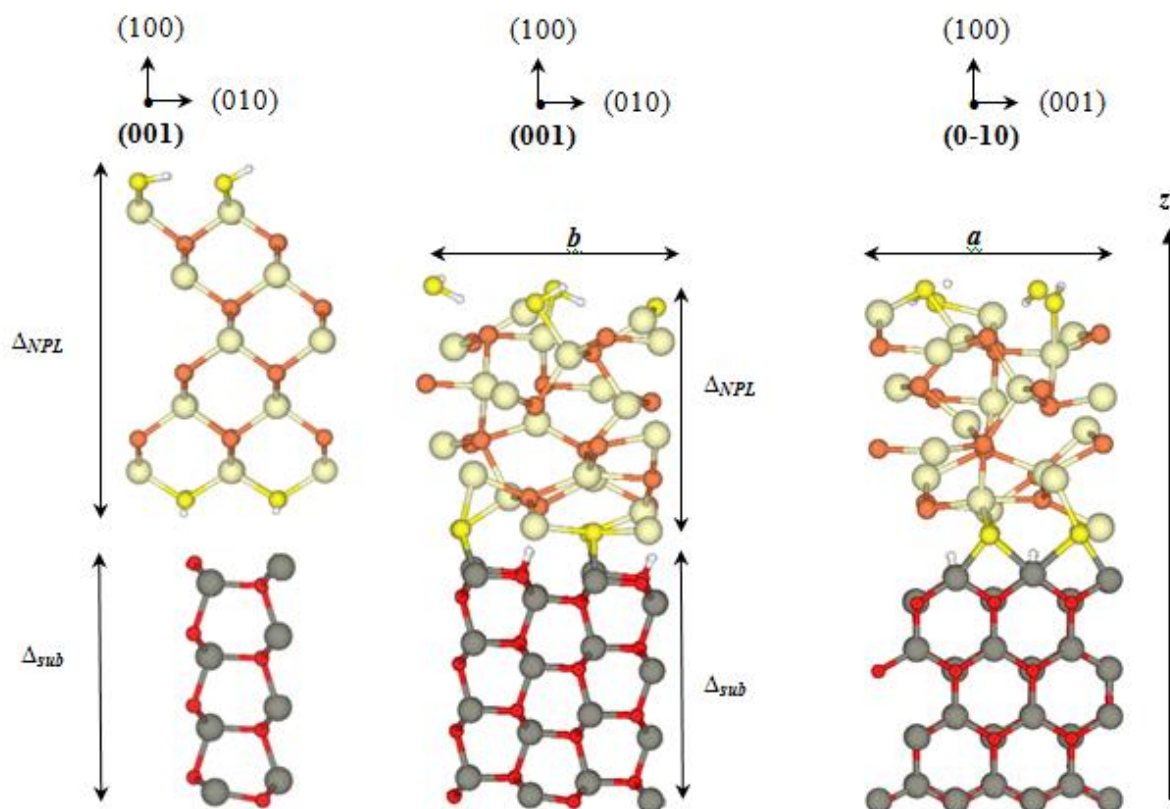


Figure AI.1. a) Structure of the isolated subsystems: 9 layers thick (9L) CdSe.SH and 8 layers thick (8L) ZnO slabs. b) Optimized geometry of the CdSe.SH (9L) – ZnO (8L) heterostructure, viewed along the (001) and (0-10) directions.

Annexes

	CdSe.SH (9L) NPL	ZnO (8L) slab	Optimized CdSe.SH (9L)– ZnO (8L) interface
a	8.79	9.93	9.88
b	8.79	10.50	10.33
Δ_{NPL}	16.16	--	11.69
Δ_{sub}	--	9.42	9.89
γ	90.00	90.00	90.25
d (Cd-Se)	2.67-2.70	--	2.59-2.84
d (Cd-S)	2.60	--	2.52-2.68
d (Zn-S)	--	--	2.39-2.69
d (O-H)	--	--	0.98-1.00
d^1 (Zn-O)	--	1.86	2.05-2.08
d^2 (Zn-O)	--	2.00	2.00
δ_z (Zn)	--	--	0.78
δ_z (O)	--	--	0.33

Table A1.1. Lattice parameters (a , b in Å and γ in degrees) and interatomic distances of the isolated subsystems and the optimized CdSe.SH (9L) – ZnO (8L) heterostructure. d^1 and d^2 correspond to Zn-O distances in the uppermost ZnO slab layer and in the second layer, respectively. δ_z^1 (Zn) and δ_z^1 (O) are the shifts, upon optimization, of Zn and O atoms along the z axis compared to their initial positions in the uppermost layer of the ZnO slab.

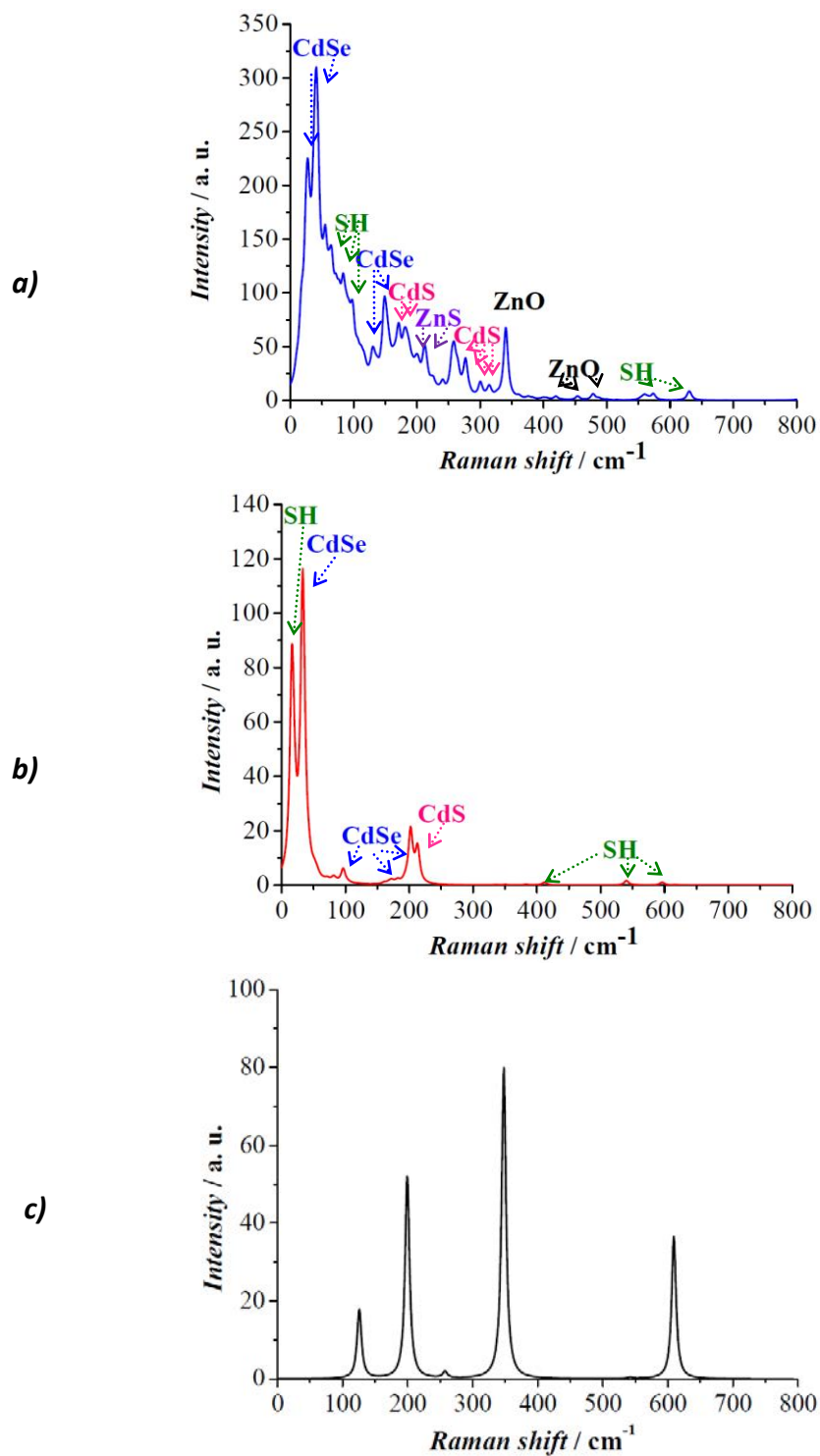


Figure A1.2. Computed Raman spectra of a) the CdSe.SH (9L) - ZnO system b) a 9 layers thick CdSe.SH slab and c) the uppermost layer of a ZnO wurtzite (10-10) slab.

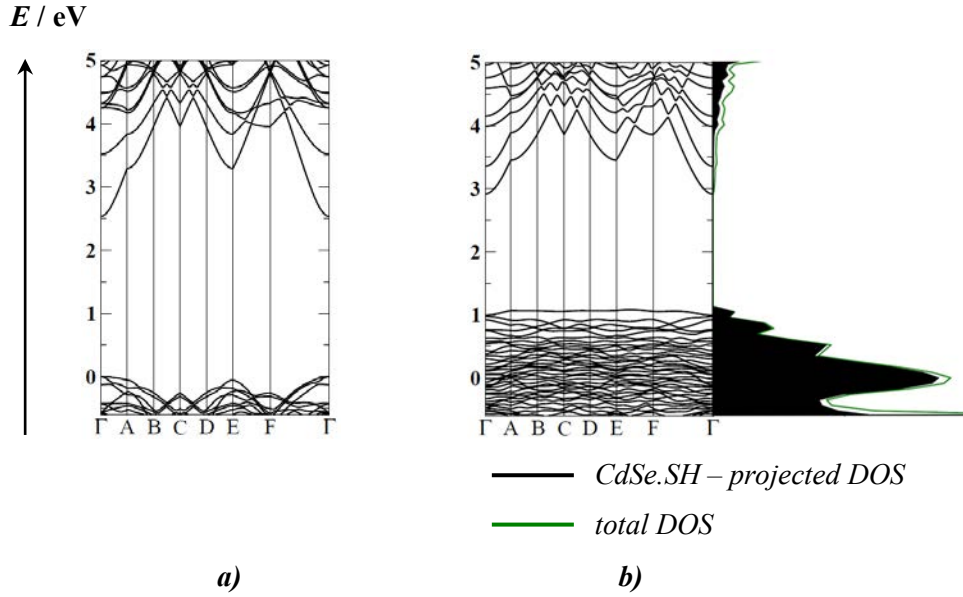


Figure A1.3. Band structures and density of states (DOS) of a) the bare 9 layers thick CdSe.SH slab and b) the CdSe.SH (9L) – ZnO (8L) heterostructure. The Fermi energy of the bare 9 layers thick CdSe.SH slab was chosen to be the zero of energy in each figure. The k points in the reciprocal space were defined as $\Gamma (0\ 0\ 0)$, A $\left(0\ \frac{1}{3}\ 0\right)$, B $\left(\frac{1}{3}\ \frac{1}{3}\ \frac{1}{3}\right)$, C $\left(\frac{2}{3}\ \frac{1}{3}\ \frac{2}{3}\right)$, D $\left(\frac{2}{3}\ \frac{2}{3}\ \frac{2}{3}\right)$, E $\left(\frac{3}{3}\ \frac{2}{3}\ 0\right)$, F $\left(\frac{2}{3}\ \frac{1}{3}\ 0\right)$.

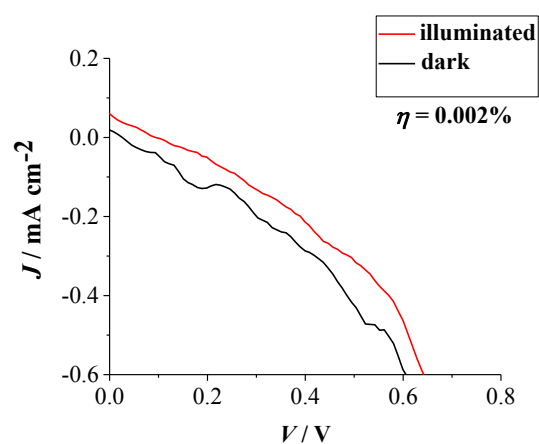
	CdSe.SH 5L	ZnO 8L	CdSe.SH (5L) - ZnO
Top of VB in k -space	$\Gamma (0\ 0\ 0)$	$\Gamma (0\ 0\ 0)$	W $\left(\frac{4}{6}\ \frac{3}{6}\ \frac{4}{6}\right)$
Bottom of CB in k -space	$\Gamma (0\ 0\ 0)$	$\Gamma (0\ 0\ 0)$	$\Gamma (0\ 0\ 0)$
	CdSe.SH 9L	ZnO 8L	CdSe.SH (9L) - ZnO
Top of VB in k -space	$\Gamma (0\ 0\ 0)$	$\Gamma (0\ 0\ 0)$	W $\left(\frac{4}{6}\ \frac{3}{6}\ \frac{4}{6}\right)$
Bottom of CB in k -space	$\Gamma (0\ 0\ 0)$	$\Gamma (0\ 0\ 0)$	$\Gamma (0\ 0\ 0)$

Table A1.2. Characteristics of the computed band gaps of the isolated subsystems and the constructed heterostructure

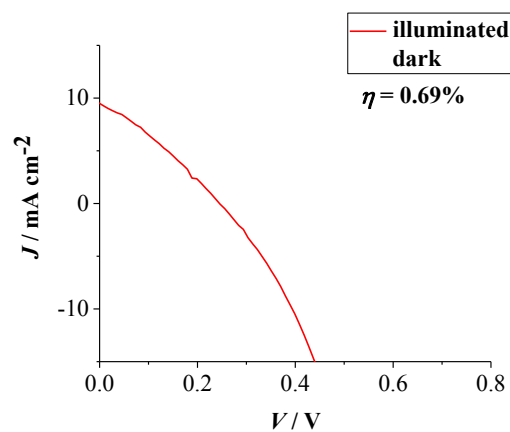
Annexe II. J-V curves of the solar cells tested in Chapter VII.

All.1. QDSCs with *ex-situ* prepared QDs

All.1.1. 7SZL solar cell J-V curves

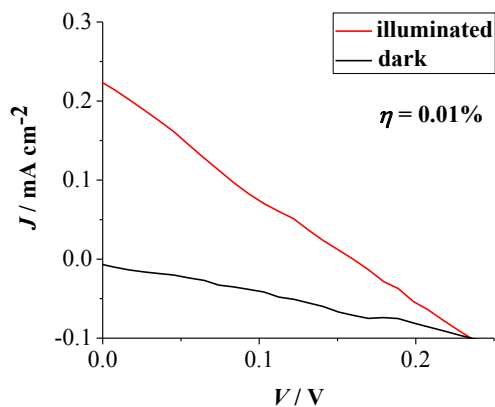
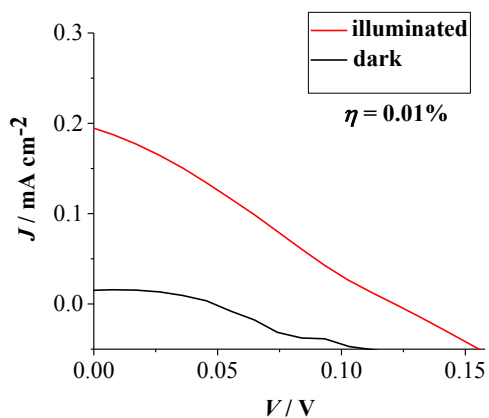


All.1.2. 9SZL solar cell J-V curves

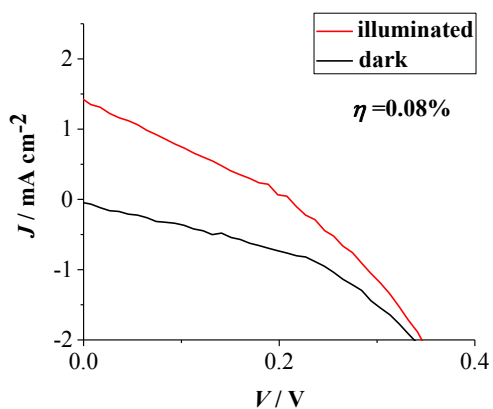
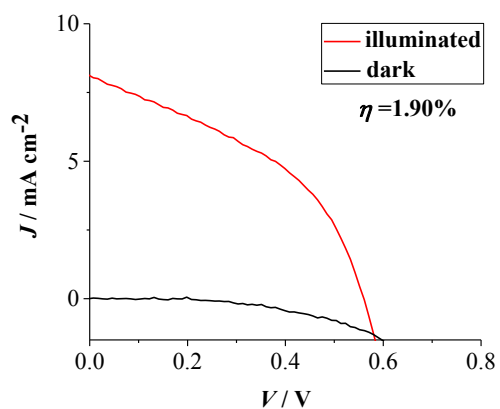


Annexes

11SZL solar cell J-V curves

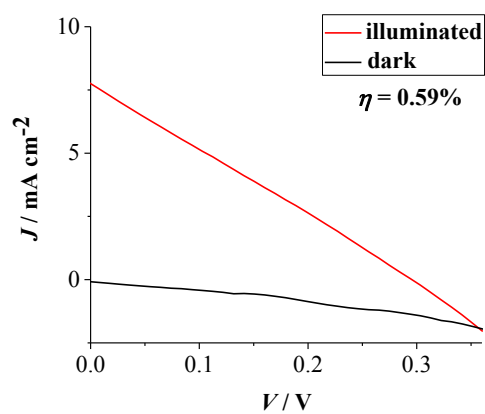
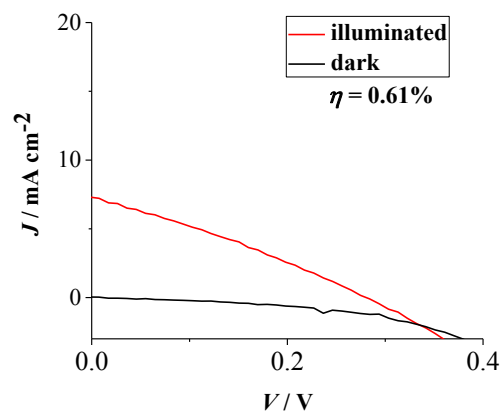
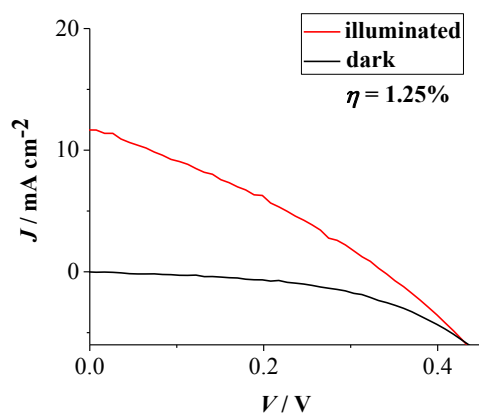


9STL solar cell J-V curves



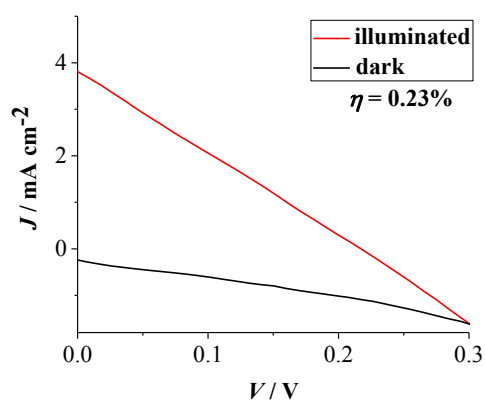
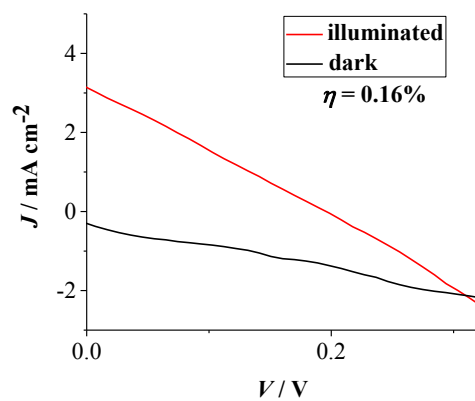
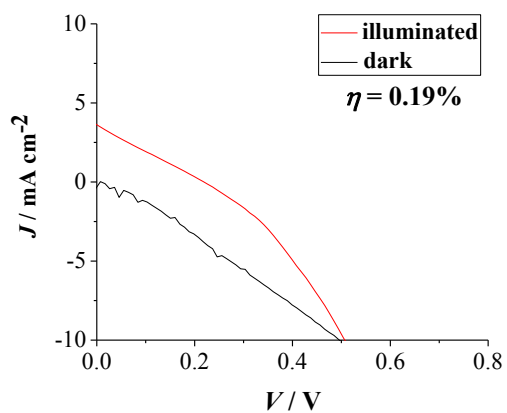
All.2. QDSCs with *in situ* prepared QDs

All.2.1. C12Z solar cell J-V curves

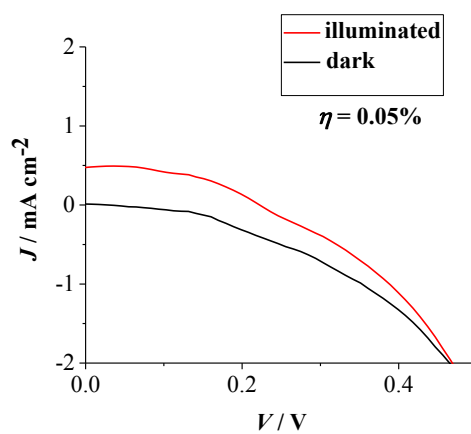


Annexes

All.2.2. CS12Z solar cell J-V curves



All.2.3. C6T solar cell J-V curves



Annexes

All.2.4. C12T solar cell J-V curves

